



저작자표시-비영리-변경금지 2.0 대한민국

이용자는 아래의 조건을 따르는 경우에 한하여 자유롭게

- 이 저작물을 복제, 배포, 전송, 전시, 공연 및 방송할 수 있습니다.

다음과 같은 조건을 따라야 합니다:



저작자표시. 귀하는 원저작자를 표시하여야 합니다.



비영리. 귀하는 이 저작물을 영리 목적으로 이용할 수 없습니다.



변경금지. 귀하는 이 저작물을 개작, 변형 또는 가공할 수 없습니다.

- 귀하는, 이 저작물의 재이용이나 배포의 경우, 이 저작물에 적용된 이용허락조건을 명확하게 나타내어야 합니다.
- 저작권자로부터 별도의 허가를 받으면 이러한 조건들은 적용되지 않습니다.

저작권법에 따른 이용자의 권리는 위의 내용에 의하여 영향을 받지 않습니다.

이것은 [이용허락규약\(Legal Code\)](#)을 이해하기 쉽게 요약한 것입니다.

[Disclaimer](#)

A THESIS  
FOR THE DEGREE OF DOCTOR OF PHILOSOPHY

**A Study on Contact-electrification Behaviour of  
Metal-Organic Frameworks for Triboelectric  
Nanogenerators and Self-powered Sensors**

GAURAV KHANDELWAL

Faculty of Applied Energy Systems  
Department of Mechatronics Engineering

GRADUATE SCHOOL  
JEJU NATIONAL UNIVERSITY

AUGUST 2020

# **A Study on Contact-electrification Behaviour of Metal-Organic Frameworks for Triboelectric Nanogenerators and Self-powered Sensors**

**Gaurav Khandelwal**

(Supervised by Professor Kim Sang-Jae)

A thesis submitted in partial fulfillment of the requirement for the degree of  
Doctor of Philosophy  
2020.06.19

The thesis has been examined and approved

---

Thesis Director,  
Prof. Kim Bumsuk

Professor, Faculty of Wind Energy Engineering  
Graduate School, Jeju National University

---

Thesis Committee Member,  
Prof. Kim Woo Young

Professor, Department of Electronic Engineering  
Jeju National University

---

Thesis Committee Member,  
Prof. Lee Hyomin

Professor, Department of Chemical Engineering  
Jeju National University

---

Thesis Committee Member,  
Prof. Choi Min Seok

Professor, Department of Telecommunication Engineering  
Jeju National University

---

Thesis Committee Member,  
Prof. Kim Sang-Jae

Professor, Department of Mechatronics Engineering  
Jeju National University

---

June 2020

**Faculty of Applied Energy System  
Department of Mechatronics Engineering  
Graduate School  
Jeju National University  
Republic of Korea**

**Dedicated  
to my Beloved  
Family and  
Friends**





## Acknowledgment

I take this privilege and pleasure to acknowledge the contributions of individuals who have been inspirational and supportive throughout my work. My work bears the imprint of all those people; I am grateful to. It is a pleasure to convey my gratitude to all of them in my humble acknowledgment.

First of all, I sincerely acknowledge my gratitude to my guide, Prof. Sang Jae Kim, for his excellent guidance, keen interest, continuous encouragement, and affection throughout this study and endowed me with the most precious knowledge to see success in my endeavor. I wish to reciprocate feelings of thanks to each member of Nano Materials and Systems Laboratory (NMSL). I express my sincere thanks to the alumni of the NMSL for their encouragement during the work. I will never forget to express thanks to all my friends, seniors, and juniors for their constant formal and informal support. My thanks are also to all other members (teaching and nonteaching) for their help at all stages of my work.

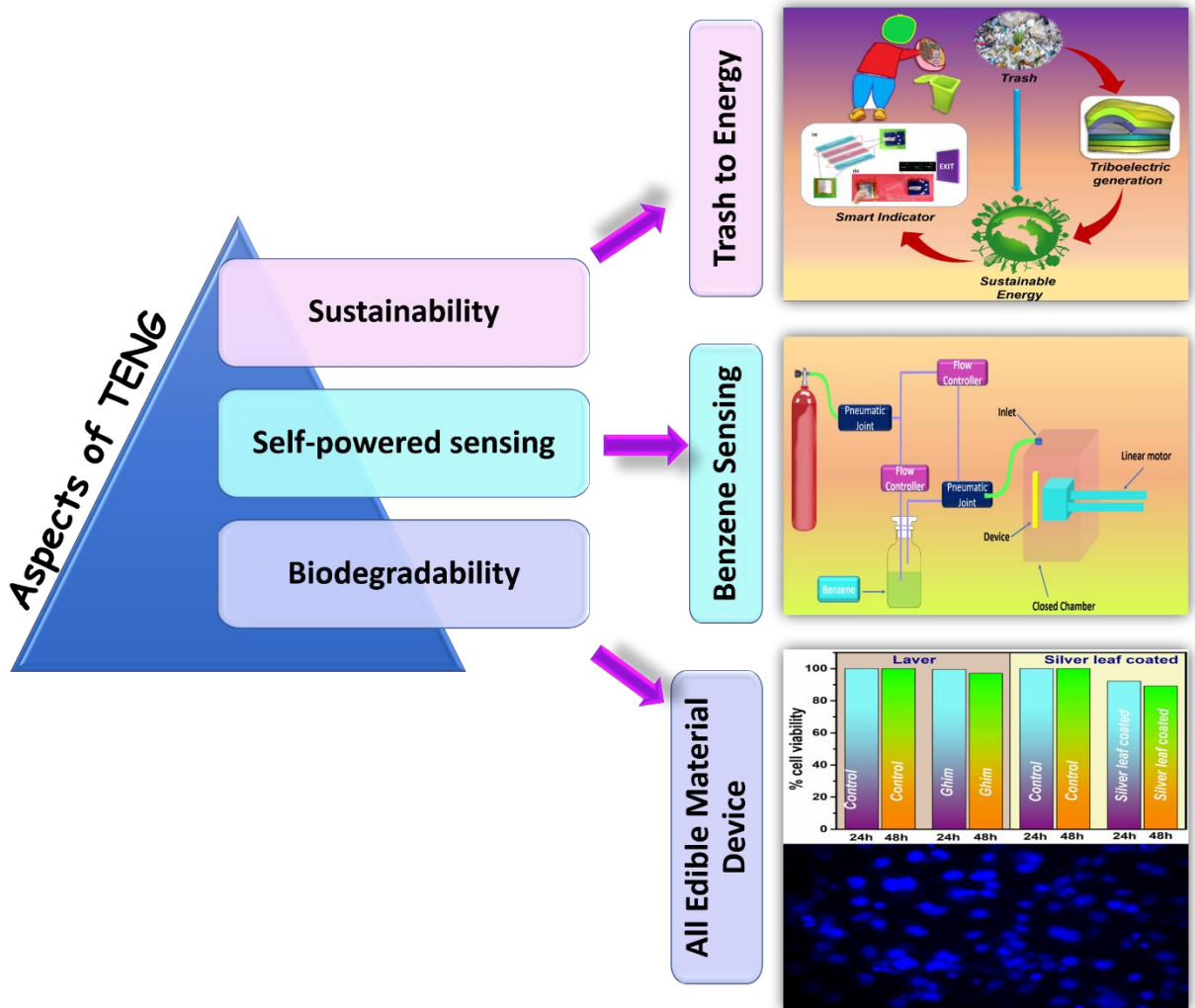
Last in the line, but first in my mind, I extend my most profound sense of gratitude to my Family and my Beloved wife for supporting in all the conditions and whose belief, love, patience, and blessings made me complete this project.

Thank you

*Gaurav Khandelwal*

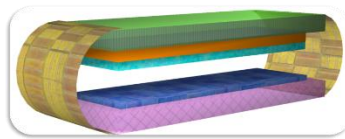
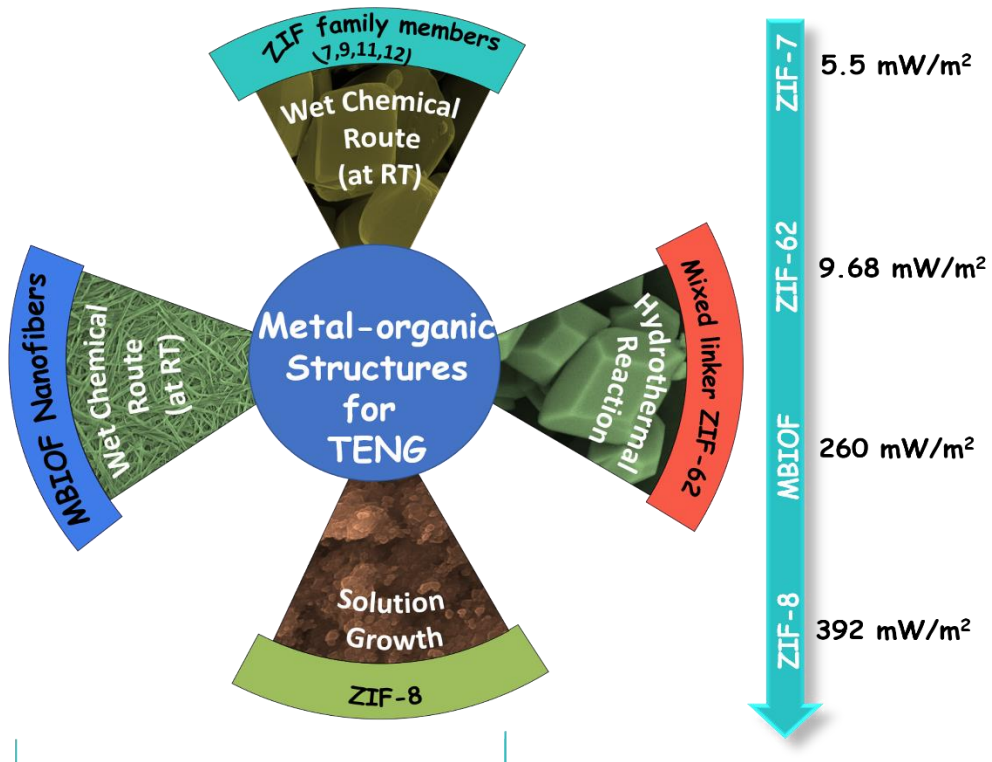
# Thesis Overview-I

## Three aspects of Triboelectric Nanogenerator

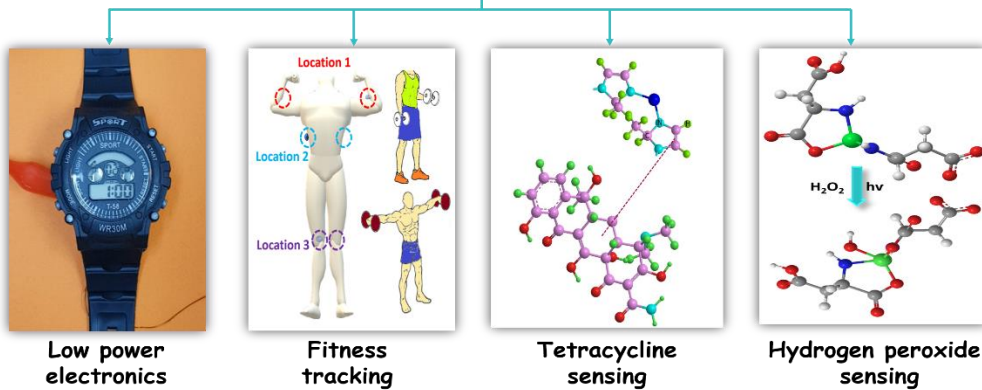


## Thesis Overview-II

### Design of metal-organic frameworks based triboelectric nanogenerators for self-powered applications



Contact-separation TENG



## Contents

<b>Contents</b>	<b>i</b>
<b>Nomenclature</b>	<b>vii</b>
<b>List of Tables</b>	<b>ix</b>
<b>List of figures</b>	<b>x</b>
<b>Abstract – Hangul</b>	<b>xxviii</b>
<b>Abstract – English</b>	<b>xxxiii</b>

## Chapter -I

### Introduction

1.1. Background	1
1.2 Fundamentals of TENG	3
1.3 Theoretical origin of TENG	5
1.4 Working modes of TENG	7
1.4.1 Vertical contact-separation (C-S) mode	7
1.4.2 Lateral sliding (LS) mode	8
1.4.3 Single electrode (SE) mode	8
1.4.4 Freestanding triboelectric-layer (FT) mode	9
1.5 Figure of merits	10
1.6 Materials for TENG	12
1.7 Research progress of TENG	16
1.8 Applications of TENG	17
1.9 Objective and scope of the thesis	19
1.10 Structure of the thesis	21

## Chapter -II

### Materials and Methods

2.1	Chemicals and reagents	30
2.2.	Cell lines	32
2.3	Apparatus	32
2.4	Electrical Characterization	34
2.5	Material Characterization	36
	2.5.1 X-ray diffraction	36
	2.5.2 Raman spectroscopy	37
	2.5.3 Fourier transform infrared spectroscopy	37
	2.5.4 Field-emission scanning electron microscopy	38
	2.5.5 Energy-dispersive X-ray spectroscopy	39
	2.5.6 Atomic force microscopy and Kelvin probe force microscopy	39
	2.5.7 3D optical surface profiler	41
	2.5.8 Thermogravimetric analysis	42
	2.5.9 Ultraviolet-visible spectroscopy	42
2.6	Cell line studies	43
	2.6.1 Method I	43
	2.6.2 Method II	44
	2.6.3 DAPI staining	44

## Chapter -III

### 3.1 Trash to Energy: A Facile, Robust and Cheap Approach for Mitigating Environment Pollutant Using Household Triboelectric Nanogenerator

3.1.1	Introduction	48
3.1.2	Experimental Section	51
3.1.2.1	Fabrication of the H-TENG	51
3.1.3	Results and Discussion	52
3.1.4	Conclusion	68

### 3.2 Phase Inversion Enabled Energy Scavenger: A Multifunctional Triboelectric Nanogenerator as Benzene Monitoring System

3.2.1	Introduction	78
3.2.2	Experimental	80
3.2.2.1	Preparation of PVDF/TiO <sub>2</sub> film	80
3.2.2.2	Preparation of PVDF/TiO <sub>2</sub> by the phase-inversion process	80
3.2.2.3	Preparation of Cellulose acetate film	81
3.2.2.4	Fabrication of triboelectric nanogenerator	81
3.2.3	Results and Discussions	82
3.2.4	Conclusion	96

### 3.3 All Edible Materials Derived Biocompatible and Biodegradable Triboelectric Nanogenerator

3.3.1	Introduction	104
3.3.2	Experimental	105
3.3.2.1	Sample preparation for Cell studies	105
3.3.2.2	Cell viability assay (MTT assay)	105
3.3.2.3	Cell imaging	106
3.3.2.4	DAPI staining	106

3.3.2.5 Device fabrication	106
3.3.3 Results and Discussions	106
3.3.4 Conclusion	119

## CHAPTER IV

### **Zeolitic Imidazole Framework: A Metal-Organic Framework Subfamily Members for Triboelectric Nanogenerator**

4.1 Introduction	126
4.2 Experimental	128
4.2.1 Synthesis of ZIFs	128
4.2.2 Fabrication of ZIF-TENG	129
4.3 Results and Discussions	129
4.4 Conclusion	144

## CHAPTER V

### **ZIF-62: A Mixed Linker Metal-organic Framework for Triboelectric Nanogenerator**

5.1 Introduction	152
5.2 Experimental	153
5.2.1 Synthesis of ZIF-62	153
5.2.2 Crystal Structure	153
5.2.3 Device fabrication	153
5.3 Results and Discussions	154
5.4 Conclusion	165

## CHAPTER VI

### **Metal-organic Framework: A Novel Material for Triboelectric Nanogenerator based Self-powered Sensors and Systems**

6.1	Introduction	172
6.2	Experimental	174
	6.2.1 Growth of ZIF-8	174
	6.2.2 Fabrication of MOF-TENG	174
6.3	Results and Discussions	174
6.4	Conclusion	193

## CHAPTER VII

### **Metal-biomolecule Nanofibers: A Novel Material for Triboelectric Nanogenerator and Self-powered Sensors**

7.1	Introduction	200
7.2	Experimental	202
	7.2.1 Synthesis of Cu-Asp NFs	202
	7.2.2 Synthesis of MgO nanosheets	202
	7.2.3 Coating on various substrate	202
	7.2.4 Fabrication of TENG	202
7.3	Results and Discussions	204
7.4	Conclusion	221



**CHAPTER VIII**  
**Summary and Future Perspective**

8.1	Summary	225
8.2	Future Perspective	228
<b>Appendix A</b>		<b>230</b>
<b>Appendix B</b>		<b>233</b>
<b>Appendix C</b>		<b>236</b>
<b>Appendix D</b>		<b>237</b>
<b>Declaration</b>		<b>238</b>

## Nomenclature

<b>COTS</b>	Commercial of-the-shelf
<b>TENG</b>	Triboelectric nanogenerator
<b>C-S</b>	Contact-separation
<b>LS</b>	Lateral sliding
<b>SE</b>	Single electrode
<b>FT</b>	Freestanding
<b>FOM</b>	Figure of merits
<b>CFT</b>	Contact freestanding triboelectric
<b>SFT</b>	Sliding freestanding triboelectric
<b>SEC</b>	Single electrode contact
<b>TECD</b>	Triboelectric charge density
<b>MOF</b>	Metal organic framework
<b>MBIOF</b>	Metal biomolecule framework
<b>XRD</b>	X-ray diffraction
<b>FE-SEM</b>	Field emission scanning electron microscope
<b>EDS</b>	Energy dispersive X-ray spectroscopy
<b>FT-IR</b>	Fourier transform infrared
<b>AFM</b>	Atomic force microscope
<b>KPFM</b>	Kelvin probe force microscope
<b>TGA</b>	Thermogravimetric

<b>UV</b>	Ultraviolet
<b>LED</b>	Light emitting diode
<b>H-TENG</b>	Household triboelectric nanogenerator
<b>PP</b>	Polypropylene
<b>PE</b>	Polyethylene
<b>PU</b>	Polyurethane
<b>AC</b>	Alternating current
<b>DC</b>	Direct current
<b>VOC</b>	Volatile organic compound
<b>E-TENG</b>	Edible TENG
<b>ZIF</b>	Zeolitic imidazole framework
<b>OC</b>	Open circuit
<b>CCDC</b>	Cambridge crystallographic data centre
<b>NF</b>	Nanofibers

## List of Tables

<b>Table No.</b>	<b>Table Caption</b>	<b>Pg. No.</b>
<b>Table 2.1</b>	List of chemicals and reagents used in the research work.	<b>30-32</b>
<b>Table 2.2</b>	The details of the used cell lines.	<b>32</b>
<b>Table 2.3</b>	List of the apparatus used for the research.	<b>32-33</b>
<b>Table 3.1.1</b>	Band assignment of polyethylene revealed from Raman spectra.	<b>54</b>
<b>Table 3.1.2</b>	Band assignment of polypropylene revealed from Raman spectra.	<b>55</b>
<b>Table 3.1.3</b>	Band assignment of polyurethane foam revealed from Raman spectra.	<b>55</b>
<b>Table 3.1.4</b>	Band assignments of the substrate as revealed from Raman spectra.	<b>56</b>
<b>Table 3.1.5</b>	Band assignments of polyethylene as revealed from FT-IR spectra.	<b>56</b>
<b>Table 3.1.6</b>	Band assignments of polypropylene as revealed from FT-IR spectra.	<b>56-57</b>
<b>Table 3.1.7</b>	Band assignments of polyurethane foam as revealed from FT-IR spectra.	<b>57</b>
<b>Table 3.1.8</b>	Band assignments of the substrate as revealed from FT-IR spectra.	<b>57</b>
<b>Table 4.1</b>	The XRD peak position and indices for ZIF-7, ZIF-9, ZIF-11, and ZIF12.	<b>133</b>
<b>Table 6.1</b>	The detailed band assignment of Raman spectra.	<b>180</b>

## List of Figures

Figure No.	Figure Caption	Pg. No.
<b>Figure 1.1</b>	The power requirement of the various COTS components	<b>2</b>
<b>Figure 1.2</b>	The comparison of various mechanical energy harvester, summarizing the principle, advantages, and disadvantages of the harvesting approach.	<b>3</b>
<b>Figure 1.3</b>	(a) Wimshurst machine and Van de Graaff generator. Reproduced with permission [7]. Copyright American Chemical Society. (b) The demonstration of van de Graaff generator at MIT museum.	<b>4</b>
<b>Figure 1.4</b>	(a) The C-S mode TENG for displacement current model. (b) The TENG representation using the capacitor model.	<b>6</b>
<b>Figure 1.5</b>	Working modes of TENG (a) Vertical contact-separation mode. (b) Lateral sliding mode. (c) Single electrode mode and (d) Freestanding triboelectric layer mode.	<b>9</b>
<b>Figure 1.6</b>	The illustration of factors affecting the output of TENG and figure of merits for TENG.	<b>11</b>
<b>Figure 1.7</b>	Triboelectric series developed by AlphaLab.	<b>12</b>
<b>Figure 1.8</b>	Triboelectric series of 2D layered materials.	<b>14</b>
<b>Figure 1.9</b>	The quantified triboelectric series developed by Zou et al.	<b>15</b>
<b>Figure 1.10</b>	The roadmap summarizing the progress in the TENG.	<b>17</b>

<b>Figure 1.11</b>	Applications of TENG.	<b>18</b>
<b>Figure 2.1</b>	Linear motor for applying force to the device during electrical measurement.	<b>34</b>
<b>Figure 2.2</b>	Electrical characterization system. (a) High impedance electrometer. (b) A mixed domain oscilloscope. (c) The electrostatic voltmeter and (d) Low noise current preamplifier.	<b>35</b>
<b>Figure 2.3</b>	PAAnalytical Empyrean XRD measurement system.	<b>36</b>
<b>Figure 2.4</b>	Horiba LabRAM HR Raman measurement system.	<b>37</b>
<b>Figure 2.5</b>	Thermo Scientific Nicolet-6700 FT-IR measurement system.	<b>38</b>
<b>Figure 2.6</b>	Tescan MIRA 3 FE-SEM system.	<b>39</b>
<b>Figure 2.7</b>	Bruker Multimode 8 AFM system.	<b>40</b>
<b>Figure 2.8</b>	Nanosystem NV 2200 3D optical surface profiler.	<b>41</b>
<b>Figure 2.9</b>	TA instruments TGA and DSC system.	<b>42</b>
<b>Figure 2.10</b>	Perkim Elmer Lambda 950, UV-VIS spectrophotometer.	<b>43</b>
<b>Figure 3.1.1</b>	Global statistics for generated plastic waste. (a) The proportion of plastic waste reaching the ocean relative to the total plastic waste produced. (b) The distribution of plastic waste in different countries according to PlasticsEurope, EuPC, EuPR, EPRO and Consultic (2009). (c) Projection of plastic waste production according to Ocean Summit 2015, plastic items collected from coastal areas according to international coastal clean-up data for 2014, and the number of taxa affected by plastic waste that reaches the ocean.	<b>49</b>

<b>Figure 3.1.2</b>	(a) The recycled waste materials used for the fabrication of household triboelectric nanogenerator (H-TENG). (b) Three-dimensional schematic illustration of the H-TENG. (c) Schematic illustration of the H-TENG fabrication.	<b>52</b>
<b>Figure 3.1.3</b>	Digital images. (a) The contact-separation distance of the device. (b) The thickness of the materials used in the device1-6.	<b>53</b>
<b>Figure 3.1.4</b>	(a–b) Raman spectra recorded at room temperature for the waste materials and supporting substrate. (c–d) Fourier transform-infrared (FT-IR) spectra recorded at room temperature for the waste materials and supporting substrate. (e) Chemical structures of the materials.	<b>54</b>
<b>Figure 3.1.5</b>	(a) The basic electricity generation mechanism for the H-TENG in the vertical contact-separation configuration. (b–c) Voltage and current measurement results of the H-TENG with a working area of 9 cm <sup>2</sup> .	<b>59</b>
<b>Figure 3.1.6</b>	Electrical performance of the H-TENG as an energy harvester. (a) Output voltage, power and power density of the PP-H-TENG for external load matching. (b) Output voltage, power and power density of the PE-H-TENG for external load matching. (c–d) Output voltages for the PP- and PE-H-TENGs during the application of the external force for 3,000 cycles.	<b>60</b>
<b>Figure 3.1.7</b>	The stability of the device in initial and after 2 months of fabrication (a) PP-H-TENG and (b) PE-H-TENG.	<b>61</b>

<b>Figure 3.1.8</b>	Charging and discharging behaviour of the capacitor. (a) Charging of five different capacitors (10, 32, 47, 69 nF, 0.1 $\mu$ F) by the PP-H-TENG. (b) Charge–discharge behaviour of a 0.1- $\mu$ F capacitor charged by the PP-H-TENG. (c) Charging of five different capacitors (10, 32, 47, 69 nF, 0.1 $\mu$ F) by the PE-H-TENG. (d) Charge–discharge behaviour of a 0.1- $\mu$ F capacitor charged by the PE-H-TENG.	<b>62</b>
<b>Figure 3.1.9</b>	Real-time data for harnessing biomechanical energy by the H-TENG. Use of the (a–b) PP-H-TENG and (c–d) PE-H-TENG to harness the biomechanical energy generated by hand and leg motions. (e) Voltage generated by biomechanical hand and leg motions using the PP- and PE-H-TENGs.	<b>63</b>
<b>Figure 3.1.10</b>	Fitted curve for short circuit current in response to dynamic force ranging from $\sim$ 2 kPa- 12 kPa.	<b>64</b>
<b>Figure 3.1.11</b>	(a) Schematic illustration of an emergency exit door indicator system where light-emitting diodes (LEDs) were connected to two stacked PP-H-TENGs. (b) The emergency indicator system; tapping the system generates triboelectricity that illuminates a directional arrow pointing towards the exit.	<b>65</b>
<b>Figure 3.1.12</b>	(a-c) Schematic illustration for the fabrication of energy harvesting chopping board. (d) Optical images during device pressing, board pressing, potato and tomato cutting. (e) The electrical response of chopping board for device pressing, board pressing, cutting potato and tomato.	<b>66</b>



<b>Figure 3.1.13</b>	The voltage output showing stability of chopping board with wetting and drying process.	<b>67</b>
<b>Figure 3.1.14</b>	Intrusion monitoring system. (a) Showing the arrangement of the devices, when a person moves from one device to other output will generate in the corresponding channel. (b) Shows the output for different devices connected to the multi-channel system, if person's feet are on the first device then output generated only in a channel connected to device 1 and so on. (c) The output in the case when the person's feet are on different devices. (d) Optical image for the real-time placement of the devices outside the door.	<b>68</b>
<b>Figure 3.2.1</b>	(a) Three-dimensional schematic representation of TENG in contact-separation mode. (b) The step by step procedure for the fabrication of TENG. (c) XRD spectra of TiO <sub>2</sub> microparticles. (d) FE-SEM micrograph of TiO <sub>2</sub> microparticles. (e) FT-IR spectra of the films at different concentration.	<b>82</b>
<b>Figure 3.2.2</b>	The XRD spectrum for PVDF-5-TiO <sub>2</sub> , PVDF-10-TiO <sub>2</sub> , PVDF-15-TiO <sub>2</sub> phase inversion films confirm that there is no change in the TiO <sub>2</sub> microstructure after incorporating in the polymer matrix.	<b>83</b>
<b>Figure 3.2.3</b>	FE-SEM micrograph of (a) PVDF-TiO <sub>2</sub> (b) PVDF-5_TiO <sub>2</sub> (c) PVDF-10-TiO <sub>2</sub> and (d) PVDF-15-TiO <sub>2</sub> films.	<b>85</b>
<b>Figure 3.2.4</b>	The working mechanism of as-fabricated TENG in vertical contact-separation mode.	<b>86</b>

<b>Figure 3.2.5</b>	(a, b) The voltage and short-circuit current output for PVDF-TiO <sub>2</sub> /CA and PVDF-5-TiO <sub>2</sub> /CA TENG respectively. (c, d) The voltage and short-circuit current output for PVDF-5-TiO <sub>2</sub> /CA, PVDF-10-TiO <sub>2</sub> /CA, PVDF-15-TiO <sub>2</sub> /CA TENG.	<b>87</b>
<b>Figure 3.2.6</b>	(a) The load matching analysis for PVDF-10-TiO <sub>2</sub> /CA TENG. (b) Stability of the PVDF-10-TiO <sub>2</sub> /CA TENG for 1500 s. (c) The voltage profile of capacitor charging (0.1, 0.22 and 1 $\mu$ F). (d) The charge-discharge cycle of 1 $\mu$ F capacitor. (e) The energy stored in various capacitors at different charged voltage. (f) Effect of filler concentration on the power density of TENG.	<b>89</b>
<b>Figure 3.2.7</b>	Biomechanical energy harvesting using (a) hand motion (b) finger tapping and (c) leg motion.	<b>91</b>
<b>Figure 3.2.8</b>	(a) A straightforward, cost-effective wind energy harvesting system. (b) Voltage output of TENG device at different rpm. (c) Charge-discharge cycle for 2.2 $\mu$ F capacitor and (d) The Lit-up of monochrome LCD, LEDs and LED strip using the energy harvested by TENG.	<b>91</b>
<b>Figure 3.2.9</b>	The utilization of TENG for VOCs sensing. (a) The schematic of in-house designed setup for the generation of VOCs and sensing measurement. (b) The image of the designed setup. (c) The voltage output with the concentration of the benzene. (d,e) The variation in the voltage with the concentration and	<b>94</b>

total flow rate respectively. (f,g) The response of the sensor with the concentration and total flow rate. (h) The integration of the benzene sensor with Arduino Uno for buzzing the alarm to evacuate the area.

<b>Figure 3.2.10</b>	The response of the TENG against various VOC vapors (20861 ppm).	<b>95</b>
<b>Figure 3.3.1</b>	(a) Schematic illustration for the device fabrication. (b) The 3D illustration of the single electrode E-TENG device. (c) The optical image of the fabricated device (i) the resistance offered by the edible silver leaf, (ii) the adherence and bending of the silver leaf coated Laver, (iii) weight of the fabricated device confirming the ultra-light weight of the device.	<b>107</b>
<b>Figure 3.3.2</b>	(a-c) The flexibility of laver in different bending conditions.	<b>108</b>
<b>Figure 3.3.3</b>	The device mechanism in single electrode mode. (a-d) Charge distribution for a complete cycle of output a) comes in complete contact, b) departs from, c) complete far away and d) approach the friction layer.	<b>109</b>
<b>Figure 3.3.4</b>	(a) The FE-SEM image of the Laver. (b) FE-SEM image and EDS mapping of the edible silver leaf. (c) 2D surface roughness profile of the Laver. (c) 3D surface roughness profile of the Laver. (e) A.F.M image of the Laver which matches with the FE-SEM image. (f) KPFM image for surface-	<b>110</b>

potential mapping confirming the positive triboelectric property of the device.

- Figure 3.3.5** The output of the device in vertical contact separation mode with Laver-FEP, Laver-PET and Laver-Paper as the materials. 111
- Figure 3.3.6** The surface potential on laver on hitting once with the kapton. 112
- Figure 3.3.7** The *in vitro* studies to examine the effects of the Laver and coated Laver on the viability of HeLa cells. (a) The viability of was examined in the control and in the cells treated for 24 and 48 h by MTT assay. (b-e) The control and treated cells were examined under a phase contrast microscope at 10X magnification. (f-i) The morphological changes in the cell nucleus was examined by DAPI staining under fluorescence microscope at 40X magnification. 113
- Figure 3.3.8** The study of the coated Laver and rice sheet in PBS buffer for 0, 1, 2, 4, 5, 6, 15 and 28 d respectively. 114
- Figure 3.3.9** The bioresorbability of the E-TENG in the simulated gastric juice. 115
- Figure 3.3.10** The detailed electrical performance of the E-TENG device. (a,b) The voltage and current output when different material comes in frictional contact with the device. The charge profile for the PVC and FEP giving high output. (d) The stability of the device for 1000 cycles. (e) The stability of the device for 5, 10, 15, and 18 days. There is a negligible change in the output up to 10 days. (f) Load matching analysis for the E-TENG 116

	across various resistances. (g) The capacitor charging for 0.1, 0.22, and 1 $\mu$ F capacitor using the E-TENG. (h) The energy stored in the capacitor corresponding to 1, 2, and 3 V charging.	
<b>Figure 3.3.11</b>	The optical image of the large device a) front view, b) back view. c) The bending of the large device showing the adherence of the silver leaf. d) The voltage and current output of the device.	<b>117</b>
<b>Figure 3.3.12</b>	The powering up of various electronics using 50 $\mu$ F capacitor for (a) commercial hygrometer, (c) wrist-watch, (e) UV-LEDs, and (g) green LEDs. The capacitor charging and discharging during lit-up of electronics for (b) commercial hygrometer, (d) wrist-watch, (f) UV-LEDs and (h) green LEDs.	<b>118</b>
<b>Figure 4.1</b>	Crystal structure of a) ZIF-7, b) ZIF-9, c) ZIF-11 and d) ZIF-12 (.cif file was downloaded from The Cambridge crystallography data centre, CCDC). E) XRD spectra of ZIFs. F) FT-IR spectra of ZIFs.	<b>130</b>
<b>Figure 4.2</b>	The FE-SEM images of 2) ZIF-7, b) ZIF-9, c) ZIF-11, and d) ZIF-12 with inset showing high magnification image.	<b>132</b>
<b>Figure 4.3</b>	The 2D surface profile image for 2) ZIF-7, b) ZIF-9, c) ZIF-11 and d) ZIF-12. E) temporal surface potential of the ZIFs obtained after 50 contacts with Kapton film. F) The bar plot is summarizing the surface potential profile of the ZIFs.	<b>133</b>
<b>Figure 4.4</b>	The x and y-direction line roughness profile for a) ZIF-7, b) ZIF-9, c) ZIF-11, and d) ZIF-12.	<b>135</b>

<b>Figure 4.5</b>	a) 3D layer view depiction of ZIF-TENG (inset showing the molecular structure of the materials). b-c) The voltage versus time and current versus time graph for different ZIF-TENG, respectively. d) Charge profile of the different ZIF-TENG devices. e) The summarized results for voltage, current, and charge generated by various ZIF-TENG.	<b>136</b>
<b>Figure 4.6</b>	The schematic representation of the ZIF-TENG working mechanism in contact-separation mode with different stages viz. pressed, releasing, released, and pressing.	<b>138</b>
<b>Figure 4.7</b>	The detailed electrical performance of ZIFs TENG with ethyl cellulose as the opposite layer. a-b) The open-circuit voltage and current for different ZIF-TENG devices. c) The charge profile for the four different ZIF-TENG devices. d) The summarized result for the voltage, current, and charge generated by different ZIF-TENG.	<b>129</b>
<b>Figure 4.8</b>	a) The 1500 s endurance test for ZIF-7 TENG. b) Load matching analysis across various loads for ZIF-7 TENG; the maximum peak power is obtained at 100 M $\Omega$ . C) The bar graph depiction for power obtained by different ZIF-TENG. d) The charging graph for various capacitors (0.22, 0.5 and 1 $\mu$ F) charged using ZIF-7 TENG. e) The charge-discharge cycle of 1 $\mu$ F capacitor charged by ZIF-7 TENG. f) The energy stored corresponding to 1 and 2 V charging of different capacitors.	<b>140</b>

<b>Figure 4.9</b>	The 1500 s endurance test for a) ZIF-9, b) ZIF-11, c) ZIF-12 TENG. The load matching analysis for d) ZIF-9, e) ZIF-11, and f) ZIF-12 TENG devices.	<b>141</b>
<b>Figure 4.10</b>	The capacitor charging graph for various capacitors (0.22, 0.5, and 1 $\mu$ F) charged using the output generated by a) ZIF-9, b) ZIF-11, and c) ZIF-12. The charge-discharge cycle for the 1 $\mu$ F capacitor charged by the output of d) ZIF-9, e) ZIF-11, and f) ZIF-12 TENG devices.	<b>143</b>
<b>Figure 4.11</b>	a) 100 $\mu$ F capacitor charging using four ZIF-7 TENG devices to drive electronics. The powering up of electronics using 100 $\mu$ F capacitor for b) calculator, c) UV LEDs, d) commercial hygro-thermometer, e) wristwatch and f) IR LEDs.	<b>144</b>
<b>Figure 5.1</b>	Structural and morphological characterization of ZIF-62. (a) Crystal structure of ZIF-62 (.cif file was retrieved from CCDC). (b) XRD spectra of ZIF-62. (C) FT-IR spectra of ZIF-62. (d) Raman spectra of ZIF-62 and (e) FE-SEM revealing the morphology of the particles and EDS mapping analysis is confirming the presence of different elements.	<b>155</b>
<b>Figure 5.2</b>	(a) KPFM, surface potential image of ZIF-62 with inset showing the corresponding AFM image. (b) 2D surface roughness profile image of ZIF-62 and (c) 3D exploded view of the ZIF-62 TENG device.	<b>156</b>

<b>Figure 5.3</b>	The schematic for the device mechanism in contact-separation mode showing the different stages that occur during the working (pressed, releasing, released, and pressing).	<b>157</b>
<b>Figure 5.4</b>	Output performance of the ZIF-62 TENG. (a-c) The generated voltage, current, and charge profile of the ZIF-62 with different opposite layers (Teflon, Kapton, and ethyl cellulose), respectively. (d) Surface potential developed on ZIF-62 after 60 contacts with Teflon, Kapton, and ethyl cellulose film and (e-f) The voltage and current versus time graph for ZIF-62/Teflon TENG at various frequency.	<b>160</b>
<b>Figure 5.5</b>	(a) The open-circuit voltage profile of the ZIF-62 TENG. (b) The endurance test for ZIF-63 TENG performed for 1600 s. (c) The load matching analysis across different loads; the maximum power density, was obtained at 500 MΩ. (d) The capacitor charging profile for 0.1, 0.22, and 1μF capacitor charged by the device. (e) The charge and self-discharge behavior of the 1 μF capacitor. (f) The stored energy in the capacitor corresponding to 1, 2, and 3V charging of various capacitors.	<b>161</b>
<b>Figure 5.6</b>	Fitness tracking and energy harvesting during (a) hand curls, (b) shoulder press, (c) lateral raises, and (d) squats exercises performed in the gym.	<b>163</b>
<b>Figure 5.7</b>	Powering of low-rating electronics via 20 μF capacitor charged by the ZIF-62 TENG device for (a) Commercial thermometer, (b) UV	<b>164</b>



LEDs, (c) wristwatch, and (d) calculator along with the capacitor charge-discharge profile during turning on the electronics.

- Figure 6.1** (a) The structure of ZIF-8 with zinc-nitrogen tetrahedra. (b) XRD spectra of ZIF-8 (c) Raman spectra of ZIF-8. (d) FT-IR spectra of ZIF-8. (e) FE-SEM and EDS mapping analysis of the ZIF-8. **175**
- Figure 6.2** The FE-SEM image of (a) 30-cyc grown ZIF-8 and (b) 50-cyc grown ZIF-8. **177**
- Figure 6.3** (a) The AFM image of the 20-cyc ZIF-8 resembles with the FE-SEM analysis. (b) The KPFM of 20-cyc ZIF-8 is confirming the positive  $V_{CPD}$ . (c-e) 2D surface profile images for 20-cyc, 30-cyc, and 50-cyc ZIF-8 respectively. (f) 3-D schematic illustration of the designed MOF-TENG. **179**
- Figure 6.4** The surface potential mapping using KPFM for (a) 30-cyc ZIF-8 and (b) 50-cyc ZIF-8. **180**
- Figure 6.5** The 3D profile, X-direction, and Y-direction line roughness profile of the (a-c) 20-cyc ZIF-8. (d-f) 30-cyc ZIF-8 and (g-i) 50-cyc ZIF-8. **181**
- Figure 6.6** The schematic illustration of mechanism in contact-separation mode with different stages viz. releasing, released, pressing and pressed. **182**
- Figure 6.7** The detailed electrical performance analysis of MOF-TENG (a) The voltage v/s time graph for different cycle grown ZIF-8. (b) The current v/s time graph for different cycle grown **183**

ZIF-8. (c) The stability analysis for the 1400 s. (d) Load matching analysis performed at different loads (e) The charging of the different capacitor (0.22  $\mu$ F, 1  $\mu$ F, 2.2  $\mu$ F) up to 2V. (f) The charging and discharging cycle of 2.2  $\mu$ F capacitor.

<b>Figure 6.8</b>	The continuity check analysis using multimeter for (a) 10-cyc ZIF-8 (b) 20-cyc ZIF-8 (c) 30-cyc ZIF-8 and (d) 50-cyc ZIF-8. The 10 cycles are not sufficient to grow the ZIF-8 over the substrate.	<b>185</b>
<b>Figure 6.9</b>	(a) The voltage of 15-cyc and 18-cyc grown ZIF-8. (b) The current profile of 15-cyc and 18-cyc grown ZIF-8.	<b>186</b>
<b>Figure 6.10</b>	The stability of the device to ensure the durability for long-term use.	<b>186</b>
<b>Figure 6.11</b>	(a) The capacitor charging circuit (b) the energy stored in different capacitors for 1 V and 2 V charging (c) the voltage v/s time graph for 100 $\mu$ F capacitor charging.	<b>187</b>
<b>Figure 6.12</b>	(a) The lit-up of the temperature sensor for 10s with 100 $\mu$ F capacitor. (b) The designed self-powered UV counterfeit system is showing the three different areas for the security feature under UV light.	<b>187</b>
<b>Figure 6.13</b>	(a) The circuit for wireless charging. (b) The time consumed for direct and wireless charging with the battery charging profile and the transferred voltage profile.	<b>188</b>

<b>Figure 6.14</b>	(a) The mechanism for the interaction of tetracycline with ZIF-8 via electrostatic and $\pi$ - $\pi$ interaction. The voltage v/s time graph for the different concentration of tetracycline. The voltage decreases with the increase in tetracycline concentration ascribed to lowered tribo positive nature of the ZIF-8. (c) The bar graph for peak to peak voltage variation with the concentration of the tetracycline. (d) The % response of the device for various concentration with a correlation coefficient ( $R^2$ ) of 0.982.	<b>190</b>
<b>Figure 6.15</b>	The MOF-TENG can be refresh by simple washing. The data with sensing and refreshing confirms the reusability of the device. The output has negligible change after washing with methanol.	<b>191</b>
<b>Figure 6.16</b>	The response of other species. The tetracycline shows the maximum response followed by phenol confirming the selectivity of the device.	<b>192</b>
<b>Figure 7.1</b>	Figure 7.1. (a) XRD spectra of the Cu-Asp NFs. (b) FT-IR spectra of Cu-Asp NFs with zoom image showing little peak $1620\text{ cm}^{-1}$ . (c) UV-Vis absorbance spectra of Cu-Asp NFs. (d) TGA analysis of the Cu-Asp NFs exhibiting three weight loses. (e) FE-SEM image of the Cu-Asp NFs confirming the morphology. (f) AFM image of the Cu-Asp NFs, where several NFs are stacked together.	<b>203</b>
<b>Figure 7.2</b>	(a) FE-SEM image of the synthesized MgO nanosheets with high magnification image shown in inset. (b) EDS mapping	<b>205</b>

confirming the presence of only Mg and O. (c) XRD spectra of MgO nanosheets confirming the purity and the cubic structure of the nanosheets.

- Figure 7.3** MTT cell viability assay of MgO and Cu-Asp NFs (MBIOF) on (a) Dermal fibroblast cells and (b) Mammary epithelial cells. **205**
- Figure 7.4** Phase contrast microscopy image of MgO and Cu-Asp NF treated dermal fibroblast cells for 24 h and 48 h. **206**
- Figure 7.5** Phase contrast microscopy image of MgO and Cu-Asp NF treated mammary epithelial cells for 24 h and 48 h. **207**
- Figure 7.6** (a-b) FE-SEM and AFM image of the Cu-Asp NF coated Al foil respectively. (c) 2D optical profile image of the coated NFs. (d) The KPFM image for the coated NFs. (e) 3D schematic illustration of freestanding layer mode MBIOF-TENG. **208**
- Figure 7.7** (a) The voltage output with different contacting material in C-S mode TENG. (b) Schematic illustrating the assigned position of Cu-Asp NFs in the triboelectric series. **210**
- Figure 7.8** Electrical performance of the MBIOF-TENG. (a-b) Voltage and current output of the MBIOF-TENG respectively. (c) Open circuit voltage and the transferred charge for MBIOF-TENG. (d) Endurance test for 2000 s to demonstrate the **211**

	stability of the device. (e-f) Voltage and current output respectively at different frequencies.	
<b>Figure 7.9</b>	(a-b) Voltage and current output stability of MBIOF-TENG for a period of 30 days. (c) Voltage output across a range of resistance. (d) Power and power density of MBIOF-TENG across various resistances. (e) Capacitor charging of 0.22, 1 and 2.2 $\mu\text{F}$ capacitors using MBIOF-TENG via a rectifier bridge. (f) Charge and self-discharge of 2.2 $\mu\text{F}$ capacitor.	<b>212</b>
<b>Figure 7.10</b>	FE-SEM image before and after device operation for MBIOF-TENG.	<b>213</b>
<b>Figure 7.11</b>	The working mechanism of the MBIOF-TENG showing different stages exists during the operation.	<b>214</b>
<b>Figure 7.12</b>	Output performance of cMBIOF-TENG. (a) 3D schematic illustration of the contact-separation device (cMBIOF-TENG). (b-d) Voltage, current and transferred charge of the cMBIOF-TENG with Teflon, PDMS and PI as the opposite layer. (e) Open-circuit voltage of the cMBIOF-TENG with Teflon as the opposite layer. (f) Stability of the device for 1000 s.	<b>215</b>
<b>Figure 7.13</b>	(a) Voltage output across different load. (b) Power and power density of the cMBIOF-TENG across different load. (c) 0.22 $\mu\text{F}$ and 1 $\mu\text{F}$ capacitor charging using cMBIOF-TENG. (d)	<b>217</b>

Effect of humidity on the output performance of cMBIOF-TENG.

- Figure 7.14** (a-b) Stability of the single electrode lateral sliding mode device with Kapton and Teflon as opposite sliding layer. (c-d) FE-SEM image of the coated layer before and after device operation. **218**
- Figure 7.15** The self-powered hydrogen peroxide sensor. (a) The effect of different hydrogen peroxide concentration on the output of the cMBIOF-TENG. (b) The response of the device with inset showing interference studies. (c) The mechanism of the sensor. (d) The Raman spectra of the Cu-Asp layer and (e) The Raman spectra after adding the hydrogen peroxide on the Cu-Asp layer. **220**

## 추상적

세계 에너지 수요의 증가는 전 세계의 에너지 부족을 야기한다. 에너지 위기는 이 문제를 부분적으로 해결하기 위한 대체에너지 개발에 초점을 맞추게 되었다. 저전력 전자 시장은 수명이 정해져 있는 폐기 및 재활용이 어려운 배터리가 주를 이루고 있다. 이 문제를 피하기 위해 2012 년 기계 에너지 변환을 위한 Triboelectric Nanogenerator(TENG)가 제안되었다. TENG 는 접촉 대전 및 정전기 유도의 결합에 의해 에너지를 생성한다. 서로 다른 특성을 가진 두 물질이 서로 마찰 접촉하여 접촉하는 물질에 반대 전하가 발생하는 경우 접촉 대전 (마찰 전기 효과)이 발생한다. 마찰 전기 효과는 일상 생활에서 자연스럽게 관찰할 수 있다. 마찰 전기 효과는 다양한 산업에서 부정적인 영향으로 간주되었다. 그럼에도 불구하고 마찰 기계 뒤이어 TENG 인 Van de Graaff 발전기의 개발은 마찰 전기 효과의 중요성을 입증했다. TENG 는 저렴하고, 설계하기 쉬우며, 고출력, 고효율, 다양한 재료 및 장치 설계 등의 고유한 장점을 제공한다. TENG 발명 이후, 이식 가능한 전자 기기, 약물 전달, 신경 자극, 물 분해, 화학 센서, 생물학 및 물리적 센서 등을 포함한 광범위한 응용 분야에 활용되었다. TENG 제작에 재료를 선택하기 위한 참고 자료로 마찰전기 시리즈가 검토되고 있다. 마찰전기 시리즈 끝에 있는 재료는 TENG 고성능 설계를 위한 최선의 선택이 될 수 있다. 중합체 및 소수의 금속이 마찰 전기 시리즈 계열에 중요한 부분을 차지하고 있으나 이는 변형이 어려워 많은 용도에 적합하지 않다. TENG 의 안정성, 기능성, 출력 성능 및 적용 가능성은 대부분 활성 물질에 의존한다. 조정할 수 있는 특성을 가진 다기능 재료를 포함하도록 마찰 전기 시리즈를 확장할 필요가 있다.

TENG 적용을 위한 마찰 전기 시리즈의 확장이 가장 중요하다. 이를 위해 본 논문은 TENG 및 자체 구동 동력 센서의 제작을 위한 금속-유기 미세/나노 구조를 조사한다. Metal-organic framework(MOF)는 큰 표면적, 다공성, 크기 조정성, 기능성 등의 예외적 특성을 제공하여 TENG의 이상적인 후보물질이다. 또한, MOF는 위상을 변경하지 않고 화학적 변형을 달성할 수 있다. 금속-생체분자는 생체적합성의 장점을 가진 또 다른 부류다.

TENG 장치의 세가지 다른 측면, 즉 지속 가능성, 자체 동력 감지 및 생분해성 장치를 다룬다.

이러한 측면은 TENG 기기 설계, 메커니즘 등의 기본 사항을 이해하기 위해 필요하다. 값싸고 설계하기 쉬운 지속가능한 가정용 TENG(H-TENG)은 어떠한 과학적인 도구를 사용하지 않고 가정용 쓰레기를 활용하여 제작되었다. 다양한 플라스틱 포장재, 폴리백은 음극 마찰 전기층의 용도로 사용되는 반면, 사용한 세척 스펀지는 반대 층의 역할을 한다.

쿠킹 호일은 전극으로 활용했고, 폐기된 CFL에서 나온 구리선이 연결선 역할을 한다. 이 기기는 자체 제작이 가능하며 5분 이내 제작할 수 있다. 또한 이 장치는 장력 센서, 비상 방향 시스템, 판자 및 침입 모니터링을 나타냈다.

두 번째 측면, 즉 TENG을 기반으로 하는 자가 동력 센서로서 polyvinylidene fluoride (PVDF)층을 포함하는 이산화 티타늄( $\text{TiO}_2$ ) 마이크로 입자에 대한 위상 발전 기술을 사용하여 나타냈다. PVDF- $\text{TiO}_2$  및 cellulose acetate가 각각 음성 및 양성 마찰 전기 층으로 사용되었다. 이 장치는 전기 성능에 대해 상세히 특정되어 전압 및 전류의 7배, 10배 향상을 확인하였다. 마지막으로, 이 장치는 독성 벤젠 증기의 특이적이고 선택적인 감지를 나타냈다. 마찰 전기 센서는 Arduino Uno와 결합하여 벤젠 증기가 있는 곳에서 경고



메시지와 경보를 발생시킨다. 생분해성 전원은 이식 가능한 전자장치 및 신경 자극, 세포 조절, 약물 전달 등과 같은 응용 분야에 중추적인 역할을 한다. 또한, 생분해성 기기는 플라스틱 폐기물이 없으므로 지속 가능하다. 단일 전극 모드에서 식용 생분해성 TENG 는 식용 물질 (E-TENG)을 사용하여 제작되었다. 한국의 김(Laver)은 마찰층에 사용되는데, 먹을 수 있는 얇은 TENG 기기의 기판으로서 전극과 라이스 시트의 역할을 한다. MTT 분석, DAPI 염색 및 세포 영상화는 TENG 장치의 생체 적합성을 확인한다.

E-TENG 는 PBS 완충제뿐만 아니라 위액에서도 생물학적 영향을 미친다. E-TENG 에서 생산된 출력을 활용하여 다양한 전자장치에 전원을 공급한다.

다음 단계는 마찰 전기 시리즈의 확장을 위한 다기능 재료의 연구를 포함한다. 이것은 제 4 장에 MOF 의 하위인 zeolitic imidazole framework(ZIF)구성들을 풀도록 동기를 제공한다. ZIF 는 MOF 의 다른 장점들과 함께 뛰어난 환경 안정성을 제공한다. 금속을 연결하는 단일 리간드를 갖는 ZIF-7, ZIF-9, ZIF-11 및 ZIF-12 는 ZIF 계열 구성들의 접촉 전기거동에 대해 분석한다. 표면 전위 측정은 Kapton 에 관한 ZIF 계열 구성들의 긍정적인 마찰 전기 거동을 나타낸다. ZIF 제품군은 of  $V_{ZIF-9} < V_{ZIF-11} < V_{ZIF-12} < V_{ZIF-7}$ 의 출력 트렌드를 따른다. ZIF-TENG 장치는 손목시계, 계산기 등에 전원을 공급하기 위해 사용된다. 처음으로 콘덴서를 통한 Kapton 과 ethyl cellulose 컨버스 층으로 상세하게 전기적 특성을 분석하여 TENG 제작을 위한 MOF 를 밝혔다. .

ZIF 구성들의 긍정적인 결과는 5 장에서 리간드가 혼합된 더 많은 ZIF 계열 구성원의 분석으로 이어졌다. ZIF-62 는 금속 이온  $Zn^{+2}$  가 benzimidazole (bIm) 및 imidazolate (Im)에

배워 된 혼합리간드 골격을 갖는 구성품 중 하나이다. ZIF-62 출력 성능은 ZIF-7 과 유사하지만, ZIF-62 장치는 내구성 테스트에서 더 안정적이고 오래 지속된다. The kelvin probe force microscopy (KPFM) 과 표면 전위 연구는 Teflon, polyimide 에 관한 ZIF-62 의 양성 전위 개발을 검증한다. 조립된 장치는 다양한 신체 활동을 관찰하여 생리학적 감지에 최종적으로 사용되었다.

상기 연구에서 ZIF 계열 구성들은 부서지기 쉽고 기판 위에서 성장하기 어려워 기기적용을 제한한다. 유연하고 제자리에서 성장하는 물질이 선택적이고 특정한 자체 구동 센서에 더 적합하다. 이를 위해 ZIF 구성중 하나가 6장에서 마찰 전기 동작 및 자체 구동 센서서 가장 널리 연구되었다. ZIF-8 은 다양한 기판에서 쉽게 성장할 수 있다는 고유한 장점이 있다. ZIF-8 은 유연한 전도성 기질에서 다양한 사이클로 성장한다. ZIF-8 은 형태학, 표면전위, 표면 거칠기와 같은 표면 형태로 광범위하게 특성화 되었다. ZIF-8 은 다른 제품군에 비해 우수한 출력 성능을 보였으며, 자체 통화 위조 시스템 및 tetracycline sensor 에서 나타났다. 자가 구동식 tetracycline sensor 는 간단한 세척으로 구체적이고 선택적이며 재사용 가능하다.

유연한 금속-생체 분자는 고유한 안정성을 제공하며, 확장이 쉽고 다기능 특성으로 생체에 적합하다고 보고된다. 금속-생체 분자 나노섬유(Cu-Asp)는 생체 적합성, 표면 및 구조적 특성화를 위해 연구된다. 오버헤드 프로젝터 필름, ITO 코팅 PET, 알루미늄 호일, 카프톤 필름 등 다양한 기판에 간단한 바 코팅 방법을 사용해 스케일 업을 보여준다. Cu-Asp 나노 섬유는 전통적인 마찰 전기 시리즈로 배열되었다. 독립형 레이어 모드 MBIOF-TENG 는 장기 안정성과 함께 뛰어난 출력 성능을 보였다. 또한, 이 물질은 접촉 분리 모드

TENG (cMBIOF-TENG)에서도 연구되었다. 습도의 영향을 분석하였다. 코팅된 층의 안정성은 단일 전극 측면 슬라이딩 모드 TENG 의 안정성을 제작하고 측정함으로써 나타났다. 마지막으로 감도가 2.3 V/Mm 인 자체 구동 과산화수소 센서가 시연되었다.

## Abstract

The rise in global energy demand introduces the energy shortage all over the globe. The energy crisis led to a focus on the development of alternative energy sources to solve the issue partially. The low power electronics market is dominated by the battery, which has a fixed lifetime, challenging to discard and recycle. To circumvent the issue, a triboelectric nanogenerator (TENG) for mechanical energy conversion was proposed in 2012. The TENG generates energy by the conjoining effect of contact electrification and electrostatic induction. The contact electrification (triboelectric effect) occurs when two materials with distinct properties come in frictional contact with each other, resulting in the development of opposite charges on the material in contact. The triboelectric effect is natural to observe in our day to day life as it is ubiquitous. The triboelectric effect was considered as a negative effect in various industries. Still, the development of the Van de Graff generator, friction machine followed by TENG, proved the importance of the triboelectric effect. The TENG offers unique advantages of being cheap, easy to design, high power, high efficiency, a wide choice of materials and device design, etc. Since its invention, TENG was utilized for a wide range of applications, including implantable electronics, drug delivery, nerve stimulation, water splitting, chemical sensors, biological and physical sensors, etc. attributed to its advantages. The triboelectric series is considered as a reference to select the material for the fabrication of the TENG. The materials lie at the far end of the triboelectric series can be the best choice for the designing of high performance TENG. The polymers and few metals are dominating the triboelectric series, which are challenging to modify and thus are not suitable for many applications. The stability, functionality, output performance, and applicability of TENG to a large extent, rely on active materials. The triboelectric series need to be expanded to include the multifunctional materials with tunable properties.

The expansion of the triboelectric series for the application of TENG is of utmost importance. For this purpose, this thesis investigates the metal-organic micro/nanostructures for the fabrication of TENG and self-powered sensors. Metal-organic framework (MOF) is one such class of material that offers exceptional properties like high surface area, porosity, size tunability, functionality, thus making them an ideal candidate for the TENG. Moreover, MOF can achieve chemical modifications without altering the topology. The metal-biomolecules are another such class that has an advantage of biocompatibility.

**Chapter III** covers the three different aspects of the TENG devices, i.e., sustainability, self-powered sensing, and biodegradable devices. These aspects are necessary to understand the basics of TENG device design, mechanism, etc. The cheap, easy to design sustainable household TENG (H-TENG) was fabricated by utilizing the household trash without the use of any scientific instrument. The various plastic packaging's, poly bags serve the purpose of the negative triboelectric layer while used cleaning sponge act as the opposite layer. The cooking foil was utilized as the electrode, and copper wire from discarded CFL serves as the connection wires. The device takes <5 min for its fabrication and can be built in-house. Furthermore, the device was demonstrated as a force sensor, emergency direction system, chopping board, and intrusion monitoring. The second aspect, i.e., self-powered sensors based on TENG, was demonstrated by using the phase inversion technology for the titanium dioxide (TiO<sub>2</sub>) microparticles incorporated polyvinylidene fluoride (PVDF) layer. The PVDF-TiO<sub>2</sub> and cellulose acetate were used as negative and positive triboelectric layers, respectively. The device was characterized in detail for its electrical performance, which confirms the 7- and 10-times enhancement in voltage and current. Finally, the device was demonstrated for the specific and selective sensing of the toxic benzene vapors. The triboelectric sensor was coupled with the Arduino Uno to trigger the warning message

and alarm in the presence of benzene vapors. The biodegradable power source is pivotal for implantable electronics and applications like nerve stimulation, cell modulation, drug delivery, etc. Moreover, biodegradable devices are sustainable with the generation of zero plastic waste. The edible, biodegradable TENG in single-electrode mode was fabricated by utilizing edible materials (E-TENG). The Korean ghim (Laver) serves the purpose of the frictional layer; the edible silver leaf was acting as electrode and rice sheet as the substrate in the TENG device. The MTT assay, DAPI staining, and cell imaging confirm the biocompatible behavior of the TENG device. The E-TENG was bioresorbable in gastric juice as well as PBS buffer. The output generated by E-TENG was utilized to power up various electronics.

The next step involves the study of the multifunctional materials for the expansion of the triboelectric series. This motivates **Chapter IV** to unravel the MOF subfamily zeolitic imidazole framework (ZIF) members. The ZIF offers excellent environmental stability along with the other advantages of the MOF. For the purpose ZIF family members ZIF-7, ZIF-9, ZIF-11, and ZIF-12 with single ligand connecting the metal are explored for their contact electrification behavior. The surface potential measurement divulges the positive triboelectric behavior of ZIF family members concerning Kapton. The ZIF family members follow an output trend of  $V_{\text{ZIF-9}} < V_{\text{ZIF-11}} < V_{\text{ZIF-12}} < V_{\text{ZIF-7}}$ . The ZIF-TENG device was utilized to power up the wristwatch, calculator, etc. via capacitor. The detailed electrical characterization with Kapton and ethyl cellulose as the converse layer for the first time unfold the MOFs for the fabrication of TENG.

The positive results of ZIF members led to the exploration of more ZIF family members with mixed ligand in **Chapter V**. The ZIF-62 is one such member that has mixed-ligand framework where metal ion  $\text{Zn}^{+2}$  is coordinated to benzimidazole (bIm) and imidazolate (Im). The

ZIF-62 output performance is similar to the ZIF-7, but the ZIF-62 device is more stable and long-lasting in the endurance test. The kelvin probe force microscopy (KPFM) and surface potential studies confirm the development of positive potential on the ZIF-62 concerning Teflon, polyimide. The as-fabricated device was finally utilized for physiological sensing by monitoring the different gym exercises.

The above studies ZIF family members are brittle and difficult to grow directly on the substrate, restricting the device application. The flexible and in-situ grown materials are more suitable for the selective and specific self-powered sensors. For the purpose, one of the most widely studied ZIF family members was explored for its triboelectric behavior and self-powered sensor in **Chapter VI**. The ZIF-8 offers a unique advantage of easy to grow on various substrates. The ZIF-8 was grown for different cycles on the flexible conducting substrate. The ZIF-8 was extensively characterized for its surface properties like morphology, surface potential, and surface roughness. The ZIF-8 showed superior output performance compared to other family members, and it is demonstrated for the self-powered currency counterfeit system and tetracycline sensor. The self-powered tetracycline sensor is specific, selective, and reusable by simple washing.

**Chapter VII** reports metal-biomolecule nanofibers, which are flexible, offer unique stability, easy to scale-up, biocompatible with multifunctional properties. The metal-biomolecule nanofibers (Cu-Asp) are explored for their biocompatibility, surface, and structural characterization. The scale-up is demonstrated by using a simple bar coating method on various substrates like overhead projector film, ITO coated PET, aluminum foil, and Kapton film. The Cu-Asp nanofibers were arranged in the traditional triboelectric series. The freestanding layer mode MBIOFO-TENG showed excellent output performance with long-term stability. Moreover, the

material was also studied in contact-separation mode TENG (cMOF-TENG). The effect of humidity was analyzed. The stability of the coated layer was demonstrated by fabricating and measuring the stability of the single electrode lateral sliding mode TENG. Finally, a self-powered hydrogen peroxide sensor with a sensitivity of 2.3 V/mM was demonstrated.

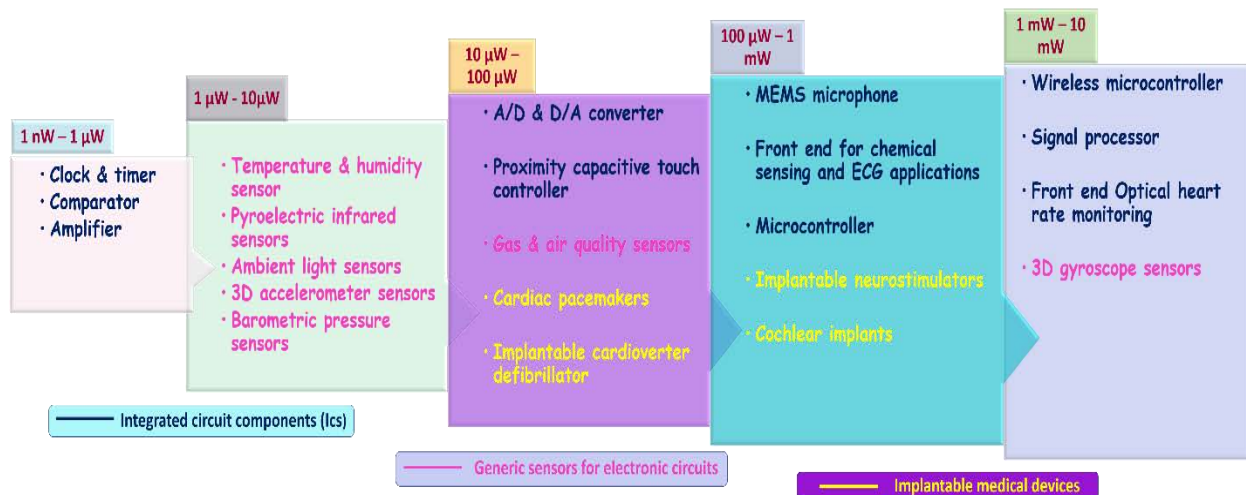


# CHAPTER- I

## Introduction


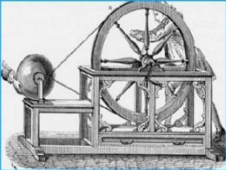
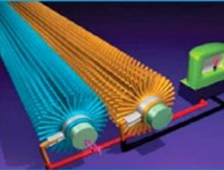
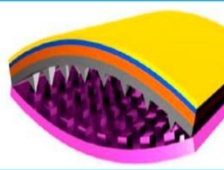
### 1.1 Background

The population growth has led to a sudden increase in global energy demand resulting in the energy crisis. Natural resources are insufficient to meet the energy requirement because they take hundreds to thousands of years to replenish. Moreover, the consumption of natural resources like coal, petroleum, etc. also suffered from the issue of generating air pollution and global warming. So, it is of utmost importance to explore and develop efficient, clean, and renewable energy sources. On the contrary, the electronics industry is continuously moving towards the miniaturization and portability. The miniaturization also allows reducing the required power consumption for powering up the devices. The present electronic components, sensors, wearable, and implantable device market is dominated by the use of batteries as a power source. The batteries suffer from the issue of a limited life-time and complicated recycling process [1]. In the case of implantable devices, the replacement of battery induces physical and financial burden to the patients. The harness of the energy from the surrounding environment to develop sustainable energy sources is the emerging area. Figure 1.1 illustrated the power requirement of the various commercial off-the-shelf (COTS) components [2]. The typical power requirement is in the range of 100 nW – 10 mW. Therefore, the focus shifts to the development of micro and nano energy harvesting techniques.



**Figure 1.1.** The power requirement of the various COTS components [2].

The nanogenerators (piezoelectric and triboelectric) get tremendous attention as an energy source to power-up the low rating electronics and sensors. The nanogenerators convert the mechanical energy to electrical energy and can utilize the low-frequency motions also [3, 4]. Figure 1.2 summarizes the principle, advantages, and disadvantages of different mechanical energy harvesters [5]. Among the mechanical energy harvesters, TENG offers several unique advantages like easy to design, cost-effective, high output, a wide range of materials and device designs [3, 6-8]. The piezoelectric nanogenerator suffers from the low output and tedious device fabrication process.

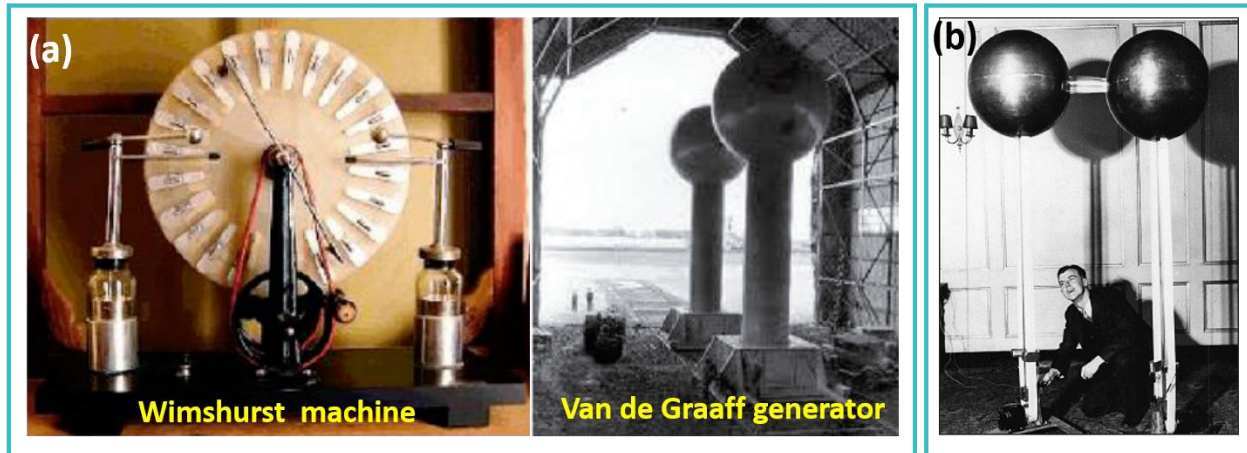
Mechanical energy harvesting	Electromagnetic	Electrostatic	Piezoelectric	Triboelectric
				
Harvesting principle	Electromagnetic induction	Electrostatic induction	Piezoelectric effect & Electrostatic induction	Contact electrification & Electrostatic induction
Impedance type	Resistive	Capacitive	Capacitive	Capacitive
Pros	High efficiency, easy to scale up	Light weight	Easy to scale down to nanoscale	Large output power, high efficiency, low weight, cost effective materials, simple fabrication
Cons	Heavy magnet required, low output for small-scale devices	Precharge required, low output, high matched impedance	Low output & low efficiency, pulsed output, high matched impedance	Pulsed output, high matched impedance

**Figure 1.2.** The comparison of various mechanical energy harvester, summarizing the principle, advantages, and disadvantages of the harvesting approach. Open Access [5].

## 1.2 Fundamentals of TENG

The triboelectric effect or contact electrification dates back to thousands of years and exists from ancient Greece. The tribo means rubbing, and electricity is from the Greek word for amber. The triboelectric effect is ubiquitous and can be easily observed in our daily life. Triboelectrification occurs when two materials with opposite surface charges come in contact with each other. In many industries, the effect was considered as unfavorable due to the damages like ignition, electronic damage and dust explosion, etc. caused by the generated electrostatic charges. However, the triboelectric effect leads to the development of initial generators like the Wimshurst machine (1880) and Van de Graaff generator (1929), as shown in Figure 1.3a [7, 9, 10]. A simple Van de Graaff generator consists of any dielectric material belt (rubber) running on the two rollers of distinct materials, one of the rollers is surrounded by the hollow metal sphere [9, 11]. Two brush

or comb-shaped electrodes are placed near the lower and over the upper roller inside the sphere. Van de Graaff generator demonstrated by himself in the MIT museum is shown in Figure 1.3b [9].



**Figure 1.3.** (a) Wimshurst machine and Van de Graaff generator. Reproduced with permission [7]. Copyright American Chemical Society. (b) The demonstration of van de Graaff generator at MIT museum. Reproduced with permission [9]. Copyright IEEE.

Recently, in 2012, Wang et al. invented a triboelectric nanogenerator (TENG) [3]. The TENG can effectively harness mechanical energy with advantages like cost-effective, wide material choice, lightweight, high efficiency, flexible, portable, etc. TENG works on the coupling effect of contact electrification and electrostatic induction [3]. In general, when two distinct material comes in frictional contact with each other, the charge transfer occurs depending on the relative position of the materials in contact. The electrostatic induction allows the development of opposite charges on the electrodes, thus creating a potential difference when two layers are separating or sliding or comes in contact. The process allows the flow of electrons, thus generating the output of the device [3, 6, 7, 12].

### 1.3 Theoretical origin of TENG

The first TENG device developed in 2012, comprised of Kapton and PET (polyester) films backed by the electrodes as active layers [3]. The device was operated in contact-separation (C-S) mode based on the coupling of contact electrification and electrostatic induction, as shown in Figure 1.4a. The origin of the mechanism in 2017 was traced back to Maxwell's displacement current [5, 10], which is defined as

$$J_D = \frac{\partial D}{\partial t} = \epsilon \frac{\partial E}{\partial t} + \frac{\partial P_s}{\partial t} \quad (1)$$

Where  $\epsilon$  is the permittivity of the medium,  $D$  is the displacement field,  $E$  is the electric field, and  $P_s$  is the contribution of surface polarization charges.

The first term in the equation was the origin of the electromagnetic waves. The second term is for the origin of the nanogenerators (piezoelectric and triboelectric), and it signifies the surface polarization contribution. In the primary C-S mode, when two layers come in contact, it gets oppositely charged. The surface charge density ( $\pm \sigma_{\text{tribo}}$ ) is independent of the gap ( $z$ ) between the layers but  $\pm \sigma_{\text{tr}}$ , i.e., the amount of charge collected on the electrodes depends on the  $z$ . The mechanical energy brings the device in periodic contact and separation, thus induces changes in the  $z$ , converting it into the electricity. The displacement current, in this case, can be calculated by equation 2.

$$J_D = \frac{\partial D_z}{\partial t} = \frac{\partial \sigma_{\text{tr}}(z,t)}{\partial t} \quad (2)$$

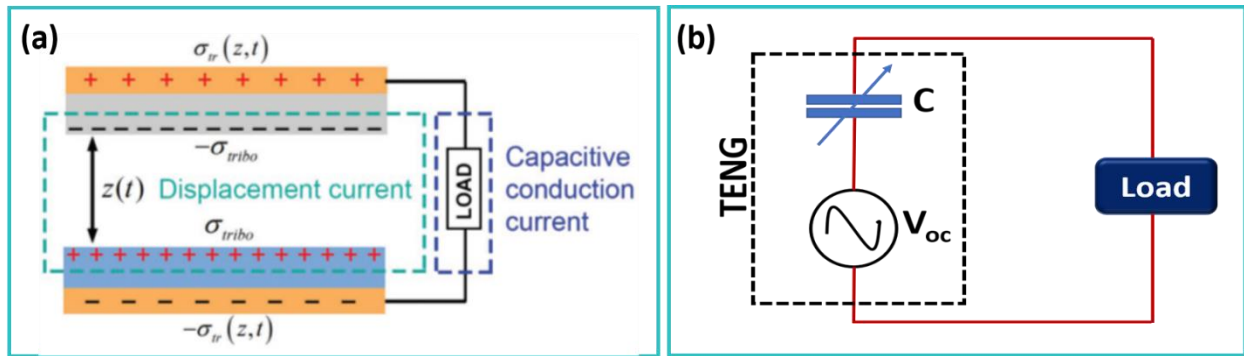
The oppositely charged layers can be considered as a capacitor of varying capacitance due to the changing gap. The equivalent capacitor model is shown in Figure 1.4b, the current of which can be given by

$$I = \frac{dQ}{dt} = A \frac{d\sigma_{tr}}{dt} \quad (3)$$

This equation confirms the foundation of the model to Maxwell's displacement current as it is equivalent to equation 2. The voltage of the TENG can be given by

$$V = -\frac{1}{C(z)} X Q + V_{oc}(z) \quad (4)$$

However, recently the output behavior of TENG was simulated more accurately by using Norton's theorem and distance-dependent electric field [13, 14].



**Figure 1.4.** (a) The C-S mode TENG for displacement current model. (b) The TENG representation using the capacitor model. Reproduced with permission [10]. Copyright John Wiley & Sons.

## 1.4 Working modes of TENG

The TENG can operate in four different working modes depending on the electrode configuration and the change in the direction of polarization. The four different working modes of TENG are vertical contact-separation (C-S) mode, single electrode (SE) mode, lateral sliding (LS) mode, and freestanding triboelectric layer (FT) mode as explained below.

### 1.4.1 Vertical contact-separation (C-S) mode

The vertical c-s mode shown in Figure 1.5a is one of the most straightforward TENG device configurations. When two distinct materials backed by electrode comes in frictional contact with each other, they developed opposite charges depending on their polarity. In the absence of external force, the two layers start to separate, thus creating a potential drop. The free electrons from one electrode flow to the opposite electrode via load to balance the potential difference, thus generating a one-half cycle of the AC output. After applying the force, the top frictional layer starts approaching the bottom layer, thus generating the reverse flow of electrons to complete the one cycle of the AC output. The C-S mode can work in the dielectric to dielectric contact and conductor to dielectric contact mode. In dielectric to dielectric type, the two dielectric layers backed by metal electrode are stacked face to face, separated with the help of a spacer. In conductor to the dielectric, only one dielectric layer is backed by a metal electrode, while the opposite layer is metal, which plays the dual role of electrode and contact layer. The C-S mode devices are reported in various designs like arc-shaped, spring-assisted, zig-zag shaped, etc. The vertical C-S mode offers the advantage of easy design, robustness, stability, and high output [3, 8, 12, 15-18].



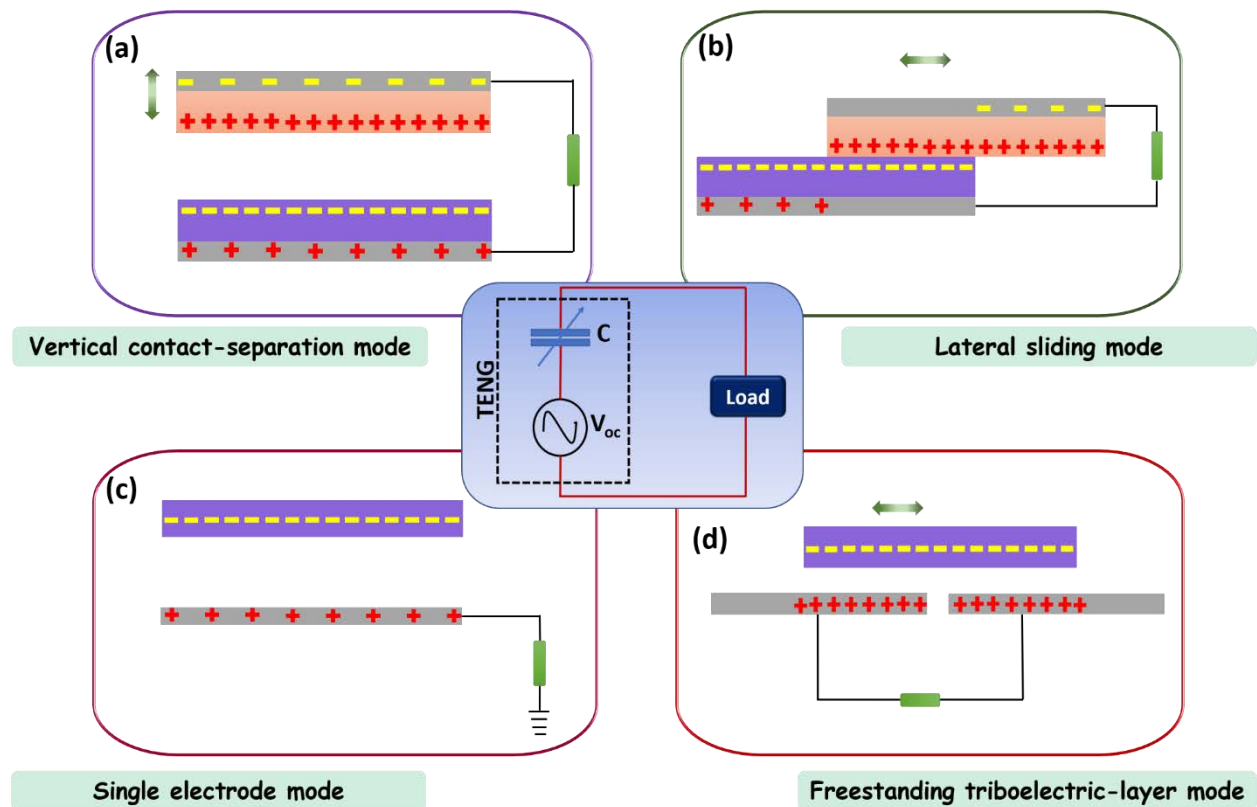
### **1.4.2 Lateral sliding (LS) mode**

The lateral sliding mode generates electricity by relative sliding of the top layer over the bottom layer, as shown in Figure 1.5b. The top and bottom layers are positive and negative in the triboelectric series, respectively. Initially, the two frictional layers are in full contact with each other, thus have equal and opposite charge density. When the top layer slides outward relative to the bottom layer, the decrease in contact area creates the charge separation. The generated potential difference leads to the flow of electrons from the bottom electrode to the top electrode until the top layer slides out completely. The motion in reverse direction generates the reverse flow of electrons until the electrostatic equilibrium achieved, thus producing the second half cycle of the output. The LS mode can be used in cylindrical rotation, disc rotation, or planar motion. The LS mode suffers from the issue of wear and tear [6, 19, 20].

### **1.4.3 Single electrode (SE) mode**

The vertical C-S mode and lateral sliding mode use two electrodes, which may restrict the device applications. The single-electrode style can work freely as the opposite contact layer is free to move without any connection, as shown in Figure 1.5c. The single-electrode mode can be designed by using a ground electrode and the movable contrasting layer. The periodic contact-separation of the movable layer generates the potential difference leading to the flow of electrons between the electrode and the ground. The single-electrode mode can work in both lateral sliding and C-S configuration. The SE mode offers the advantage of straightforward design and one free layer, but the issue is of connection to the ground [21-24].





**Figure 1.5.** Working modes of TENG (a) Vertical contact-separation mode. (b) Lateral sliding mode. (c) Single electrode mode and (d) Freestanding triboelectric layer mode [18].

#### 1.4.4 Freestanding triboelectric-layer (FT) mode

The freestanding TENG (FTENG) mode can be easy to apply as the moving layer need not be attached to the electrode and wires. The FTENG has much higher efficiency compared to the single-electrode mode and can also work in non-contact mode. In freestanding mode, two symmetric electrodes are placed at a small gap underneath the dielectric layer with a little distance. The size of the dielectric layer and electrodes are of the same order. Considering the movable layer is pre-charged by the triboelectrification process, the movement of the layer concerning the electrodes generates asymmetric charge distribution, leading to the flow of electrons from one electrode to the other to balance the developed potential (Figure 1.5d). The movement of electrons

between the electrode creates the AC output. The FT mode provides the advantage of a free moving layer, high output but has a complex structure [25-27].

### 1.5 Figure of merits

The TENG can operate in four different working modes with a wide range of material availability. The figure of merits (FOM) was proposed in 2015 by Zi et al. to create a common standard for the comparison of different TENGs [28]. The figure of merits and factors affecting the TENG output are summarized in Figure 1.6, where the performance figure of merit ( $FOM_P$ ) for TENG comprises of a material FOM ( $FOM_M$ ) and structural FOM ( $FOM_S$ ). The  $FOM_P$  can be considered as a standard to evaluate the performance of the TENG. The relationship of  $FOM_S$  for different working mode is contact freestanding triboelectric (CFT) > CS > sliding FT (SFT) > LS > SE contact mode (SEC) [28]. The only material related parameter is surface charge density ( $\sigma$ ). The dimensionless  $FOM_S$  is given as

$$FOM_S = \frac{2\epsilon_0}{\sigma^2 A} \frac{E_m}{x_{max}} \quad (5)$$

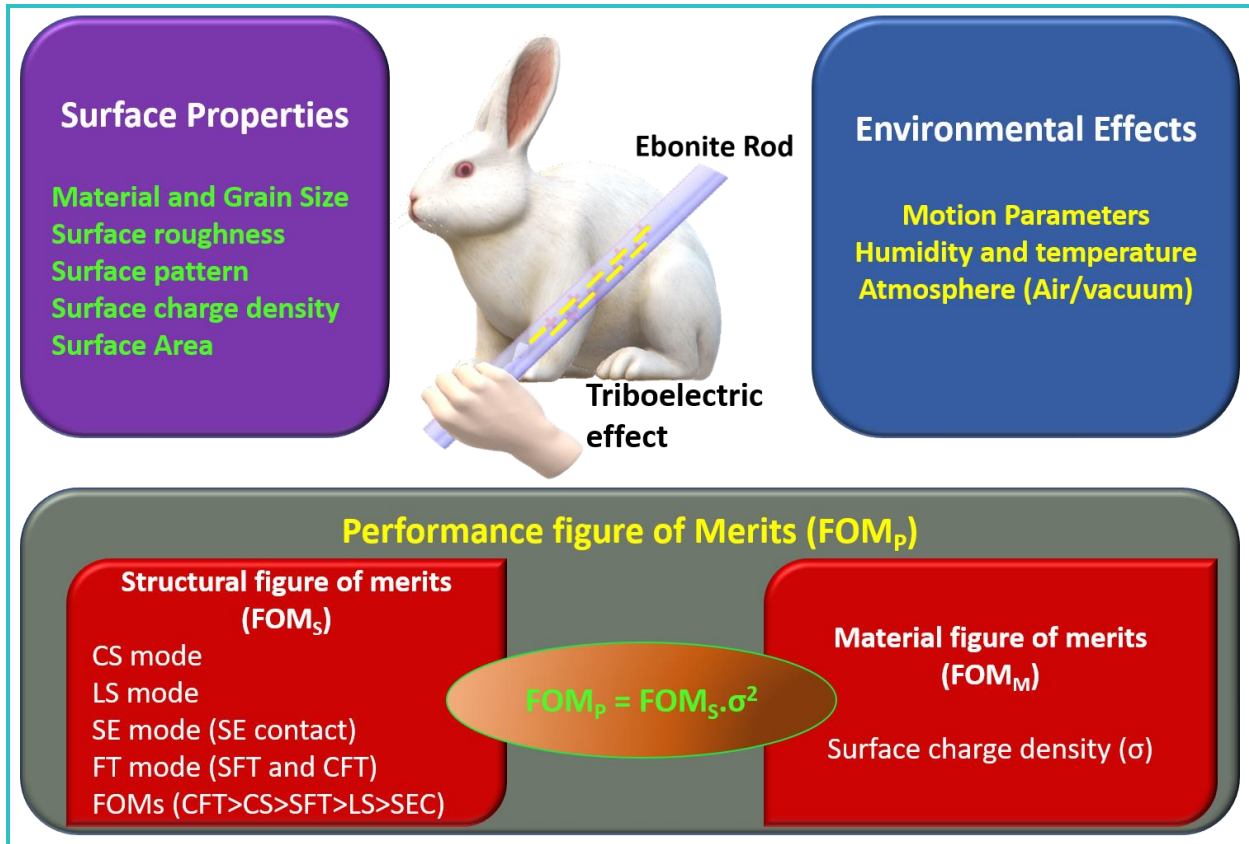
Where A is the area of triboelectrification in TENG and  $\epsilon_0$  is the permittivity of the vacuum. The material properties and device size are not considered in the  $FOM_S$ . The  $FOM_P$  is given by

$$FOM_P = FOM_S \cdot \sigma^2 \quad (6)$$

The  $\sigma^2$  is the  $FOM_M$ . To quantify the triboelectric performance of a material, a dimensionless material FOM ( $FOM_{DM}$ ) was also proposed. For the purpose, the charge density of the material under test can be measured with a liquid metal-like Galinstan. The  $FOM_{DM}$  is given as

$$FOM_{DM} = (\sigma_N)^2 = \frac{\sigma_{material/liquid\ metal}^2}{\sigma_{FEP/liquid\ metal}^2} \quad (7)$$

Where FEP is the reference material. The negative  $\sigma_N$  signifies that the material is more tribo positive considering the liquid metal and  $\sigma_N > 1$  denotes that the material is more negative compared to FEP [10, 28]. The in-between value stands for more positive than FEP and more negative than liquid metal. The development of FOM can be treated as standards for the TENG performance, which can also act as a foundation for the industrialization of TENG based systems.



**Figure 1.6.** The illustration of factors affecting the output of TENG and figure of merits for TENG.

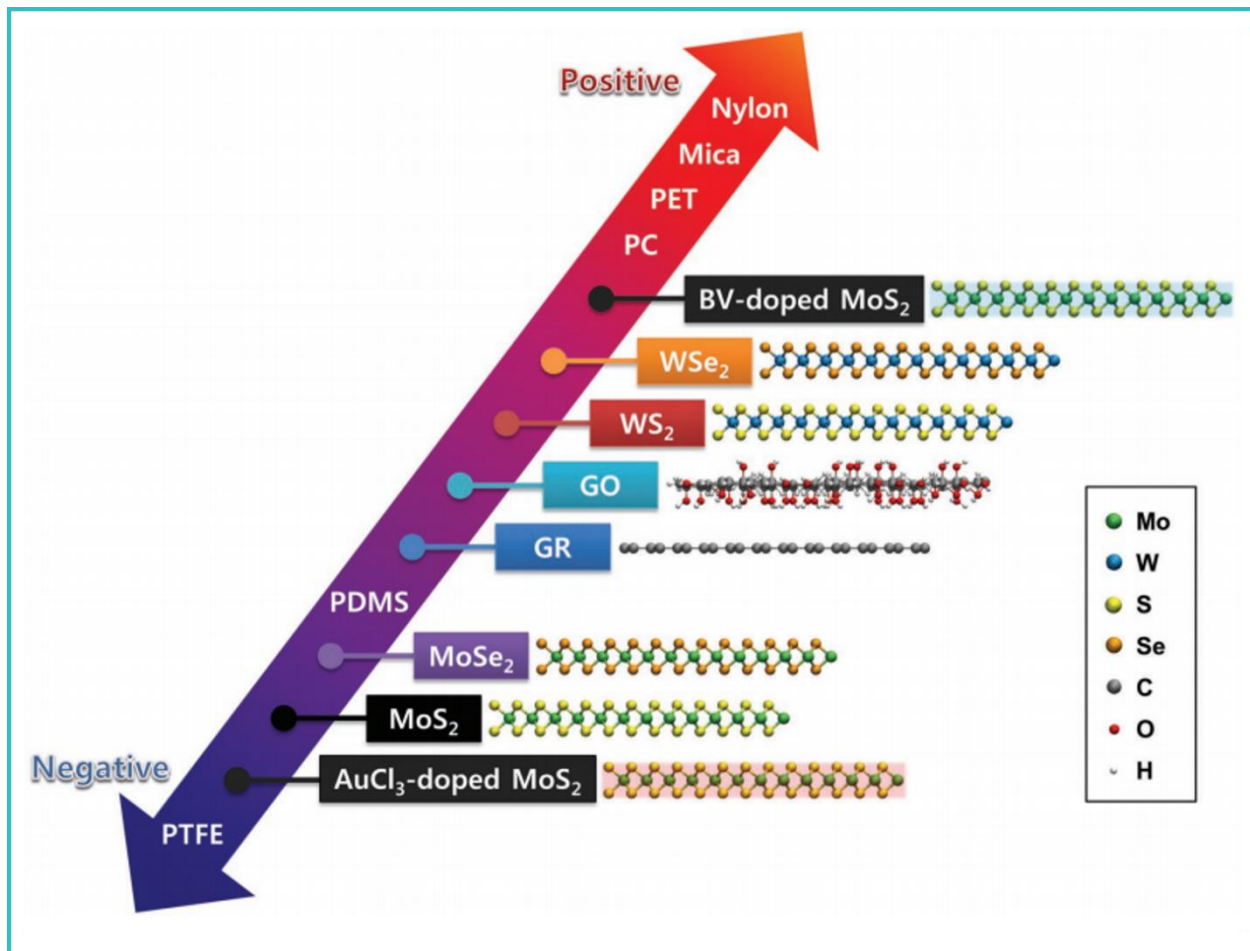
## 1.6 Materials for TENG

Insulator Name	Charge Affinity (nC/J)		Insulator Name	Charge Affinity (nC/J)
Polyurethane foam	+60		Sorbothane	+58
Hair, oily skin	+45		Solid polyurethane	+40
Magnesium fluoride	+35		Nylon, dry skin	+30
Machine oil	+29		Nylatron	+28
Glass (soda)	+25		Paper	+10
Wood (pine)	+7		Cotton	+5
Nitrile rubber	+3		Wool	0
Polycarbonate	-5		Acrylic	-10
Epoxy	-32		Styrene-butadiene rubber	-35
PET (mylar) solid	-40		EVA rubber	-55
Gum rubber	-60		Polystyrene	-70
Polyimide	-70		Silicones	-72
Vinyl: flexible	-75		LDPE	-90
Polypropylene	-90		HDPE	-90
Cellulose nitrate	-93		UHMWPE	-95
Polychloroprene	-98		PVC (rigid vinyl)	-100
Latex (natural rubber)	-105		Viton, filled	-117
Epichlorohydrin rubber	-118		Santoprene rubber	-120
Hypalon rubber, filled	-130		Butyl rubber, filled	-135
EDPM rubber, filled	-140		PTFE (Teflon)	-190

Figure 1.7. Triboelectric series developed by AlphaLab (© 2009).

Almost all materials can be used for triboelectrification, ranging from metal, polymers, textile to wood, nanomaterials, etc. The various materials are arranged in the triboelectric series, depending on their tendency to lose or gain electrons. The triboelectric series thus can be used as a reference for the development of TENG. Recent efforts were made by John Wilcke and Harper to arrange the materials in the triboelectric series. Figure 1.7 shows the triboelectric series developed by AlphaLab (© 2009). The data was acquired at 22°C and 35 % relative humidity (RH) by using a surface voltmeter (AlphaLab) [18, 29]. The materials at the opposite end or far apart in triboelectric series can be used for high performance device. The triboelectric series thus can be used as a reference for the development of TENG. In 2018, Seol et al. arranged the 2D layered materials MoSe<sub>2</sub>, MoS<sub>2</sub>, WSe<sub>2</sub>, WS<sub>2</sub>, graphene, and graphene oxide in the triboelectric series [30]. The triboelectric order was supported by the work function values of the materials. The triboelectric series of 2D materials is shown in Figure 1.8.

In 2019, Zou et al. proposed a standard method for the quantification of the triboelectric series. The triboelectric series of polymers were developed using the liquid metal as opposite contact under well-defined and controlled experimental conditions. The intrinsic ability of a polymer to either gain or lose electrons was derived by using the normalized triboelectric charge density (TECD) [31]. Figure 1.9 shows the quantified triboelectric series developed by Zou et al. The factors like surface roughness, material functionalization, etc. also play a key role in the output of the TENG [32-34]. Various morphologies like nanowire, pyramid, square, and other micro-nano patterns are well reported to enhance the output of TENG. The temperature and humidity are other critical parameters that influence the output of TENG [34, 35].



**Figure 1.8.** Triboelectric series of 2D layered materials. Reproduced with permission [30].  
Copyright John Wiley & Sons.



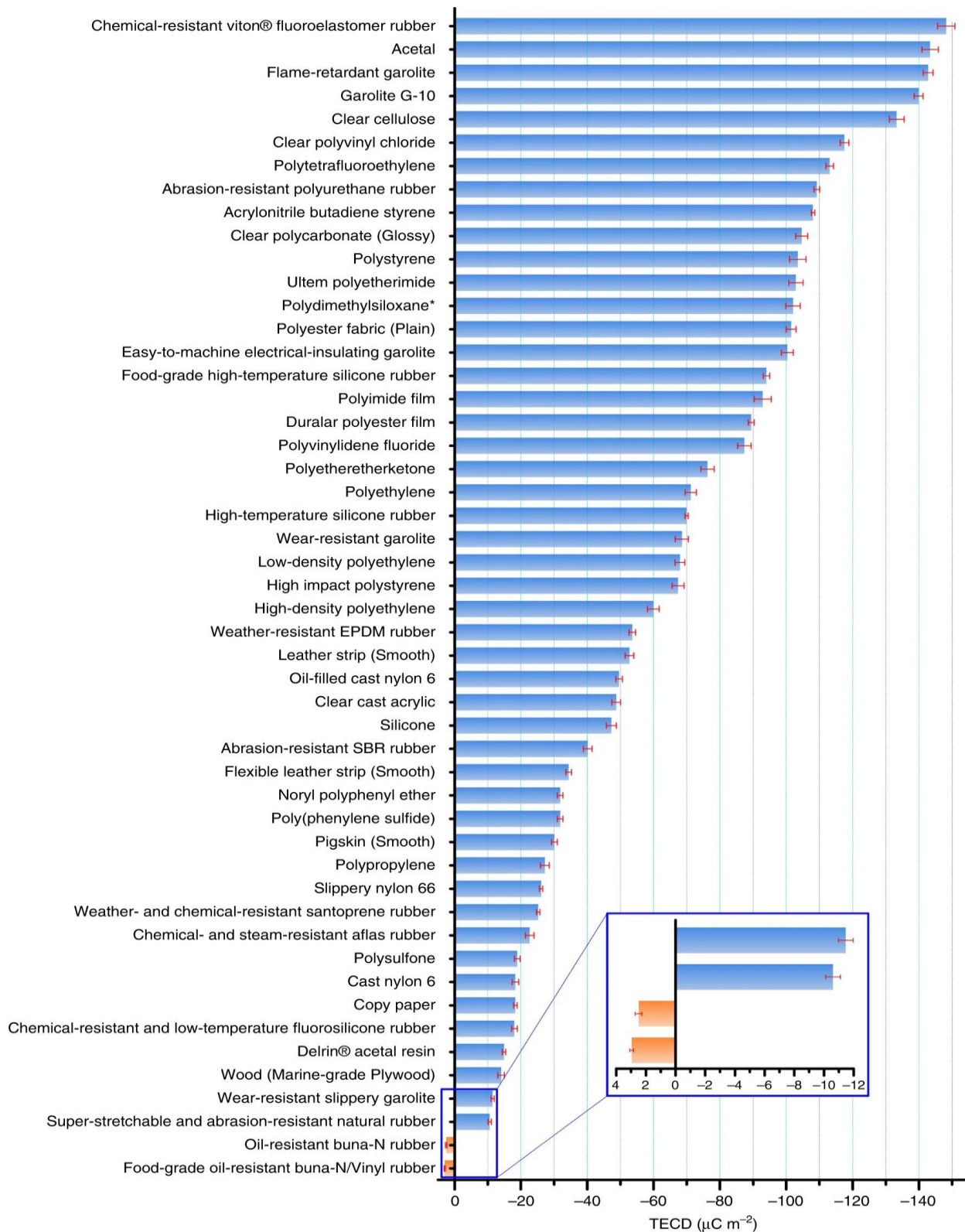


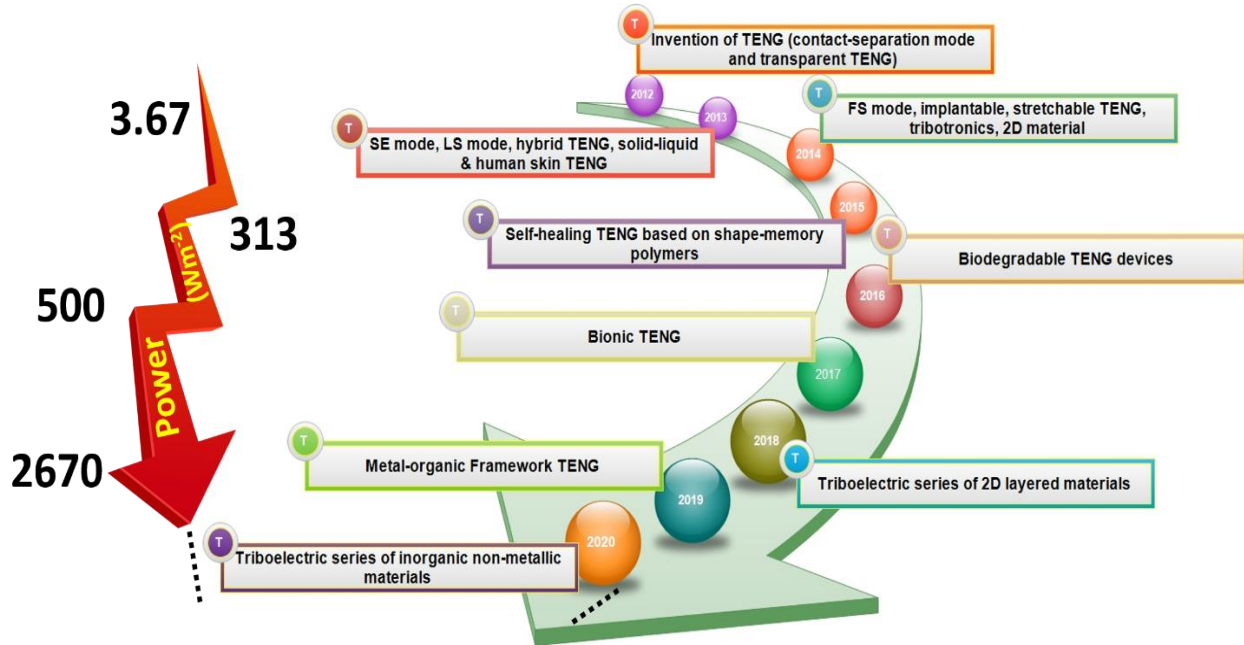
Figure 1.9. The quantified triboelectric series developed by Zou et al. Open Access [31].

## 1.7 Research progress of TENG

Since its invention in 2012, TENG is explored for a vast range of applications. In the past years, the TENG is incorporated with a more significant number of features, device designs, and materials, etc. The TENG, which was invented in 2012, operates in vertical contact-separation mode with two dielectric layers [3]. Transparent TENG device was also proposed in the same year, which was of great significance in the field of optoelectronics [36]. The research proceeds with the development of a single electrode and lateral sliding mode in the year 2013 [19, 37-41]. Moreover, liquid-solid contact, human skin as one layer also emerge for different applications [42]. During the same time, the TENG was combined with other energy harvesters (piezoelectric, electromagnetic, etc.) for the development of hybrid devices with the advantages of both the devices [43]. Later on, in 2014, freestanding mode TENG was proposed [27, 44, 45]. The four modes of TENG were explored experimentally and theoretically at that time. One of the exciting areas that were developed is triboelectronics, i.e., the use of TENG to control the FET [46]. The research was followed by the development of textile-based and implantable devices [47, 48]. The TENG produces AC output, which needs to be converted to a DC signal for practical use. The issue was solved by the development of DC-TENG, which eliminate the use of a rectifier [49]. In the year 2015, shape-memory alloy based self-healable TENG was demonstrated to enhance the durability and life of the device [50]. A biodegradable TENG for in-vivo energy harvesting was developed in 2016 [51]. The progress was continuing with the concept of bionic TENG and wireless power delivery in 2018, which further extends the application of TENG [52, 53]. Harnessing water wave energy, i.e., blue energy becomes a growing area for TENG. In the year 2018, the triboelectric series of 2D layer material was developed [4, 30]. The significant development in the current year starts with quantified triboelectric series of non-metallic materials.



During the development, the power density of the TENG was significantly improved to 2.67 kW/m<sup>2</sup> from 3.67 W/m<sup>2</sup>. The research roadmap of TENG is summarized in Figure 1.10.



**Figure 1.10.** The roadmap summarizing the progress in the TENG.

### 1.8 Applications of TENG

The aim behind the development of nanogenerators is to partially solve the issue of the energy crisis and the creation of self-powered sensors and systems. The TENG is a discontinuous source of energy, so it was coupled with the energy storage and power management units to achieve the applications that require continuous output. The sustainable power source like TENG is of great need as the current market is dominated by batteries, which are difficult to recycle. Furthermore, in the case of implantable devices like a pacemaker, the battery needs to be replaced by the surgery, which created not only financial suffering but also creates physical suffering to the patients. The advantages of the TENG led to its exploration as a power source for a wide range of applications. The TENG is reported for a wide range of applications like biological sensors,



## 1.9 Objective and scope of the thesis

The growing population raises the issue of energy crisis as natural resources to take thousand of years to replenish. Moreover, the burning of natural fuels is a threat to the environment. Hence, the focus shift towards to development of portable energy harvesting devices to partially solve the issue. The TENG is one such energy harvesting device with easy fabrication and a wide range of available device designs. The thesis starts with the origin and the fundamentals of TENG. The first part of the thesis is based on the literature review where, three main aspects (sustainable devices, the device for chemical sensing, and biodegradable device) are explored to gain the necessary understanding. During the process, the main lag found in the research is the materials available in the triboelectric series for the fabrication of TENG. The triboelectric series predominantly consists of polymers and few metals, which are challenging to modify and functionalize. The applications requiring high selectivity and specificity is thus hard to achieve with the available materials. The multifunctional materials with tunable properties are highly desirable for extending the triboelectric series and application of TENG. The MOF is one such class of material that is not explored for the TENG. The MOF, composed of a metal ion coordinated with an organic ligand. The porous structure of the MOF provides a high surface area to improve the functionality of TENG devices. Thus, careful selection of the MOF component can yield a crystal framework with high porosity and high chemical and thermal stability. So, the main focus of the thesis is to explore the various MOF for their contact-electrification behavior, potential in the field of TENG, and self-powered sensor. The objectives of the thesis are described below

- To understand the basics of TENG by studying the sustainable device, a device for chemical sensing, and biodegradable devices.
- To fabricate all waste material (trash to energy) based device.
- To demonstrate the in-house fabrication by using the day to day life waste materials.
- To demonstrate the essential applications to give an idea for the utilization of TENG for a layman.
- To fabricate an enhanced output TENG for chemical sensing application.
- To fabricate all edible material based biodegradable and biocompatible device.
- To study cytotoxicity of the edible TENG device.
- To fabricate the large size device to demonstrate the suitability of the materials for scale-up.
- To synthesize ZIF family member ZIF-7, ZIF-9, ZIF-11, and ZIF-12 at room temperature by a wet chemical approach.
- To synthesize mixed linker framework ZIF-62 by hydrothermal route.
- To grow ZIF-8 for different cycles on conducting ITO coated PET substrate by using the solution growth process.
- To synthesize MBIOF using a wet chemical approach.
- To investigate the formation of the materials by employing various characterization tools and techniques.
- To study the contact-electrification behavior of the ZIF family members, ZIF-62, ZIF-8, and MBIOF.
- To study the surface roughness and surface potential behavior of the different MOF material.

- To coat and demonstrate the scale-up of MBIOF coating using simple tape cast coater on various substrates.
- To study cytotoxicity of MBIOF on dermal fibroblasts and mammary epithelial cells.
- To study the stability of the MBIOF coating.
- To study the electrical performance of the fabricated TENG devices by using the different MOF materials.
- To study the effect of the ZIF-8 growth cycles on the output performance of the C-S mode TENG.
- To power up various low-power electronics like calculator, UV LEDs, IR LEDs, etc. using the ZIF-7 TENG device.
- To demonstrate the ZIF-62 TENG device for fitness tracking while performing various gym exercises.
- To demonstrate the UV currency counterfeit system using the ZIF-8 TENG device.
- To demonstrate the selective, specific, and reusable tetracycline sensor using ZIF-8 TENG.
- To demonstrate the MBIOF based TENG for self-powered hydrogen peroxide sensor.

### 1.10 Structure of the thesis

The thesis is classified into eight chapters

**Chapter I** focus on the fundamentals of TENG. The chapter detailed the origin, mechanism, and requirement of TENG. The chapter explains the triboelectric series, applications of TENG, and research roadmap of the TENG.

**Chapter II** explains the materials, methods, and apparatus used to carry out the research work. The chapter provides insight into various characterization techniques used during the analysis of the material and the fabricated TENG devices.

**Chapter III** focuses on gaining a basic understanding of the TENG by exploring the three aspects, i.e., sustainable devices, an enhanced output device for chemical sensing, and biodegradable devices. The sustainable device is based on in-house, generated waste materials. The device can be fabricated anywhere without any scientific instrument in less than 5 min. The enhanced output device was fabricated by the doping of the semiconductor material and employing the phase inversion technique. The device was demonstrated for benzene sensing. The biocompatible and biodegradable device is designed by using all edible materials. The cytotoxicity studies of the devices put light on the compatibility of the used materials.

**Chapter IV** explores four members (ZIF-7, ZIF-9, ZIF-11, and ZIF-12) of the ZIF family as a potential candidate for the TENG. The materials were studied for their surface roughness and surface potential behavior. The materials are used to fabricate contact-separation devices, followed by detailed electrical characterization. The various low rating electronics were powered by the ZIF-7 TENG device.

**Chapter V** is based on the study of mixed linker framework ZIF-62 for its contact electrification behavior. The ZIF-62 was characterized by its surface potential and surface roughness parameters. The device was demonstrated for fitness tracking while performing different gym exercises.

**Chapter VI** focuses on the study of different cycles grown ZIF-8 on the conducting ITO coated PET substrate. The ZIF-8 overcomes the issue of coating and flexibility faced by the materials studied in Chapter IV and V. The different cycles grown ZIF-8 were studied for electrical

performance. A portable and straightforward UV currency counterfeit system were demonstrated by charging a Li-ion battery. Finally, a highly selective, specific, and reusable self-powered tetracycline sensor was demonstrated.

**Chapter VII** explores the MBIOF for TENG. The MBIOF is demonstrated for scale-up coating with excellent adhesion on various substrates. The MBIOF studied for cytotoxicity on two different cell lines by considering MgO nanosheets as reference material. The MBIOF is arranged in the triboelectric series by fabricating the device in C-S mode with different opposite materials. The electrical performance was studied for FT and C-S mode TENG devices. Finally, the C-S mode device was demonstrated for a self-powered hydrogen peroxide sensor.

## References

- [1] Stauss S, Honma I. Biocompatible Batteries—Materials and Chemistry, Fabrication, Applications, and Future Prospects. *Bulletin of the Chemical Society of Japan*. 2018;91:492-505.
- [2] Proto A, Penhaker M, Conforto S, Schmid M. Nanogenerators for Human Body Energy Harvesting. *Trends in Biotechnology*. 2017;35:610-24.
- [3] Fan F-R, Tian Z-Q, Lin Wang Z. Flexible triboelectric generator. *Nano Energy*. 2012;1:328-34.
- [4] Khandelwal G, Chandrasekhar A, Maria Joseph Raj NP, Kim S-J. Metal–Organic Framework: A Novel Material for Triboelectric Nanogenerator–Based Self-Powered Sensors and Systems. *Advanced Energy Materials*. 2019;9:1803581.
- [5] Wang ZL. On Maxwell's displacement current for energy and sensors: the origin of nanogenerators. *Materials Today*. 2017;20:74-82.
- [6] Wang ZL. Triboelectric nanogenerators as new energy technology and self-powered sensors - Principles, problems and perspectives. *Faraday Discussions*. 2014;176:447-58.
- [7] Wang ZL. Triboelectric Nanogenerators as New Energy Technology for Self-Powered Systems and as Active Mechanical and Chemical Sensors. *ACS Nano*. 2013;7:9533-57.
- [8] Khandelwal G, Chandrasekhar A, Alluri NR, Vivekananthan V, Maria Joseph Raj NP, Kim S-J. Trash to energy: A facile, robust and cheap approach for mitigating environment pollutant using household triboelectric nanogenerator. *Applied Energy*. 2018;219:338-49.
- [9] Furfari FA. A history of the Van de Graaff generator. *IEEE Industry Applications Magazine*. 2005;11:10-4.
- [10] Wu C, Wang AC, Ding W, Guo H, Wang ZL. Triboelectric Nanogenerator: A Foundation of the Energy for the New Era. *Advanced Energy Materials*. 2019;9:1802906.



- [11] Boag JW. The design of the electric field in a Van de Graaff generator. Proceedings of the IEE - Part IV: Institution Monographs 1953. p. 63-82.
- [12] Niu S, Wang S, Lin L, Liu Y, Zhou YS, Hu Y, et al. Theoretical study of contact-mode triboelectric nanogenerators as an effective power source. Energy & Environmental Science. 2013;6:3576-83.
- [13] Dharmasena RDIG, Jayawardena KDGI, Mills CA, Deane JHB, Anguita JV, Dorey RA, et al. Triboelectric nanogenerators: providing a fundamental framework. Energy & Environmental Science. 2017;10:1801-11.
- [14] Dharmasena RDIG, Deane JHB, Silva SRP. Nature of Power Generation and Output Optimization Criteria for Triboelectric Nanogenerators. Advanced Energy Materials. 2018;8:1802190.
- [15] Yang B, Zeng W, Peng Z-H, Liu S-R, Chen K, Tao X-M. A Fully Verified Theoretical Analysis of Contact-Mode Triboelectric Nanogenerators as a Wearable Power Source. Advanced Energy Materials. 2016;6:1600505.
- [16] Khandelwal G, Chandrasekhar A, Pandey R, Maria Joseph Raj NP, Kim S-J. Phase inversion enabled energy scavenger: A multifunctional triboelectric nanogenerator as benzene monitoring system. Sensors and Actuators B: Chemical. 2019;282:590-8.
- [17] Wang ZL, Lin L, Chen J, Niu S, Zi Y. Triboelectric Nanogenerator: Vertical Contact-Separation Mode. Triboelectric Nanogenerators. Cham: Springer International Publishing; 2016. p. 23-47.
- [18] Khandelwal G, Maria Joseph Raj NP, Kim S-J. Triboelectric nanogenerator for healthcare and biomedical applications. Nano Today. 2020;33:100882.
- [19] Niu S, Liu Y, Wang S, Lin L, Zhou YS, Hu Y, et al. Theory of Sliding-Mode Triboelectric Nanogenerators. Advanced Materials. 2013;25:6184-93.
- [20] Wang ZL, Lin L, Chen J, Niu S, Zi Y. Triboelectric Nanogenerator: Lateral Sliding Mode. Triboelectric Nanogenerators. Cham: Springer International Publishing; 2016. p. 49-90.

- [21] Wang ZL, Lin L, Chen J, Niu S, Zi Y. Triboelectric Nanogenerator: Single-Electrode Mode. *Triboelectric Nanogenerators*. Cham: Springer International Publishing; 2016. p. 91-107.
- [22] Niu S, Liu Y, Wang S, Lin L, Zhou YS, Hu Y, et al. Theoretical Investigation and Structural Optimization of Single-Electrode Triboelectric Nanogenerators. *Advanced Functional Materials*. 2014;24:3332-40.
- [23] Khandelwal G, Minocha T, Yadav SK, Chandrasekhar A, Maria Joseph Raj NP, Gupta SC, et al. All edible materials derived biocompatible and biodegradable triboelectric nanogenerator. *Nano Energy*. 2019;65:104016.
- [24] Li Y, Cheng G, Lin Z-H, Yang J, Lin L, Wang ZL. Single-electrode-based rotary triboelectric nanogenerator and its applications as self-powered contact area and eccentric angle sensors. *Nano Energy*. 2015;11:323-32.
- [25] Wang ZL, Lin L, Chen J, Niu S, Zi Y. Triboelectric Nanogenerator: Freestanding Triboelectric-Layer Mode. *Triboelectric Nanogenerators*. Cham: Springer International Publishing; 2016. p. 109-53.
- [26] Jiang T, Chen X, Han CB, Tang W, Wang ZL. Theoretical Study of Rotary Freestanding Triboelectric Nanogenerators. *Advanced Functional Materials*. 2015;25:2928-38.
- [27] Wang S, Xie Y, Niu S, Lin L, Wang ZL. Freestanding Triboelectric-Layer-Based Nanogenerators for Harvesting Energy from a Moving Object or Human Motion in Contact and Non-contact Modes. *Advanced Materials*. 2014;26:2818-24.
- [28] Zi Y, Niu S, Wang J, Wen Z, Tang W, Wang ZL. Standards and figure-of-merits for quantifying the performance of triboelectric nanogenerators. *Nature Communications*. 2015;6:8376.
- [29] Chen J, Wang ZL. Reviving Vibration Energy Harvesting and Self-Powered Sensing by a Triboelectric Nanogenerator. *Joule*. 2017;1:480-521.
- [30] Seol M, Kim S, Cho Y, Byun K-E, Kim H, Kim J, et al. Triboelectric Series of 2D Layered Materials. *Advanced Materials*. 2018;30:1801210.

- [31] Zou H, Zhang Y, Guo L, Wang P, He X, Dai G, et al. Quantifying the triboelectric series. *Nature Communications*. 2019;10:1427.
- [32] Zhai L, Cui S, Tong B, Chen W, Wu Z, Soutis C, et al. Bromine-Functionalized Covalent Organic Frameworks for Efficient Triboelectric Nanogenerator. *Chemistry – A European Journal*. 2020;26:5784-8.
- [33] Pan S, Zhang Z. Fundamental theories and basic principles of triboelectric effect: A review. *Friction*. 2019;7:2-17.
- [34] Lu CX, Han CB, Gu GQ, Chen J, Yang ZW, Jiang T, et al. Temperature Effect on Performance of Triboelectric Nanogenerator. *Advanced Engineering Materials*. 2017;19:1700275.
- [35] Nguyen V, Yang R. Effect of humidity and pressure on the triboelectric nanogenerator. *Nano Energy*. 2013;2:604-8.
- [36] Fan F-R, Lin L, Zhu G, Wu W, Zhang R, Wang ZL. Transparent Triboelectric Nanogenerators and Self-Powered Pressure Sensors Based on Micropatterned Plastic Films. *Nano Letters*. 2012;12:3109-14.
- [37] Wang S, Lin L, Xie Y, Jing Q, Niu S, Wang ZL. Sliding-Triboelectric Nanogenerators Based on In-Plane Charge-Separation Mechanism. *Nano Letters*. 2013;13:2226-33.
- [38] Zhu G, Chen J, Liu Y, Bai P, Zhou YS, Jing Q, et al. Linear-Grating Triboelectric Generator Based on Sliding Electrification. *Nano Letters*. 2013;13:2282-9.
- [39] Yang Y, Zhang H, Chen J, Jing Q, Zhou YS, Wen X, et al. Single-Electrode-Based Sliding Triboelectric Nanogenerator for Self-Powered Displacement Vector Sensor System. *ACS Nano*. 2013;7:7342-51.
- [40] Yang Y, Zhou YS, Zhang H, Liu Y, Lee S, Wang ZL. A Single-Electrode Based Triboelectric Nanogenerator as Self-Powered Tracking System. *Advanced Materials*. 2013;25:6594-601.
- [41] Zhang H, Yang Y, Zhong X, Su Y, Zhou Y, Hu C, et al. Single-Electrode-Based Rotating Triboelectric Nanogenerator for Harvesting Energy from Tires. *ACS Nano*. 2014;8:680-9.
- [42] Lin Z-H, Cheng G, Lin L, Lee S, Wang ZL. Water–Solid Surface Contact Electrification and its Use for Harvesting Liquid-Wave Energy. *Angewandte Chemie International Edition*. 2013;52:12545-9.

- [43] Han M, Zhang X, Liu W, Sun X, Peng X, Zhang H. Low-frequency wide-band hybrid energy harvester based on piezoelectric and triboelectric mechanism. *Science China Technological Sciences*. 2013;56:1835-41.
- [44] Xie Y, Wang S, Niu S, Lin L, Jing Q, Yang J, et al. Grating-Structured Freestanding Triboelectric-Layer Nanogenerator for Harvesting Mechanical Energy at 85% Total Conversion Efficiency. *Advanced Materials*. 2014;26:6599-607.
- [45] Wang S, Niu S, Yang J, Lin L, Wang ZL. Quantitative Measurements of Vibration Amplitude Using a Contact-Mode Freestanding Triboelectric Nanogenerator. *ACS Nano*. 2014;8:12004-13.
- [46] Zhang C, Tang W, Zhang L, Han C, Wang ZL. Contact Electrification Field-Effect Transistor. *ACS Nano*. 2014;8:8702-9.
- [47] Zhou T, Zhang C, Han CB, Fan FR, Tang W, Wang ZL. Woven Structured Triboelectric Nanogenerator for Wearable Devices. *ACS Applied Materials & Interfaces*. 2014;6:14695-701.
- [48] Zheng Q, Shi B, Fan F, Wang X, Yan L, Yuan W, et al. In Vivo Powering of Pacemaker by Breathing-Driven Implanted Triboelectric Nanogenerator. *Advanced Materials*. 2014;26:5851-6.
- [49] Zhang C, Zhou T, Tang W, Han C, Zhang L, Wang ZL. Rotating-Disk-Based Direct-Current Triboelectric Nanogenerator. *Advanced Energy Materials*. 2014;4:1301798.
- [50] Lee JH, Hinchet R, Kim SK, Kim S, Kim S-W. Shape memory polymer-based self-healing triboelectric nanogenerator. *Energy & Environmental Science*. 2015;8:3605-13.
- [51] Zheng Q, Zou Y, Zhang Y, Liu Z, Shi B, Wang X, et al. Biodegradable triboelectric nanogenerator as a life-time designed implantable power source. *Science Advances*. 2016;2:e1501478.
- [52] Chen BD, Tang W, He C, Deng CR, Yang LJ, Zhu LP, et al. Water wave energy harvesting and self-powered liquid-surface fluctuation sensing based on bionic-jellyfish triboelectric nanogenerator. *Materials Today*. 2018;21:88-97.

[53] Cao X, Zhang M, Huang J, Jiang T, Zou J, Wang N, et al. Inductor-Free Wireless Energy Delivery via Maxwell's Displacement Current from an Electrodeless Triboelectric Nanogenerator. *Advanced Materials*. 2018;30:1704077.

[54] Chandrasekhar A, Vivekananthan V, Khandelwal G, Kim S-J. A Sustainable Blue Energy Scavenging Smart Buoy toward Self-Powered Smart Fishing Net Tracker. *ACS Sustainable Chemistry & Engineering*. 2020;8:4120-7.

[55] Khan U, Kim S-W. Triboelectric Nanogenerators for Blue Energy Harvesting. *ACS Nano*. 2016;10:6429-32.

## CHAPTER – II

### Materials and Methods

#### 2.1 Chemicals and reagents

The experiments in the thesis were conducted by using the chemicals and reagents purchased from various vendors. All the chemicals are of analytical grade and were used without any further purification. Table 2.1 elucidated the list of chemicals and reagents used in the research work.

**Table 2.1.** List of chemicals and reagents used in the research work.

S.No.	Chemical Name	Supplier
1.	Titanium oxide (TiO <sub>2</sub> )	Daejung Chemicals, Korea
2.	Polyvinylidene fluoride (PVDF)	Alfa Aesar, USA
3.	Cellulose acetate	Daejung Chemicals, Korea
4.	Silver leaf	Online store
5.	Rice sheet	Local market
6.	Zinc acetate dihydrate (Zn (CH <sub>3</sub> COO) <sub>2</sub> .2H <sub>2</sub> O)	Daejung Chemicals, Korea
7.	Cobalt (II) acetate tetrahydrate Co (CH <sub>3</sub> COO) <sub>2</sub> .4H <sub>2</sub> O	Daejung Chemicals, Korea
8.	Benzimidazole (C <sub>7</sub> H <sub>6</sub> N <sub>2</sub> )	Merck KgaA (Germany)
9.	Zinc nitrate hexahydrate (Zn (NO <sub>3</sub> ) <sub>2</sub> .6H <sub>2</sub> O)	Daejung Chemicals, Korea

10.	Magnesium nitrate hexahydrate (Mg (NO <sub>3</sub> ) <sub>2</sub> ·6H <sub>2</sub> O)	Daejung Chemicals, Korea
11.	Ethyl cellulose, ethoxyl content 48 %, 22cps	Agros organics, USA
12.	Poly (methyl methacrylate) (PMMA)	Sigma Aldrich, USA
13.	Imidazole (C <sub>3</sub> N <sub>2</sub> H <sub>4</sub> )	Merck KgaA (Germany)
14.	2-methylimidazole (CH <sub>3</sub> C <sub>3</sub> H <sub>2</sub> N <sub>2</sub> H)	Sigma Aldrich, USA
15.	L-aspartic acid (C <sub>4</sub> H <sub>7</sub> NO <sub>4</sub> )	Daejung Chemicals, Korea
16.	Copper nitrate trihydrate (CuN <sub>2</sub> O <sub>6</sub> ·3H <sub>2</sub> O)	Daejung Chemicals, Korea
17.	Kapton film	Eleparts, Korea
18.	Fluorinated ethylene propylene (FEP)	Eleparts, Korea
19.	Teflon film	Eleparts, Korea
20.	Polyethylene terephthalate (PET)	Eleparts, Korea
21.	Conducting adhesive aluminum tape	Eleparts, Korea
22.	N, N-Dimethylformamide (DMF)	Daejung Chemicals, Korea
23.	Benzene	Daejung Chemicals, Korea
24.	Ethanol	Daejung Chemicals, Korea
25.	Methanol	Daejung Chemicals, Korea
26.	Ammonium hydroxide (25% solution)	Daejung Chemicals, Korea
27.	Dimethyl Sulfoxide (DMSO)	Sigma Aldrich, USA
28.	Hydrogen peroxide (H <sub>2</sub> O <sub>2</sub> ), 35%	Daejung Chemicals, Korea
29.	3-(4,5-Dimethylthiazol-2-yl)-2,5-Diphenyltetrazolium Bromide (MTT)	Sigma Aldrich, USA
30.	Dulbecco's Modified Eagle Medium (DMEM)	Invitrogen, USA

31.	Fetal bovine serum (FBS)	Invitrogen, USA
32.	Mammary epithelial cell growth basal medium (MEBM)	Lonza, USA
33.	Growth factors	Lonza, USA

## 2.2. Cell lines

**Table 2.2.** The details of the used cell lines.

S.No.	Type	Supplier
1.	HeLa Cell line	National centre for cell science, India
2.	Mammary epithelial cells (MCF-10A)	American type culture collection, USA
3.	Dermal fibroblast	American type culture collection, USA

## 2.3 Apparatus

The apparatus used for the synthesis, coating, film fabrication, and device fabrication are mentioned in Table 2.3.

**Table 2.3.** List of the apparatus used for the research.

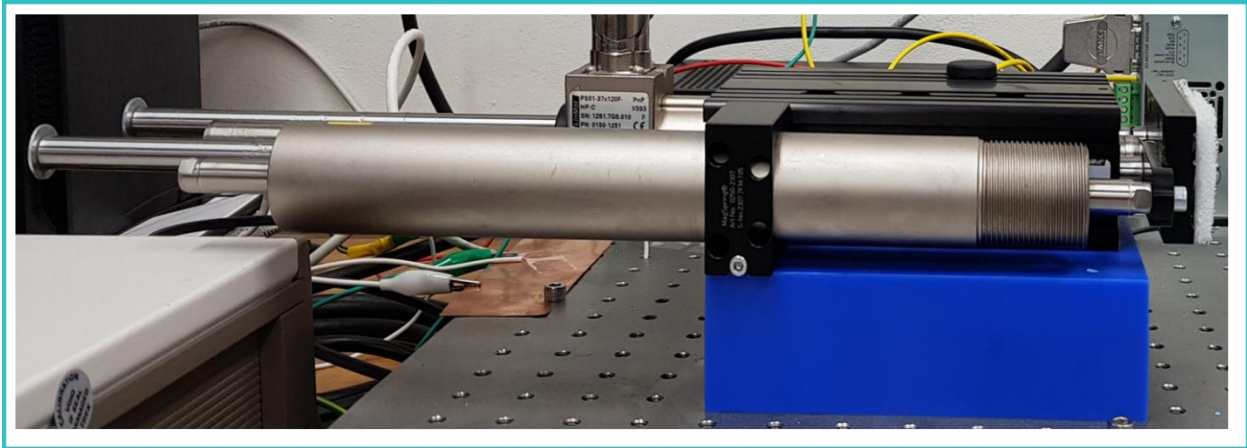
S.No.	Apparatus	Specifications	Company
1.	Spin coater	Spin 1200	Midas System
2.	Probe sonicator	Sonic VCX 500 model	Sonics and Materials Inc.



3.	Ultrasonic bath	S15H	Elma
4.	Weighing balance	AUW220D	Shimadzu
5.	Centrifuge	1580 MG	Gyrozen
6.	Hot air oven	OF-02-GW	JIEO Tech
7.	Vacuum oven	JSVO-30T	JSR
8.	Stainless steel lined autoclave	PTFE container	Latech
9.	Magnetic stirrer	MS300HS	M Tops
10.	Tape casting coater	MSK-AFA-HC-100	MTI
11.	Micropipete	Piept-Lite-XLS	Rainin
12.	Phase-contrast microscope	IX73	Olympus
13.	Micro plate reader	VersaMax	Molecular devices, USA

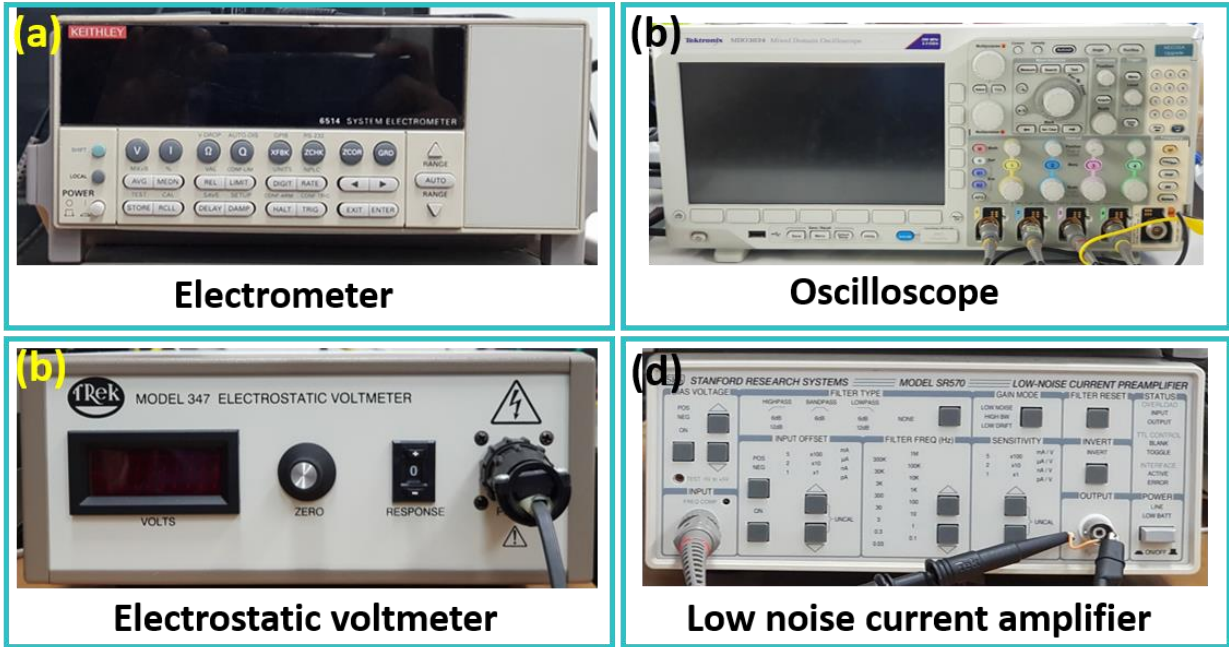
## 2.4 Electrical Characterization

All the electrical analysis was carried out under a homemade Faraday cage by applying an external force using a commercial linear motor (LinMot Inc. Lake Geneva, WI, USA) shown in Figure 2.1.



**Figure 2.1.** Linear motor for applying force to the device during electrical measurement.

A 6514 electrometer (Keithley Instruments, Cleveland, OH, USA) was used to measure the voltage output of the device. A Stanford system low noise current preamplifier (SR570) and oscilloscope (MDO3000 series; Tektronix, Inc., Beaverton, OR, USA) were used for the current analysis of the device. The surface potential was measured by Trek 347 (Walnut St, Lockport, New York, USA) electrostatic voltmeter. The instruments used for electrical measurement are shown in Figure 2.2.



**Figure 2.2.** Electrical characterization system. (a) High impedance electrometer. (b) A mixed domain oscilloscope. (c) The electrostatic voltmeter and (d) Low noise current preamplifier.

## 2.5 Material Characterization

### 2.5.1 X-ray diffraction

X-ray diffraction (XRD) is the most widely used analytical technique for the phase recognition of the materials. It can be used to study the unit cell dimensions, sample purity, identification of material, to determine crystal structure, etc. The XRD measurements were recorded on Empyrean (Malvern PANalytical, Almelo, The Netherlands) at tube current of 30 mA and a generator voltage of 40 kV. All the measurements were carried out room temperature.



**Figure 2.3.** PANalytical Empyrean XRD measurement system.

### 2.5.2 Raman spectroscopy

Raman spectroscopy provides information about the crystallinity, structural fingerprint, phase and polymorph, structural defects, and molecular interactions. Raman spectroscopy is a non-destructive technique that works on the principle of Raman scattering i.e., inelastic scattering of the photons. Raman spectra were recorded using LabRAM HR (Horiba Jobin-Yvon, Lille, France) using an Ar<sup>+</sup> laser with an excitation wavelength of 514 nm. The data was collected in the various spectral region using a 10-s data point acquisition.



**Figure 2.4.** Horiba LabRAM HR Raman measurement system.

### 2.5.3 Fourier transform infrared spectroscopy

The Fourier transform infrared spectroscopy (FT-IR) provide information on the molecular fingerprint of the sample. The FT-IR generates a spectrum which can be used to identify the structure as the different chemical structure has different spectral fingerprint. FT-IR spectra were

recorded on a Thermo Scientific Nicolet-6700 system (Waltham, MA, USA) using KBr pellet. The samples were also recorded in attenuated total reflection (ATR) mode.

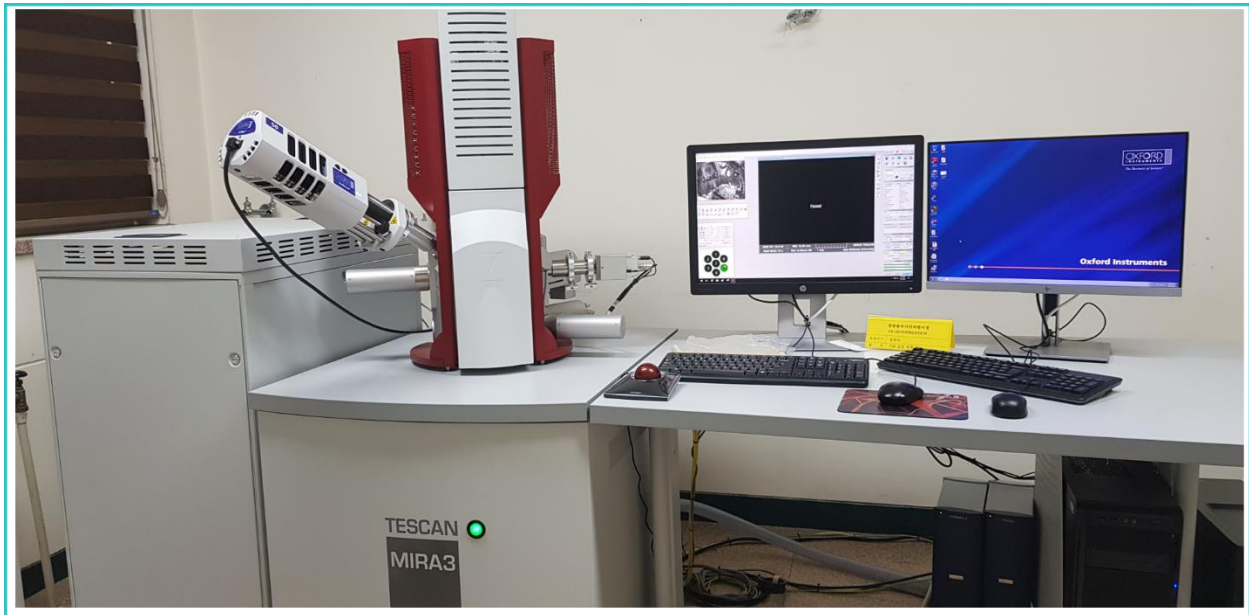


**Figure 2.5.** Thermo Scientific Nicolet-6700 FT-IR measurement system.

#### **2.5.4 Field-emission scanning electron microscopy**

Field-emission scanning electron microscopy (FE-SEM) is the most widely used microscopy technique to analyze the morphology and the size of the samples. The interaction of the electron beam with the material creates the interaction volume and gives rise to various signals that contain information about the composition and topography of the sample. The surface morphology analysis was carried out on the Tescan MIRA-3 FE-SEM system (Kohoutovice, Czech Republic). The samples were sputter-coated with platinum and placed on the metal stub with the help of carbon tape.





**Figure 2.6.** Tescan MIRA 3 FE-SEM system.

### **2.5.5 Energy-dispersive X-ray spectroscopy**

The Energy-dispersive X-ray spectroscopy (EDS) is an analytical technique that is widely used for the elemental mapping or analysis of the material. The EDS was analyzed on the Tescan MIRA-3 FE-SEM system equipped with an Oxford EDS detector. The electron beam was used as an excitation source for the EDS in the FE-SEM system.

### **2.5.6 Atomic force microscopy and Kelvin probe force microscopy**

Atomic force microscopy (AFM) is a high-resolution microscopy technique that can also provide three-dimensional information about topography. The AFM works by scanning a sharp tip over the sample surface. The tip was mounted on a cantilever. The deflection in the cantilever due to the attractive force between the tip and sample surface was used to generate the image. The AFM was taken on Bruker Multimode 8 system using an SCM-PIT probe (Pt/Ir- coated probe) in the tapping mode. The Kelvin probe force microscopy (KPFM) is a technique used to map the

surface potential on a wide range of samples. The surface potential can be used to calculate the work function of the material. The KPFM was performed in amplitude modulation (AM) mode on Bruker Multimode 8 system using an SCM-PIT probe. The instrument was calibrated with the highly oriented pyrolytic graphite (HOPG). The HOPG sample was cleaved fresh with the scotch tape.



**Figure 2.7.** Bruker Multimode 8 AFM system.



### 2.5.7 3D optical surface profiler

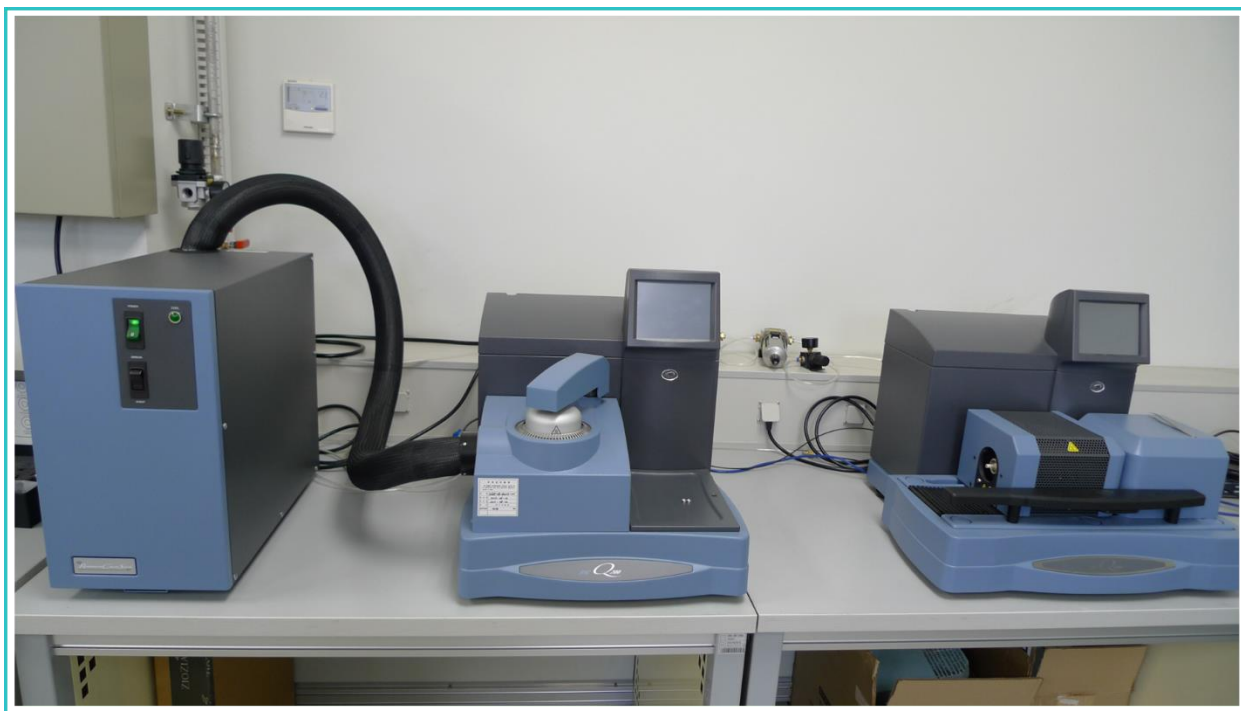
The optical profiler is a non-destructive technique to precisely characterize the micro and nanoscale surface features. The surface roughness parameters of the samples were measured using the images captured by the NV2200 3D optical surface profiler (NanoSystem, South Korea).



**Figure 2.8.** Nanosystem NV 2200 3D optical surface profiler.

### 2.5.8 Thermogravimetric analysis

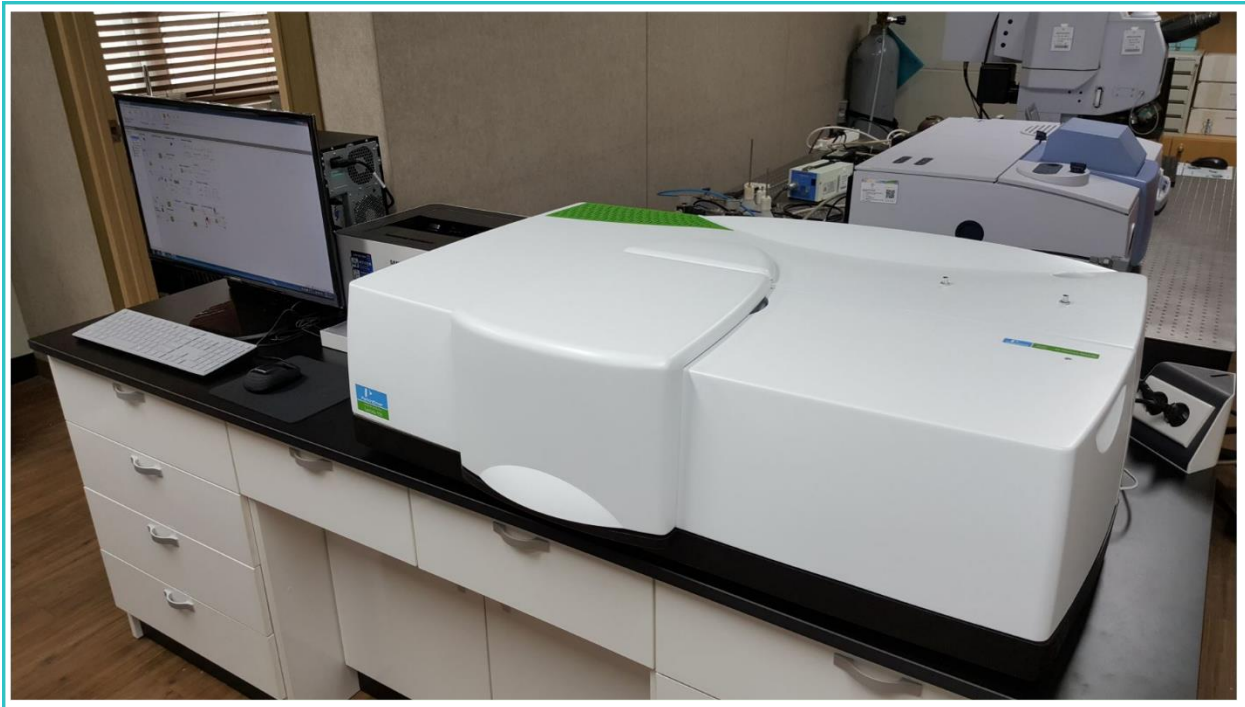
Thermogravimetric analysis (TGA) analysis is used to measure the thermal stability of the materials by checking the weight change in the sample during the constant heating. The TGA analysis was carried on Q1600 SDT (TA instruments, New Castle, DE, USA), in air atmosphere.



**Figure 2.9.** TA instruments TGA and DSC system.

### 2.5.9 Ultraviolet-visible spectroscopy

The Ultraviolet-visible (UV-Vis) spectroscopy measures the amount of light absorbed by the material. UV-Vis has applications in many fields like chemistry, life science, material science, quality control, etc. The UV-Vis spectra were recorded on Perkin Elmer, Lambda 950, at a data interval of 1.0 nm.



**Figure 2.10.** Perkin Elmer Lambda 950, UV-VIS spectrophotometer.

## 2.6 Cell line studies

### 2.6.1 Method I

Uncoated and silver leaf-coated laver devices were dried and manually ground using a mortar and pestle. The material was suspended in absolute ethanol, and each volume made up to 1 mL. The suspensions were shaken overnight at 37 °C and 150 rpm, the tubes centrifuged at 3000 g, the supernatants collected and filtered, the solutions kept in a dry bath at 40 °C until 90% of the ethanol had evaporated, the mixtures lyophilized, the dry weights measured, and the extracts dissolved in 200- $\mu$ L amounts of DMSO to a concentration of 1 mg/mL and used in biological studies. The HeLa cell cytotoxicities of coated and non-coated laver were evaluated. HeLa cells (104-105/well) were seeded into a 96-well plate, grown for 24 h, exposed to coated and non-coated laver for 24 and 48 h and MTT (10  $\mu$ L of a 5 mg/mL stock) then added to each well followed by

incubation at 37 °C for 3 h under CO<sub>2</sub>. Viable cells convert MTT to purple formazan. The reaction was stopped by addition of 100 µL DMSO to each well, and absorbances read using an ELISA plate reader operating at 570 nm. The effects of coated and non-coated layer on HeLa cell morphology were examined using a phase-contrast microscope. HeLa cells (10<sup>4</sup>-10<sup>5</sup>/ well) were seeded into a 96-well plate, grown for 24 h, exposed to coated and non-coated layer for 24 h, washed with PBS, and visualized at 10X.

### **2.6.2 Method II**

Briefly, MCF-10A and dermal fibroblasts cells (5,000 cells/well) were cultured in 96-well cell culture plates and incubated for 24 h. Following 24 h of incubation, cells were exposed to different concentrations (400, 200, 100, 50, 25 and 12.5 µg/mL) of the prepared metal-biomolecule framework (dissolved in phosphate buffer saline) for 24 and 48 h. Parallely, cells were exposed to magnesium oxide (MgO) at the same concentrations as a reference. Following incubation periods, cells were photographed under a phase-contrast microscope, washed two times with phosphate buffer saline, and wells were filled with fresh DMEM containing MTT (0.5 mg/mL). After 4 h of incubation, the medium was removed, and 100 µL of DMSO was added to each well to solubilize formazan crystals. The absorbance of each well was recorded at 570 nm using a microplate reader.

### **2.6.3 DAPI staining**

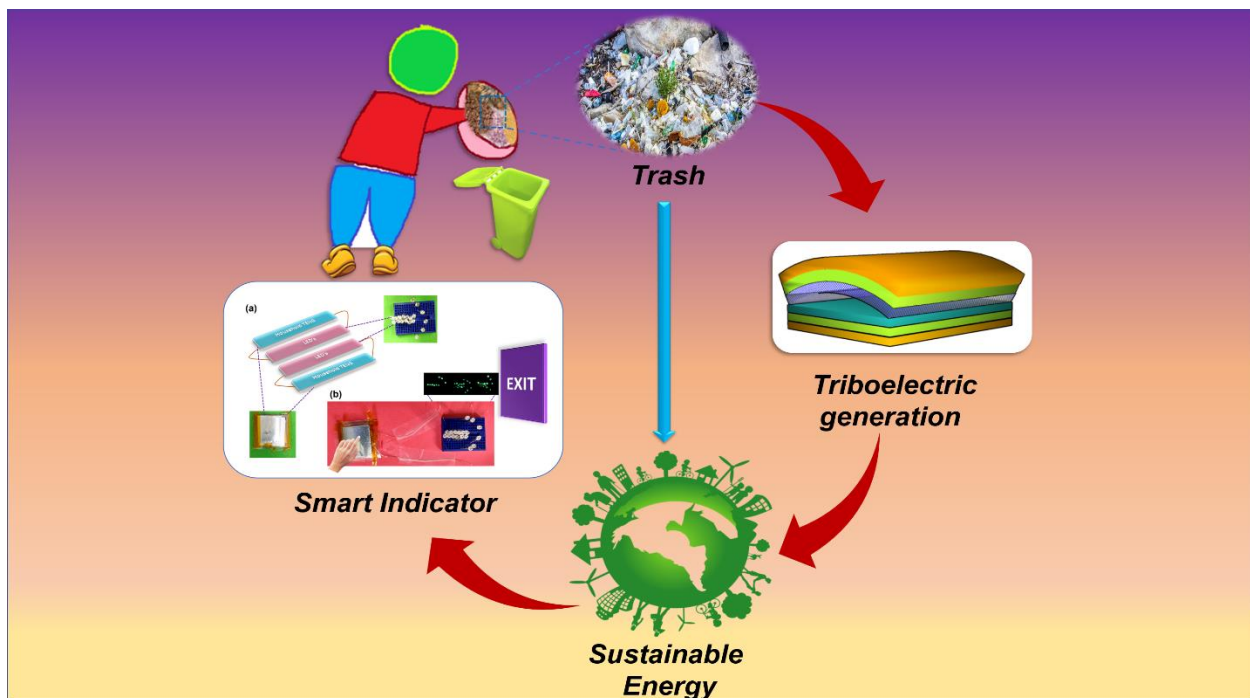
Morphological changes of HeLa cell nuclei were examined via DAPI staining. HeLa cells (10<sup>4</sup>-10<sup>5</sup>/well) were seeded into a 96-well plate, grown for 24 h, and exposed to coated and non-coated layer for 24 h; the cells were fixed and permeabilized with methanol (100 µL/well) for 30 min at -20 °C and then washed with PBS to remove all methanol. Finally, the cells were stained

with DAPI (2  $\mu\text{g}/\text{mL}$ ) for 15 min at room temperature in the dark, and the cells imaged under a fluorescence microscope at 40X.

## CHAPTER III

### 3.1 Trash to Energy: A Facile, Robust and Cheap Approach for Mitigating Environment Pollutant Using Household Triboelectric Nanogenerator

#### Graphical Overview



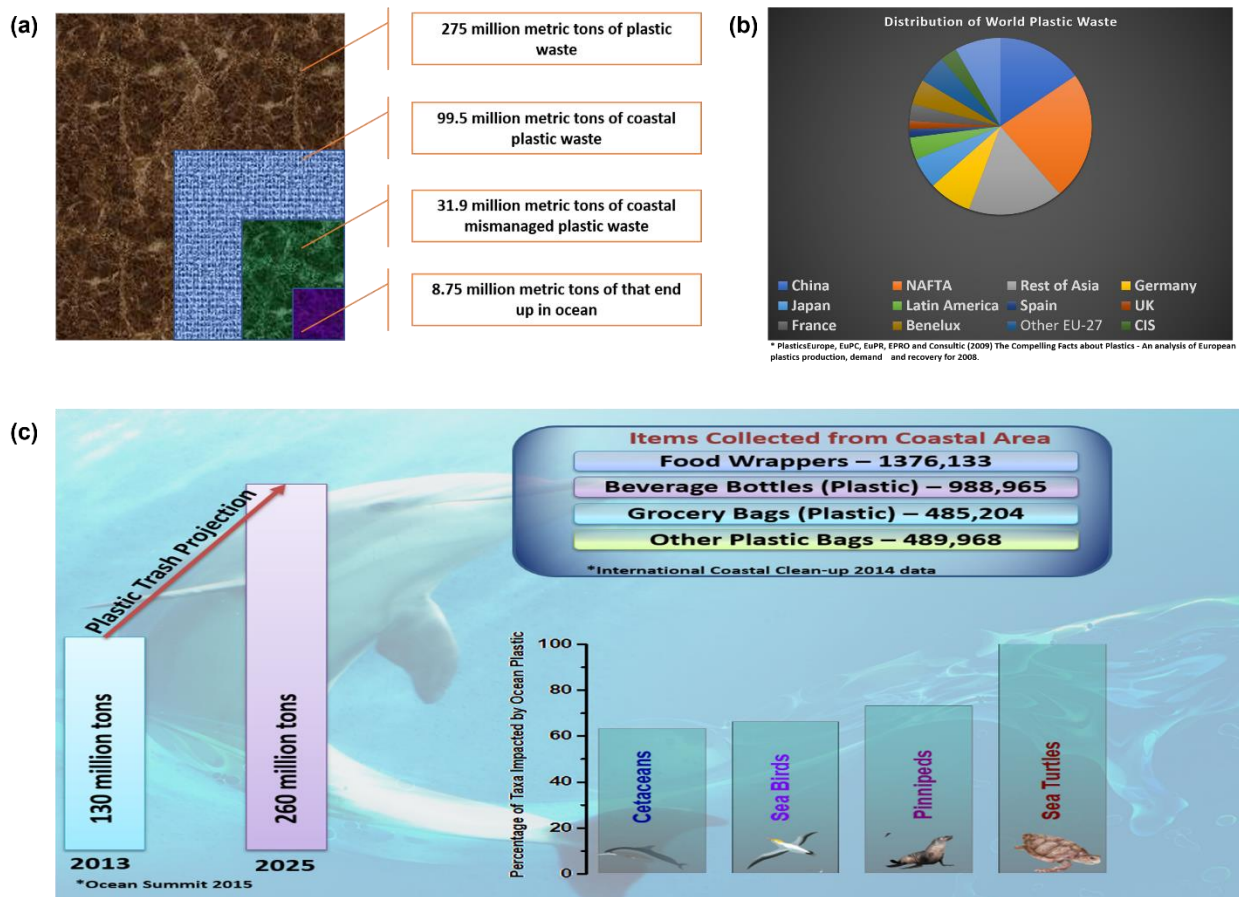
## Highlights

- Circumvention of plastic pollution using household H-TENG.
- The device fabrication is straightforward, cheap, and needs <5 min.
- All the materials used in the fabrication are recycled waste materials like food packaging, cleaning sponge, used aluminum foil, etc.
- Fabrication is possible at any place without the need for scientific equipment.
- Demonstration of the biomechanical energy harvesting, emergency direction system, smart chopping board etc.

### 3.1.1 Introduction

Plastic waste is currently one of the greatest environmental threats. It is present in all marine environments, ranging from the seafloor to coastlines to the open ocean, and is even found in Arctic Ocean ice [1]. Recent studies have provided evidence that plastic waste accumulates in organisms and may cause the death of marine life and sea birds [2]. A previous review reported that plastic waste in the order of thousands of tons covers the surface of the open oceans [2]. Data collected in the year 2010 from coastal countries indicated that of 275 million megatonnes (MT) of plastic waste produced, 5~12 million MT entered the ocean [1]. Furthermore, only a small proportion of plastic waste is recycled, with most of the waste being dumped in landfills and water. Such disposal methods constitute a significant threat to the environment. Figure 3.1.1 shows global statistics for the generation of plastic waste and the harm it causes to taxa of the ocean [1]. Recently, Orb Media reported test results for 159 samples of drinking water obtained from cities spread among five continents [3]. Of the 33 samples obtained from the United States, 31 contained plastic fibres. The Orb Media data showed that, worldwide, plastic fibres were present in more than 70% of the samples. For example, plastic fibres were found in 82, 81, 76, 75, and 72% of the samples obtained from Delhi (India), Kampala (Uganda), Jakarta (Indonesia), Quito (Ecuador) and Europe, respectively. Population growth has led to a sudden increase in global energy demand. Natural resources are insufficient to meet this requirement because they take hundreds to thousands of years to replenish; this highlights the great need for alternative sustainable energy sources.





**Figure 3.1.1.** Global statistics for generated plastic waste. (a) The proportion of plastic waste reaching the ocean relative to the total plastic waste produced. (b) The distribution of plastic waste in different countries, according to PlasticsEurope, EuPC, EuPR, EPRO, and Consultic (2009). (c) Projection of plastic waste production according to Ocean Summit 2015, plastic items collected from coastal areas according to international coastal clean-up data for 2014, and the number of taxa affected by plastic waste that reaches the ocean.

The development of the triboelectric nanogenerator (TENG) by the group of ZL. Wang has revolutionized the field of energy harvesting. Mechanical energy is ubiquitous and includes wind, wave, and biomechanical energy [4-10]. The TENG uses triboelectrification coupled with electrostatic induction to harness mechanical energy and can operate in four different modes, i.e.,

vertical contact-separation, freestanding layer, lateral sliding, and single electrode modes [11-14]. In the vertical contact-separation case, an applied force brings two triboelectric materials into frictional contact with each other, which results in oppositely charged surfaces. Upon removal of the external force, the electron cloud shared between the electrodes redistributes unevenly, resulting in the generation of a potential difference between the electrodes. This can be harnessed to generate electrical energy via an external circuit [11-14]

There is extensive literature on using TENGs to harvest energy from vibrations, wind, water, and human motion by leveraging the nanostructured surface of the material [9, 15-17]. TENGs have been reported in sensing, molecule degradation, drug delivery, self-charging, and hybrid device applications. Wang et al. reported using a TENG as a nanosensor for various sensing applications, such as phenol detection, vibration and force sensing, and mercury ion detection [18-23]. The majority of the previously reported sensors involve nanomaterials and surface functionalization [19, 23], while all of the previously reported TENGs require some technical expertise and cannot be fabricated by a layperson. Thus, they cannot be readily implemented in daily life. Kim et al. reported polydimethylsiloxane (PDMS)- and dimethyl aminopyridine (DMAP)-coated gold nanoparticle-based TENGs that provided an output voltage of 60 V in the contact-separation mode [24]. The fabrication process was a complicated and involved surface modification and coating processes. Chandrasekhar et al. reported a cellulose/PDMS TENG, with an output of 28 V, as a self-powered locomotion detector [5]. Recently, a TENG has been reported for self-charging applications [25-27]. Dong et al. developed a stretchable and washable yarn-based self-charging textile by combining a TENG with a supercapacitor [26]. Wen et al. made hybrid wearable electronics by combining nanogenerators with solar cells and supercapacitors [25]. Other high-performance hybrid devices have combined piezoelectric and pyroelectric materials

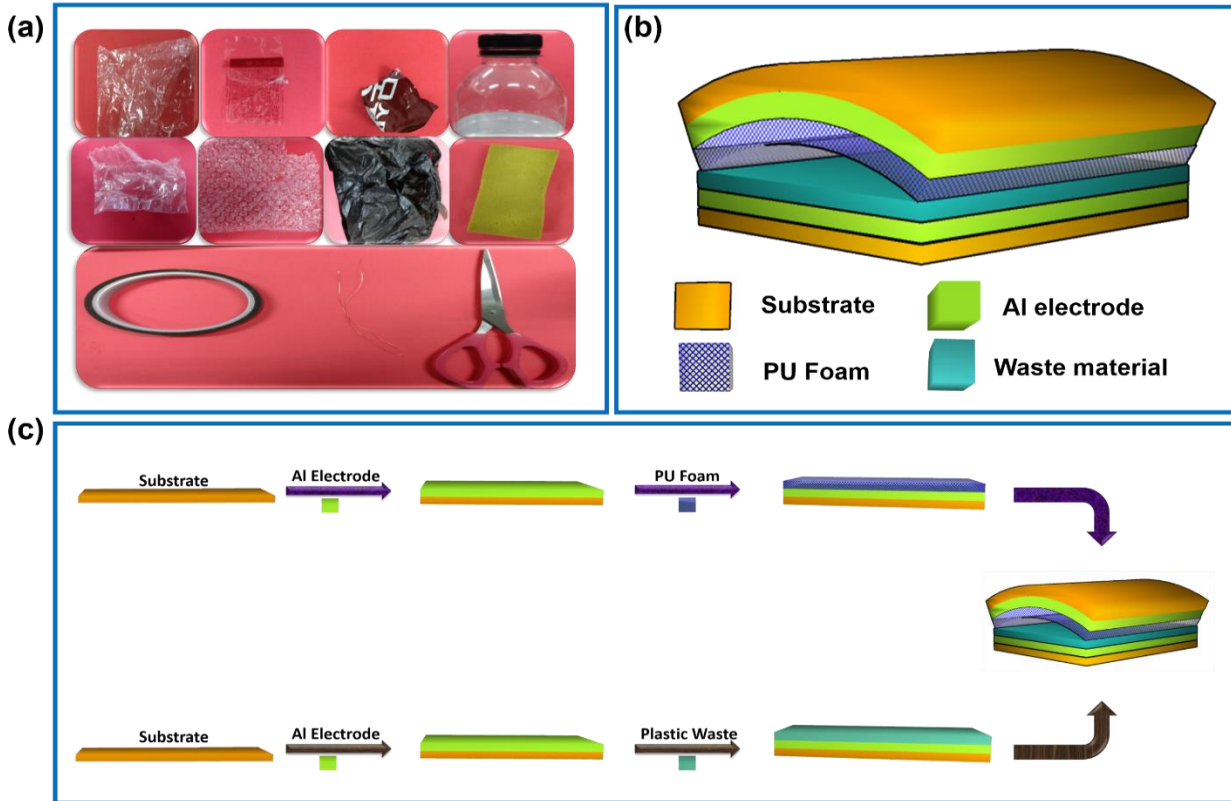
with TENGs [28]. The electrical performance of TENGs can be enhanced by various approaches, such as increasing the surface roughness, chemical functionalization, engineering surface dipoles, providing an electric double layer effect, and poling the ferroelectric polymer [19, 29-32]. Rasel et al. reported the use of sandpaper to create microstructures on PDMS for a human skin-based TENG [33]. This section demonstrates a facile, robust, inexpensive, easy-to-fabricate household triboelectric nanogenerator (H-TENG) that harnesses energy from waste material. The H-TENG takes less than 5 min to make, and its fabrication does not require any scientific equipment, chemicals, or scientific expertise, i.e., it can be made even by a layperson. Furthermore, it can be used to scavenge biomechanical energy from daily plastic waste and thereby help to curb environmental pollution. The maximum generated peak-to-peak voltage was 44 V, and the corresponding peak-to-peak short circuit current ( $I_{sc}$ ) was 289 nA. The H-TENG was systematically studied for applications such as an emergency indicator system and an energy-harvesting chopping board.

### **3.1.2 Experimental Section**

#### **3.1.2.1 Fabrication of the H-TENG**

Pieces from plastic bottles were reclaimed from the garbage and used as the supporting substrate. Waste materials such as polybags, food wrappers, grocery bags, and plastic bottles ( $3 \times 3 \text{ cm}^2$ ) were selected and used to make the negative triboelectric layer. A used kitchen sponge served as the positive triboelectric layer, and cooking-grade aluminum foil was used as an electrode. Finally, copper wires were extracted from the transformer of a compact fluorescent light (CFL) and attached to the aluminum electrode for electrical measurements. Figure 3.1.2 (c) details the fabrication process.

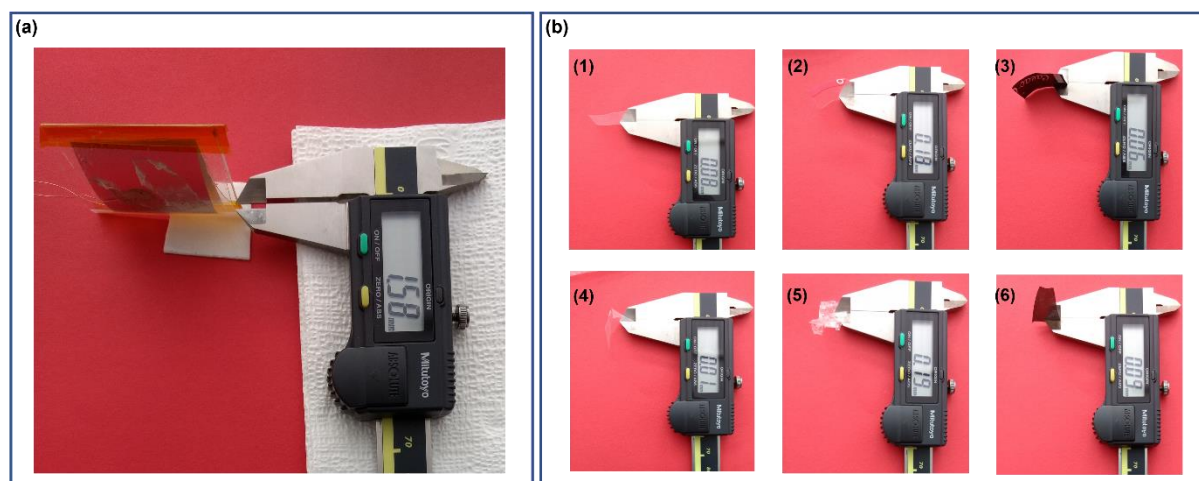
### 3.1.3 Results and Discussion



**Figure 3.1.2.** (a) The recycled waste materials used for the fabrication of household triboelectric nanogenerator (H-TENG). (b) Three-dimensional schematic illustration of the H-TENG. (c) Schematic illustration of the H-TENG fabrication.

The rationale underlying the fabrication of the H-TENG is to use waste materials and fabrication using the aid of a few stationery items. The purpose of the H-TENG is to provide an accessible and rapid way to mitigate plastic pollutions and assist the sustainable development of a green and clean environment. Figure 3.1.2 (a) shows a digital photograph of the recycled materials used in the fabrication of the H-TENG. A three-dimensional schematic illustration of the H-TENG is shown in Figure 3.1.2 (b), and its stepwise fabrication is schematically depicted in Figure 3.1.2 (c). The H-TENG has the multilayer architecture of a traditional TENG, with a working electrode

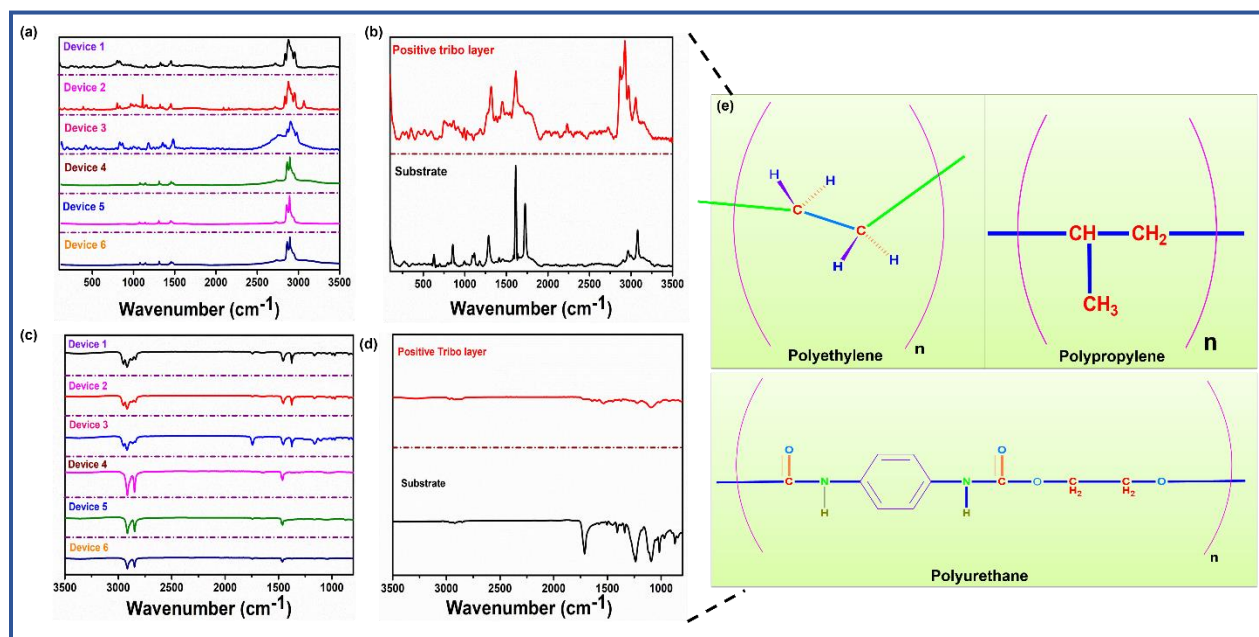
area of 9 cm<sup>2</sup>. Six devices (labeled 1 to 6) were made using randomly selected waste materials. The contact-separation distance for the device was kept constant at 15.8 mm. A digital image of the thickness measurement of the material is shown in Figure 3.1.3.



**Figure 3.1.3.** Digital images. (a) The contact-separation distance of the device. (b) The thickness of the materials used in the device 1-6.

Figure 3.1.4 (a–b) shows the Raman spectra of the six waste materials used as a negative triboelectric layer, for the positive triboelectric layer and the supporting substrate. The Raman spectra identified the material used in devices 1–3 as polypropylene (PP), and that used in devices 4–6 as polyethylene (PE) [34-38]. The positive triboelectric layer was identified as polyurethane foam, and the supporting substrate was a mixture of PE and polystyrene [37-40]. The supporting substrate may vary depending on the plastic bottle composition. The corresponding Raman band assignments are given in the Tables 3.1.1–3.1.4. Figure 3.1.4 (c–d) shows the FT-IR spectrum; the detailed band assignments can be found Tables 3.1.5–3.1.8 [36, 37, 39-42]. Raman and FT-IR data were used to identify the type of materials. The chemical structures of the identified polymers are depicted in Figure 3.1.4 (e).





**Figure 3.1.4.** (a–b) Raman spectra recorded at room temperature for the waste materials and supporting substrate. (c–d) Fourier transform-infrared (FT-IR) spectra recorded at room temperature for the waste materials and supporting substrate. (e) Chemical structures of the materials.

**Table 3.1.1.** Band assignment of polyethylene revealed from Raman spectra.

Frequency (cm <sup>-1</sup> )	Assignment
1060 cm <sup>-1</sup> and 1127 cm <sup>-1</sup>	C-C Stretching
1293 cm <sup>-1</sup>	CH <sub>2</sub> Twisting
1374 cm <sup>-1</sup>	CH <sub>2</sub> Wagging
1434 cm <sup>-1</sup>	CH <sub>2</sub> Bending
2849 cm <sup>-1</sup> and 2882 cm <sup>-1</sup>	C-H Stretching

**Table 3.1.2.** Band assignment of polypropylene revealed from Raman spectra.

Frequency (cm <sup>-1</sup> )	Assignment
808 cm <sup>-1</sup>	CH <sub>2</sub> Rocking and C-C Vibration
842 cm <sup>-1</sup>	CH <sub>2</sub> Rocking
1151 cm <sup>-1</sup>	C-C Vibration and C-H Bending
1221 cm <sup>-1</sup>	CH <sub>2</sub> Twisting, C-H Wagging, and C-C Vibration
1458 cm <sup>-1</sup>	CH <sub>2</sub> Bending
2883 cm <sup>-1</sup>	CH <sub>3</sub> Vibration

**Table 3.1.3.** Band assignment of polyurethane foam revealed from Raman spectra.

Frequency (cm <sup>-1</sup> )	Assignment
1000-1200 cm <sup>-1</sup>	C-O Stretching
1274 cm <sup>-1</sup>	C-N Stretching and N-H Bending in amide III
1325 cm <sup>-1</sup>	CH <sub>2</sub> Wagging/Twisting
1455 cm <sup>-1</sup>	CH <sub>2</sub> Bending
1541 cm <sup>-1</sup>	C-N Stretching and N-H bending in amide II
1620 cm <sup>-1</sup>	C=C Stretching from aromatic ring
2872 cm <sup>-1</sup> and 2932 cm <sup>-1</sup>	CH <sub>2</sub> Stretching
2972 cm <sup>-1</sup>	CH <sub>3</sub> Stretching
3060 cm <sup>-1</sup>	C-H Stretching from aromatic ring
3175 cm <sup>-1</sup> and 3412 cm <sup>-1</sup>	N-H stretching

**Table 3.1.4.** Band assignments of the substrate as revealed from Raman spectra.

Frequency (cm <sup>-1</sup> )	Assignment
1060 cm <sup>-1</sup> , 1127 cm <sup>-1</sup>	C-C Stretching (Polyethylene)
1293 cm <sup>-1</sup>	CH <sub>2</sub> Twisting (Polyethylene)
1637 cm <sup>-1</sup>	C=C (Polystyrene)
2935 cm <sup>-1</sup>	Symmetric CH <sub>2</sub> valency vibrations (Polystyrene)
3138 cm <sup>-1</sup>	V <sub>7B(B<sub>1</sub>)</sub> Similar to mode of Benzene (Polystyrene)

**Table 3.1.5.** Band assignments of polyethylene as revealed from FT-IR spectra.

Frequency (cm <sup>-1</sup> )	Assignment
1374 cm <sup>-1</sup>	CH <sub>3</sub> Bending
1460 cm <sup>-1</sup>	CH <sub>2</sub> Bending
2851 cm <sup>-1</sup> and 2920 cm <sup>-1</sup>	CH <sub>2</sub> Vibration

**Table 3.1.6.** Band assignments of polypropylene as revealed from FT-IR spectra.

Frequency (cm <sup>-1</sup> )	Assignment
972 cm <sup>-1</sup>	CH <sub>3</sub> Rocking and C-C Vibration
1163 cm <sup>-1</sup>	C-C Vibration, CH <sub>3</sub> Rocking, and C-H Bending
1373 cm <sup>-1</sup>	CH <sub>3</sub> Bending symmetric, CH <sub>2</sub> Wagging, C-H Bending, and C-C vibration



1455 cm <sup>-1</sup>	CH <sub>3</sub> Bending asymmetric, CH <sub>2</sub> Bending
2838 cm <sup>-1</sup> and 2863 cm <sup>-1</sup>	CH <sub>2</sub> Vibration symmetric
2920 cm <sup>-1</sup>	CH <sub>2</sub> vibration asymmetric
2957 cm <sup>-1</sup>	CH <sub>3</sub> vibration asymmetric

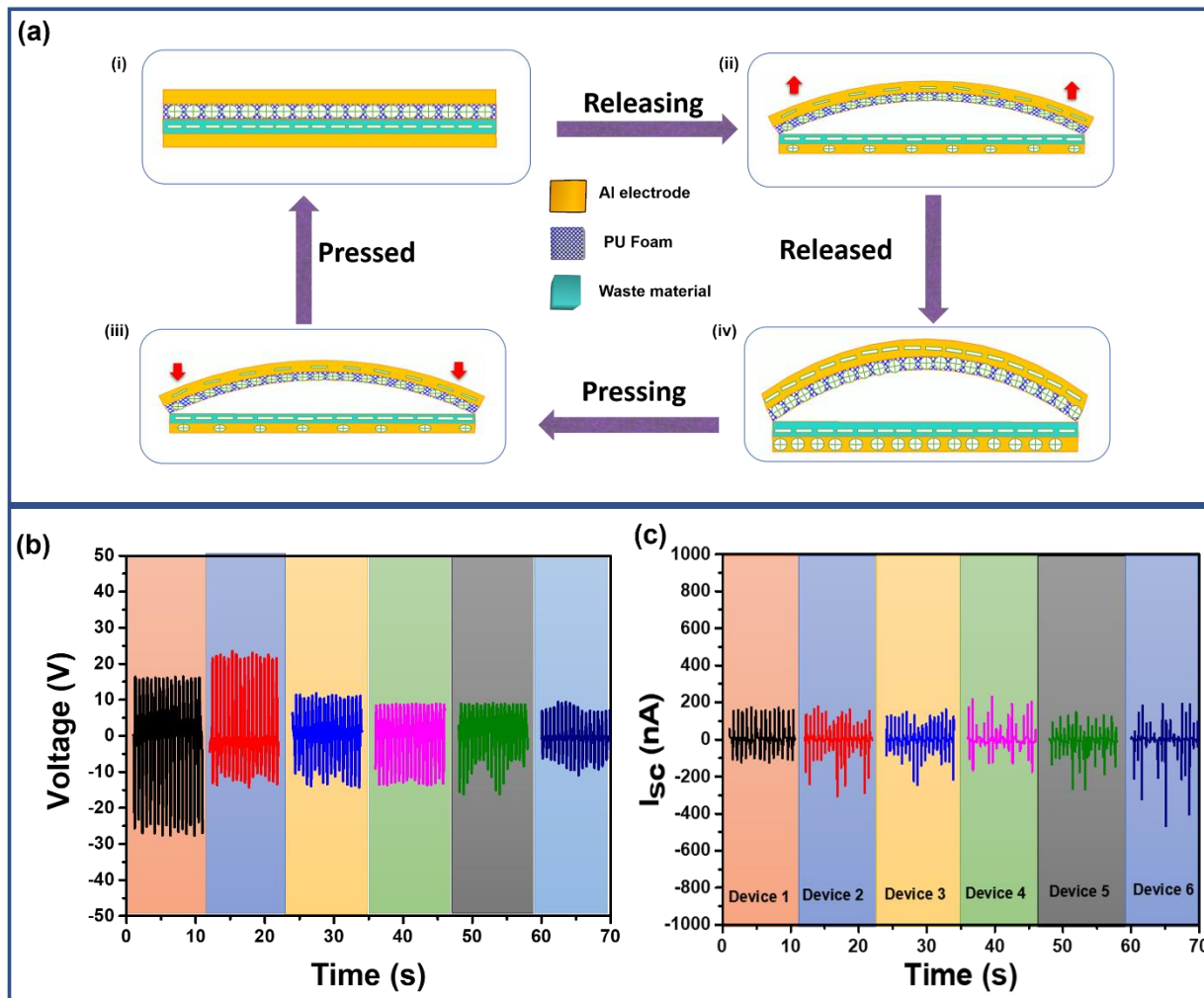
**Table 3.1.7.** Band assignments of polyurethane foam as revealed from FT-IR spectra.

Frequency (cm <sup>-1</sup> )	Assignment
1220 cm <sup>-1</sup> , 1371 cm <sup>-1</sup>	Modes of CH <sub>2</sub> vibration
1535 cm <sup>-1</sup>	NH vibrations
1715 cm <sup>-1</sup>	Non-hydrogen bonded carbonyl group
2855 cm <sup>-1</sup> , 2922 cm <sup>-1</sup>	CH <sub>2</sub> Stretching

**Table 3.1.8.** Band assignments of the substrate as revealed from FT-IR spectra.

Frequency (cm <sup>-1</sup> )	Assignment
325 cm <sup>-1</sup>	C-C-C bending (polystyrene)
650 cm <sup>-1</sup> to 900 cm <sup>-1</sup>	Aromatic CH deformation vibration (polystyrene)
1748 cm <sup>-1</sup>	Aromatic CH combination frequency overtone
1374 cm <sup>-1</sup>	CH <sub>3</sub> bending (Polyethylene)
1460 cm <sup>-1</sup>	CH <sub>2</sub> bending (Polyethylene)
2851 cm <sup>-1</sup> , 2920 cm <sup>-1</sup>	CH <sub>2</sub> Vibration (Polyethylene)

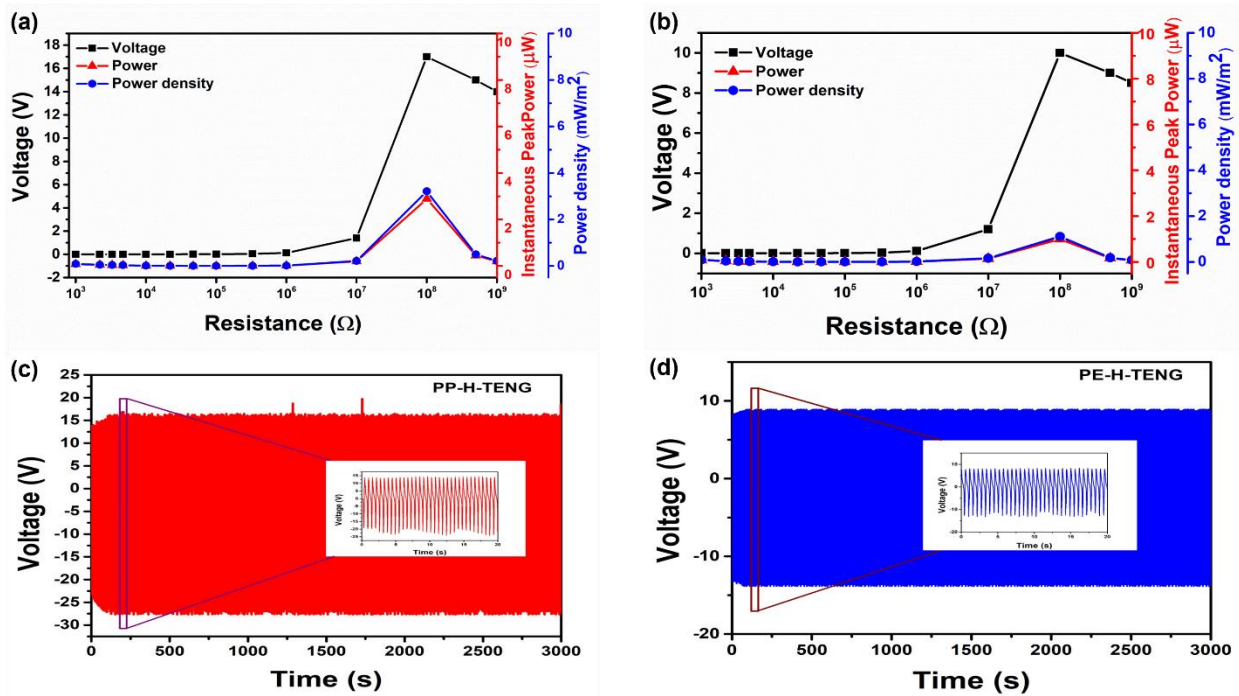
The operation of the H-TENG is based on contact electrification and electrostatic induction [14, 43, 44], and it functions in the vertical contact-separation mode. Figure 3.1.5 (a) illustrates the underlying working mechanism of the H-TENG during the interaction of the waste materials with the PU foam. Initially, the upper layer of PU foam was in contact with the bottom layer of waste material (Figure 3.1.5 (a) <i>). Hence, there was no change in the electric potential across the load. When the upper layer began to separate, the restoring force of the supporting substrate acted to return both layers to their original shapes. During this process, the electric potential difference drove the electrons to flow from the bottom to the top electrode through an external circuit, resulting in the generation of the positive half cycle of the electrical signal (Figure 3.1.5 (a) <ii>); the equilibrium state is shown in Figure 3.1.5 (a) <iii>. Under the influence of the external force, the upper layer approached the bottom layer, which led to an electric potential difference and generation of the negative half cycle of the AC signal (Figure 3.1.5 (a) <iv>). The electrical response of the H-TENG was measured in the vertical contact-separation mode under an external cyclic compressive force of ca. 12 N. The force was applied to the top surface of the device, which pushed the upper surface periodically into contact with the bottom substrate. The output voltages and  $I_{sc}$  for the six devices are shown in Figure 3.1.5 (b–c). Raman and FT-IR spectra confirmed that PP was used in devices 1, 2, and 3, while PE was used in devices 4, 5, and 6. Devices 1 and 4 were selected for further electrical analysis and labeled as PP-H-TENG and PE-H-TENG, respectively.



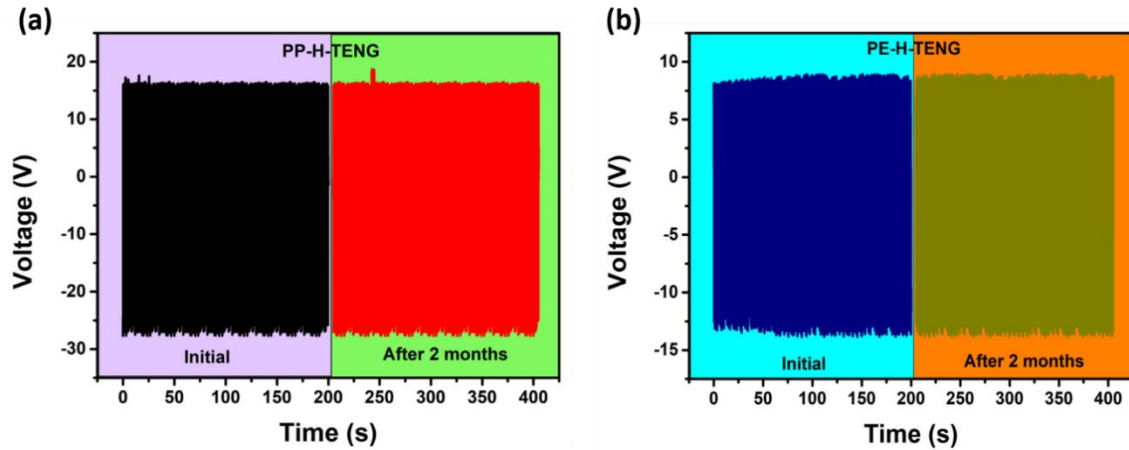
**Figure 3.1.5.** (a) The underlying electricity generation mechanism for the H-TENG in the vertical contact-separation configuration. (b–c) Voltage and current measurement results of the H-TENG with a working area of 9 cm<sup>2</sup>.

The maximum generated voltage, and the effective power of the H-TENG are important attributes. Thus, we performed a load-matching resistance for a wide range of external loads (Figure 3.1.6 (a–b)). For the PP-H-TENG, the instantaneous power reached 2.9  $\mu$ W, and the maximum power density reached 3.2 mW/m<sup>2</sup>. For the PE-H-TENG, the instantaneous power and maximum power density were 1  $\mu$ W and 1.1 mW/m<sup>2</sup>, respectively. To test the stability of the device, an endurance test was performed by repeatedly pressing and releasing the H-TENG with a

cyclic compressive force for 3,000 cycles. The device maintained a stable output and there was no physical damage to its device structure during the test. The stability results for the two devices (Figure 3.1.6 (c–d)) confirmed that they were stable and could be used for prolonged periods. We also tested the stability of the devices after 2 months. The devices remained stable in terms of electrical output (Figure 3.1.7). Thus, the H-TENG has high utility in various respects.

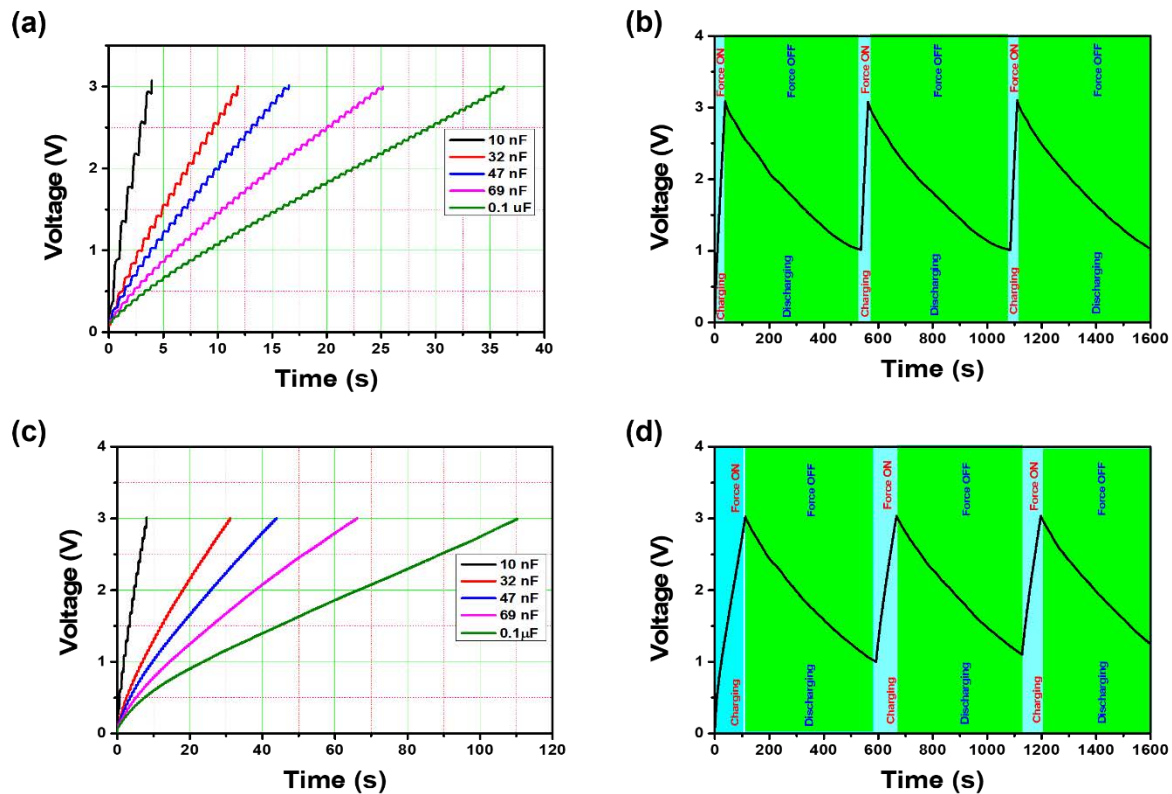


**Figure 3.1.6.** Electrical performance of the H-TENG as an energy harvester. (a) The output voltage, power, and power density of the PP-H-TENG for external load matching. (b) The output voltage, power, and power density of the PE-H-TENG for external load matching. (c–d) Output voltages for the PP- and PE-H-TENGs during the application of the external force for 3,000 cycles.



**Figure 3.1.7.** The stability of the device in initial and after 2 months of fabrication (a) PP-H-TENG and (b) PE-H-TENG.

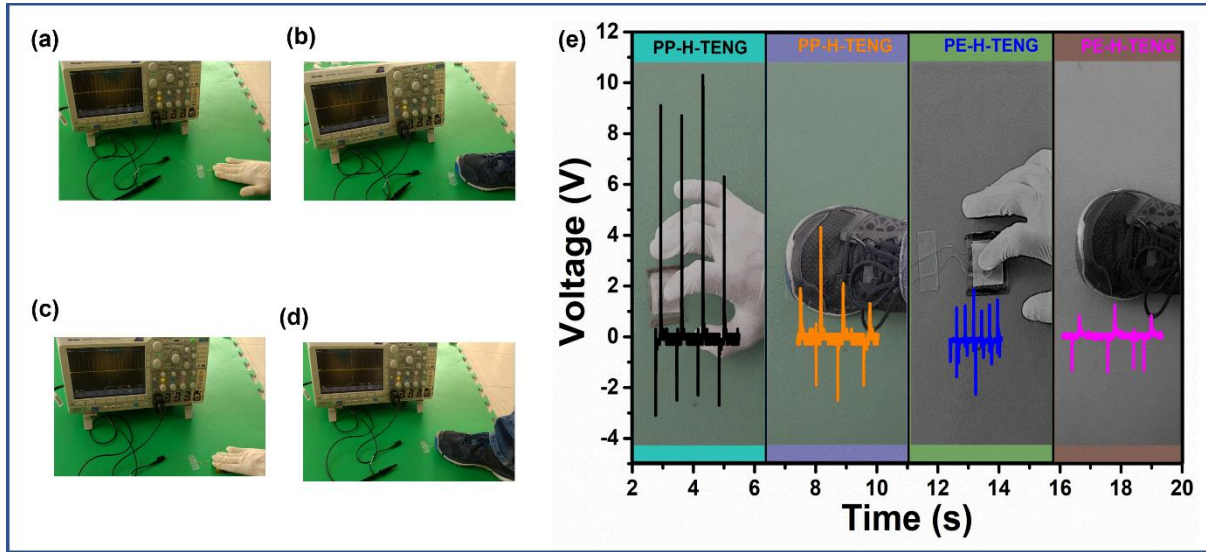
A constant DC signal is required to drive low-power electronic devices. The AC signal generated from a TENG thus cannot be used directly to power such devices. Therefore, the output generated from the TENG was rectified via a rectifier circuit and used to charge a capacitor ((10, 32, 47, 69 nF or 0.1  $\mu$ F) via the PP- and PE-H-TENG to 3 V, as shown in Figure 3.1.8 (a, c). The time taken by the PP-H-TENG to charge the capacitor was less than the time taken by the PE-H-TENG. Furthermore, Figure 3.1.8 (b, d) shows the charge and discharge cycles of the 0.1- $\mu$ F capacitor for the two H-TENGs. Here, the continuous charging and discharging cycles show that the fabricated devices could be used to power light-emitting diodes (LED), liquid crystal displays (LCDs) and other low-power electronic devices.



**Figure 3.1.8.** Charging and discharging behavior of the capacitor. (a) Charging of five different capacitors (10, 32, 47, 69 nF, 0.1  $\mu$ F) by the PP-H-TENG. (b) Charge–discharge behavior of a 0.1- $\mu$ F capacitor charged by the PP-H-TENG. (c) Charging of five different capacitors (10, 32, 47, 69 nF, 0.1  $\mu$ F) by the PE-H-TENG. (d) Charge–discharge behavior of a 0.1- $\mu$ F capacitor charged by the PE-H-TENG.

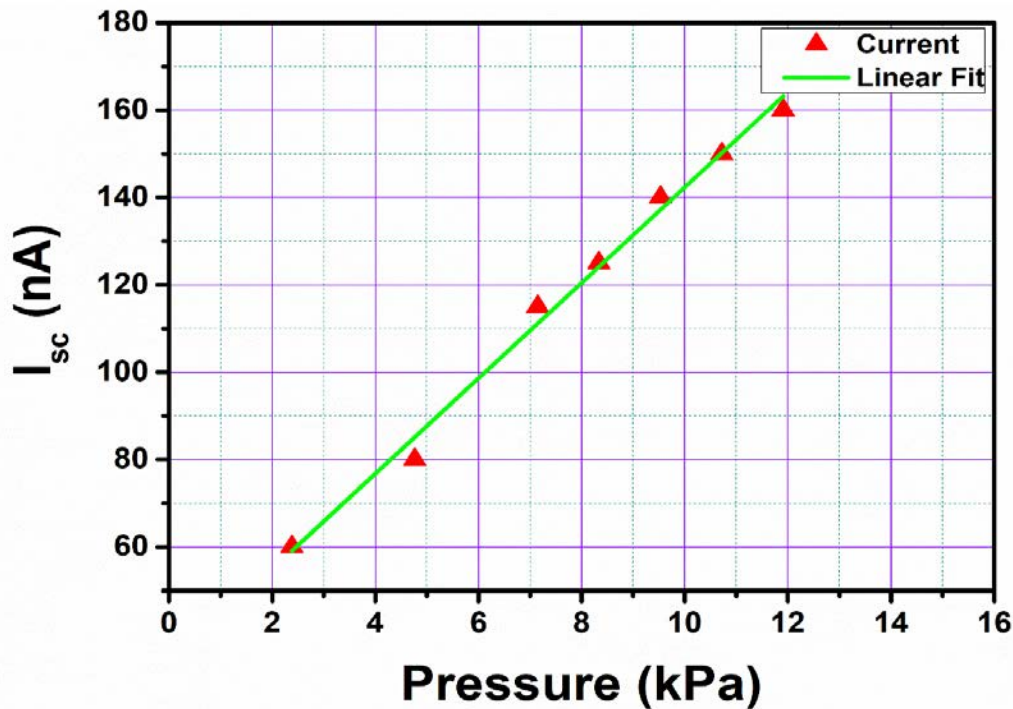
The main goal when fabricating an H-TENG is to be able to use it in daily life applications. We investigated the energy harvesting capability of the H-TENG during various human motions. Real-time data demonstrated that the H-TENG could successfully harness such biomechanical energy (Figure 3.1.9 (a–e)). Moreover, we explored the use of the PP-H-TENG in a force-sensing application. The current of the PP-H-TENG increased linearly with increasing applied force [45]. Figure 3.1.10 shows that the  $I_{SC}$  generated by dynamic force rose from 2 to 12 kPa, with an

excellent sensitivity of  $10.92 \text{ nA} \cdot \text{kPa}^{-1}$ . The correlation coefficient ( $R^2$ ) was 0.991, which indicated that the PP-H-TENG could detect small dynamic forces with reasonable accuracy.



**Figure 3.1.9.** Real-time data for harnessing biomechanical energy by the H-TENG. Use of the (a–b) PP-H-TENG and (c–d) PE-H-TENG to harness the biomechanical energy generated by hand and leg motions. (e) The voltage generated by biomechanical hand and leg motions using the PP- and PE-H-TENGs.



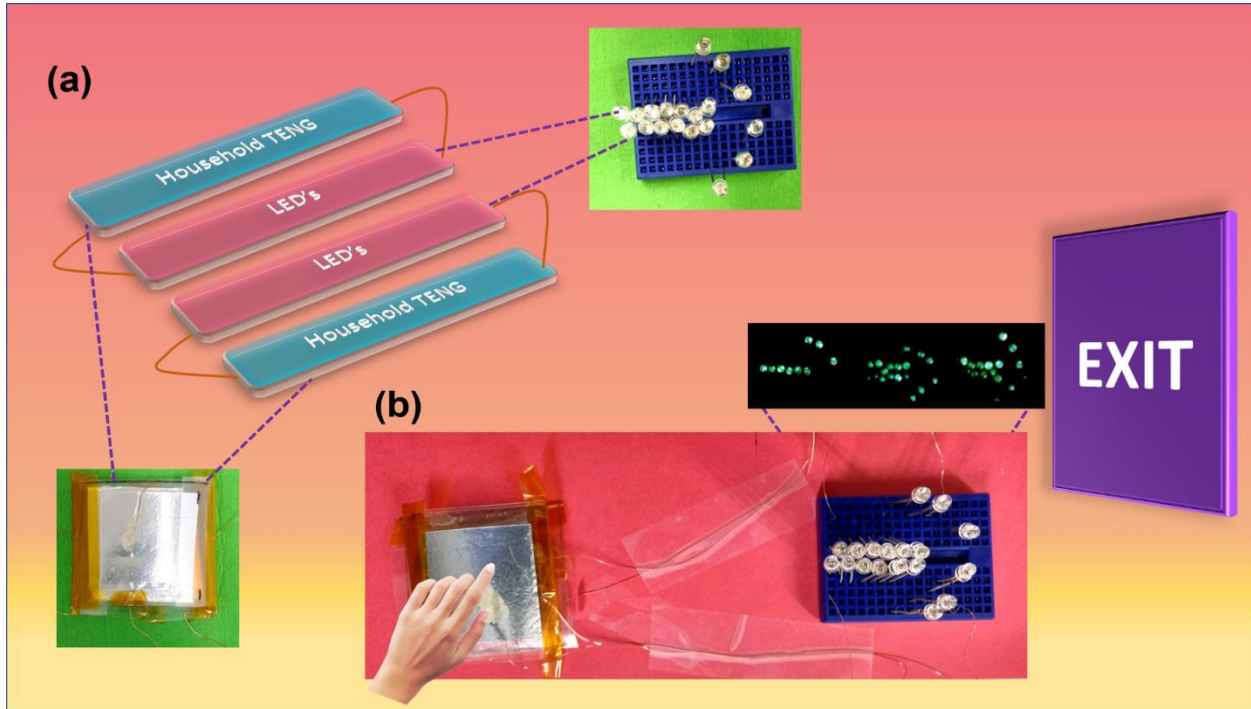


**Figure 3.1.10.** The fitted curve for short circuit current in response to dynamic force ranging from ~ 2 kPa- 12 kPa.

Our H-TENG needs less than 5 min to fabricate and can be made anywhere and without any stringent requirements. Thus, it could be used for various applications, including emergency direction systems, energy harvesting chopping boards, and intruder-monitoring security systems. Because the main objective of our work is sustainable development, we suggest some straightforward applications to provide an idea about the utilization of H-TENG in day-to-day life. In emergency situations, when there is no power source in a building, our device could be used as an indicator providing directions to objects such as exit doors, fire extinguishers, and hose pumps. Figure 3.1.11 demonstrates that our H-TENG could be used to indicate the location of exit doors under many local building safety codes in emergency situations. To demonstrate this, we illuminated a directional arrow by placing two devices on the wall; we firmly believe that H-TENGs can be used to provide directions in emergency situations. Similarly, LEDs could be



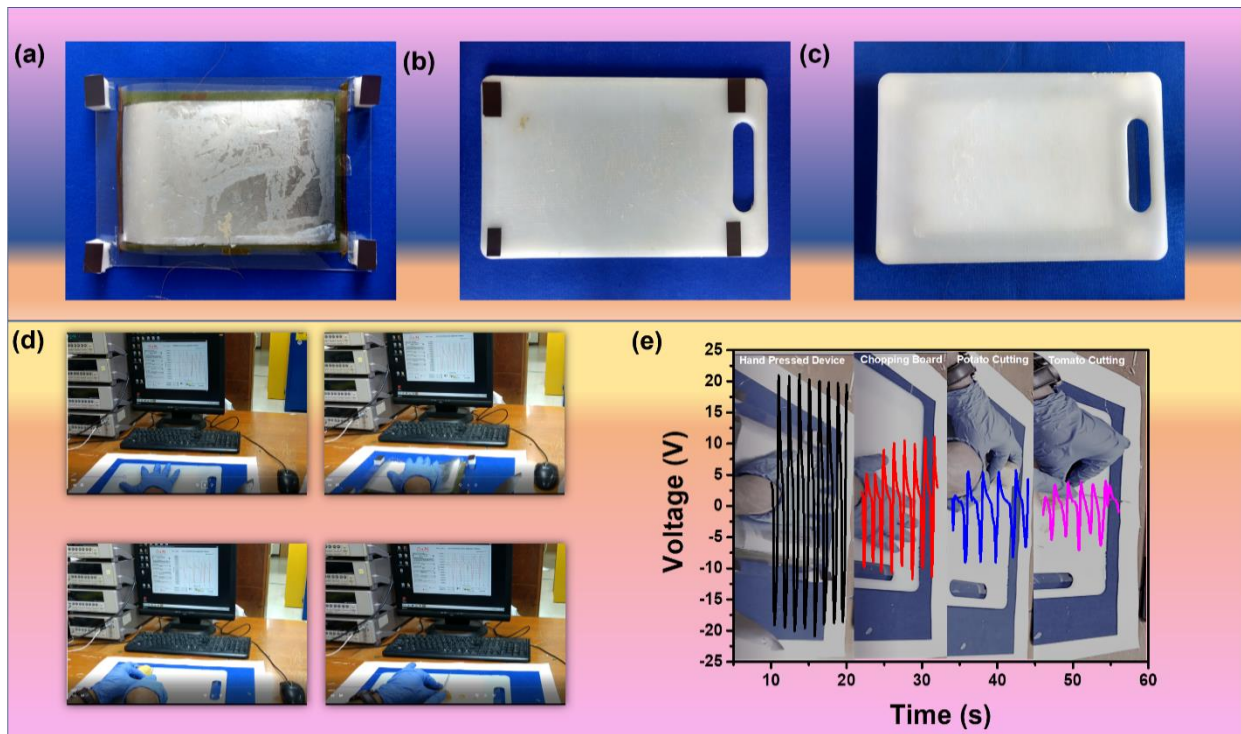
arranged to form letters and thus illuminate an exit sign (E), as well as the location of water (W), hose pumps (H), and other essential items.



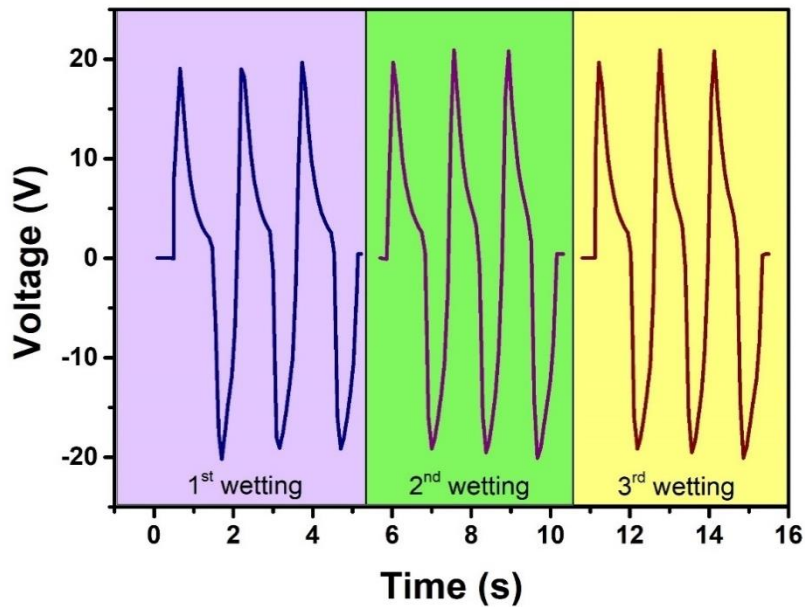
**Figure 3.1.11.** (a) Schematic illustration of an emergency exit door indicator system where light-emitting diodes (LEDs) were connected to two stacked PP-H-TENGs. (b) The emergency indicator system, tapping the system generates triboelectricity that illuminates a directional arrow pointing towards the exit.

We also fabricated an H-TENG for the purpose of converting a chopping board into an energy harvester. Cooking begins with cutting, shredding, or chopping of food, and every kitchen needs at least one chopping board. Thus, we converted this commonly used kitchen utensil into an energy harvester. Our “smart” chopping board used an H-TENG to harness the biomechanical energy generated during the cutting of vegetables and fruits. Any chopping board can be converted into a smart chopping board. The materials required for making such a board are an H-TENG, an acrylic sheet, spring/foam, and magnetic tape/Velcro. The first step is to fabricate an H-TENG

according to the size of the chopping board. In the second step, the H-TENG is placed on the acrylic sheet. The final step uses the foam/spring as a spacer and the magnetic tape/Velcro to allow the system to be easily attached and detached, such as for cleaning. Figure 3.1.12 shows the smart chopping board is used to cut potatoes and tomatoes. The effect of the wetting of the chopping board was also evaluated. The device was wetted with 1 mL of water and then dried at 40°C, its electrical properties were then measured, and this process was repeated three times. The device worked well after three wetting and drying cycles. Figure 3.1.13 shows its electrical performance. The energy generated can be stored in a capacitor for various purposes, depending on the requirement.

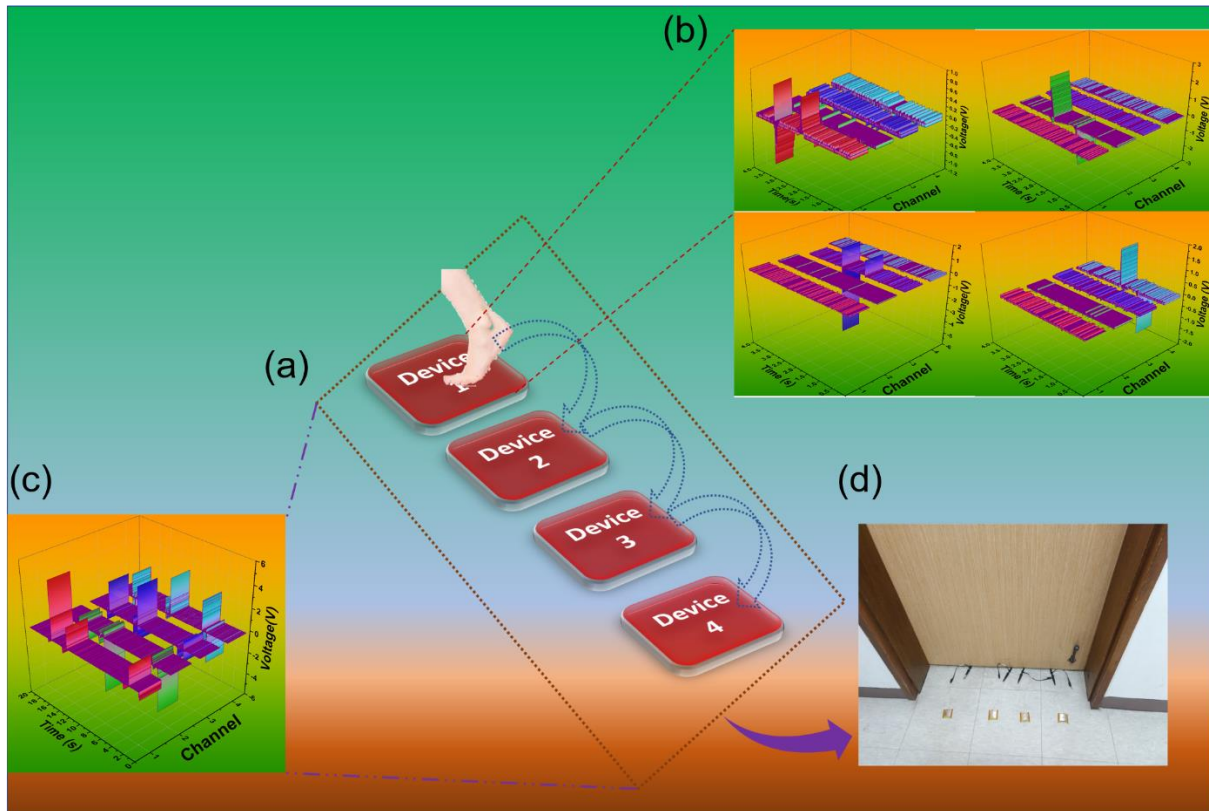


**Figure 3.1.12.** (a-c) Schematic illustration for the fabrication of energy harvesting chopping board. (d) Optical images during device pressing, board pressing, potato, and tomato cutting. (e) The electrical response of the chopping board for device pressing, board pressing, cutting potato, and tomato.



**Figure 3.1.13.** The voltage output is showing the stability of the chopping board with the wetting and drying process.

The other aspect regarding application for H-TENG is the intrusion monitoring system for the small area. Intrusion or unauthorized entry into an area, building, or house is commonplace. An H-TENG could easily be used to monitor such events. To demonstrate this, we placed four H-TENG devices connected to different channels, outside a door. Whenever someone stepped on one of the devices, a corresponding output was generated (Figure 3.1.14). This intrusion monitoring system is an example of direct use of an H-TENG without the requirement for any electrical component. We believe that such examples will prompt laypeople to develop novel applications for H-TENGs in their daily lives.



**Figure 3.1.14.** Intrusion monitoring system. (a) Showing the arrangement of the devices, when a person moves from one device to another output will generate in the corresponding channel. (b) Shows the output for different devices connected to the multi-channel system; if a person's feet are on the first device, then output generated only in a channel connected to device 1 and so on. (c) The output in the case when the person's feet are on different devices. (d) Optical image for the real-time placement of the devices outside the door.

### 3.1.4. Conclusion

An inexpensive H-TENG was fabricated to harvest biomechanical energy to drive low-power electronics. The proposed H-TENG was developed using waste materials, thereby helping to reduce environmental pollution. The competitive features of an H-TENG include its low-cost and ease of manufacture. Furthermore, neither prior laboratory experience nor sophisticated assembly equipment is needed; the device can be fabricated anywhere and shows stable

performance. We demonstrated that our H-TENG could be used as a dynamic force sensor and in various household applications. We believe that this study reveals a new approach to building simple TENG devices from inexpensive and waste materials, an approach that will lead to more sustainable development.

## References

- [1] Jambeck JR, Geyer R, Wilcox C, Siegler TR, Perryman M, Andrady A, et al. Plastic waste inputs from land into the ocean. *Science*. 2015;347:768-71.
- [2] Cózar A, Sanz-Martín M, Martí E, González-Gordillo JI, Ubeda B, Gálvez JÁ, et al. Plastic Accumulation in the Mediterranean Sea. *PLOS ONE*. 2015;10:e0121762.
- [3] Tyree DMaC. if-youre-drinking-tap-water-youre-consuming-plastic-pollutants. if-youre-drinking-tap-water-youre-consuming-plastic-pollutants  
pri.org: pri.org; 2017.
- [4] Wang ZL, Song J. Piezoelectric Nanogenerators Based on Zinc Oxide Nanowire Arrays. *Science*. 2006;312:242-6.
- [5] Chandrasekhar A, Alluri NR, Saravanakumar B, Selvarajan S, Kim S-J. A microcrystalline cellulose ingrained polydimethylsiloxane triboelectric nanogenerator as a self-powered locomotion detector. *Journal of Materials Chemistry C*. 2017;5:1810-5.
- [6] Chandrasekhar A, Alluri NR, Sudhakaran MSP, Mok YS, Kim S-J. A smart mobile pouch as a biomechanical energy harvester towards self-powered smart wireless power transfer applications. *Nanoscale*. 2017.
- [7] Alluri NR, Chandrasekhar A, Vivekananthan V, Purusothaman Y, Selvarajan S, Jeong JH, et al. Scavenging Biomechanical Energy Using High-Performance, Flexible BaTiO<sub>3</sub> Nanocube/PDMS Composite Films. *ACS Sustainable Chemistry & Engineering*. 2017;5:4730-8.
- [8] Purusothaman Y, Alluri NR, Chandrasekhar A, Kim S-J. Harnessing low frequency-based energy using a K<sub>0.5</sub>Na<sub>0.5</sub>NbO<sub>3</sub> (KNN) pigmented piezoelectric paint system. *Journal of Materials Chemistry C*. 2017;5:5501-8.



- [9] Zhang L, Zhang B, Chen J, Jin L, Deng W, Tang J, et al. Lawn Structured Triboelectric Nanogenerators for Scavenging Sweeping Wind Energy on Rooftops. *Advanced Materials*. 2016;28:1650-6.
- [10] Balasingam SK, Lee M, Kim BH, Lee JS, Jun Y. Freeze-dried MoS<sub>2</sub> sponge electrodes for enhanced electrochemical energy storage. *Dalton Transactions*. 2017;46:2122-8.
- [11] Wang ZL. Triboelectric nanogenerators as new energy technology and self-powered sensors - Principles, problems and perspectives. *Faraday Discussions*. 2014;176:447-58.
- [12] Wang ZL. Triboelectric Nanogenerators as New Energy Technology for Self-Powered Systems and as Active Mechanical and Chemical Sensors. *ACS Nano*. 2013;7:9533-57.
- [13] Wang ZL, Lin L, Chen J, Niu S, Zi Y. Triboelectric Nanogenerator: Lateral Sliding Mode. *Triboelectric Nanogenerators*. Cham: Springer International Publishing; 2016. p. 49-90.
- [14] Wang ZL, Lin L, Chen J, Niu S, Zi Y. Triboelectric Nanogenerator: Vertical Contact-Separation Mode. *Triboelectric Nanogenerators*. Cham: Springer International Publishing; 2016. p. 23-47.
- [15] Chandrasekhar A, Alluri NR, Vivekananthan V, Purusothaman Y, Kim S-J. A sustainable freestanding biomechanical energy harvesting smart backpack as a portable-wearable power source. *Journal of Materials Chemistry C*. 2017;5:1488-93.
- [16] Jin C, Kia DS, Jones M, Towfighian S. On the contact behavior of micro-/nano-structured interface used in vertical-contact-mode triboelectric nanogenerators. *Nano Energy*. 2016;27:68-77.
- [17] Yang W, Chen J, Zhu G, Wen X, Bai P, Su Y, et al. Harvesting vibration energy by a triple-cantilever based triboelectric nanogenerator. *Nano Research*. 2013;6:880-6.

- [18] Yang Y, Zhu G, Zhang H, Chen J, Zhong X, Lin Z-H, et al. Triboelectric Nanogenerator for Harvesting Wind Energy and as Self-Powered Wind Vector Sensor System. *ACS Nano*. 2013;7:9461-8.
- [19] Chen J, Zhu G, Yang W, Jing Q, Bai P, Yang Y, et al. Harmonic-Resonator-Based Triboelectric Nanogenerator as a Sustainable Power Source and a Self-Powered Active Vibration Sensor. *Advanced Materials*. 2013;25:6094-9.
- [20] Lin Z-H, Zhu G, Zhou YS, Yang Y, Bai P, Chen J, et al. A Self-Powered Triboelectric Nanosensor for Mercury Ion Detection. *Angewandte Chemie International Edition*. 2013;52:5065-9.
- [21] Xie Y, Wang S, Lin L, Jing Q, Lin Z-H, Niu S, et al. Rotary Triboelectric Nanogenerator Based on a Hybridized Mechanism for Harvesting Wind Energy. *ACS Nano*. 2013;7:7119-25.
- [22] Ko K-W, Lee M, Sekhon SS, Balasingam SK, Han C-H, Jun Y. Efficiency Enhancement of Dye-Sensitized Solar Cells by the Addition of an Oxidizing Agent to the TiO<sub>2</sub> Paste. *ChemSusChem*. 2013;6:2117-23.
- [23] Li Z, Chen J, Yang J, Su Y, Fan X, Wu Y, et al. [small beta]-cyclodextrin enhanced triboelectrification for self-powered phenol detection and electrochemical degradation. *Energy & Environmental Science*. 2015;8:887-96.
- [24] Kim KN, Jung YK, Chun J, Ye BU, Gu M, Seo E, et al. Surface dipole enhanced instantaneous charge pair generation in triboelectric nanogenerator. *Nano Energy*. 2016;26:360-70.
- [25] Wen Z, Yeh M-H, Guo H, Wang J, Zi Y, Xu W, et al. Self-powered textile for wearable electronics by hybridizing fiber-shaped nanogenerators, solar cells, and supercapacitors. *Science Advances*. 2016;2.



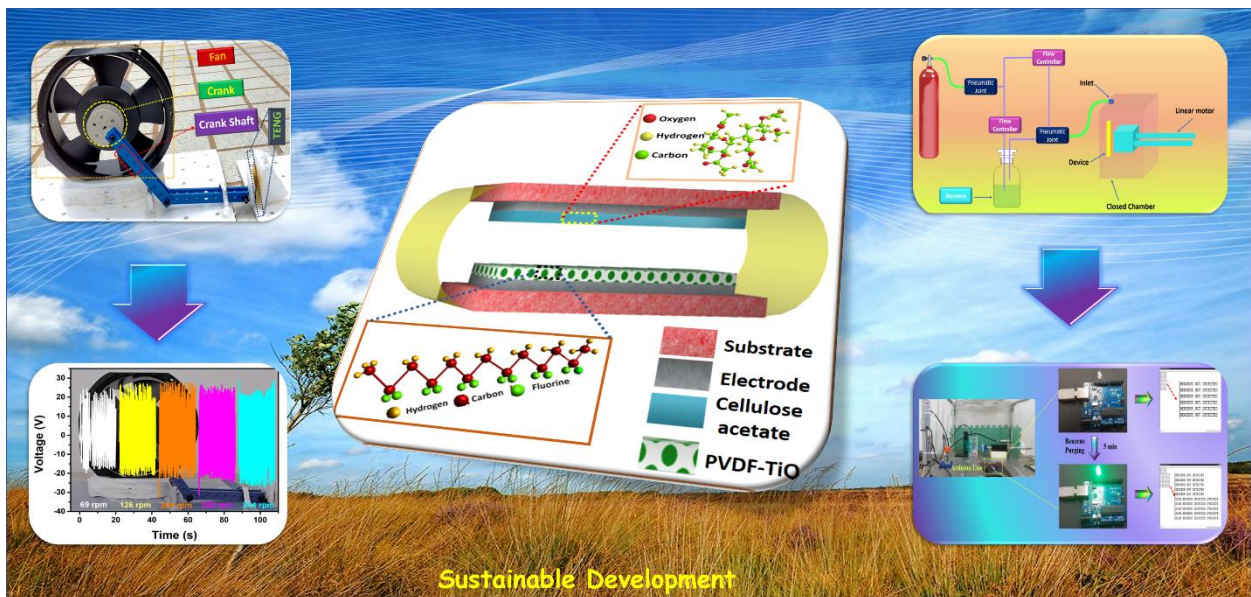
- [26] Dong K, Wang Y-C, Deng J, Dai Y, Zhang SL, Zou H, et al. A Highly Stretchable and Washable All-Yarn-Based Self-Charging Knitting Power Textile Composed of Fiber Triboelectric Nanogenerators and Supercapacitors. *ACS Nano*. 2017;11:9490-9.
- [27] Lee M, Balasingam SK, Ko Y, Jeong HY, Min BK, Yun YJ, et al. Graphene modified vanadium pentoxide nanobelts as an efficient counter electrode for dye-sensitized solar cells. *Synthetic Metals*. 2016;215:110-5.
- [28] Kim J, Lee JH, Ryu H, Lee J-H, Khan U, Kim H, et al. High-Performance Piezoelectric, Pyroelectric, and Triboelectric Nanogenerators Based on P(VDF-TrFE) with Controlled Crystallinity and Dipole Alignment. *Advanced Functional Materials*. 2017;27:1700702-n/a.
- [29] Balasingam SK, Jun Y. Recent Progress on Reduced Graphene Oxide-Based Counter Electrodes for Cost-Effective Dye-Sensitized Solar Cells. *Israel Journal of Chemistry*. 2015;55:955-65.
- [30] Byun K-E, Cho Y, Seol M, Kim S, Kim S-W, Shin H-J, et al. Control of Triboelectrification by Engineering Surface Dipole and Surface Electronic State. *ACS Applied Materials & Interfaces*. 2016;8:18519-25.
- [31] Chun J, Ye BU, Lee JW, Choi D, Kang C-Y, Kim S-W, et al. Boosted output performance of triboelectric nanogenerator via electric double layer effect. *Nature Communications*. 2016;7:12985.
- [32] Seung W, Yoon H-J, Kim TY, Ryu H, Kim J, Lee J-H, et al. Boosting Power-Generating Performance of Triboelectric Nanogenerators via Artificial Control of Ferroelectric Polarization and Dielectric Properties. *Advanced Energy Materials*. 2017;7:1600988-n/a.

- [33] Rasel MSU, Park J-Y. A sandpaper assisted micro-structured polydimethylsiloxane fabrication for human skin based triboelectric energy harvesting application. *Applied Energy*. 2017;206:150-8.
- [34] Arruebarrena de Báez M, Hendra PJ, Judkins M. The Raman spectra of oriented isotactic polypropylene. *Spectrochimica Acta Part A: Molecular and Biomolecular Spectroscopy*. 1995;51:2117-24.
- [35] Nielsen AS, Batchelder DN, Pyrz R. Estimation of crystallinity of isotactic polypropylene using Raman spectroscopy. *Polymer*. 2002;43:2671-6.
- [36] Andreassen E. Infrared and Raman spectroscopy of polypropylene. In: Karger-Kocsis J, editor. *Polypropylene: An A-Z reference*. Dordrecht: Springer Netherlands; 1999. p. 320-8.
- [37] Krimm S, Liang CY, Sutherland GBBM. Infrared Spectra of High Polymers. II. Polyethylene. *The Journal of Chemical Physics*. 1956;25:549-62.
- [38] Sato H, Shimoyama M, Kamiya T, Amari T, Šašić S, Ninomiya T, et al. Raman spectra of high-density, low-density, and linear low-density polyethylene pellets and prediction of their physical properties by multivariate data analysis. *Journal of Applied Polymer Science*. 2002;86:443-8.
- [39] França de Sá S, Ferreira JL, Matos AS, Macedo R, Ramos AM. A new insight into polyurethane foam deterioration – the use of Raman microscopy for the evaluation of long-term storage conditions. *Journal of Raman Spectroscopy*. 2016;47:1494-504.
- [40] Palm A. Raman Spectrum of Polystyrene. *The Journal of Physical Chemistry*. 1951;55:1320-4.
- [41] Gulmine JV, Janissek PR, Heise HM, Akcelrud L. Polyethylene characterization by FTIR. *Polymer Testing*. 2002;21:557-63.

- [42] Asefnejad A, Khorasani MT, Behnamghader A, Farsadzadeh B, Bonakdar S. Manufacturing of biodegradable polyurethane scaffolds based on polycaprolactone using a phase separation method: physical properties and in vitro assay. *International Journal of Nanomedicine*. 2011;6:2375-84.
- [43] Niu S, Wang S, Lin L, Liu Y, Zhou YS, Hu Y, et al. Theoretical study of contact-mode triboelectric nanogenerators as an effective power source. *Energy & Environmental Science*. 2013;6:3576-83.
- [44] Yang B, Zeng W, Peng Z-H, Liu S-R, Chen K, Tao X-M. A Fully Verified Theoretical Analysis of Contact-Mode Triboelectric Nanogenerators as a Wearable Power Source. *Advanced Energy Materials*. 2016;6:1600505-n/a.
- [45] Guo H, Li T, Cao X, Xiong J, Jie Y, Willander M, et al. Self-Sterilized Flexible Single-Electrode Triboelectric Nanogenerator for Energy Harvesting and Dynamic Force Sensing. *ACS Nano*. 2017;11:856-64.
- [46] Chandrasekhar A, Alluri NR, Saravanakumar B, Selvarajan S, Kim S-J. Human Interactive Triboelectric Nanogenerator as a Self-Powered Smart Seat. *ACS Applied Materials & Interfaces*. 2016;8:9692-9.
- [47] Wu JM, Chang CK, Chang YT. High-output current density of the triboelectric nanogenerator made from recycling rice husks. *Nano Energy*. 2016;19:39-47.
- [48] Lee JH, Hinchet R, Kim SK, Kim S, Kim S-W. Shape memory polymer-based self-healing triboelectric nanogenerator. *Energy & Environmental Science*. 2015;8:3605-13.

### 3.2 Phase Inversion Enabled Energy Scavenger: A Multifunctional Triboelectric Nanogenerator as Benzene Monitoring System

#### Graphical Overview



## Highlights

- Phase inversion and semi conducting  $\text{TiO}_2$  based TENG with enhanced performance.
- The TENG shows 7 times and 10 times enhancement for voltage and current.
- Fabricated TENG is multifunctional energy harvester. It can harvest wind energy using crank-shaft mechanism.
- Demonstration of TENG as VOC's sensor with good selectivity and sensitivity.
- Integration of TENG with Arduino for warning message and alarm to evacuate.

### 3.2.1 Introduction

Globally, the population relies on fossil fuel for energy requirements. The energy crisis is one of the major issues faced by the current generation [1]. Taking this into consideration, across the globe, various researchers are focusing on the development of sustainable energy harvesting devices. Recent growth in technology has made faster, smarter, portable, and efficient electronic devices. Such type of latest devices requires low power to operate. Nowadays, the emphasis is on harvesting waste mechanical energy using nanogenerators to power up the electronic devices and for self-powered applications [2, 3].

The triboelectric nanogenerator (TENG) introduced by Wang et al. in 2012 has gained much attention. The TENG exhibits the unique feature of being easy to fabricate, cheap, high efficiency with reasonable output [4, 5]. The rationale behind the TENG is to harness the energy when two materials of opposite polarity come in frictional contact with each other utilizing the electrification and electrostatic effects. The clear principle of triboelectricity is unclear, but it is believed that certain chemical bonds are formed between the surface of the materials in contact with the moving charges to balance the potential. When materials separated, some of the bonded atoms have a tendency either to lose an electron or to gain electron depending on the material [6, 7]. The trend of a material to gain or lose electrons depends on its position in the triboelectric series [4]. Currently, vigorous efforts have been made for enhancing the output performance of TENG generally by improving the surface charge density ( $\sigma$ ) and surface area [8, 9]. Various methods such as (i) selection of triboelectric material with a large difference in their polarity (ii) increasing the active contact area [9] (iii) enhancement of charge density [10] and (iv) incorporation of dielectric materials for strong charge trapping have been implemented for the enhancement of the nanogenerator performance [11, 12].

The TENG has been widely used for various applications such as sensing, air purification, self-powered toys, smart backpack etc. [13-18]. The detection of the toxic components in the surrounding environment is one of the life-saving information for the workers in the various industries. The multiple contaminants are present in the air; among them, VOCs, such as toluene, benzene, and acetone, are very dangerous as they have a direct effect on human health [19]. The TENG can be used to develop VOCs sensor with high sensitivity and selectivity depending on the material of the triboelectric layer in the TENG device. Polyvinylidene fluoride (PVDF) is an excellent choice for the negative layer in the TENG device due to the presence of the fluorine group. In addition to strong negative polarity, PVDF also exhibits polarization capabilities [20, 21]. Soin et al. reported the high performance TENG based on phase inversion of the piezoelectric membrane of PVDF and polyamide-6 (PA-6). Moreover, they incorporated strong piezoelectric material zinc stannate with large spontaneous polarization value in the PVDF. The enhancement occurs due to the increase in the crystallinity of the piezoelectric membrane (PVDF/PA-6) supported by strong stress-induced polarization of piezoelectric  $\text{ZnSnO}_3$  [21]. The piezoelectric nanomaterials are reported to boost the power generation performance of TENG [22]. The phase inversion process can lead to improvement in the  $\beta$  phase of PVDF (>95%) [23]. On the other hand,  $\text{TiO}_2$  is a semiconducting, biocompatible material with high dielectric constant with substantial charge trapping capabilities [24, 25]. The nanoparticles are well reported for promoting and enhancing the adsorption of particular gas by establishing more adsorption sites on the surface [26]. The  $\text{TiO}_2$  was reported for the adsorption and desorption of the benzene with no dissociative reactivity of benzene [27]. Herein, an enhanced triboelectrification TENG based on a simple phase inversion process, which is a straightforward route to achieve porous structure and high crystallinity without the use of any piezoelectric material, is proposed. The results demonstrated

the enhancement because of the phase inversion process of PVDF and tuned concentration of the non-piezoelectric TiO<sub>2</sub> microparticles. Under vertical contact-separation mode, the voltage and current output for PVDF-10-TiO<sub>2</sub>/CA system enhanced to 7 times and 10 times, respectively. The fabricated device can be used to harvest biomechanical as well as wind energy. To demonstrate, we designed a simple, cost-effective, easy to develop, and implement wind energy harvesting system using TENG, which produces nearly constant output at different rpm. Our design can be fabricated without the requirement of any specific technique and can be used to harvest wind energy at remote locations as well as at home. Finally, we studied the capability of the device as an effective VOCs (benzene) sensor. Specifically, the voltage output of the sensor gradually decreases as the concentration of benzene increases. The device can monitor benzene with excellent sensitivity, selectivity, and recoverability. The device was integrated with microcontroller board Arduino Uno which is based on ATmega328P for the automatic detection of benzene vapor's and raising the alarm to evacuate the area.

### **3.2.2 Experimental**

#### **3.2.2.1 Preparation of PVDF/TiO<sub>2</sub> film**

The dope solution was prepared by dispersing 5 wt.% TiO<sub>2</sub> microparticles in DMF with the help of continuous stirring. After complete dispersion, 20 wt.% PVDF was added to the solution and allowed to dissolve completely. The prepared solution was spin-coated on a PET substrate with an aluminum electrode at 1000 rpm for 35 s. The coated substrate was then allowed to dry in an oven at 70 °C. This film was labeled as PVDF-TiO<sub>2</sub>.

#### **3.2.2.2 Preparation of PVDF/TiO<sub>2</sub> by the phase-inversion process**

The dope solution was prepared first by dispersing TiO<sub>2</sub> (5 wt.%, 10 wt.%, 15 wt.%) microparticles in DMF with the help of probe sonication. After complete dispersion, 20 wt.%



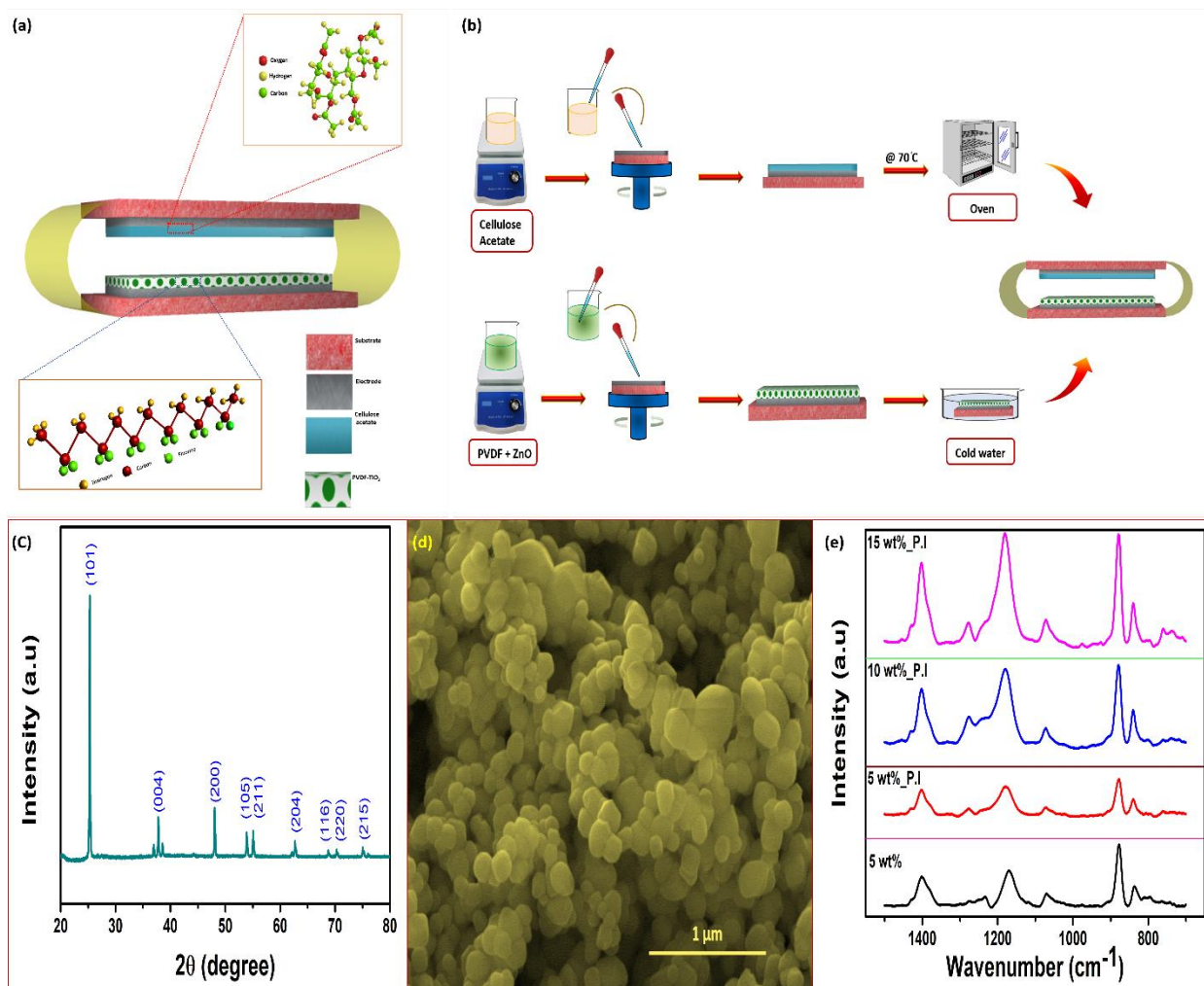
PVDF was added to the solution and allowed to dissolve completely by stirring. The prepared solution was spin-coated on a PET substrate with an aluminum electrode at 1000 rpm for 35 s. The coated substrate was then immersed immediately in the anti-solvent bath (water) at a temperature of 5 °C, followed by repeated rinsing in distilled water and left over-night in water to remove any residual solvent as shown in Figure 3.2.1(b).

### **3.2.2.3 Preparation of Cellulose acetate film**

The dope solution was prepared by using 20 wt.% of cellulose acetate in N, N-Dimethylformamide by continuously stirring. After the preparation of the dope solution, a specific volume of solution was spin-coated on the PET substrate with an aluminum electrode at 3000 rpm for 35s. The spin-coated substrate could dry first in the air than in an oven at 70 °C, as shown in Figure 3.2.1(b).

### **3.2.2.4 Fabrication of triboelectric nanogenerator**

The 3D schematic representation of double-layered structure TENG is shown in Figure 3.2.1(a). The first layer is cellulose acetate spin-coated on the conductive adhesive aluminum tape (2.5 cm x 2.5 cm) attached to the PET substrate while the opposite side is of PVDF-TiO<sub>2</sub> spin-coated on conductive aluminum tape (2.5 cm x 2.5 cm) adhered to PET substrate. These two substrates were then connected in the arc-shaped structure using the PET sheet to maintain the desired spacing between the layer, as shown in Figure 3.2.1(b). The device prepared by using PVDF-TiO<sub>2</sub> film was labeled as PVDF-TiO<sub>2</sub>/CA, and devices developed at the different concentrations using phase inversion process are labeled as PVDF-5-TiO<sub>2</sub>/CA (5 wt.%), PVDF-10-TiO<sub>2</sub>/CA (10 wt.%), PVDF-15-TiO<sub>2</sub>/CA (15 wt.%) respectively.

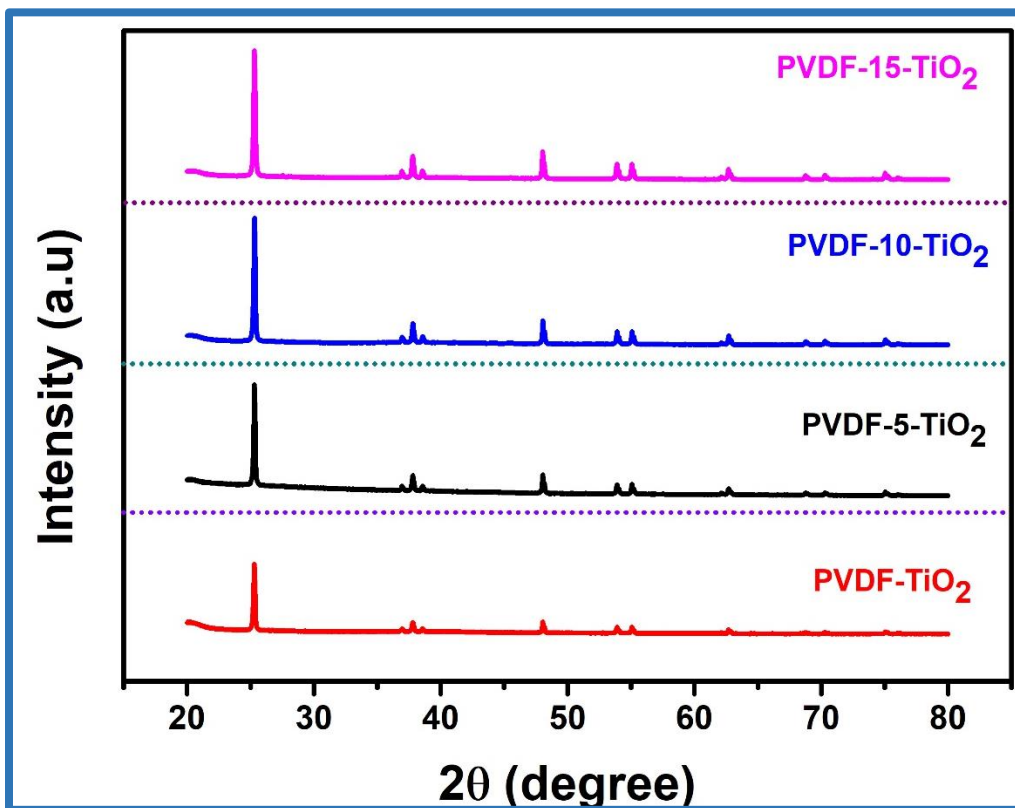


**Figure 3.2.1.** (a) Three-dimensional schematic representation of TENG in contact-separation mode. (b) The step by step procedure for the fabrication of TENG. (c) XRD spectra of  $\text{TiO}_2$  microparticles. (d) FE-SEM micrograph of  $\text{TiO}_2$  microparticles. (e) FT-IR spectra of the films at different concentrations.

### 3.2.3 Results and Discussions

The  $\text{TiO}_2$  microparticles are introduced in the polymer works as charge trapping sites due to their high dielectric constant [25]. The XRD data is shown in Figure 3.2.1(c) confirms the anatase phase of the  $\text{TiO}_2$  [28]. The characteristic  $2\theta$  peak and [hkl] planes are  $25.28^\circ$  [101],  $37.80^\circ$

[004],  $48.05^\circ$  [200],  $53.91^\circ$  [105],  $55.06^\circ$  [211],  $63.07^\circ$  [204],  $69.23^\circ$  [116],  $70.89^\circ$  [220],  $75.38^\circ$  [215] corresponding to anatase phase confirmed with JCPD card no. 21-1272 [28]. The XRD of PVDF-TiO<sub>2</sub> at different wt.% is shown in Figure 3.2.2, confirming that there is no change in TiO<sub>2</sub> after incorporation in the PVDF. The FE-SEM image of TiO<sub>2</sub> microstructures is shown in Figure 3.2.1 (d). The average particle size of the microstructure was  $214 \text{ nm} \pm 5 \text{ nm}$ , as confirmed by the FE-SEM analysis.

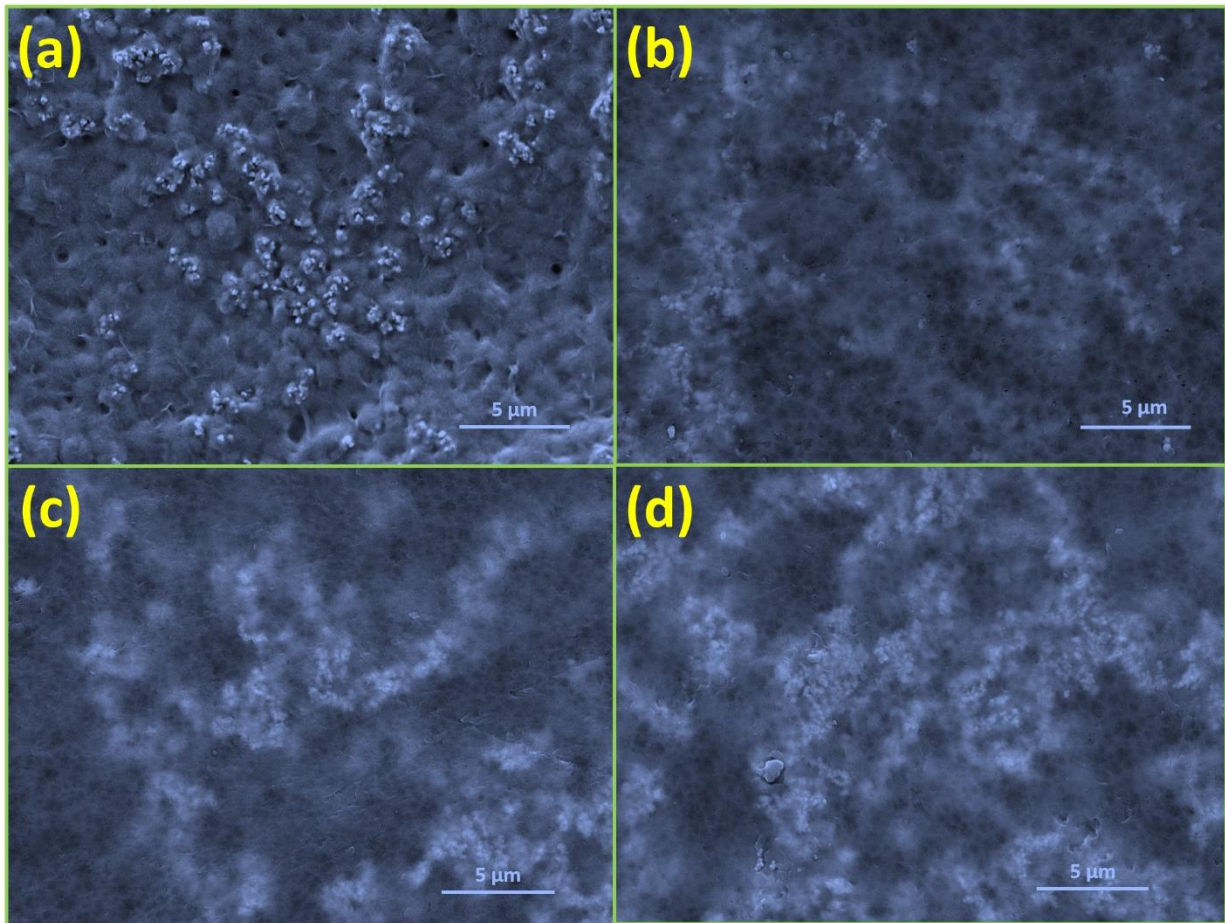


**Figure 3.2.2.** The XRD spectrum for PVDF-5-TiO<sub>2</sub>, PVDF-10-TiO<sub>2</sub>, PVDF-15-TiO<sub>2</sub> phase inversion films confirms that there is no change in the TiO<sub>2</sub> microstructure after incorporating in the polymer matrix.

The polymer film was formed by a phase inversion process, in which spin-coated film was quenched into a non-solvent bath for rapid phase separation events [23, 29, 30]. The FT-IR data for the films with different weight percent is shown in Fig. 3.2.1(e). The quantification of  $\beta$ -phase was carried out using the  $840\text{ cm}^{-1}$  (assigned to  $\text{CH}_2$  rocking and  $\text{CF}_2$  asymmetric stretching) and  $760\text{ cm}^{-1}$  ( $\text{CF}_2$  bending and skeletal bending) using the formula:

$$F(\beta) = \frac{A_{\beta}}{1.26 A_{\alpha} + A_{\beta}} \quad - (1)$$

Where  $F(\beta)$  is the fraction of the  $\beta$  phase, and  $A_{\alpha}$  and  $A_{\beta}$  are absorption band at  $760\text{ cm}^{-1}$  and  $840\text{ cm}^{-1}$  for the  $\alpha$  phase and  $\beta$  phase respectively [23, 31]. The  $\beta$  phase content was maximum in the case of PVDF-10-TiO<sub>2</sub> films, i.e., around 90%. The  $\beta$  phase content for PVDF-TiO<sub>2</sub>, PVDF-5-TiO<sub>2</sub>, PVDF-15-TiO<sub>2</sub> was 52.3%, 62.4% and 69.09% respectively. The increased  $\beta$  phase content leads to large charge density, thus increases the tendency to acquire electron from cellulose acetate (CA) layer [21]. The FE-SEM analysis for PVDF-TiO<sub>2</sub> (Figure 3.2.3 (a)) and PVDF-5-TiO<sub>2</sub> (Figure 3.2.3 (b)), PVDF-10-TiO<sub>2</sub> (Figure 3.2.3 (c)) and PVDF-15-TiO<sub>2</sub> (Figure 3.2.3 (d)) films which show the formation of a porous structure on the surface of the film due to the phase inversion process [21, 23]. The PVDF-10-TiO<sub>2</sub> film shows a perfect trade-off between crystallinity and porous structure. On increasing the concentration of filler, the crystallinity of the film decreases, and segregation of large-sized particles occurs.

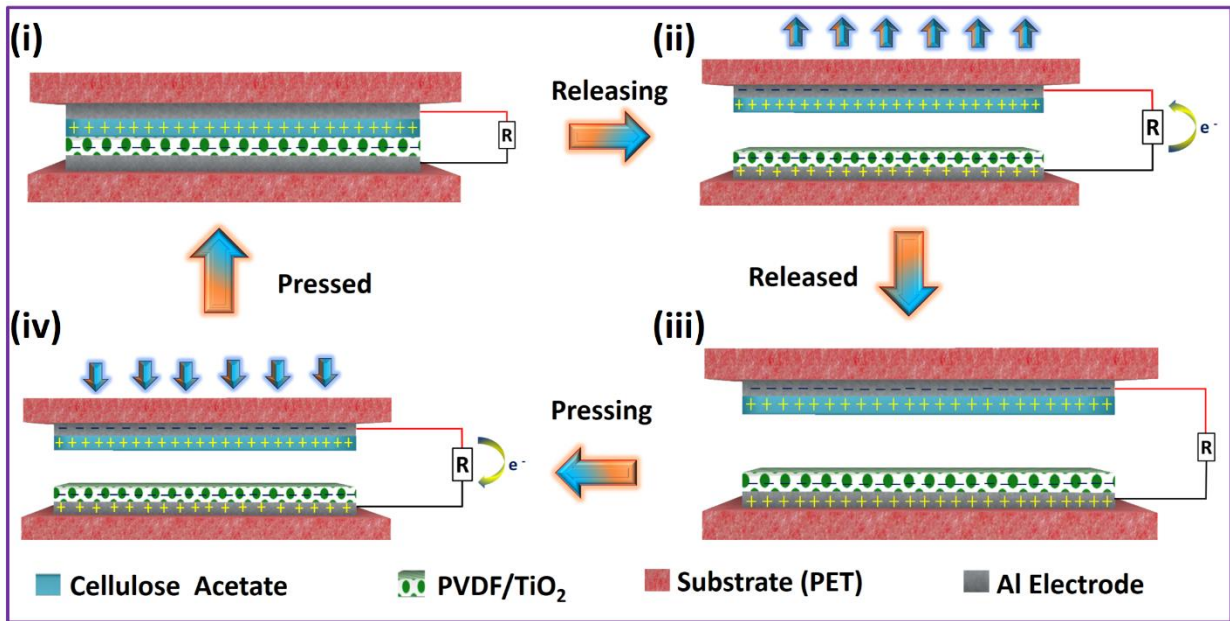


**Figure 3.2.3.** FE-SEM micrograph of (a) PVDF-TiO<sub>2</sub> (b) PVDF-5\_TiO<sub>2</sub> (c) PVDF-10-TiO<sub>2</sub> and (d) PVDF-15-TiO<sub>2</sub> films.

The TENG in the proposed work has a multilayered architecture, operating in a traditional contact-separation mode with an active working area of 6.25 cm<sup>2</sup>. The contact-separation distance for all the devices was kept constant at 0.5 cm. Figure 3.2.4 (a) illustrates the detailed working mechanism of the TENG device. Initially, the upper layer (cellulose acetate) was in firm contact with the bottom PVDF-TiO<sub>2</sub> layer, as shown in Figure 3.2.4 -i. In this condition, there is no change in the potential across the external load. When the upper layer begins to separate, the restoring force of the PET allowed both the segment to return its original shape. During this process, the electrical potential difference arises, driving the electrons to flow from the bottom electrode to the



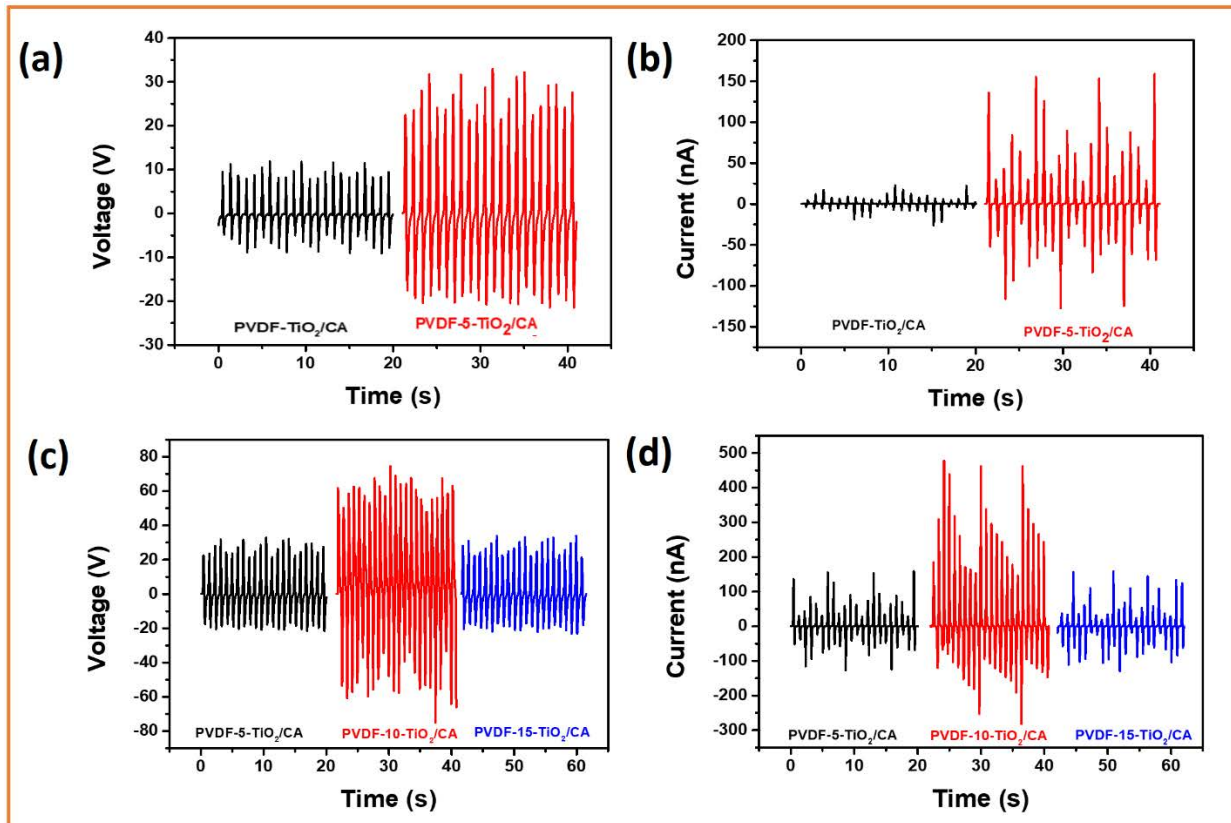
top electrode through the external circuit. This process results in the generation of the first-half cycle of the AC signal (Figure 3.2.4 -ii) and followed by an equilibrium state (Figure 3.2.4 -iii). When an external force was applied on the device, the upper layer starts approaching the bottom layer, thus creating the potential difference resulting in the generation of the second-half cycle of the AC signal (Figure 3.2.4 -iv) [6].



**Figure 3.2.4.** The working mechanism of as-fabricated TENG in vertical contact-separation mode.

The electrical performance of TENG was measured by applying an external cyclic compressive force of 10 N. The force was applied on the upper surface of the device using a linear motor, which gradually pushes the top surface in periodic contact with the bottom substrate. Figure 3.2.5(a-b) shows the output voltage and short-circuit current ( $I_{sc}$ ) for the PVDF-TiO<sub>2</sub>/CA and PVDF-5-TiO<sub>2</sub>/CA film based TENG, respectively. The output in the case of phase inversion was enhanced attributed to the crystallinity and high surface area induced by the phase inversion process. Figure 3.2.5 (c-d) shows the output voltage and short-circuit current for the PVDF-5-TiO<sub>2</sub>/CA, PVDF-10-TiO<sub>2</sub>/CA, and PVDF-15-TiO<sub>2</sub>/CA TENG. In this case, 10 wt.% filler is the

most optimum amount while maintaining the balance of the crystallinity and surface area for the high output, as evident from FT-IR and FE-SEM analysis. The PVDF-10-TiO<sub>2</sub>/CA TENG gives an output voltage of ~65V with I<sub>sc</sub> of ~400 nA. The high filler amount is resulting in the reduced crystallinity and segregation of large particles, as explained earlier.



**Figure 3.2.5.** (a, b) The voltage and short-circuit current output for PVDF-TiO<sub>2</sub>/CA and PVDF-5-TiO<sub>2</sub>/CA TENG, respectively. (c, d) The voltage and short-circuit current output for PVDF-5-TiO<sub>2</sub>/CA, PVDF-10-TiO<sub>2</sub>/CA, PVDF-15-TiO<sub>2</sub>/CA TENG.

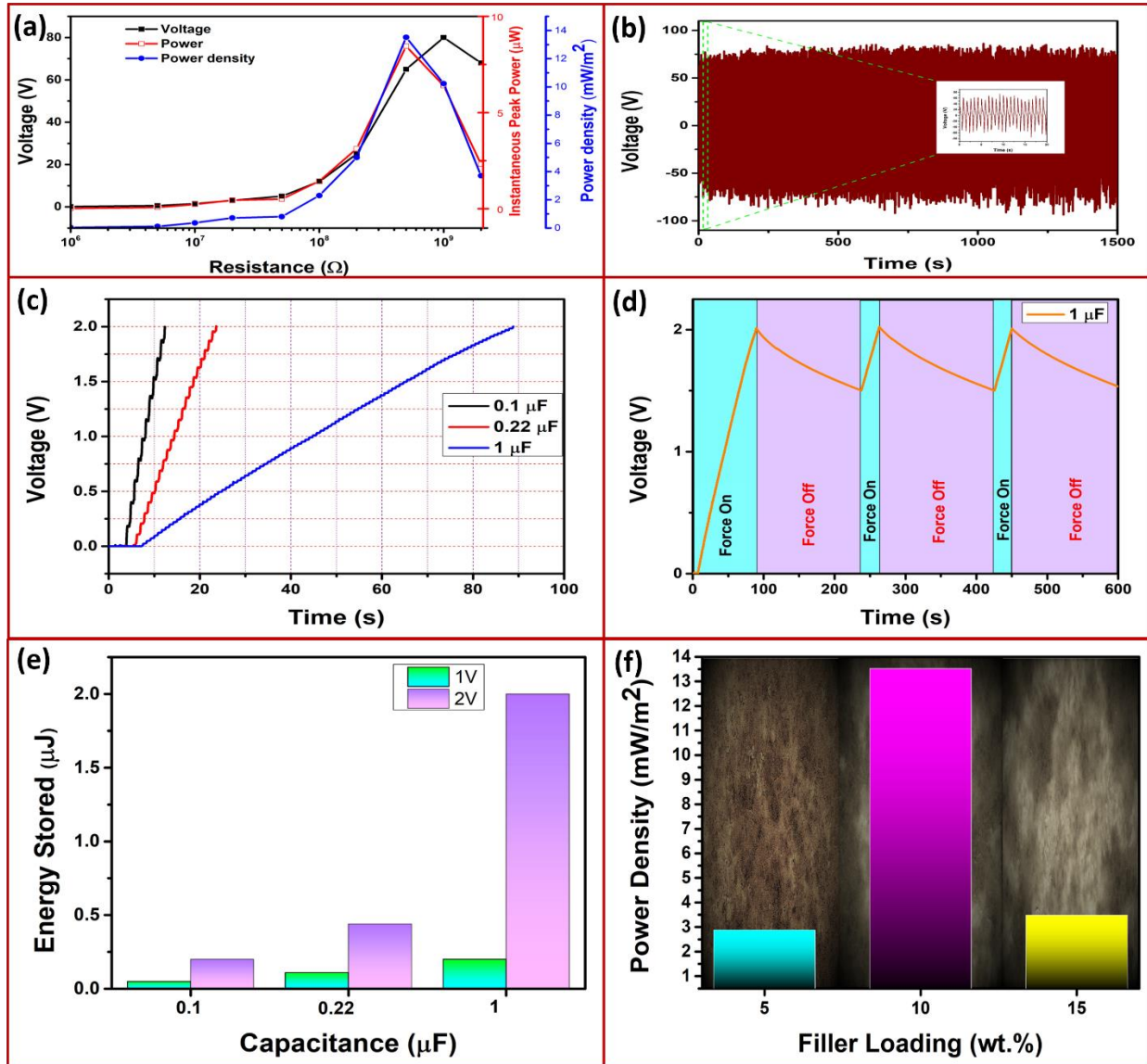
The maximum generated voltage, and effective power density is the critical parameters for a TENG device. Hence, we analyzed the load matching resistance for PVDF-10-TiO<sub>2</sub>/CA TENG over a wide range of loads, as shown in Figure 3.2.6(a). For PVDF-10-TiO<sub>2</sub>/CA TENG, the instantaneous power reached 8.45  $\mu$ W, and the corresponding maximum power density reached

13.52 mW/m<sup>2</sup>. For the practical application of the device, stability is one of the critical parameters for real-time applications. So, an endurance test was performed by continuously pressing and releasing the device for 1500 s, as shown in Figure 3.2.6 (b). The device maintained a stable output with no physical damage to the device structure during the test. The endurance test confirms that the device can be utilized for a prolonged period with a negligible change in electrical performance. The TENG device produces an AC signal, which cannot be used directly to drive low-power electronic devices. Therefore, the output generated was rectified using a bridge rectifier via a rectifying circuit and used to charge 0.1 $\mu$ F, 0.22 $\mu$ F, and 1 $\mu$ F capacitor up to 2V, as shown in Figure 3.2.6 (c). Furthermore, Figure 3.2.6 (d) shows the charge-discharge cycle for the 1 $\mu$ F capacitor. The energy stored in the capacitor at different voltage is shown in Figure 3.2.6 (e). The output of TENG depends on the concentration of the filler (TiO<sub>2</sub>). The 10 wt% filler loading shows the maximum voltage and current output in comparison to 5 and 15 wt% filler loading. Therefore, the effect of filler concentration on the power density of the as-fabricated device is shown in Figure 3.2.6 (f) for the direct visualization of the device power with filler amount. The PVDF-10-TiO<sub>2</sub>/CA TENG exhibits maximum power density followed by PVDF-15-TiO<sub>2</sub>/CA and PVDF-5-TiO<sub>2</sub>/CA. The TENG devices are widely reported for mechanical energy harvesting. For daily life applications, biomechanical energy, wind energy are the most commonly available sources of mechanical energy for TENG. Thus, we tested the device for multifunctional energy harvesting.

The energy harvesting capability of the device was demonstrated by utilizing the biomechanical and wind energy harvesting. These are the two abundant sources of waste energy that can be used to harvest energy for driving low power electronics and other purposes. The biomechanical energy harvesting with finger, hand, and leg motion is shown in Figure 3.2.7. Real-

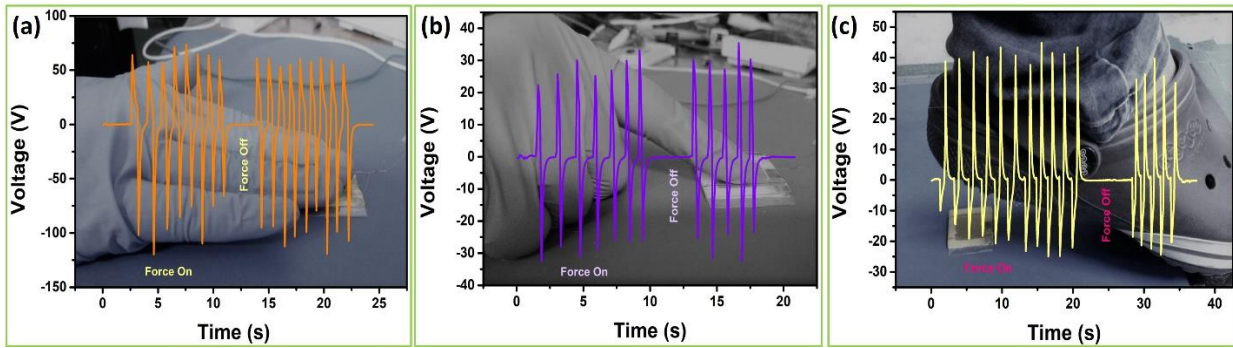


time analysis of the device with human motion confirms the potential of the device for harnessing energy from various body movements.

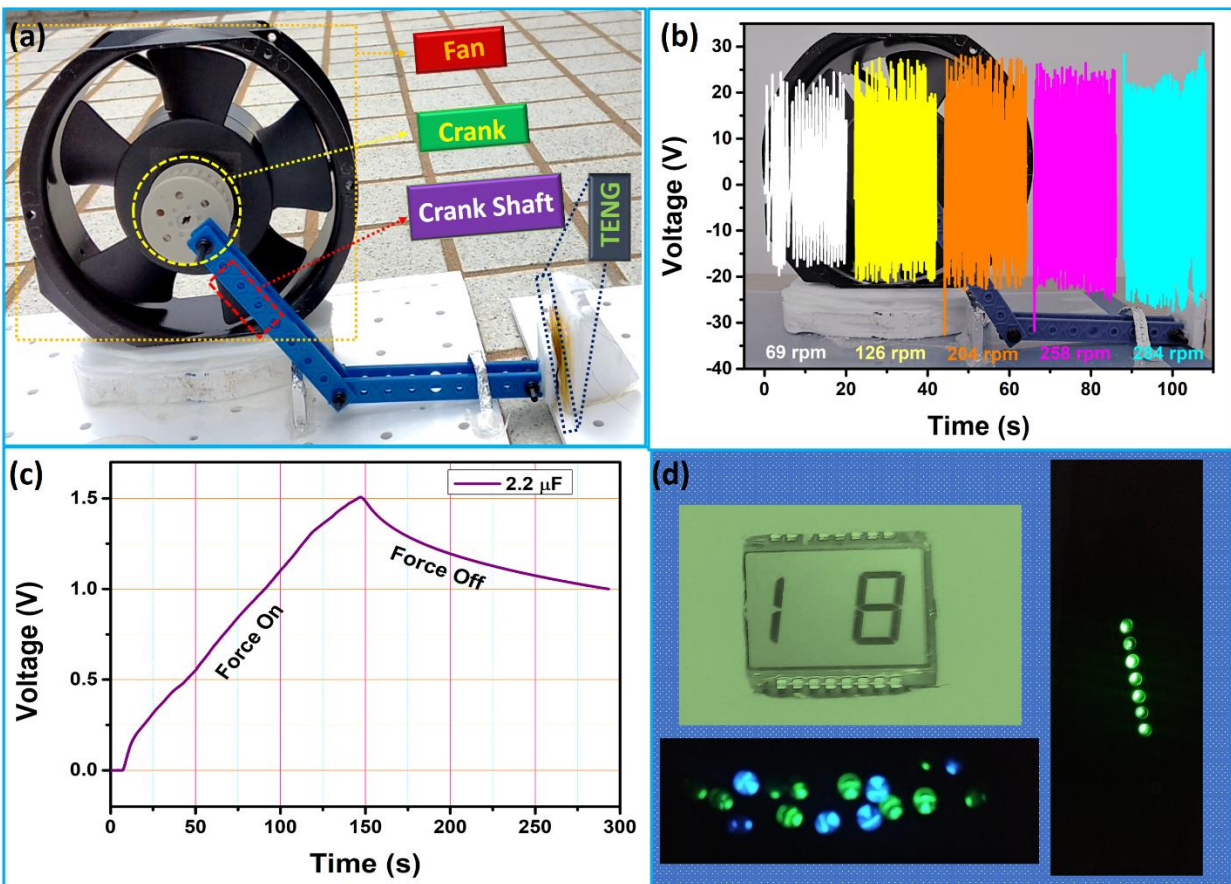


**Figure 3.2.6.** (a) The load matching analysis for PVDF-10-TiO<sub>2</sub>/CA TENG. (b) Stability of the PVDF-10-TiO<sub>2</sub>/CA TENG for 1500 s. (c) The voltage profile of capacitor charging (0.1, 0.22, and 1 μF). (d) The charge-discharge cycle of the 1 μF capacitor. (e) The energy stored in various capacitors at different charged voltage. (f) Effect of filler concentration on the power density of TENG.

The wind is one of the abundant sources of free energy which has been utilized for hundreds of years using a wind turbine. The wind turbines have many drawbacks like bulky, heavy, costly, and easy to corrode. Furthermore, it is challenging to install massive structures at remote locations like mountains [32, 33]. Due to these problems, there is a need for lightweight, cheap, easy to use, and maintain wind energy harvesters. Few researchers reported the use of 3D printed CAM for harnessing wind energy using TENG [34, 35]. 3D printing is expensive, limited by the material property, and not available everywhere, but wind energy is ubiquitous. To leverage the universal wind energy using TENG, the critical requirement is easy to design intermediate structures. Here, we utilized a slider-crank mechanism to convert the rotational motion generated by the wind into linear motion, which impacts on the TENG. The design is straightforward to fabricate, easy to implement, cheap, and can be utilized to harness wind energy even at home in exhaust fans. Furthermore, the model can be used to implement the TENG in the exhaust fans of the industry for various energy harvesting applications. The model for the wind energy harvesting system is shown in Figure 3.2.8 (a). The designed model can harness the energy at different rpm. The capability of the design to harness the wind energy is demonstrated in video 1. The generated output increased slightly, with an increase in rpm (Figure 3.2.8 (b)). The output was used to charge the 2.2 $\mu$ F capacitor. The charging and discharging of the capacitor is shown in Figure 3.2.8 (c). Furthermore, we utilized the generated energy to lit-up LEDs, LED strip, and monochrome LCD, as demonstrated in Figure 3.2.8 (d).



**Figure 3.2.7.** Biomechanical energy harvesting using (a) hand motion, (b) finger tapping and (c) leg motion.



**Figure 3.2.8.** (a) A straightforward, cost-effective wind energy harvesting system. (b) The voltage output of the TENG device at different rpm. (c) Charge-discharge cycle for  $2.2\mu\text{F}$  capacitor and (d) The Lit-up of monochrome LCD, LEDs, and LED strip using the energy harvested by TENG.

VOCs such as toluene, benzene, acetone is the most common and potentially dangerous contaminants in the air which can directly affect the humans. The benzene is a well known organic compound for its high toxicity and carcinogenicity. The breathing air containing benzene can cause headaches, drowsiness, confusion, dizziness, increase heartbeat, blurred vision, etc. On the other hand, acetone exhibits slight toxicity [19]. Regardless of the toxicity, benzene is widely used in various industries[19]. The commercially available benzene sensors generally work in the range of 0-100 ppm. There is a great need to develop a benzene sensor that can work in the high range to potentially coupled with the currently available benzene sensor for detection of high concentration or leakage. Nguyen et al. reported a gas sensor for the detection of VOCs at high concentration utilizing the electrical properties of the nanorod. This sensor exhibits a high response for acetone, followed by ethanol and benzene. The concentration of benzene varied from 25000 ppm to 100000 ppm. The resistance of the material increases with the increase in the flow rate [19]. Fu et al. reported TENG based VOCs sensor exhibiting good response for methanol and ethanol but very poor response to toluene, which is highly toxic. Furthermore, the work by Fu et al. doesn't provide the details about the generation and the regulation of the concentration of the VOCs [36]. We demonstrated the use of as-fabricated TENG for the detection of benzene in the environment. The in-house fabricated closed chamber was used for the sensing measurements. The complete system is depicted in Figure 3.2.9 (a,b). The setup consists of two flow controllers and a sealed chamber connected to the linear motor shaft. The flow controllers are used to maintain the desired concentration by controlling the bubbling and the dilution gas. The pneumatic joints are used for connecting the pipes with zero leakage. The sealed chamber helps in maintaining the desired constant concentration in the chamber. Thus, in the present case, the only parameter affecting the device output is VOC concentration. The high purity nitrogen gas was used as a carrier as well as

bubbling gas. The test gases were generated by bubbling the gas through the solution. The concentration of the VOCs was regulated by controlling the flow rate of the carrier and bubbling gas. The level of the generated VOCs was calculated using the equation –

$$C(ppm) = 10^6 * \left( \frac{P_s f}{P(f + F)} \right)$$

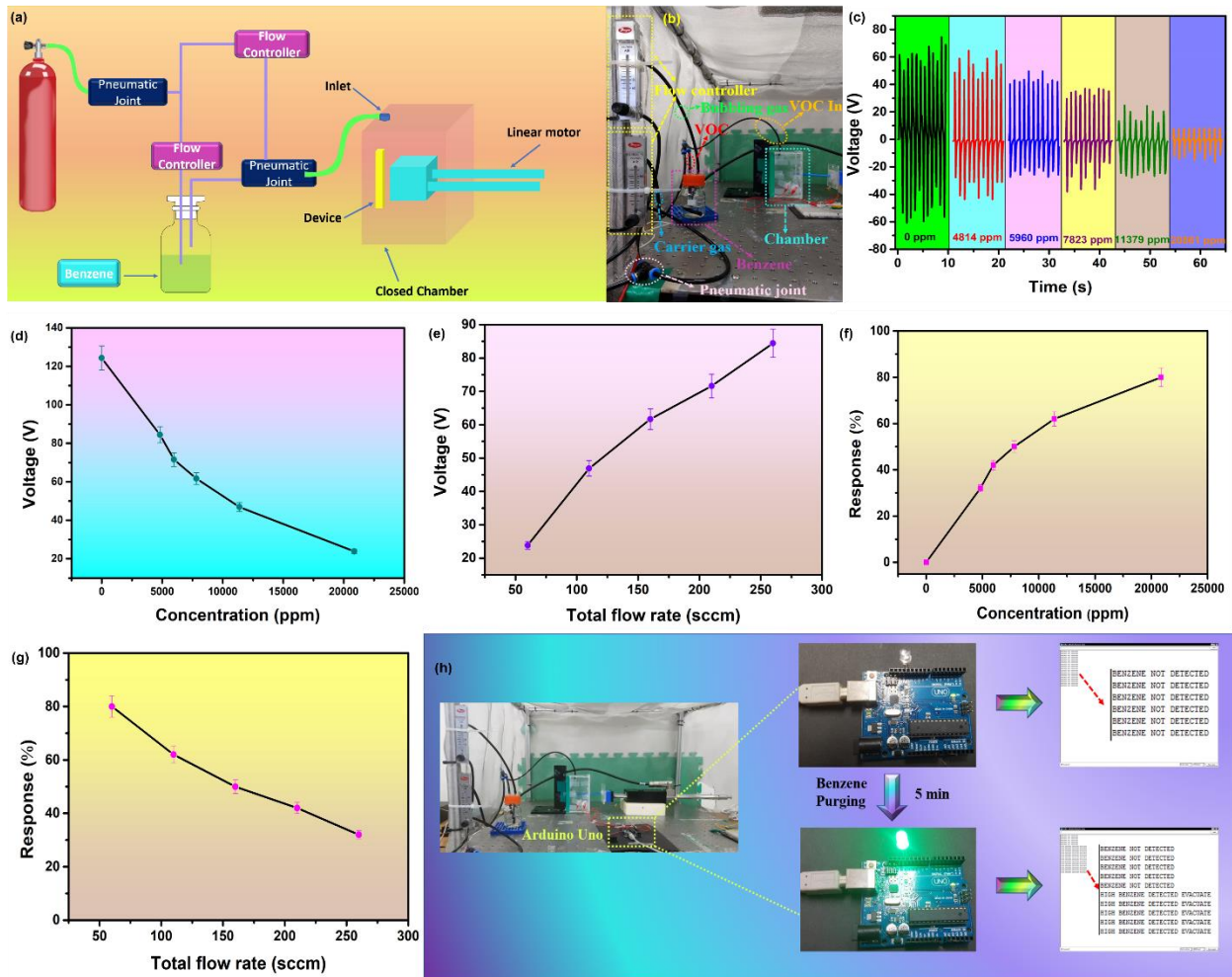
Where  $f$  and  $F$  are the flow rates of the bubbling gas and dilution gas.  $P$  is the total pressure, and  $P_s$  is the saturated partial vapor pressure that can be obtained using the Antoine equation [19, 37]. The chamber was purged with benzene for 5 min to create the environment before measurement. After every measurement, the nitrogen was aerated into the chamber for 3 min, and then the device is allowed to refresh in the air condition for 10 min. The device was capable of recovering after every exposure of benzene effectively. The voltage of the TENG device decreases with the increase in the concentration of the benzene, as shown in Figure 3.2.9 (c). The developed PVDF-TiO<sub>2</sub> films are porous in nature, which helps in the adsorption of the benzene. Moreover, the nanoparticles are well reported to promote the adsorption by further creating the adsorption site [26]. The PVDF is resistant to benzene, but benzene can be absorbed in the pores and can interact with TiO<sub>2</sub> via OH- $\pi$  interaction [27, 38]. The benzene can be desorbed in environmental conditions as there is no dissociative reactivity of benzene on TiO<sub>2</sub> [27, 38]. The decrease in the voltage output can be ascribed to the two factors. One is the occupancy of the porous sites in the film. The second is the weak hybridization between the Ti d-states and C p-states, which results in the alteration of the local density of states, thereby changing the capabilities of the TiO<sub>2</sub> [27, 38]. The benzene adsorption results in space charge limited conduction resulting in restraint of triboelectrification effect [39, 40]. The variation of voltage with concentration is shown in Figure 3.2.9 (d). The total flow rate has an inverse relationship with the concentration, thus following the



reverse trend, as evident from Figure 3.2.9 (e). The response with respect to concentration and the total flow rate is shown in Figure 3.2.9 (f,g). The response (%) against 4814, 5960, 7823, 11379 and 20861 ppm were 32, 42, 50, 62, and 80 respectively. The response of the TENG can be simply defined as [36]:

$$R\% = \frac{V_0 - V}{V} \times 100 \%$$

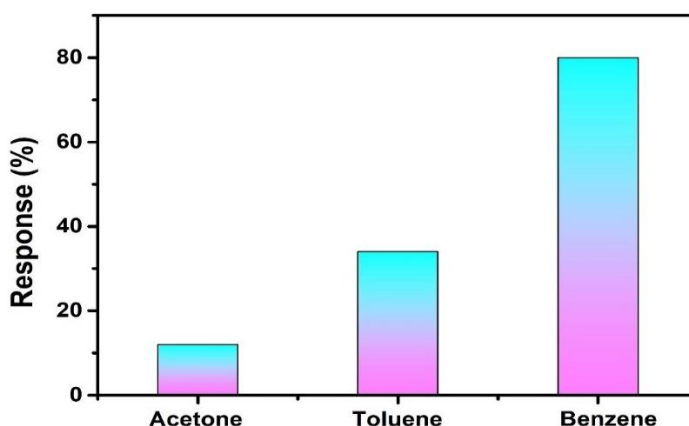
Where  $V_0$  is the initial voltage and  $V$  is the voltage obtained after exposure.



**Figure 3.2.9.** The utilization of TENG for VOCs sensing. (a) The schematic of the in-house designed setup for the generation of VOCs and sensing measurement. (b) The image of the

designed setup. (c) The voltage output with the concentration of the benzene. (d,e) The variation in the voltage with the concentration and total flow rate, respectively. (f,g) The response of the sensor with the concentration and total flow rate. (h) The integration of the benzene sensor with Arduino Uno for buzzing the alarm to evacuate the area.

The sensitivity of the detection was 0.0035V/ppm concerning concentration and 0.29176 V/sccm concerning the total flow rate. The device was successfully recovered in 10 min. The recovery time is defined as the time required by the device to reach a stable output voltage again after removing the exposure or changing the environment. Figure 3.2.10 shows that the device can also detect other VOC vapors, but the response is very poor compared to that for benzene. Against 20861 ppm of benzene, toluene, acetone, the response was 80 %, 34%, and 12%, respectively (Figure 3.2.10). The different responses can be ascribed to discordant molecule size and polarity of VOC vapor [36]. Finally, we integrated the Arduino Uno for automatic detection and buzzing alarm to evacuate the area. The Arduino Uno display the message “Benzene not detected” in case of absence of the benzene vapors and “High benzene detected evacuate” in the presence of the benzene vapors as shown in Figure 3.2.9 (h). We believe that our work will open up a new approach for the detection of VOCs in the atmosphere using TENG.



**Figure 3.2.10.** The response of the TENG against various VOC vapors (20861 ppm).

### 3.2.4 Conclusion

A high performance PVDF-10-TiO<sub>2</sub> TENG was fabricated utilizing the concept of phase inversion chemistry. The porosity and enhanced crystallinity of the film lead to a significant increase in the performance of nanogenerator. The voltage and short circuit current improved by 7 times and 10 times from a value of 10V and 40 nA to 70V and 400nA by employing the phase inversion process. Finally, we designed a wind energy harvesting system by utilizing the slider-crank mechanism for efficient wind energy harvesting. The model can generate a voltage output of ~25 V. The designed model was cheap, easy to fabricate, and can be used to harvest wind energy at various locations, including home. Finally, we demonstrated the benzene sensing using the TENG. The device can recover in 10 min after purging nitrogen for 3 min. The sensitivity of the sensor is 0.0035 V/ppm or 0.29176 V/sccm. We believe that as our approach is simple for multifunction energy harvesting and it can be utilized in the future for the development of various TENG based sensors.



## References

- [1] M. Höök, X. Tang, Depletion of fossil fuels and anthropogenic climate change—A review, *Energy Policy*, 52(2013) 797-809.
- [2] M. Ha, J. Park, Y. Lee, H. Ko, Triboelectric Generators and Sensors for Self-Powered Wearable Electronics, *ACS Nano*, 9(2015) 3421-7.
- [3] F.-R. Fan, L. Lin, G. Zhu, W. Wu, R. Zhang, Z.L. Wang, Transparent Triboelectric Nanogenerators and Self-Powered Pressure Sensors Based on Micropatterned Plastic Films, *Nano Letters*, 12(2012) 3109-14.
- [4] Z.L. Wang, Triboelectric Nanogenerators as New Energy Technology for Self-Powered Systems and as Active Mechanical and Chemical Sensors, *ACS Nano*, 7(2013) 9533-57.
- [5] G. Zhu, B. Peng, J. Chen, Q. Jing, Z. Lin Wang, Triboelectric nanogenerators as a new energy technology: From fundamentals, devices, to applications, *Nano Energy*, 14(2015) 126-38.
- [6] Z.L. Wang, L. Lin, J. Chen, S. Niu, Y. Zi, Triboelectric Nanogenerator: Vertical Contact-Separation Mode, *Triboelectric Nanogenerators*, Springer International Publishing, Cham, 2016, pp. 23-47.
- [7] L.S. McCarty, G.M. Whitesides, Electrostatic Charging Due to Separation of Ions at Interfaces: Contact Electrification of Ionic Electrets, *Angewandte Chemie International Edition*, 47(2008) 2188-207.
- [8] M.-L. Seol, J.-H. Woo, S.-B. Jeon, D. Kim, S.-J. Park, J. Hur, et al., Vertically stacked thin triboelectric nanogenerator for wind energy harvesting, *Nano Energy*, 14(2015) 201-8.
- [9] M. Choi, G. Murillo, S. Hwang, J.W. Kim, J.H. Jung, C.-Y. Chen, et al., Mechanical and electrical characterization of PVDF-ZnO hybrid structure for application to nanogenerator, *Nano Energy*, 33(2017) 462-8.

- [10] X.-S. Zhang, M.-D. Han, R.-X. Wang, F.-Y. Zhu, Z.-H. Li, W. Wang, et al., Frequency-Multiplication High-Output Triboelectric Nanogenerator for Sustainably Powering Biomedical Microsystems, *Nano Letters*, 13(2013) 1168-72.
- [11] F.-R. Fan, Z.-Q. Tian, Z. Lin Wang, Flexible triboelectric generator, *Nano Energy*, 1(2012) 328-34.
- [12] G. Zhu, Z.-H. Lin, Q. Jing, P. Bai, C. Pan, Y. Yang, et al., Toward Large-Scale Energy Harvesting by a Nanoparticle-Enhanced Triboelectric Nanogenerator, *Nano Letters*, 13(2013) 847-53.
- [13] Y. Feng, L. Ling, J. Nie, K. Han, X. Chen, Z. Bian, et al., Self-Powered Electrostatic Filter with Enhanced Photocatalytic Degradation of Formaldehyde Based on Built-in Triboelectric Nanogenerators, *ACS Nano*, 11(2017) 12411-8.
- [14] A. Chandrasekhar, N.R. Alluri, V. Vivekananthan, Y. Purusothaman, S.-J. Kim, A sustainable freestanding biomechanical energy harvesting smart backpack as a portable-wearable power source, *Journal of Materials Chemistry C*, 5(2017) 1488-93.
- [15] A. Chandrasekhar, G. Khandelwal, NR Alluri, V. Vivekananthan, S.-J. Kim, Battery-Free Electronic Smart Toys: A Step toward the Commercialization of Sustainable Triboelectric Nanogenerators, *ACS Sustainable Chemistry & Engineering*, 6(2018) 6110-6.
- [16] ASMI. Uddin, G.-S. Chung, Wide-ranging impact-competent self-powered active sensor using a stacked corrugated-core sandwich-structured robust triboelectric nanogenerator, *Sensors and Actuators B: Chemical*, 245(2017) 1-10.
- [17] D. Gu, X. Li, H. Wang, M. Li, Y. Xi, Y. Chen, et al., Light enhanced VOCs sensing of WS2 microflakes based chemiresistive sensors powered by triboelectronic nangenerators, *Sensors and Actuators B: Chemical*, 256(2018) 992-1000.

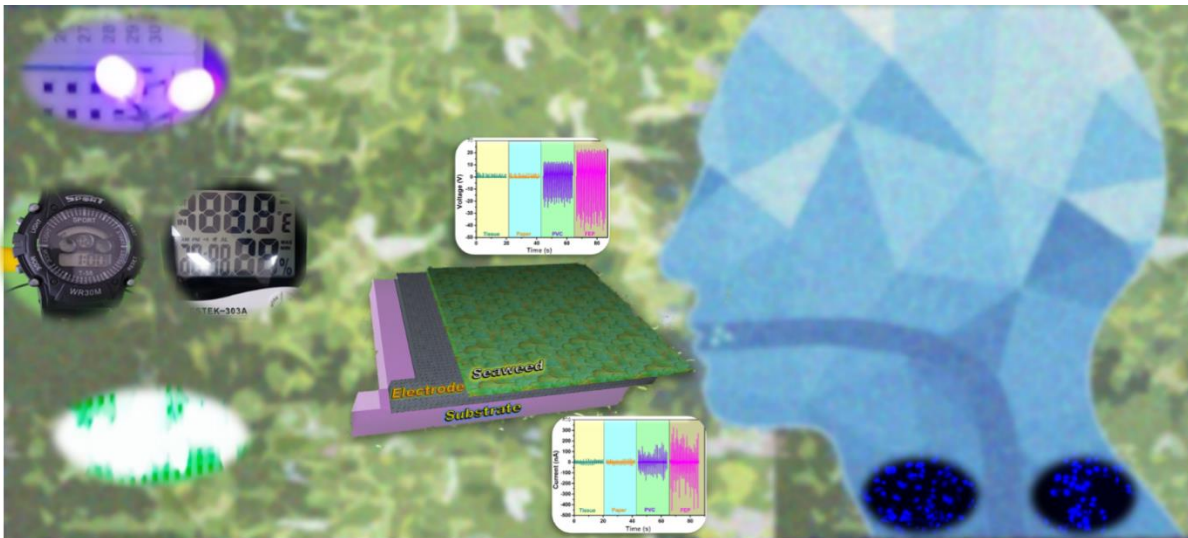
- [18] Y. Su, G. Xie, S. Wang, H. Tai, Q. Zhang, H. Du, et al., Novel high-performance self-powered humidity detection enabled by triboelectric effect, *Sensors and Actuators B: Chemical*, 251(2017) 144-52.
- [19] H. Nguyen, S.A. El-Safty, Meso- and Macroporous Co<sub>3</sub>O<sub>4</sub> Nanorods for Effective VOC Gas Sensors, *The Journal of Physical Chemistry C*, 115(2011) 8466-74.
- [20] X. Yang, W.A. Daoud, Triboelectric and Piezoelectric Effects in a Combined Tribo-Piezoelectric Nanogenerator Based on an Interfacial ZnO Nanostructure, *Advanced Functional Materials*, 26(2016) 8194-201.
- [21] N. Soin, P. Zhao, K. Prashanthi, J. Chen, P. Ding, E. Zhou, et al., High performance triboelectric nanogenerators based on phase-inversion piezoelectric membranes of poly(vinylidene fluoride)-zinc stannate (PVDF-ZnSnO<sub>3</sub>) and polyamide-6 (PA6), *Nano Energy*, 30(2016) 470-80.
- [22] S. Wanchul, Y. Hong-Joon, K.T. Yun, R. Hanjun, K. Jihye, L. Ju-Hyuck, et al., Boosting Power-Generating Performance of Triboelectric Nanogenerators via Artificial Control of Ferroelectric Polarization and Dielectric Properties, *Advanced Energy Materials*, 7(2017) 1600988.
- [23] N. Soin, D. Boyer, K. Prashanthi, S. Sharma, A.A. Narasimulu, J. Luo, et al., Exclusive self-aligned [small beta]-phase PVDF films with abnormal piezoelectric coefficient prepared via phase inversion, *Chemical Communications*, 51(2015) 8257-60.
- [24] S. Kalaiarasi, M. Jose, Dielectric functionalities of anatase phase titanium dioxide nanocrystals synthesized using water-soluble complexes, *Applied Physics A*, 123(2017) 512.
- [25] W. Seung, H.J. Yoon, T.Y. Kim, H. Ryu, J. Kim, J.H. Lee, et al., Boosting Power-Generating Performance of Triboelectric Nanogenerators via Artificial Control of Ferroelectric Polarization and Dielectric Properties, *Advanced Energy Materials*, 7(2017) 1600988.

- [26] A. Mirzaei, J.-H. Kim, H.W. Kim, S.S. Kim, Resistive-based gas sensors for detection of benzene, toluene and xylene (BTX) gases: a review, *Journal of Materials Chemistry C*, 6(2018) 4342-70.
- [27] J. Zhou, S. Dag, S.D. Senanayake, B.C. Hathorn, S.V. Kalinin, V. Meunier, et al., Adsorption, desorption, and dissociation of benzene on  $\text{TiO}_2(110)$  and  $\text{Pd}/\text{TiO}_2(110)$ : Experimental characterization and first-principles calculations, *Physical Review B*, 74(2006) 125318.
- [28] B.S. Shirke, P.V. Korake, P.P. Hankare, S.R. Bamane, K.M. Garadkar, Synthesis and characterization of pure anatase  $\text{TiO}_2$  nanoparticles, *Journal of Materials Science: Materials in Electronics*, 22(2011) 821-4.
- [29] M. Zhang, A.-Q. Zhang, B.-K. Zhu, C.-H. Du, Y.-Y. Xu, Polymorphism in porous poly(vinylidene fluoride) membranes formed via immersion precipitation process, *Journal of Membrane Science*, 319(2008) 169-75.
- [30] X. Li, Y. Wang, X. Lu, C. Xiao, Morphology changes of polyvinylidene fluoride membrane under different phase separation mechanisms, *Journal of Membrane Science*, 320(2008) 477-82.
- [31] A. Salimi, A.A. Yousefi, Analysis Method: FTIR studies of  $\beta$ -phase crystal formation in stretched PVDF films, *Polymer Testing*, 22(2003) 699-704.
- [32] D. Weisser, R.S. Garcia, Instantaneous wind energy penetration in isolated electricity grids: concepts and review, *Renewable Energy*, 30(2005) 1299-308.
- [33] S. Wang, X. Wang, Z.L. Wang, Y. Yang, Efficient Scavenging of Solar and Wind Energies in a Smart City, *ACS Nano*, 10(2016) 5696-700.

- [34] B. Dudem, N.D. Huynh, W. Kim, D.H. Kim, H.J. Hwang, D. Choi, et al., Nanopillar-array architected PDMS-based triboelectric nanogenerator integrated with a windmill model for effective wind energy harvesting, *Nano Energy*, 42(2017) 269-81.
- [35] Y. Lee, W. Kim, D. Bhatia, H.J. Hwang, S. Lee, D. Choi, Cam-based sustainable triboelectric nanogenerators with a resolution-free 3D-printed system, *Nano Energy*, 38(2017) 326-34.
- [36] Y. Fu, H. He, Y. Liu, Q. Wang, L. Xing, X. Xue, Self-powered, stretchable, fiber-based electronic-skin for actively detecting human motion and environmental atmosphere based on a triboelectrification/gas-sensing coupling effect, *Journal of Materials Chemistry C*, 5(2017) 1231-9.
- [37] ND. Hoa, N. Van Quy, D. Kim, Nanowire structured SnO<sub>x</sub>-SWNT composites: High performance sensor for NO<sub>x</sub> detection, *Sensors and Actuators B: Chemical*, 142(2009) 253-9.
- [38] M. Nagao, Y. Suda, Adsorption of benzene, toluene, and chlorobenzene on titanium dioxide, *Langmuir*, 5(1989) 42-7.
- [39] M. Mabrook, P. Hawkins, Benzene Sensing Using Thin Films of Titanium Dioxide Operating at Room Temperature, *Sensors*, 2(2002) 374.
- [40] Y. Dai, Y. Fu, H. Zeng, L. Xing, Y. Zhang, Y. Zhan, et al., A Self-Powered Brain-Linked Vision Electronic-Skin Based on Triboelectric-Photodetecting Pixel-Addressable Matrix for Visual-Image Recognition and Behavior Intervention, *Advanced Functional Materials*, 28(2018) 1800275.

### 3.3 All Edible Materials Derived Biocompatible and Biodegradable Triboelectric Nanogenerator

#### Graphical Overview



## Highlights

- A single electrode, lightweight edible TENG (E-TENG), was fabricated using Laver.
- The MTT assay, live-dead imaging, and DAPI staining suggests a minimal effect on the cells.
- The bioresorbable nature was tested in the PBS buffer and simulated gastric juice.
- The E-TENG generates an output of 23 V and 315 nA with FEP as the opposite layer.
- The large device was used to drive wristwatch, hygrometer, green, and UV LEDs.

### 3.3.1 Introduction

Triboelectric nanogenerators (TENGs) simply and effectively convert waste mechanical energy into electricity [1, 2]. TENGs are based on contact electrification and electrostatic induction in vertical contact-separation, lateral sliding, single-electrode, or freestanding modes [1, 3]. Most TENGs use a polymer either as an active layer or a substrate, thus contributing to plastic pollution worldwide [4]; cheap, disposable plastic electronics must be phased out as plastic waste kills many aquatic animals [4, 5]. Many environmental plastics are degraded to environmentally harmful nanoplastics [6]; plastic fibers can even be found in drinking water [5, 7]. In the USA, 39,000 to 52,000 particles are consumed by each person daily, depending on sex and age [8]. Biodegradable/edible materials are alternatives to plastics. Edible electronics can be eaten in an emergency, and are easily metabolized. Fully biodegradable TENGs based on cellulose, rice sheets, silk fibroin, poly-lactic acid, and gelatin are reported [9-11]. Such devices can be used in remote locations for emergency power generation and later consumed or discarded. Their lightweight suggests many military applications.

Here, we develop an ultra-lightweight edible TENG (E-TENG) operating in the single-electrode mode. Laver (Gim) (an edible Korean seaweed) served as the active triboelectric layer. Edible silver leaf (widely used in sweets and Eastern cuisine) served as the electrode and an edible rice sheet as the substrate. All materials can be easily metabolized. Gold and silver leaf are commonly used in edible electronics [12-14]. The positive surface potential of Laver was confirmed via Kelvin probe force microscopy (KPFM), and the surface roughness studied using a three-dimensional (3D) nanop profiler. The 3-(4,5-dimethylthiazol-2-yl)-2,5-diphenyl tetrazolium bromide (MTT) assay, cell imaging, and 4',6-diamidino-2-phenylindole (DAPI) staining suggest that the device minimally affected cell viability. Bioresorbability in phosphate-buffered saline



(PBS) and simulated gastric juice was studied. Output performance was tested using paper, tissue paper, polyvinyl chloride (PVC), and fluorinated ethylene propylene (FEP). The FEP-laver device produced the best output (23 V and 315 nA). The electrical performance was systematically studied. Finally, the device was used to power green light-emitting diodes (LEDs), UV-LEDs, a hygrometer, and a wristwatch. We believe that our work will enhance energy harvesting using edible devices.

### **3.3.2 Experimental**

#### **3.3.2.1 Sample preparation for Cell studies**

Uncoated and silver leaf-coated laver devices were dried and manually ground using a mortar and pestle. The material was suspended in absolute ethanol, and each volume made up to 1 mL. The suspensions were shaken overnight at 37°C and 150 rpm, the tubes centrifuged at 3,000 g, the supernatants collected and filtered, the solutions kept in a dry bath at 40°C until 90% of the ethanol had evaporated, the mixtures lyophilized, the dry weights measured, and the extracts dissolved in 200- $\mu$ L amounts of DMSO to a concentration of 1 mg/mL and used in biological studies.

#### **3.3.2.2 Cell viability assay (MTT assay)**

The HeLa cell cytotoxicities of coated and non-coated Laver were evaluated. HeLa cells ( $10^4$ - $10^5$ /well) were seeded into a 96-well plate, grown for 24 h, exposed to coated and non-coated Laver for 24 and 48 h and MTT (10  $\mu$ L of a 5 mg/mL stock) then added to each well followed by incubation at 37°C for 3 h under CO<sub>2</sub>. Viable cells convert MTT to purple formazan. The reaction was stopped by addition of 100  $\mu$ L DMSO to each well, and absorbances read using an ELISA plate reader operating at 570 nm [15, 16].

### 3.3.2.3 Cell imaging

The effects of coated and non-coated Laver on HeLa cell morphology were examined using a phase-contrast microscope. HeLa cells ( $10^4$ - $10^5$ /well) were seeded into a 96-well plate, grown for 24 h, exposed to coated and non-coated Laver for 24 h, washed with PBS, and visualized at 10X [17].

### 3.3.2.4 DAPI staining

Morphological changes of HeLa cell nuclei were examined via DAPI staining. HeLa cells ( $10^4$ - $10^5$ /well) were seeded into a 96-well plate, grown for 24 h, and exposed to coated and non-coated Laver for 24 h; the cells were fixed and permeabilized with methanol (100  $\mu$ L/well) for 30 min at  $-20^\circ\text{C}$  and then washed with PBS to remove all methanol. Finally, the cells were stained with DAPI (2  $\mu$ g/mL) for 15 min at room temperature in the dark, and the cells imaged under a fluorescence microscope at 40X [15, 18].

### 3.3.2.5 Device fabrication

The device is fabricated in a single electrode mode configuration. The Laver is used as it is without any processing or modifications. The edible silver leaf is transferred to Laver by applying pressure. The adherence of the silver leaf is shown in the Figure 3.3.1. The silver leaf coated Laver is attached on the rice sheet with the help of wheat paste.

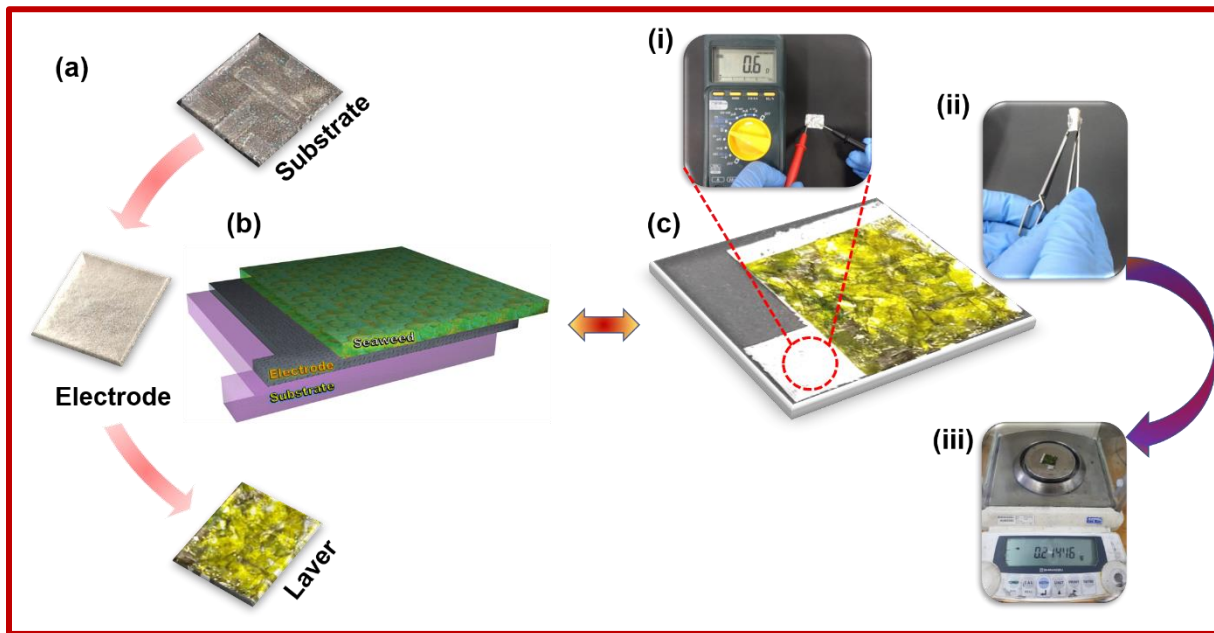
## 3.3.3 Results and Discussions

The single-electrode E-TENG features an edible rice sheet as the substrate and edible, silver leaf-coated laver as the active TE layer. Figure 3.3.1a shows the transfer of a silver leaf to the Laver. Figure 3.3.1b presents the 3D architecture of the E-TENG; the active area is 2 x 2 cm in the single-electrode mode. Figure 3.3.1c is an optical image of the device; Figure 3.3.1c (i)

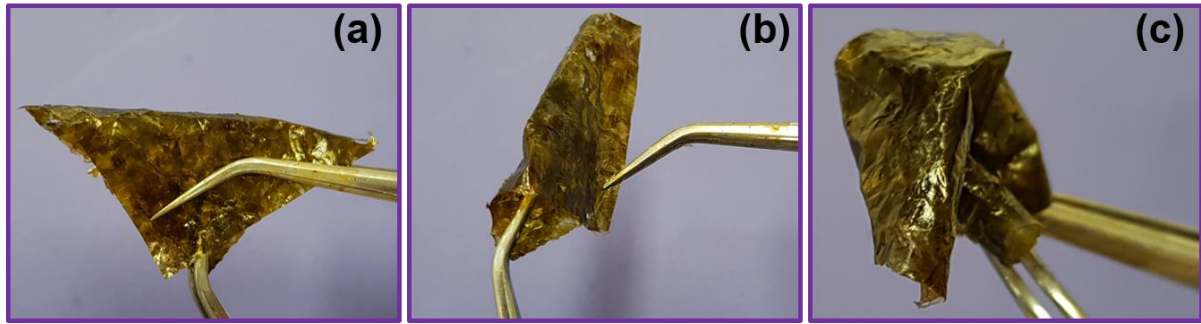
shows the resistance of the silver leaf. The sheet resistance ( $R_s$ ) of the silver leaf, as measured using the the formula [19]:

$$R_s = R \frac{l}{W}$$

where  $R_s$  is the sheet resistance,  $R$  the measured resistance,  $l$  the distance between the two electrodes, and  $W$  the sample width. The calculated  $R_s$  was  $0.3 \Omega$ ; this very low value indicates that edible silver leaf is an appropriate electrode. The adherence and flexibility of silver leaf-coated laver are shown in Figure 3.3.1c (ii). The device weighed  $0.2144 \text{ g}$ , and was thus lightweight. Laver flexibility and robustness were confirmed by repeated bending and crushing (Figure 3.3.2).

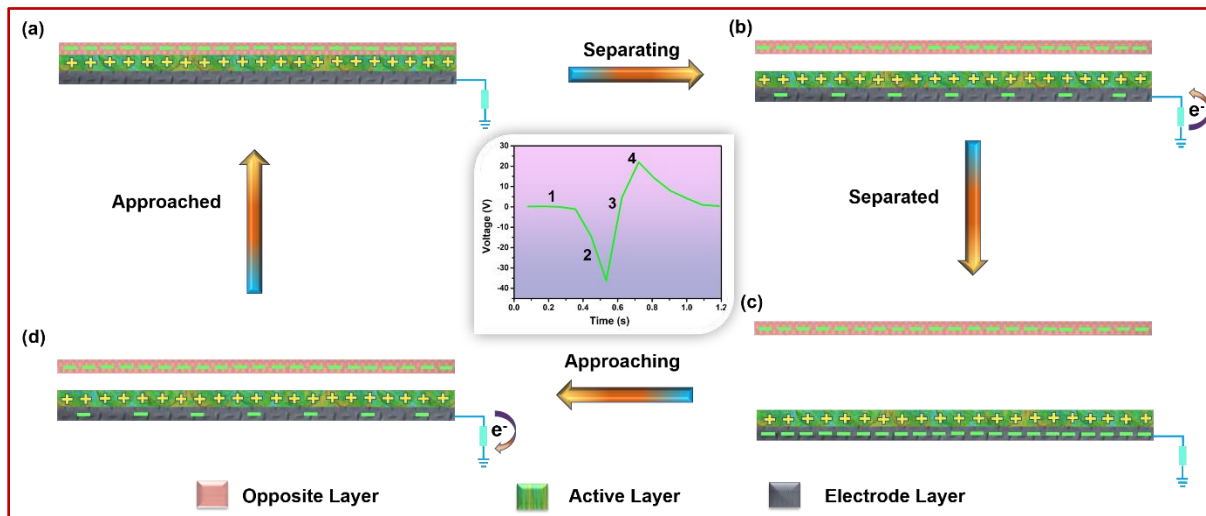


**Figure 3.3.1.** (a) Schematic illustration for the device fabrication. (b) The 3D illustration of the single electrode E-TENG device. (c) The optical image of the fabricated device (i) the resistance offered by the edible silver leaf, (ii) the adherence and bending of the silver leaf coated Laver, (iii) weight of the fabricated device confirming the ultra-light weight of the device.



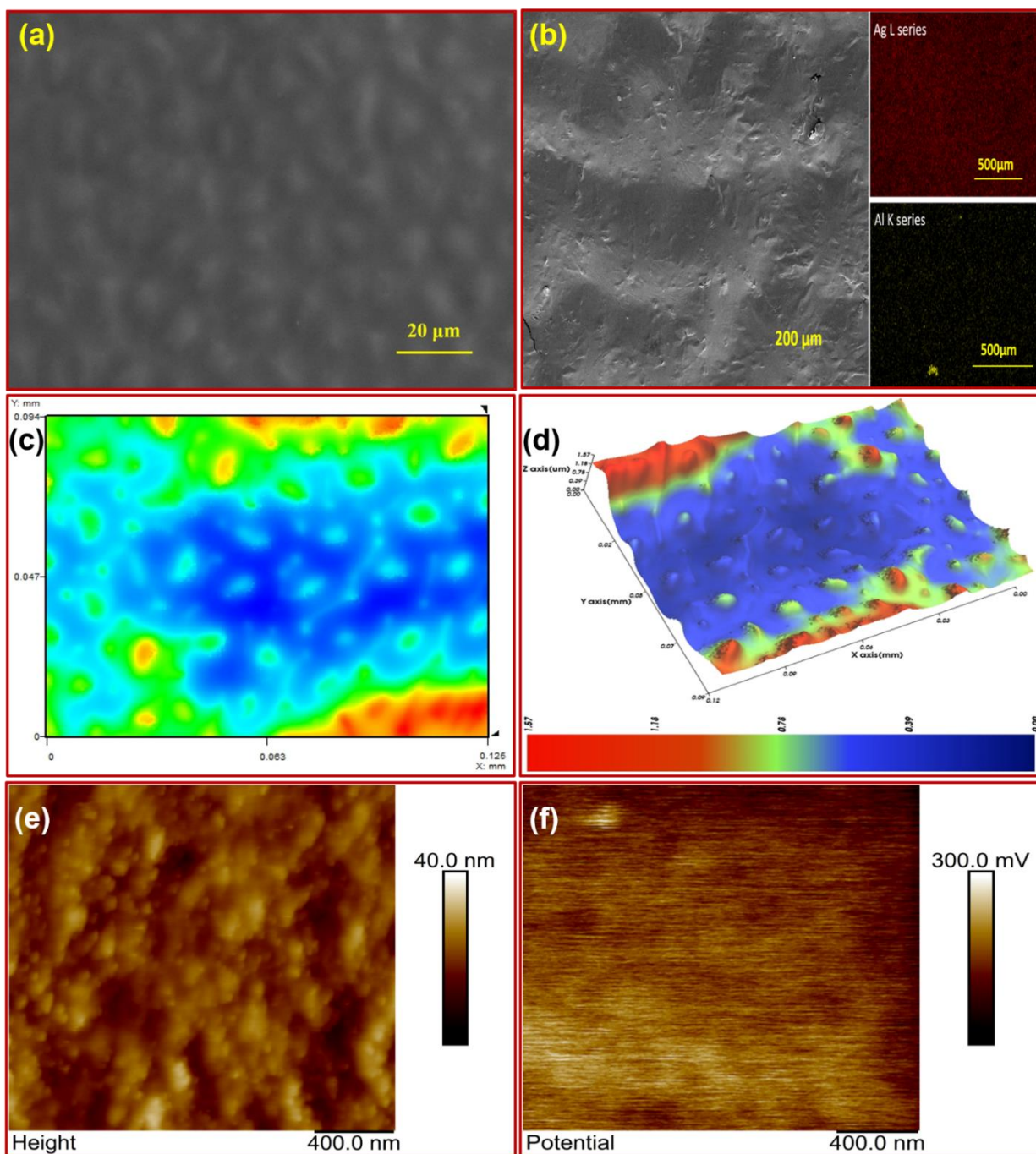
**Figure 3.3.2.** (a-c) The flexibility of Laver in different bending conditions.

Figure 3.3.3 shows the mechanism of action and the electrical performance [20, 21]. The output voltage signal is shown in the center of the Figure 3.3.3. The sections numbered 1-4 correspond to the operating steps of Figure 3.3.3. Notably, Laver was positively triboelectric. At first (Figure 3.3.3a), the opposite layer was in full contact with the Laver (section 1), generating equivalent positive and negative charges. When the opposite and frictional layers were separated (Figure 3.3.3b), electrons transferred from the ground to the silver leaf electrode given the potential difference, generating the first output half-cycle (section 2). This current ceased when the opposite layer separated further from the friction layer, and equilibrium was achieved (Figure 3.3.3c, section 3). As the opposite layer began to approach the friction layer once more, a reverse electron flow occurred, generating the other output half-cycle (Figure 3.3.3d, section 4). This flow continued until the friction and opposite layers come into contact (Figure 3.3.3d) [20-22].



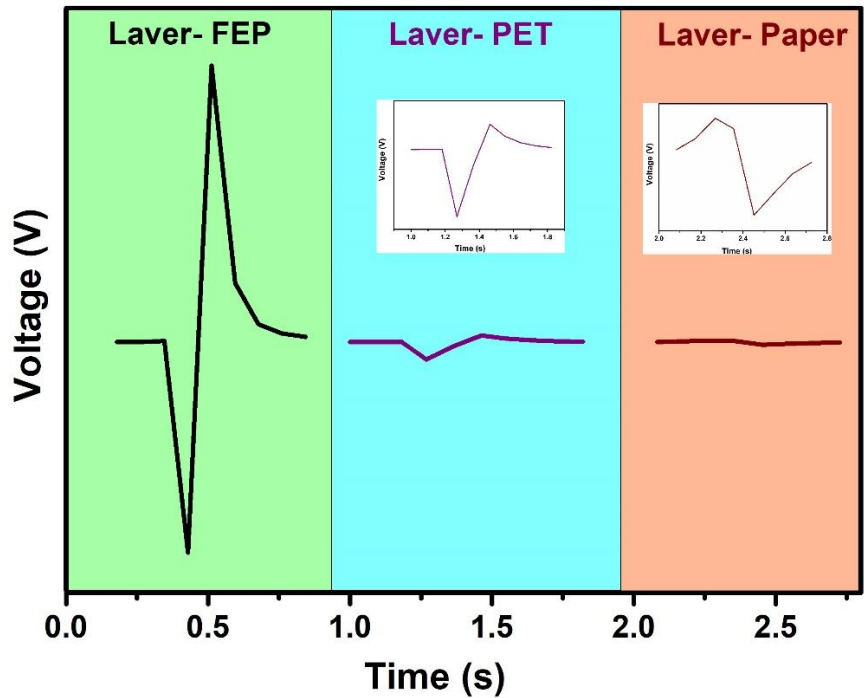
**Figure 3.3.3.** The device mechanism in single electrode mode. (a-d) Charge distribution for a complete cycle of output a) comes in complete contact, b) departs from, c) complete far away and d) approach the friction layer.

An FE-SEM image of Laver is shown in Figure 3.3.4a. Fig. Figure 3.3.4b shows the surface morphology (FE-SEM) and EDS map of the edible silver leaf; the leaf contains aluminum. Surface roughness is critical in terms of TENG performance [23, 24]. Figure 3.3.4c and 3.3.4d show the 2D and 3D surface profiles of Laver. The average surface roughness ( $R_a$ ) is 108.82 nm in the x-direction and 259.65 nm in the y-direction. The materials used for fabrication affect the surface potential. Figure 3.3.4e shows an AFM image of Laver; this is similar to the FE-SEM image. Figure 3.3.4f shows the surface potential map (KPFM) of Laver; the surface potential is positive so Laver will become positively charged when in contact with materials of negative potential such as FEP, Kapton, and PVC.



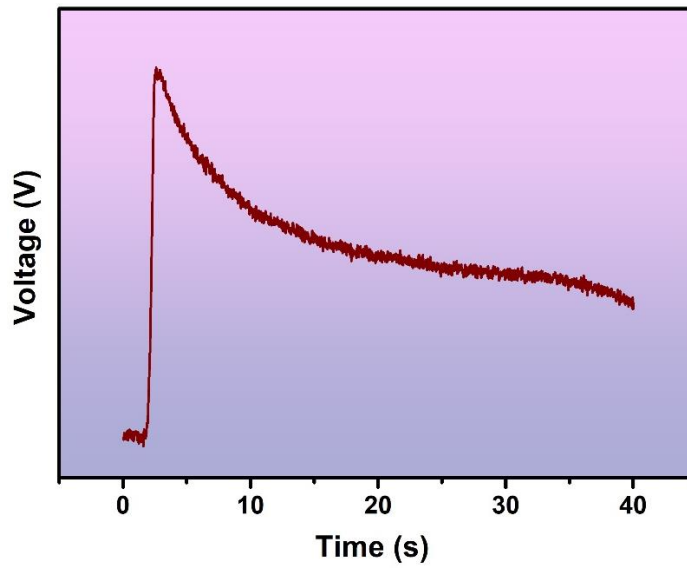
**Figure 3.3.4.** (a) The FE-SEM image of the Laver. (b) FE-SEM image and EDS mapping of the edible silver leaf. (c) 2D surface roughness profile of the Laver. (d) 3D surface roughness profile of the Laver. (e) AFM image of the Laver which matches with the FE-SEM image. (f) KPFM image for surface-potential mapping confirming the positive triboelectric property of the device.





**Figure 3.3.5.** The output of the device in vertical contact separation mode with Laver-FEP, Laver-PET and Laver-Paper as the materials.

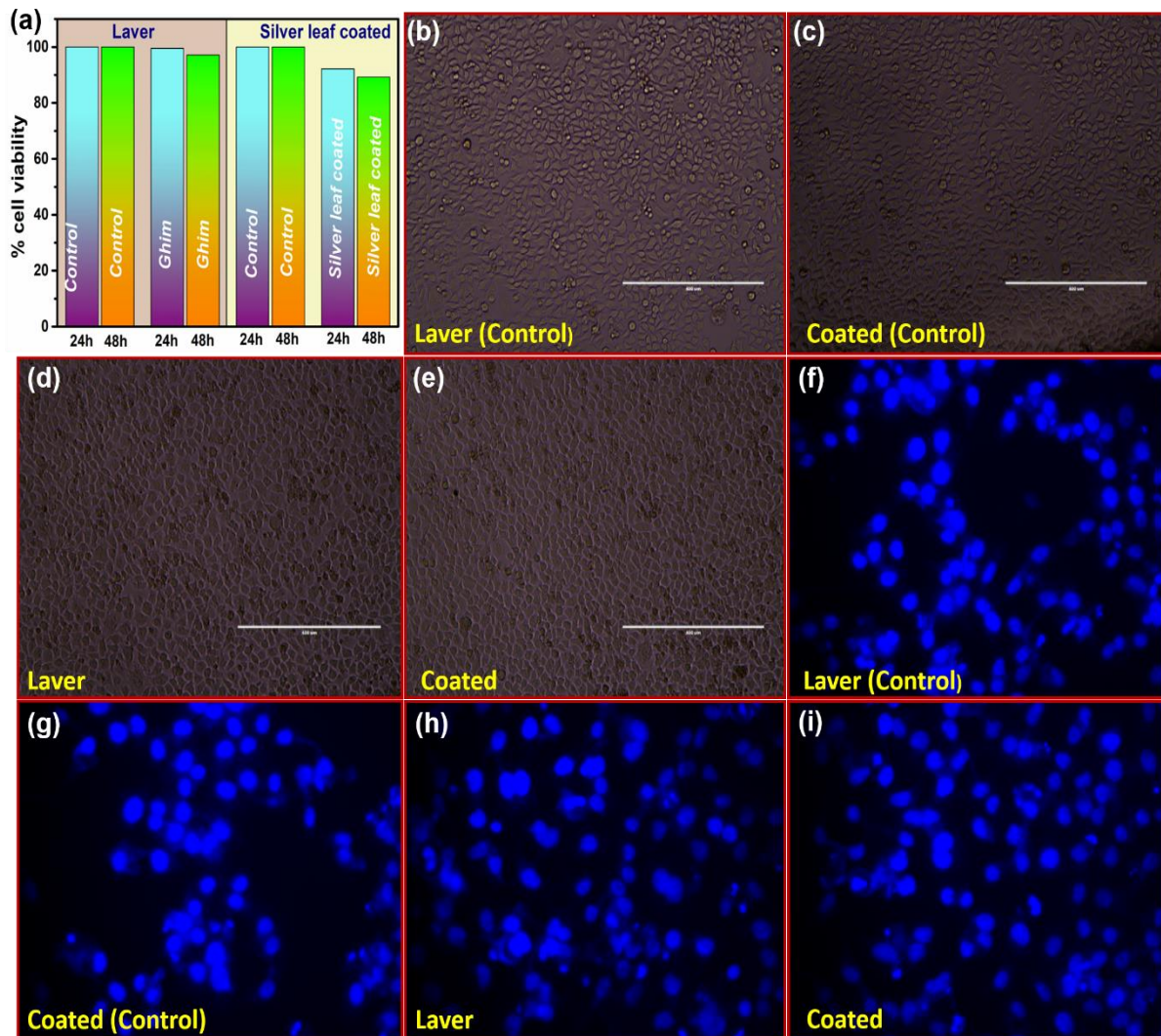
The laver feature was confirmed using a vertical contact separation device and laver-FEP, laver-PET, and laver-paper as test materials. The outputs are shown in Figure 3.3.5. The laver-paper device generated a positive peak, suggesting that paper was positive concerning the Laver. However, FEP-laver and PET-laver devices generated negative peaks, suggesting that FEP and PET were negative with respect to Laver as per the TENG mechanism [25]. The outputs of the devices indicate that Laver lies between paper and PET in terms of triboelectricity generation [25]. Moreover, Laver developed a positive surface potential after a single touch with Kapton, further confirming the positive nature of Laver (Figure 3.3.6). In addition to the KPFM image, the outputs, and the surface potential data, provides clear evidence for the surface positivity of Laver with respect to Kapton, which readily attracts Laver because the triboelectric natures of the materials are opposite.



**Figure 3.3.6.** The surface potential on Laver on hitting once with the kapton.

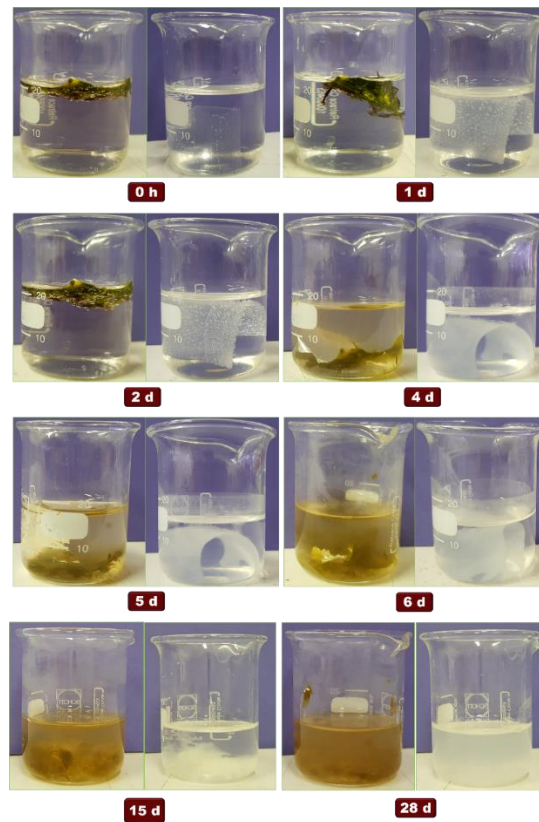
The coated, and non-coated Laver tested on HeLa cell lines to analyze the toxicity. First, mitochondrial reductase activity using MTT as the substrate was measured (Figure 3.3.7a). When cells were exposed to Laver for 48 h, viability was minimally affected and was completely unaffected after 24 h. Edible silver leaf-coated Laver reduced cell viability only slightly at 24 and 48 h. Next, cell morphology was examined under a phase-contrast microscope; morphology was unaffected by Laver (Figure 3.3.7d; the control is Figure 3.3.7b). Morphology was minimally affected by the coating (Figure 3.3.7e; the control is Figure 3.3.7c). Finally, nuclear morphological changes was examined by DAPI staining. HeLa cells were treated with Laver and coated Laver and, after 24 h, were fixed, permeabilized, and mounted with DAPI. Cells exposed to coated Laver exhibited fragmented nuclei (Figure 3.3.7i); control nuclei were round or oval (Figure 3.3.7g). Thus, the MTT assay, live-dead cell imaging, and DAPI staining suggested that coating affected cell viability only minimally. EDS indicated that the silver leaf contained aluminum. However, the final amount of aluminum used in the culture (0.001  $\mu\text{g}/\text{mL}$ ) is reported to be non-toxic and minimally effect on cell viability [26].



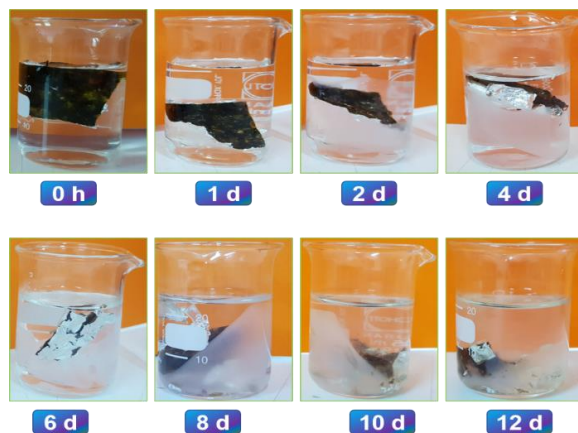


**Figure 3.3.7.** The *in vitro* studies to examine the effects of the Laver and coated Laver on the viability of HeLa cells. (a) The viability of was examined in the control and in the cells treated for 24 and 48 h by MTT assay. (b-e) The control and treated cells were examined under phase contrast microscope at 10X magnification. (f-i) The morphological changes in the cell nucleus was examined by DAPI staining under fluorescence microscope at 40X magnification.

The E-TENG is composed exclusively of edible materials; the E-TENG is bioresorbable. The untreated E-TENGs was placed in the PBS [9]. Figure 3.3.8 shows the coated Laver and the rice sheet 1 day later; the coated Laver maintains its structural integrity, but the rice sheet is swollen. The rice sheet began to dissolve after 5 days. Bulk degradation of both coated Laver and the rice sheet was evident after 15 d, and both structures became completely dissolved by 28 d [9]. Furthermore, the degradation of E-TENG is carried out in simulated gastric juice [27, 28]. There is no significant change after 1 day. The rice sheet starts separating from the Laver after 1 day. The rice sheet completely separates and swollen at day 4. After day 4, the coated Laver start degrading, as shown in Figure 3.3.9.



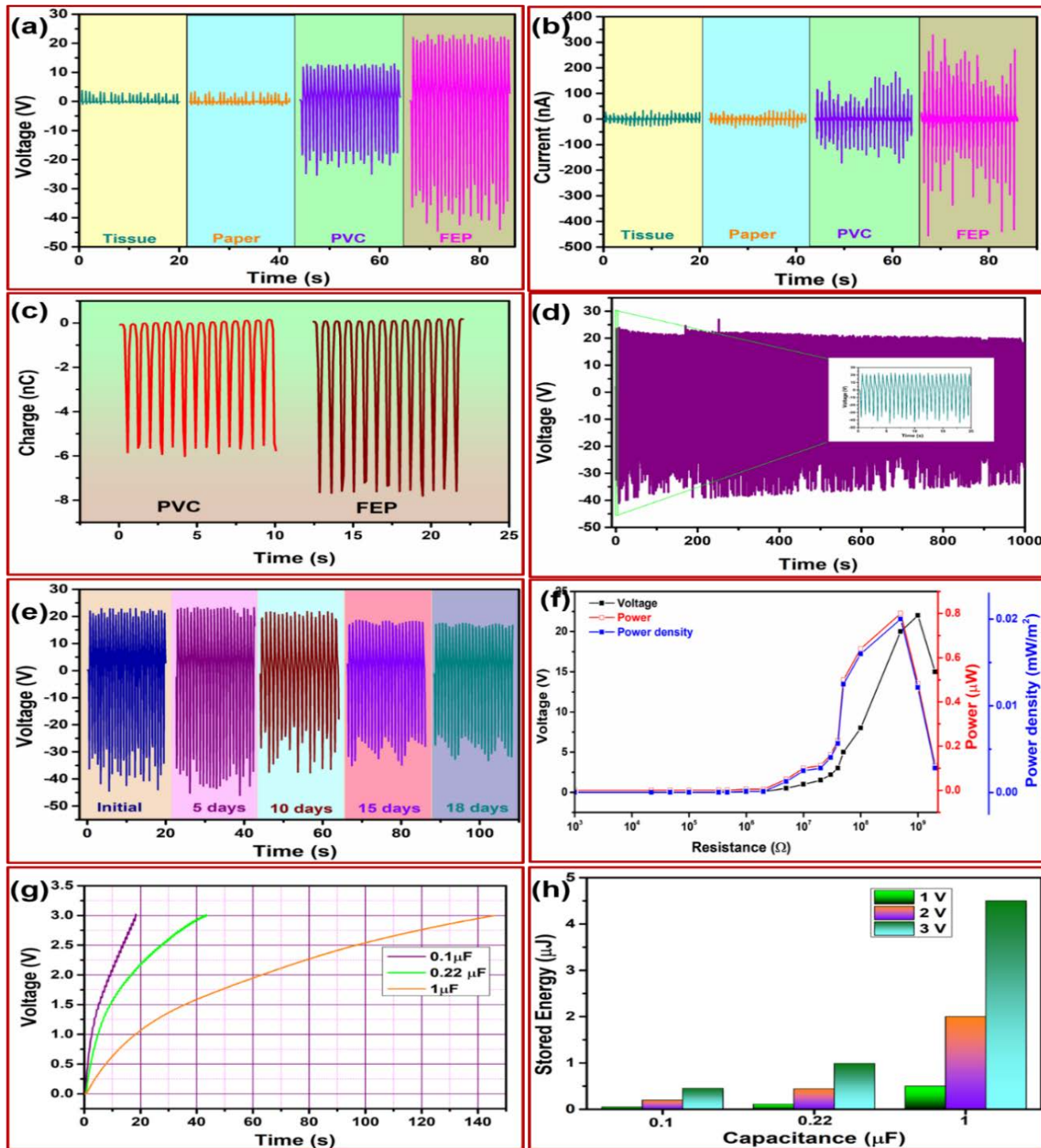
**Figure 3.3.8.** The study of the coated Laver and rice sheet in PBS buffer for 0, 1, 2, 4, 5, 6, 15 and 28 d respectively.



**Figure 3.3.9.** The bioresorbability of the E-TENG in the simulated gastric juice.

Figure 3.3.10 describes the detailed electrical performances of E-TENGs. Figure 3.3.10a and 3.3.10b show the output voltages and currents for different materials in contact with Laver. The FEP-laver E-TENG displayed the best output performance (23 V and 315 nA), attributable to the highly negative triboelectric property of FEP. The tissue paper and paper are positively triboelectric, yielding very low outputs when in contact with Laver. Both PVC and FEP afforded good outputs; their charge profiles are shown in Figure 3.3.10(c), which are in line with output performance, and the best performer is FEP. The FEP-laver E-TENG was studied further. In practice, TENGs must be stable long-term. An endurance test (1,000 cycles; Figure 3.3.10d) was performed, and then the device was tested over 18 days (Figure 3.3.10e). The output changed negligibly over 10 days, and then decreased slightly. However, the output changed negligibly from 15 to 18 days [Figure 3.3.10(e)]. Thus, the device is both practicable and edible. Figure 3.3.10(f) shows the output voltages at various resistances. The maximum power density was  $0.02 \text{ mW/m}^2$  and the peak power  $0.8 \text{ }\mu\text{W}$  at a load of  $500 \text{ M}\Omega$ . In practice, most applications require continuous and DC power. The E-TENG was used to charge various capacitors ( $0.1$ ,  $0.22$ , and  $1 \text{ }\mu\text{F}$ ). Figure 3.3.10(g) shows the charging profiles up to 3 V and the energy stored in the capacitors (Figure 3.3.10h).

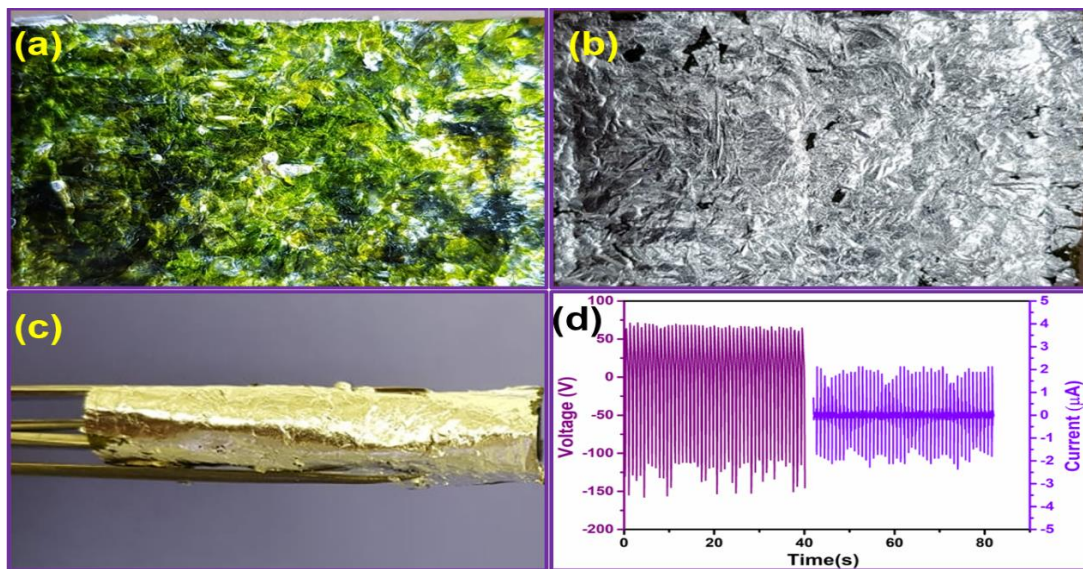




**Figure 3.3.10.** The detailed electrical performance of the E-TENG device. (a,b) The voltage and current output when different material comes in frictional contact with the device. The charge profile for the PVC and FEP giving high output. (d) The stability of the device for 1000 cycles. (e) The stability of the device for 5, 10, 15, and 18 days. There is a negligible change in the output up

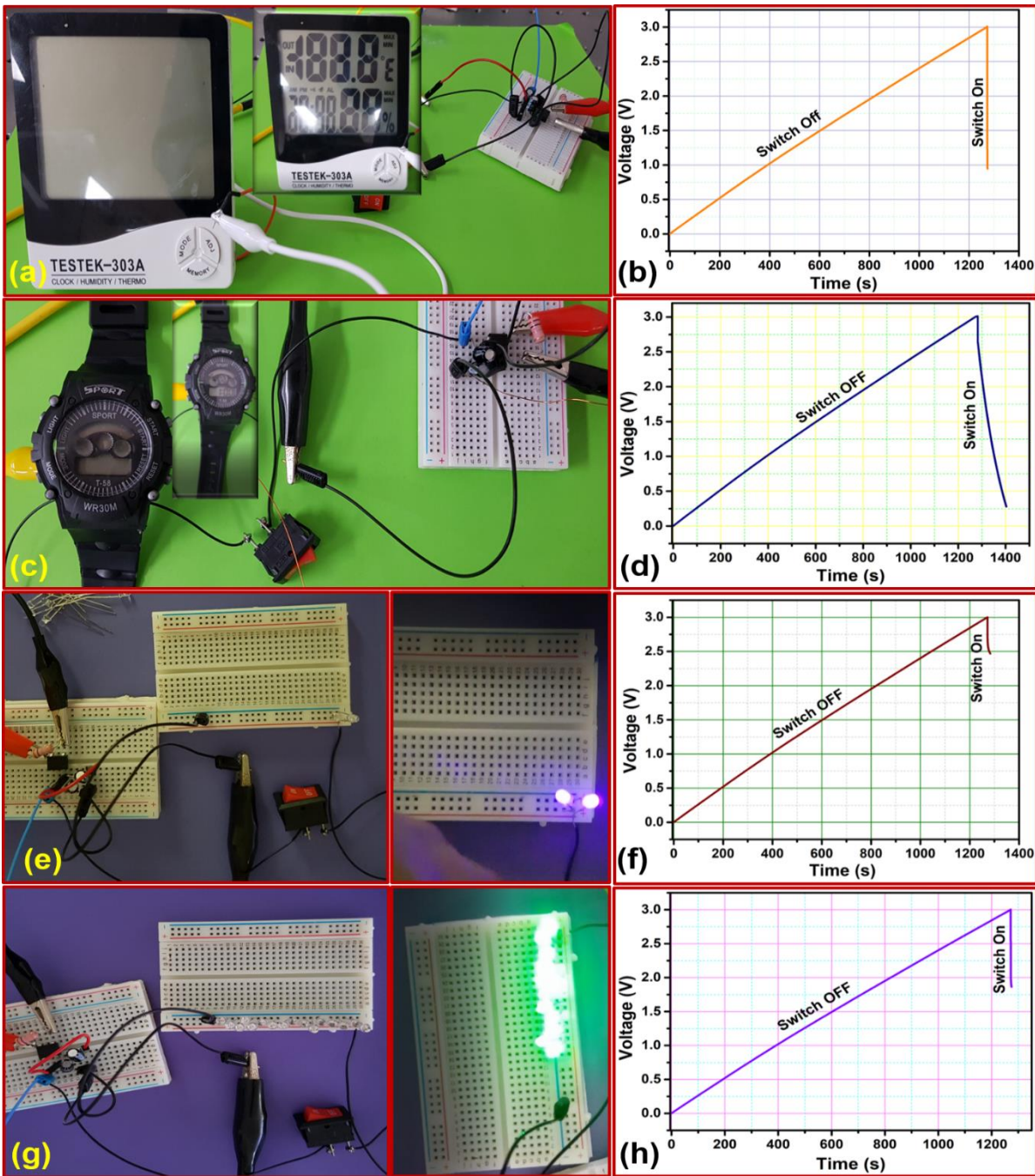
to 10 days. (f) Load matching analysis for the E-TENG across various resistances. (g) The capacitor charging for 0.1, 0.22, and 1  $\mu\text{F}$  capacitor using the E-TENG. (h) The energy stored in the capacitor corresponding to 1, 2, and 3 V charging.

Finally, we fabricated a large device (5 x 10 cm) to demonstrate that the E-TENG can charge a 50- $\mu\text{F}$  capacitor for practical applications. Figure 3.3.11 shows an image of a large coated laver sheet, and its flexibility and output. Figure 3.3.12 displays electronics powered by the 50- $\mu\text{F}$  capacitor. Figure 3.3.12a shows a commercial hygrometer and the capacitor charge/discharge profile while powering the hygrometer. Figure 3.3.12b shows a wristwatch and the capacitor charge/discharge profile; the wristwatch functions for more than 100 s. Figure 3.3.12c and 3.3.12d display lit up of UV and green LEDs and the capacitor charge/discharge profiles. Such electronics are widely used, and the E-TENG is practicable. Our edible TENG devices will benefit the environment, flora, and fauna.



**Figure 3.3.11.** The optical image of the large device a) front view, b) back view. c) The bending of the large device showing the adherence of the silver leaf. d) The voltage and current output of the device.





**Figure 3.3.12.** The powering up of various electronics using  $50\ \mu\text{F}$  capacitor for (a) commercial hygrometer, (c) wristwatch, (e) UV-LEDs, and (g) green LEDs. The capacitor charging and discharging during lit-up of electronics for (b) commercial hygrometer, (d) wristwatch, (f) UV-LEDs and (h) green LEDs.

### 3.3.4 Conclusion

We developed fully bioresorbable, lightweight edible E-TENGs using Laver as the active layer, silver leaf as the electrode, and a rice sheet as the substrate. KPFM confirmed that Laver had a positive surface potential. The MTT assay, live/dead imaging, and DAPI staining showed that the device minimally affected cells and is non-toxic. Paper, tissue paper, PVC, and FEP served as the frictional layers. An FEP-laver E-TENG exhibited the maximum output of 23 V and 315 nA. The FEP also allowed of maximal charging, in line with the high electrical outputs. The device was studied in terms of stability, capacitor charging, and load-matching. The E-TENG powered a hygrometer, wristwatch, and green and UV LEDs. The E-TENG is biodegradable, bioresorbable, and metabolizable, and will be suitable for various applications.

## References

- [1] Wang ZL. Triboelectric nanogenerators as new energy technology and self-powered sensors – Principles, problems and perspectives. *Faraday Discussions*. 2014;176:447-58.
- [2] Khandelwal G, Chandrasekhar A, Maria Joseph Raj NP, Kim S-J. Metal–Organic Framework: A Novel Material for Triboelectric Nanogenerator–Based Self-Powered Sensors and Systems. *Advanced Energy Materials*. 2019;9:1803581.
- [3] Wang ZL. Triboelectric Nanogenerators as New Energy Technology for Self-Powered Systems and as Active Mechanical and Chemical Sensors. *ACS Nano*. 2013;7:9533-57.
- [4] Jambeck JR, Geyer R, Wilcox C, Siegler TR, Perryman M, Andrady A, et al. Plastic waste inputs from land into the ocean. *Science*. 2015;347:768-71.
- [5] Khandelwal G, Chandrasekhar A, Alluri NR, Vivekananthan V, Maria Joseph Raj NP, Kim S-J. Trash to energy: A facile, robust and cheap approach for mitigating environment pollutant using household triboelectric nanogenerator. *Applied Energy*. 2018;219:338-49.
- [6] Ekvall MT, Lundqvist M, Kelpsiene E, Šileikis E, Gunnarsson SB, Cedervall T. Nanoplastics formed during the mechanical breakdown of daily-use polystyrene products. *Nanoscale Advances*. 2019;1:1055-61.
- [7] Tyree DMaC. if-youre-drinking-tap-water-youre-consuming-plastic-pollutants. if-youre-drinking-tap-water-youre-consuming-plastic-pollutants pri.org: pri.org; 2017.
- [8] Cox KD, Covernton GA, Davies HL, Dower JF, Juanes F, Dudas SE. Human Consumption of Microplastics. *Environmental Science & Technology*. 2019;53:7068-74.
- [9] Jiang W, Li H, Liu Z, Li Z, Tian J, Shi B, et al. Fully Bioabsorbable Natural-Materials-Based Triboelectric Nanogenerators. *Advanced Materials*. 2018;30:1801895.



- [10] Pan R, Xuan W, Chen J, Dong S, Jin H, Wang X, et al. Fully biodegradable triboelectric nanogenerators based on electrospun polylactic acid and nanostructured gelatin films. *Nano Energy*. 2018;45:193-202.
- [11] Chi Y, Xia K, Zhu Z, Fu J, Zhang H, Du C, et al. Rice paper-based biodegradable triboelectric nanogenerator. *Microelectronic Engineering*. 2019;216:111059.
- [12] Bonacchini GE, Bossio C, Greco F, Mattoli V, Kim Y-H, Lanzani G, et al. Tattoo-Paper Transfer as a Versatile Platform for All-Printed Organic Edible Electronics. *Advanced Materials*. 2018;30:1706091.
- [13] Wang X, Xu W, Chatterjee P, Lv C, Popovich J, Song Z, et al. Food-Materials-Based Edible Supercapacitors. *Advanced Materials Technologies*. 2016;1:1600059.
- [14] Tao H, Brenckle MA, Yang M, Zhang J, Liu M, Siebert SM, et al. Silk-Based Conformal, Adhesive, Edible Food Sensors. *Advanced Materials*. 2012;24:1067-72.
- [15] Zhao YR, Li HM, Zhu M, Li J, Ma T, Huo Q, et al. Non-Benzoquinone Geldanamycin Analog, WK-88-1, Induces Apoptosis in Human Breast Cancer Cell Lines. *Journal of microbiology and biotechnology*. 2018;28:542-50.
- [16] Awasthee N, Rai V, Verma SS, Sajin Francis K, Nair MS, Gupta SC. Anti-cancer activities of Bharangin against breast cancer: Evidence for the role of NF- $\kappa$ B and lncRNAs. *Biochimica et Biophysica Acta (BBA) - General Subjects*. 2018;1862:2738-49.
- [17] Qin S, Zhang Z, Li J, Zang L. FRZB knockdown upregulates beta-catenin activity and enhances cell aggressiveness in gastric cancer. *Oncology reports*. 2014;31:2351-7.
- [18] Mishra S, Verma SS, Rai V, Awasthee N, Arya JS, Maiti KK, et al. Curcuma raktakanda Induces Apoptosis and Suppresses Migration in Cancer Cells: Role of Reactive Oxygen Species. *Biomolecules*. 2019;9:159.

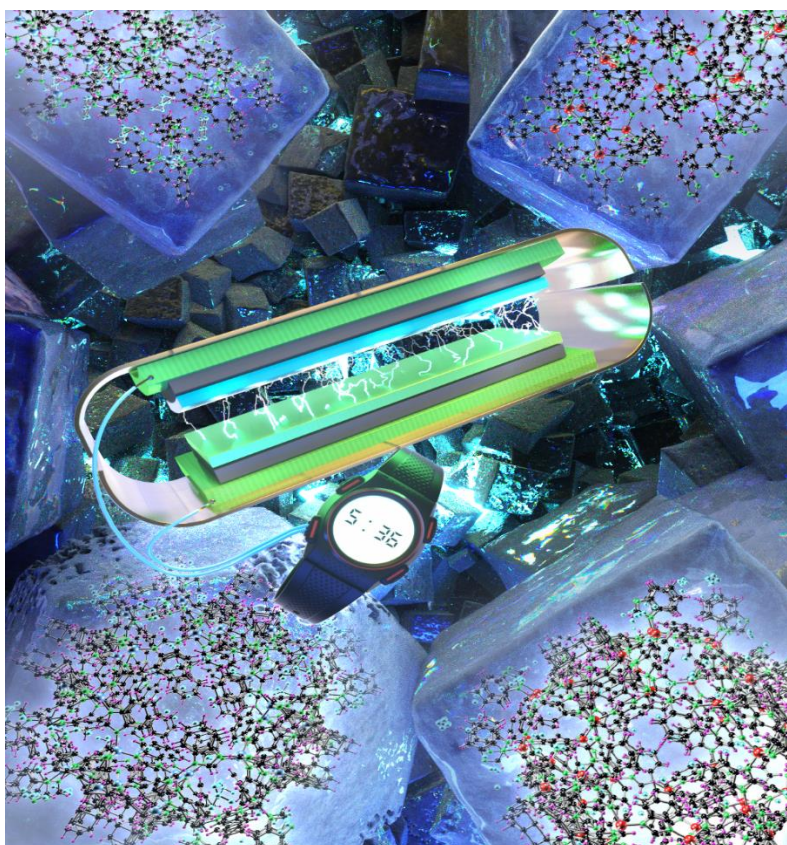
- [19] Ghorbani MM, Taherian R. 12 - Methods of Measuring Electrical Properties of Material\*\*Hereby from Keithley Co. and Dr. Michael B. Heaney is appreciated due to valuable content used in this chapter. In: Taherian R, Kausar A, editors. Electrical Conductivity in Polymer-Based Composites: William Andrew Publishing; 2019. p. 365-94.
- [20] Chen SW, Cao X, Wang N, Ma L, Zhu HR, Willander M, et al. An Ultrathin Flexible Single-Electrode Triboelectric-Nanogenerator for Mechanical Energy Harvesting and Instantaneous Force Sensing. *Advanced Energy Materials*. 2017;7:1601255.
- [21] Guo H, Li T, Cao X, Xiong J, Jie Y, Willander M, et al. Self-Sterilized Flexible Single-Electrode Triboelectric Nanogenerator for Energy Harvesting and Dynamic Force Sensing. *ACS Nano*. 2017;11:856-64.
- [22] Cheng L, Xi Y, Hu C, Yue X, Wang G. Ag Nanowires Single Electrode Triboelectric Nanogenerator and Its Angle Sensors. *Energy Harvesting and Systems*2016. p. 91.
- [23] Lee S, Lee Y, Kim D, Yang Y, Lin L, Lin Z-H, et al. Triboelectric nanogenerator for harvesting pendulum oscillation energy. *Nano Energy*. 2013;2:1113-20.
- [24] Jeong CK, Baek KM, Niu S, Nam TW, Hur YH, Park DY, et al. Topographically-Designed Triboelectric Nanogenerator via Block Copolymer Self-Assembly. *Nano Letters*. 2014;14:7031-8.
- [25] Seol M, Kim S, Cho Y, Byun K-E, Kim H, Kim J, et al. Triboelectric Series of 2D Layered Materials. *Advanced Materials*. 2018;30:1801210.
- [26] Bowman PD, Wang X, Meledeo MA, Dubick MA, Kheirabadi BS. Toxicity of Aluminum Silicates Used in Hemostatic Dressings Toward Human Umbilical Veins Endothelial Cells, HeLa Cells, and RAW267.4 Mouse Macrophages. *Journal of Trauma and Acute Care Surgery*. 2011;71:727-32.

- [27] Malinauskytė E, Ramanauskaitė J, Leskauskaitė D, Devold TG, Schüller RB, Vegarud GE. Effect of human and simulated gastric juices on the digestion of whey proteins and carboxymethylcellulose-stabilised O/W emulsions. *Food Chemistry*. 2014;165:104-12.
- [28] Herman RA, Korjagin VA, Schafer BW. Quantitative measurement of protein digestion in simulated gastric fluid. *Regulatory Toxicology and Pharmacology*. 2005;41:175-84.

## CHAPTER IV

### Zeolitic Imidazole Framework: A Metal-Organic Framework Subfamily Members for Triboelectric Nanogenerator

#### Graphical Overview



## Highlights

- Zeolitic imidazole framework (ZIF) subfamily members ZIF-7, ZIF-9, ZIF-11 and ZIF-12 are analyzed for their triboelectric behavior.
- The TENG based on the ZIF subfamily materials with two different opposite layers are studied in detail.
- The surface potential analysis confirms the positive behavior of the members with regard to Kapton.
- The material follows an output trend of  $V_{\text{ZIF-7}} > V_{\text{ZIF-12}} > V_{\text{ZIF-9}} \sim V_{\text{ZIF-11}}$ .
- The ZIF-7 TENG generates the highest output of 60 V and 1.1  $\mu\text{A}$  in vertical contact-separation mode.
- Low-power electronics are successfully driving with the capacitor charged by the output of ZIF-7 TENG.

## 4.1 Introduction

Metal-organic framework (MOF) are crystalline materials comprises of a 3D network formed by metal ion and an organic molecule known as a ligand [1]. MOFs can be used for broad range of applications (energy storage, energy conversion, gas storage, catalysis, gas separation, filters, self-charging power cells, self-powered sensors etc.) ascribed to its appealing properties [1-10]. The large surface area, porosity, high crystallinity and are easy to functionalize among few of the advantages of MOFs. MOF subfamily Zeolitic imidazolate frameworks (ZIFs) are 3-D assemblies formed by metal ions (such as Zn and Co) linked to the nitrogen atom of the organic ligand to form a porous structure [2]. The tremendous increase in the fame for ZIF subfamily is attributed to their unique thermal and chemical stability. The bond angle between metal-ligand-metal matches with that of Si-O-Si linkage in zeolites resulting in similar crystal structure [11]. Moreover, ZIFs are reported in diverse topologies like SOD, RHO, LTA, MER, ANA, etc. by employing different linkers [2]. ZIFs with same metal ion and linker can subsist in different topologies; ZIF-7 (SOD) and ZIF-11 (RHO) are one such excellent example.

The TENG functions by the coupling effect of contact electrification and electrostatic induction when two different triboelectric materials come in contact with each other [12-14]. The TENG is widely reported to utilize the biomechanical, wind, and ocean wave energy [15, 16] with various applications like sensing big data [17], biological and chemical sensors [3, 15], self-charging [18] and therapeutics etc. The TENG is in growing demand for the wide range of self-powered applications due to their easy fabrication, material choice, high power, can generate direct current by different approaches [12, 14]. The triboelectric series mainly consists of polymers and few metals, polymers being dominant for the fabrication of TENG [13]. The polymers are challenging to functionalize and modify which generates a great need to explore multifunctional

materials. The chemical and biological sensor demands high selectivity which is troublesome to achieve using the current materials highlighted in the triboelectric series [3, 13, 15]. ZIF is one such class of materials which has excellent chemical and thermal stability, easy to synthesize, high surface area in combination with tunable functionalities. These MOFs are the potential candidates to expand the triboelectric series as well as application in the domain of self-powered systems, sensors, wearable electronics etc. ascribed to their tunable properties.

In this work, the ZIF subfamily members ZIF-7, ZIF-9, ZIF-11, and ZIF-12 are probe as a potential triboelectric layer in the TENG device. ZIF-7 forms a sodalite (SOD) topology, where divalent zinc cations are linked by benzimidazolate (bIm) anions [2, 11]. ZIF-9 also forms SOD topology where bIm is the linker, and cobalt is the metal ion. The 3D structure of ZIF-11 consists of RHO topology, where each zinc ions are coordinated to four nitrogen atoms of the linker (bIm) [2]. Similar to ZIF-11, ZIF-12 also possess RHO topology with cobalt ions coordinated to bIm [2]. Structural (X-ray diffraction; XRD and Fourier transform infrared spectroscopy; FT-IR) and morphological analysis (field emission scanning electron microscopy; FE-SEM) confirmed the formation of the ZIF family members. The surface roughness analysis explored the average roughness ( $R_a$ ) value, which is critical for TENG devices. The polyimide and ethyl cellulose are selected as opposite layer to ZIFs in the TENG device due to their negative and extreme positive position in the triboelectric series. The surface potential measurement and the detailed electrical characterization confirms the positive behavior of ZIF family members concerning polyimide (Kapton). The ZIF-7/Kapton exhibits the highest output following the trend  $V_{ZIF-7} > V_{ZIF-12} > V_{ZIF-9} \sim V_{ZIF-11}$ . The fabricated device was characterized for its stability, load-matching analysis, and capacitor charging. Finally, the device was used to power various low rating electronics like wrist



watch, calculator, hygro-thermometer, ultraviolet (U.V), and infrared (IR) light-emitting diodes (LEDs).

## 4.2 Experimental

### 4.2.1 Synthesis of ZIFs

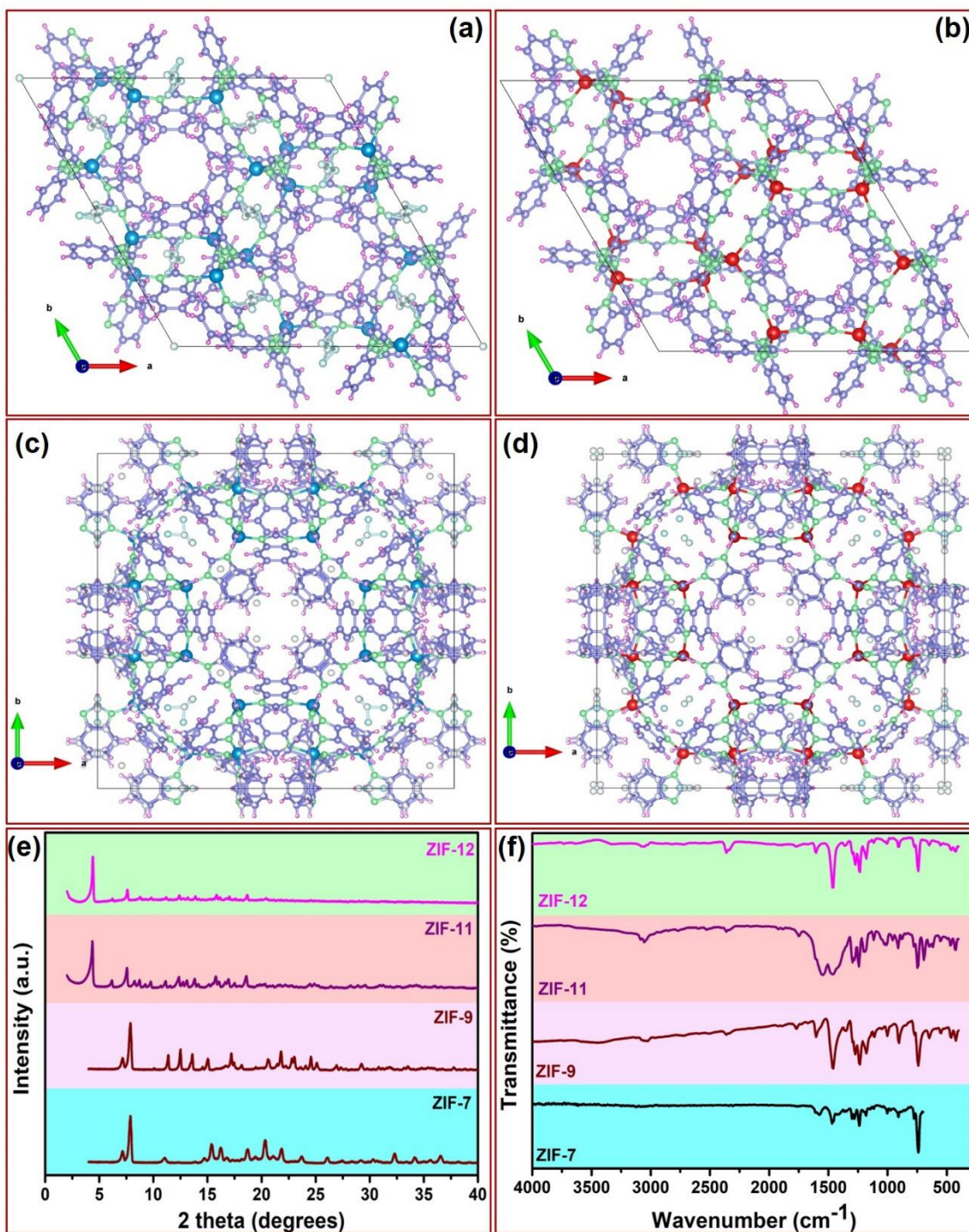
The ZIFs are synthesized by a similar method reported in the literature [2]. Briefly, for ZIF-7, 1mmol of bIm was dissolved in 6.8g of ethanol, followed by the 1mmol ammonium hydroxide addition at room temperature. Then, 0.5mmol of zinc acetate dihydrate was added and stirred to allow the complete crystallization for 3 h at room temperature. The product was washed and collected by centrifugation. The synthesis procedure for ZIF-9 is same as ZIF-7; only zinc acetate dihydrate was replaced by same molar solution of cobalt acetate tetrahydrate. In a typical process for the synthesis of ZIF-11, 1 mmol of bIm was dissolved in 6.8 g of ethanol, followed by the addition of 50 mmol toluene and 1 mmol of ammonia solution at room temperature. After dissolution, 0.5 mmol of zinc acetate dihydrate was added and stirred at room temperature for 3 h. The product was collected by centrifugation and washed using ethanol. The sample was first dried at room temperature followed by drying at 200 °C for complete removal of toluene. For ZIF-12, 1mmol of bIm was dissolved in 4.8 g of methanol, followed by adding 50 mmol of toluene and 1 mmol of ammonium hydroxide solution. After complete dissolution, 0.5 mmol of cobalt acetate tetrahydrate was added and stirred at room temperature for 3 h. The product was washed and collected by centrifugation. The product was dried at room temperature and heated at 200 °C for complete removal of toluene.

### 4.2.2 Fabrication of ZIF-TENG

The ZIF-TENG was fabricated using ZIFs and Kapton/ethyl cellulose as triboelectric layers in vertical contact-separation mode. The Al tape with conductive adhesive and PET was used as electrode and substrate, respectively. The different ZIFs are covered uniformly and fixed on the conductive adhesive side of Al tape followed by the removal of excess powder using an air gun [10]. The Kapton layer was prepared directly by attaching Kapton sheet on Al tape. The ethyl cellulose (10 wt.% in 1:4 ethanol: toluene) layer was made using spin coating on Al. Finally, a copper wire was attached by silver paste. Combining the positive and negative layers, the ZIF-TENG was obtained. The active contact area of the ZIF-TENG is  $2.5 * 2.5 \text{ cm}^2$ .

### 4.3 Results and Discussions

Figure 4.1a shows the structure of the ZIF-7. ZIF-7 forms SOD topology with divalent  $\text{Zn}^{+2}$  cations linked by bIm [11]. ZIF-9 also forms SOD topology consists of  $\text{CoN}_4$  tetrahedral units with hexagonal symmetry (Figure 4.1b). In ZIF-9, two cobalt ions are bridged by each bIm linker [19]. Figure 4.1c shows an extended 3D RHO network of ZIF-11, composed of 48 zinc ions in a unit cell. In the structure, each  $\text{Zn}^{+2}$  ion is coordinated tetrahedrally to four N atoms of bIm linker. ZIF-11 possess larger cages compared to ZIF-7 [2]. RHO type ZIF-12 is a cubic structure consist of cobalt as metal ion and bIm as a linker as shown in Figure 4.1d [2]. The ZIF family members ZIF-7, ZIF-9, ZIF-11, and ZIF-12, are synthesized at room temperature as explained in the experimental section [2]. Figure 4.1e shows the X-ray diffraction (XRD) pattern of the synthesized ZIFs which matches well with the reported literature [20]. The peak position and peak indices are shown in Table S1 [20-22].



**Figure 4.1.** Crystal structure of a) ZIF-7, b) ZIF-9, c) ZIF-11 and d) ZIF-12 (.cif file was downloaded from The Cambridge crystallography data centre, CCDC). E) XRD spectra of ZIFs. F) FT-IR spectra of ZIFs.

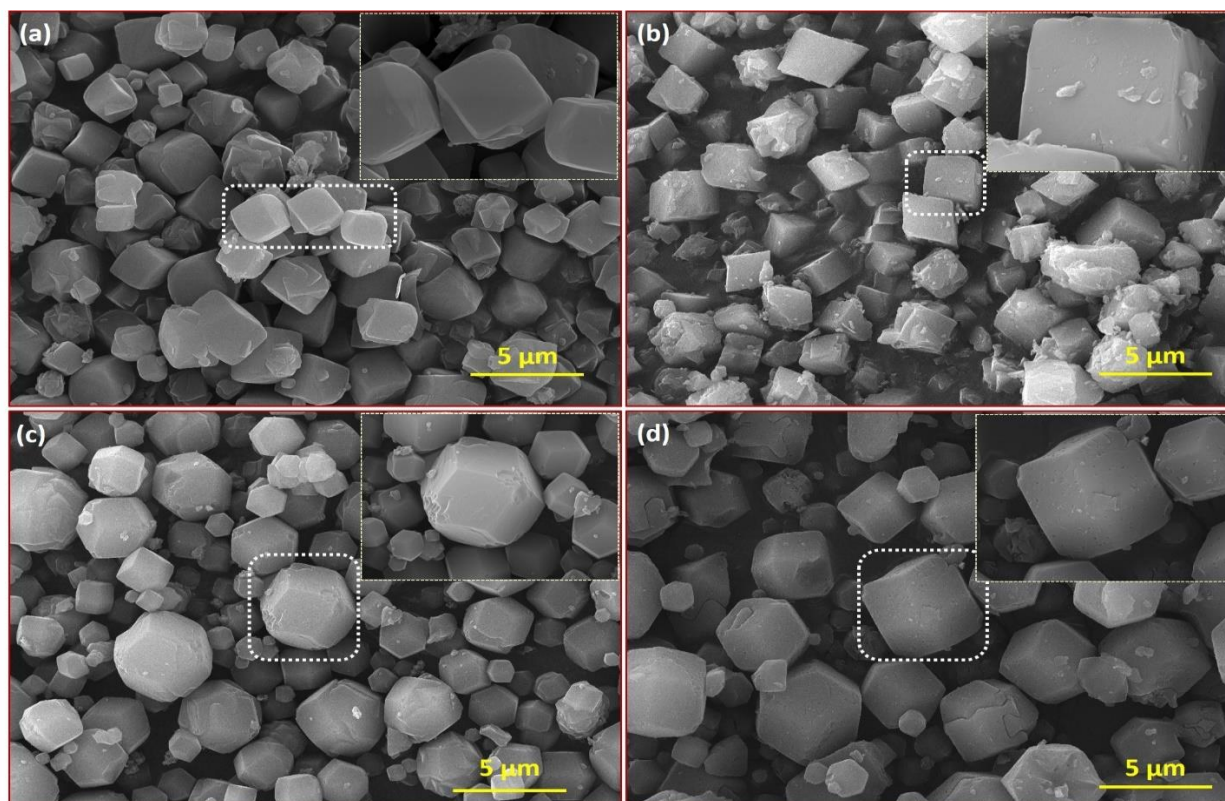
**Table 4.1.** The XRD peak position and indices for ZIF-7, ZIF-9, ZIF-11, and ZIF-12.

<b>ZIF-7</b>		<b>ZIF-9</b>	
<b>XRD Peak</b>	<b>Indices (hkl)</b>	<b>XRD Peak</b>	<b>Indices (hkl)</b>
7.14	-111	7.2	101
7.8	110	7.8	2-10
15.42	220	10.3	110
16.25	-132	12.6	111
18.67	113		
19.53	312		
21.08	042		
21.75	-333		
32.1	-663		
<b>ZIF-11</b>		<b>ZIF-12</b>	
<b>XRD Peak</b>	<b>Indices (hkl)</b>	<b>XRD Peak</b>	<b>Indices (hkl)</b>
4.3	011	4.3	011
6.16	002	6.11	002
7.52	112	7.5	112
8.7	022	8.7	022
9.72	013	9.8	013
11.09	023	15.8	015
12.31	004	18.6	006
12.68	223		
13.08	033		
13.76	024		
15.75	015		
17.45	044		
18.51	006		

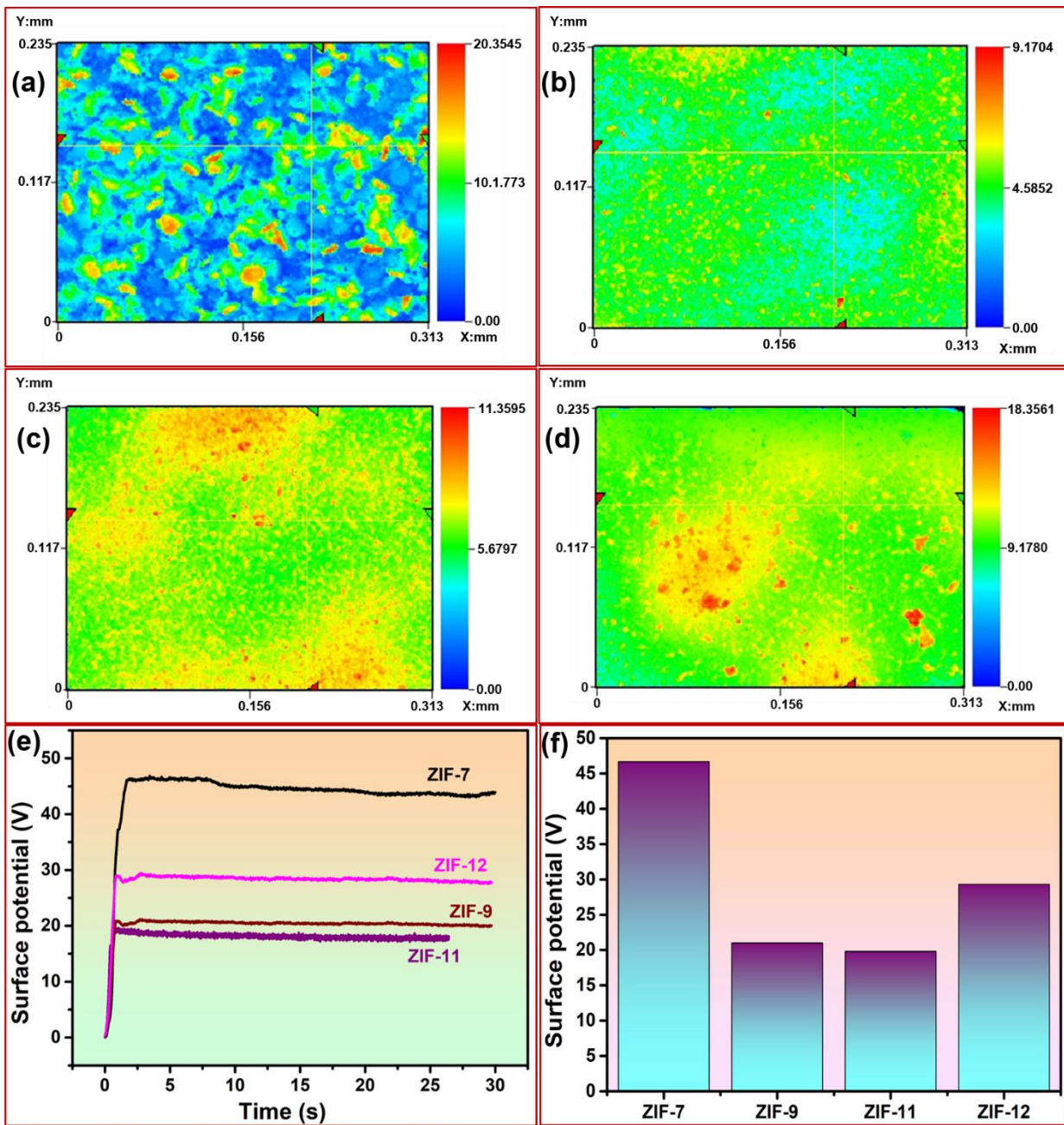
Figure 4.1f shows the FT-IR spectra of the synthesized ZIFs, which is in accord with the literature. The peaks at 1464 and 747  $\text{cm}^{-1}$  for ZIF-7 are associated with C=C and C-H bonds,



resulting from the benzene group of bIm [23]. In the case of ZIF-9, the band at  $1607\text{ cm}^{-1}$  is attributed to the C=N stretching mode, while band in the region  $400\text{-}650\text{ cm}^{-1}$  are assigned to the Co-N bonds. The ZIF-9 also exhibits a broad band at  $3432\text{ cm}^{-1}$  ascribed to the hydroxyl group of the absorbed water [19]. For ZIF-11, peak at  $426\text{ cm}^{-1}$  is assigned to Zn-N, a coordination covalent bond. The band in the range of  $600\text{-}1500\text{ cm}^{-1}$  is due to the stretching and bending in benzimidazole ring [24]. The characteristic absorption band at  $3070$  and  $3027\text{ cm}^{-1}$  (weak peak) in ZIF-12 crystal is assigned to =C-H stretching of aromatics. The band at  $1606$  and  $1460\text{ cm}^{-1}$  arises due to C-C stretching in the aromatic ring while band at  $426\text{ cm}^{-1}$  attributed to Co-N bonding [21]. Figure 4.2a-d shows the surface morphology analysis of ZIFs using FE-SEM with inset showing the high magnification image.



**Figure 4.2.** The FE-SEM images of a) ZIF-7, b) ZIF-9, c) ZIF-11, and d) ZIF-12 with inset showing high magnification image.



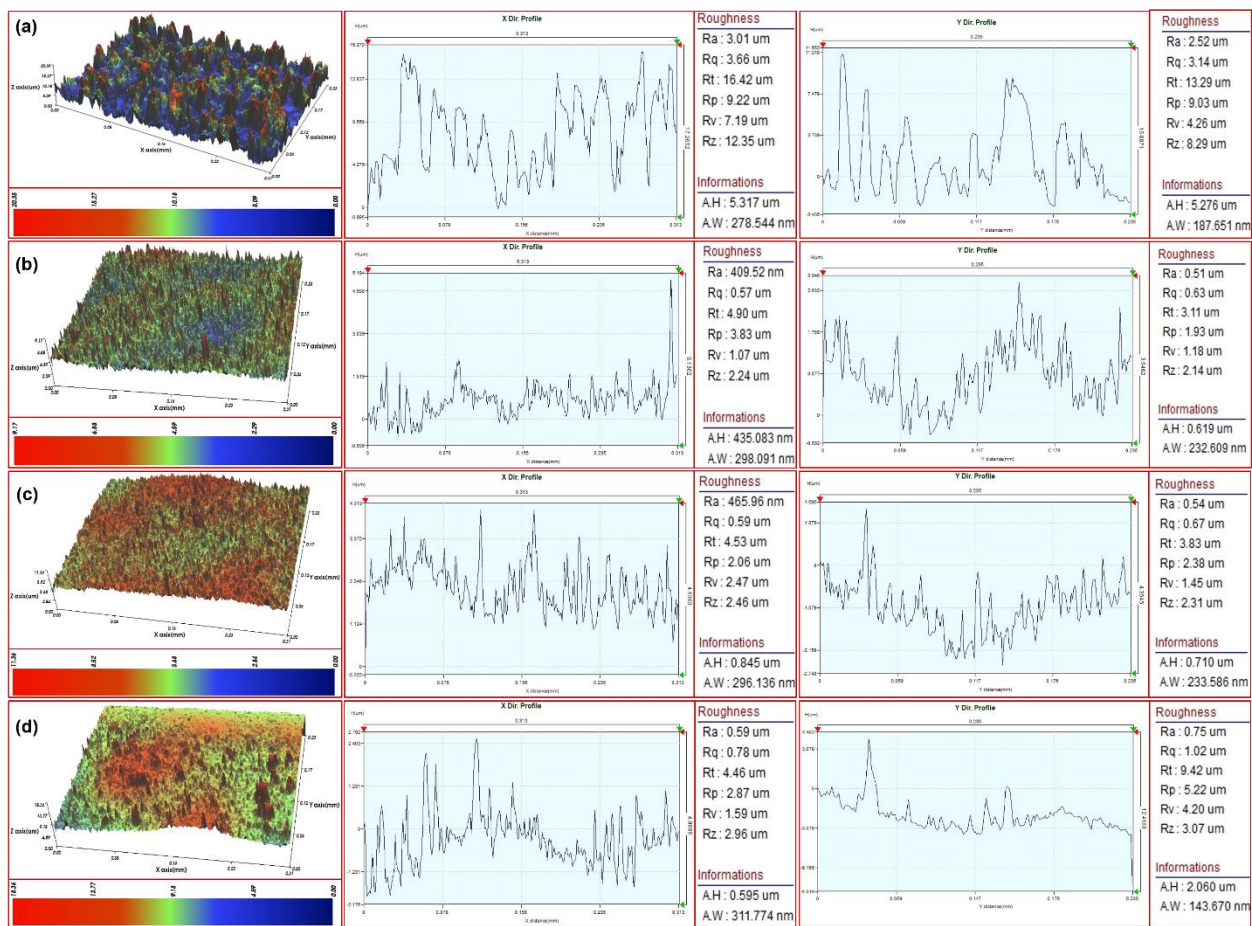
**Figure 4.3.** The 2D surface profile image for a) ZIF-7, b) ZIF-9, c) ZIF-11 and d) ZIF-12. E) temporal surface potential of the ZIFs obtained after 50 contacts with Kapton film. F) The bar plot is summarizing the surface potential profile of the ZIFs.

Surface roughness is a crucial factor for the performance of the TENG. The average surface roughness ( $R_a$ ) is well reported to alter the output of the TENG [25, 26]. The output of TENG

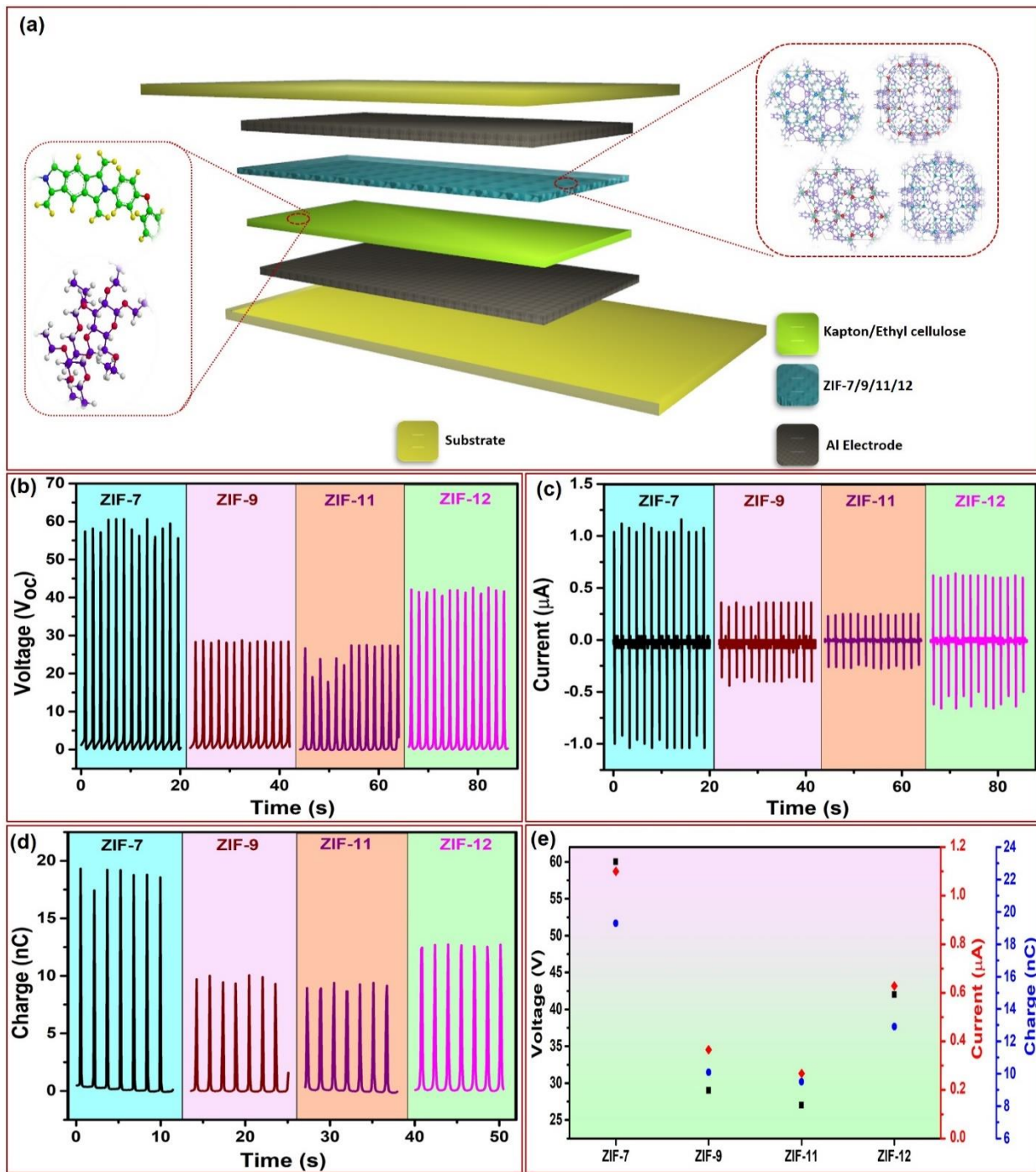
increases with the increase in  $R_a$  value up to a particular level as it brings more area for optimal contact between the materials, thus generating large amount of charge [3, 25-27]. Figure 4.3a-d shows 2D surface profile of ZIF-7, ZIF-9, ZIF-11, and ZIF-12 respectively. Moreover, Figure 4.4 shows 3D profile of the ZIFs. The  $R_a$  in the x-direction line profile corresponding to crosshair marking in 2D images is 3.01, 0.41, 0.46, and 0.59  $\mu\text{m}$  for ZIF-7, ZIF-9, ZIF-11, and ZIF-12 respectively. The  $R_a$  in y-direction line profile are 2.52, 0.51, 0.54 and 0.75  $\mu\text{m}$  for ZIF-7, ZIF-9, ZIF-11 and ZIF-12 respectively. The  $R_a$  parameter is superior for ZIF-7 compared to other ZIFs. Figure 4.3e shows the surface potential ( $\phi_s$ ) developed on ZIFs after 50 contacts with Kapton that is used as negative layer [28]. The developed surface potential is higher for the ZIF-7, and all the ZIFs exhibit positive surface potential in reference to Kapton. Figure 4.3f depicts the bar graph for the developed surface potential on the ZIFs.

Figure 4.5a illustrates the 3D architecture of the fabricated ZIF-TENG, designed in vertical contact-separation mode with Kapton and ZIF family members as the negative and positive material, respectively. The aluminum and polyethylene terephthalate (PET) is used as electrode and substrate respectively.





**Figure 4.4.** The x and y-direction line roughness profile for a) ZIF-7, b) ZIF-9, c) ZIF-11, and d) ZIF-12.

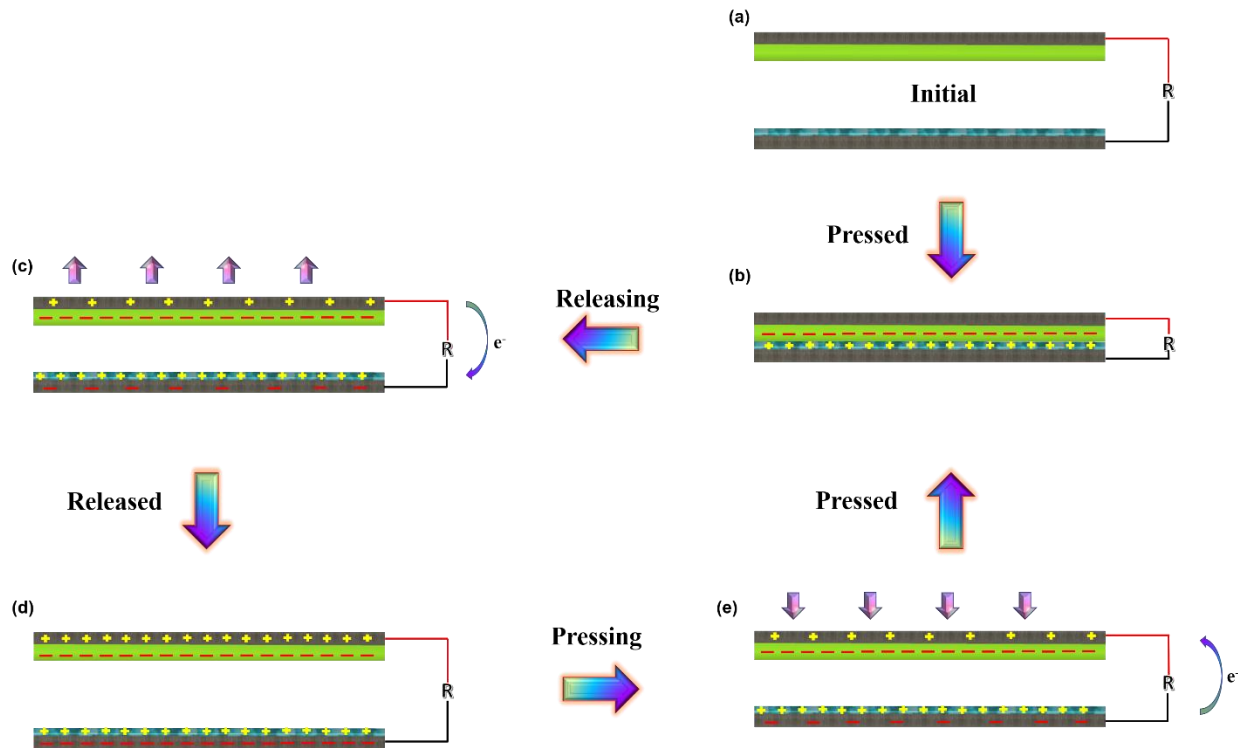


**Figure 4.5.** a) 3D layer view depiction of ZIF-TENG (inset showing the molecular structure of the materials). b-c) The voltage versus time and current versus time graph for different ZIF-TENG, respectively. d) Charge profile of the different ZIF-TENG devices. e) The summarized results for voltage, current, and charge generated by various ZIF-TENG.

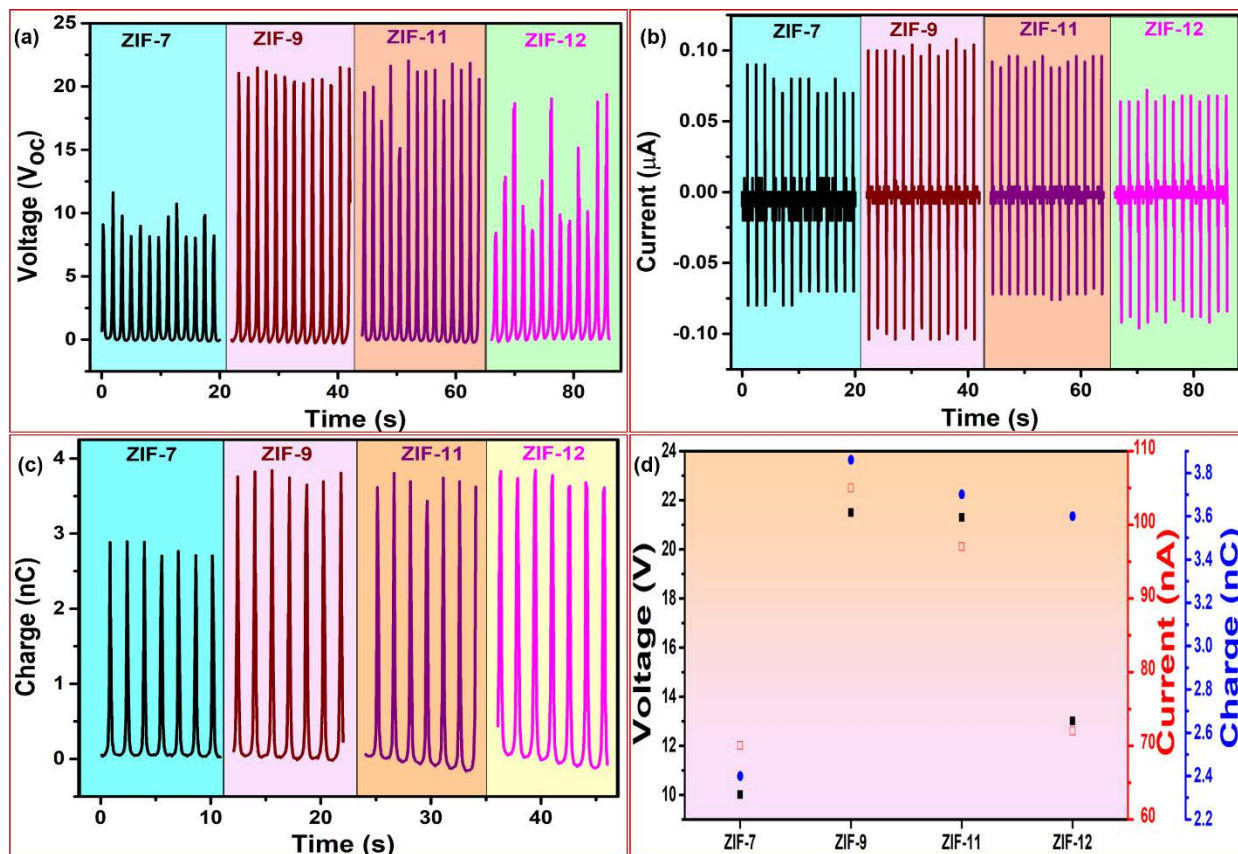
The coupling effect of electrostatic induction and contact electrification is the underlying working mechanism for the TENG [12, 13]. Figure 4.6 illustrates the working mechanism of ZIF-TENG with Kapton and ZIFs as interacting layers. Figure 4.6a shows the initial state of the device, and in the absence of force there is no charge generation on the layers resulting in zero potential difference. Figure 4.6b shows fully pressed state; the two-layer comes in full contact and generates equal opposite charges. The electron transfers from ZIF to the Kapton ascribed to its positive triboelectric behavior, thus leaving negative charge on the Kapton and positive charge on the ZIF (Figure 4.6b). Once the external force is abolishing (Figure 4.6c), the ZIF-TENG tends to regain its original shape, resulting in the generation of the electrical potential difference. The potential difference propels the flow of electrons from the Kapton side top electrode to the bottom electrode; generating the first half cycle of the output. The ZIF-TENG reaches a full released state, the condition with a maximum potential difference (Figure 4.6d). On applying the force, the ZIF-TENG is pressing, thus creating the reverse flow of electrons. The reverse flow generates the other half cycle of the output (Figure 4.6e). When two layers come in full contact i.e. pressed state, the charges are neutralized thus reaching an equilibrium state (Figure 4.6b). The process is then repeating in the presence/absence of the force-generating the output of the ZIF-TENG.

Figure 4.5b-c shows the output voltage and current for the ZIFs as one layer and Kapton as an opposite layer. The ZIF-7 TENG exhibits the highest open-circuit voltage of 60 V and a current of  $\sim 1.1 \mu\text{A}$ . The high surface roughness and surface potential of ZIF-7 reflecting its superior performance (Figure 4.4a and 4.3e) [3, 28]. Figure 4.5d shows the charge for the four ZIFs which corroborates with the trend of current output (Figure 4.5c). The ZIF-TENG follows an output performance trend of  $\text{ZIF-7} > \text{ZIF-12} > \text{ZIF-9} \sim \text{ZIF-11}$ . Figure 4.5e summarized the voltage,

current and charge behavior of ZIF-TENG. Furthermore, the behavior of ZIFs was also confirmed by fabricating the devices with ethyl cellulose as opposite layer. Figure 4.7 shows the output performance of ZIF-TENG with ethyl cellulose as opposite layer. The output follows a trend of ZIF-9 ~ ZIF-11 > ZIF-12 > ZIF-7 which supports the data shown in Figure 4.5b-d. The Kapton and ethyl cellulose are selected as opposite layers to ZIFs due to their negative and extreme positive position in the triboelectric series making them an ideal candidate to test the new materials. The further analysis was carried out using Kapton as opposite layer otherwise mentioned.



**Figure 4.6.** The schematic representation of the ZIF-TENG working mechanism in contact-separation mode with different stages viz. pressed, releasing, released, and pressing.

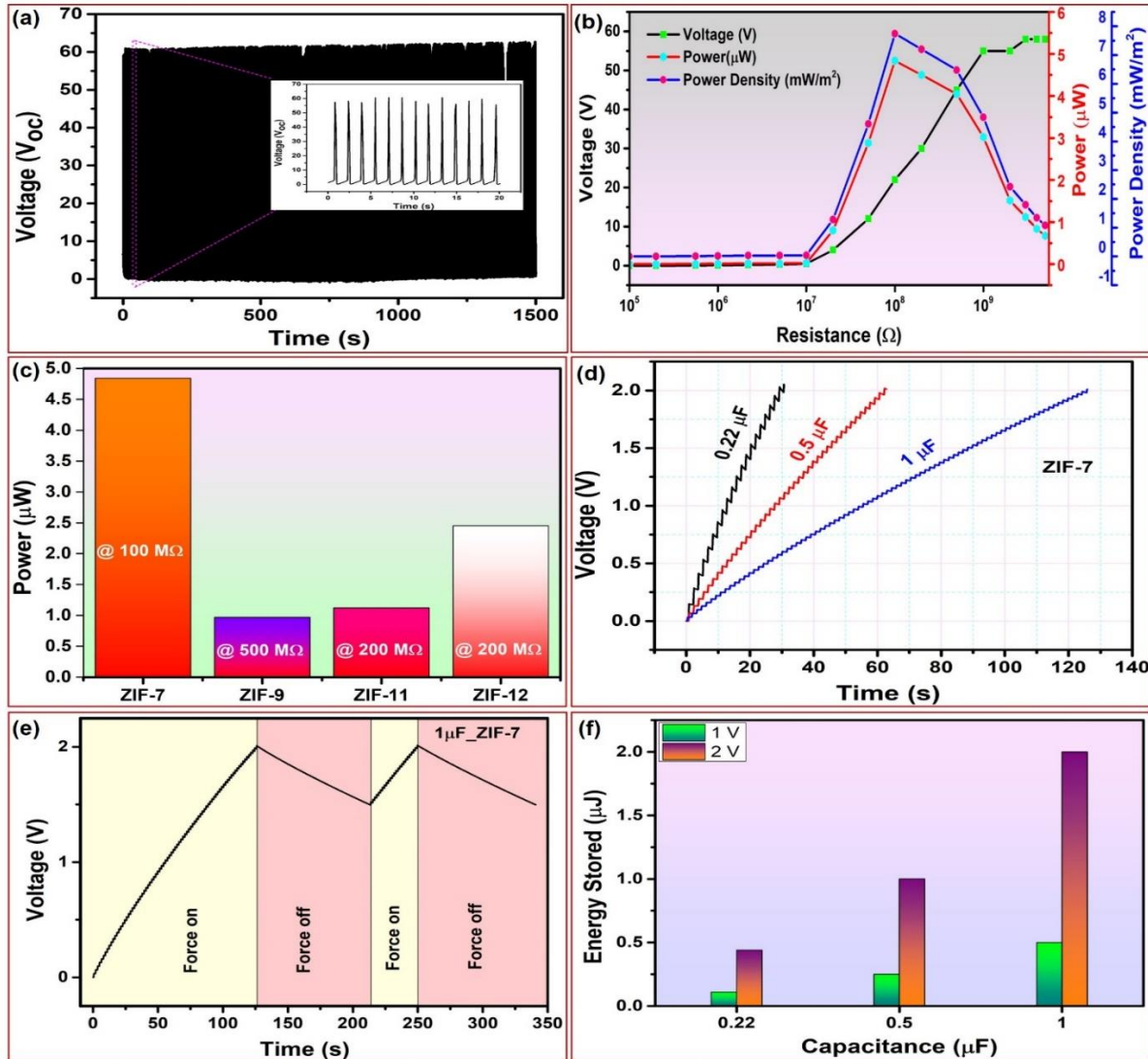


**Figure 4.7.** The detailed electrical performance of ZIFs TENG with ethyl cellulose as the opposite layer. a-b) The open-circuit voltage and current for different ZIF-TENG devices. c) The charge profile for the four different ZIF-TENG devices. d) The summarized result for the voltage, current, and charge generated by different ZIF-TENG.

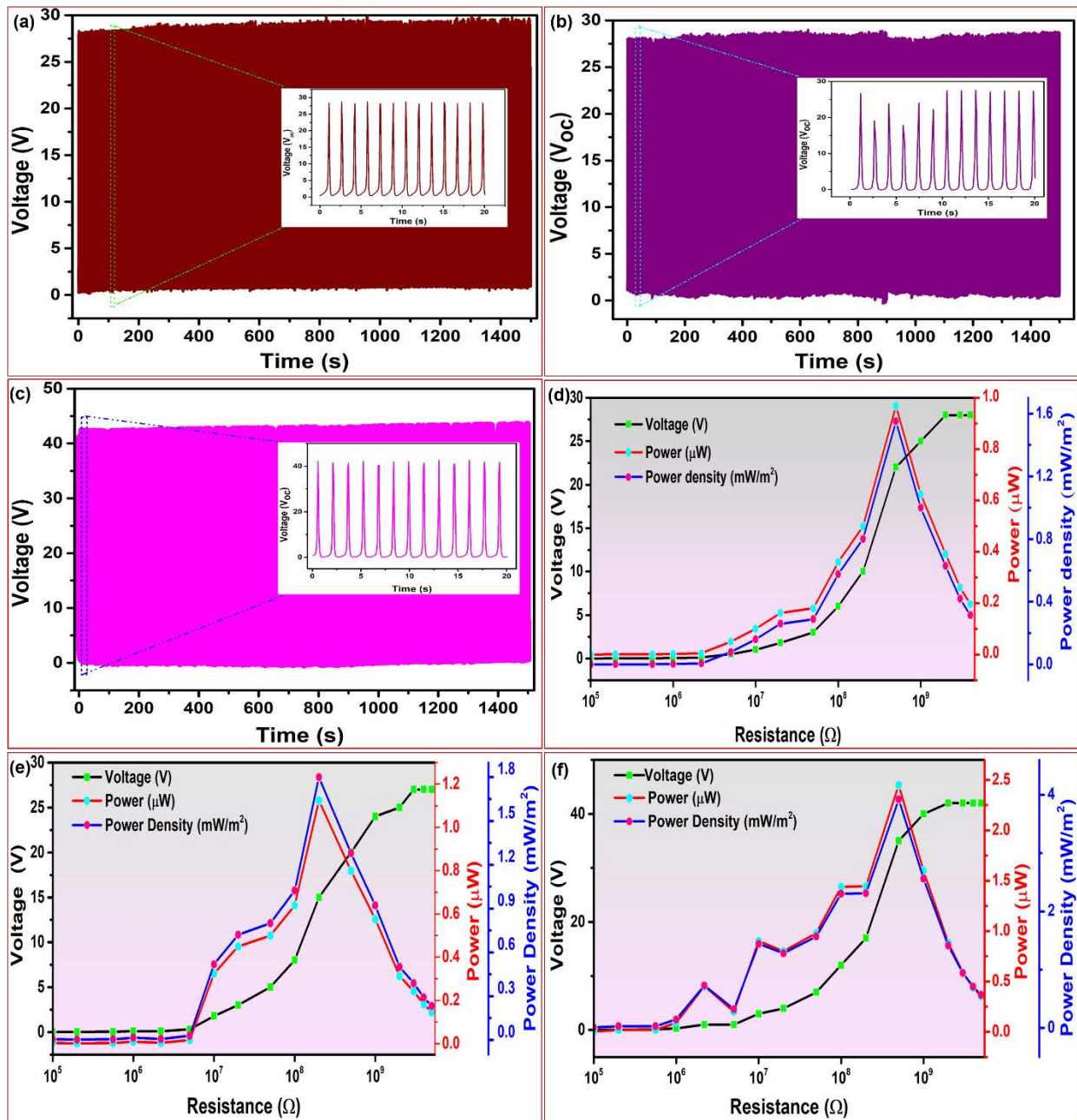
The stability analysis is critical for the practicability of the TENG. We performed a stability test for the 1500s (Figure 4.8a and 4.9a-c) to confirm the ZIFs endurance during continuous operation. There is no significant change in the device output, establishing the stability of the ZIFs. The ZIF-TENG was also analyzed for the load matching to find the optimized power and its utilization in real-time applications. Figure 4.8b describes the output voltage across a range of resistance for the ZIF-7 TENG. The load matching analysis for ZIF-9, ZIF-11, and ZIF-12 is shown in Figure 4.9d-f. The ZIF-7 TENG exhibits maximum peak power of  $4.84 \mu\text{W}$  at  $100 \text{ M}\Omega$ . The



ZIF-9, ZIF-11, and ZIF-12 TENG exhibit a maximum peak power of 0.968, 1.12 and 2.45  $\mu\text{W}$  at an equivalent load of 500, 200 and 200  $\text{M}\Omega$ , respectively, as summarized in Figure 4.8c.



**Figure 4.8.** a) The 1500 s endurance test for ZIF-7 TENG. b) Load matching analysis across various loads for ZIF-7 TENG; the maximum peak power is obtained at 100  $\text{M}\Omega$ . c) The bar graph depiction for power obtained by different ZIF-TENG. d) The charging graph for various capacitors (0.22, 0.5 and 1  $\mu\text{F}$ ) charged using ZIF-7 TENG. e) The charge-discharge cycle of 1  $\mu\text{F}$  capacitor charged by ZIF-7 TENG. f) The energy stored corresponding to 1 and 2 V charging of different capacitors.



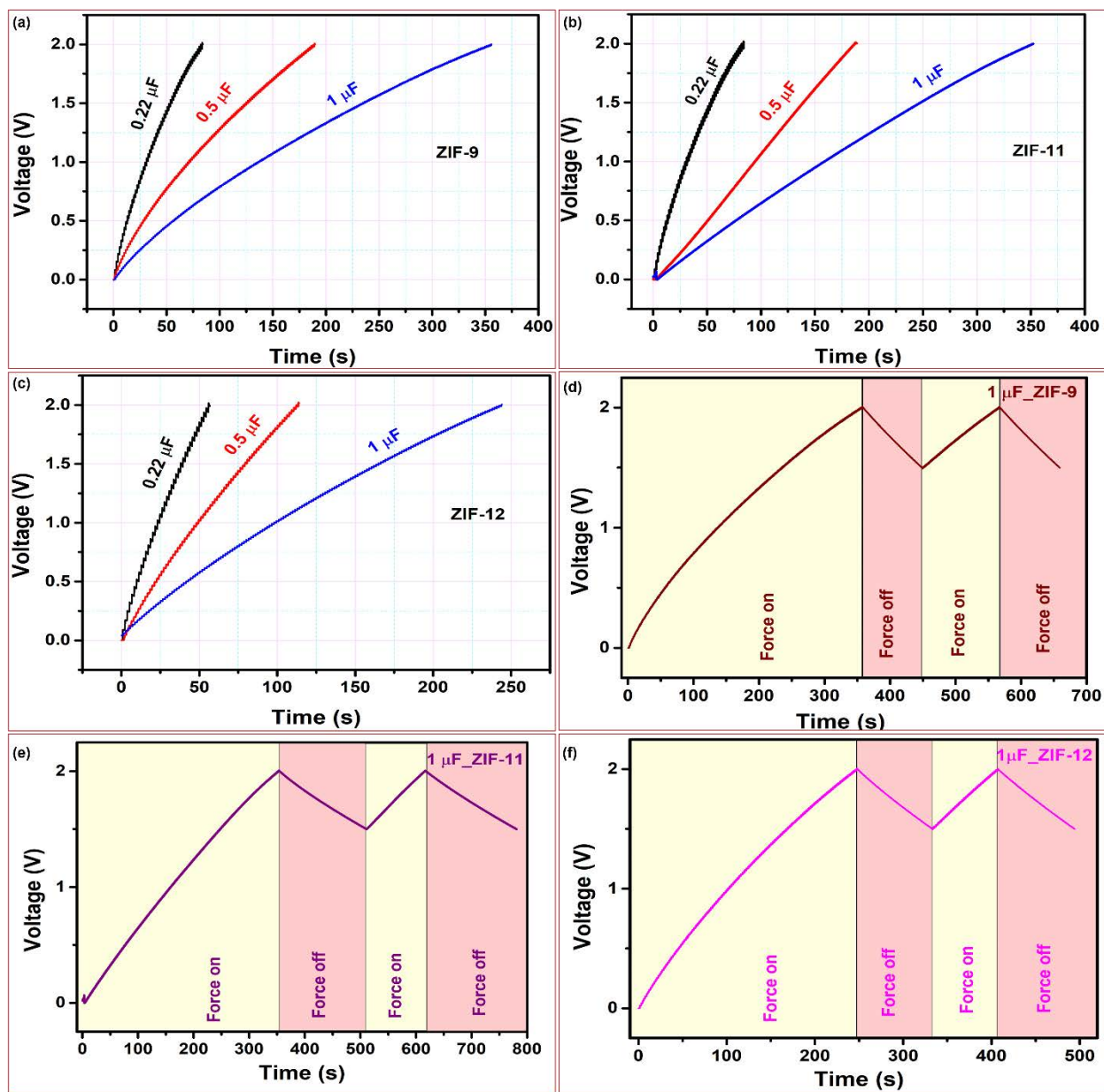
**Figure 4.9.** The 1500 s endurance test for a) ZIF-9, b) ZIF-11, c) ZIF-12 TENG. The load matching analysis for d) ZIF-9, e) ZIF-11, and f) ZIF-12 TENG devices.

The low-power daily life electronic requires a constant DC signal to operate; the AC signal generated by the TENG is not suitable. Thus, AC signal of TENG was rectified and used to charge various capacitors. Figure 4.8d shows 0.22, 0.5 and 1  $\mu\text{F}$  capacitor charging using the generated

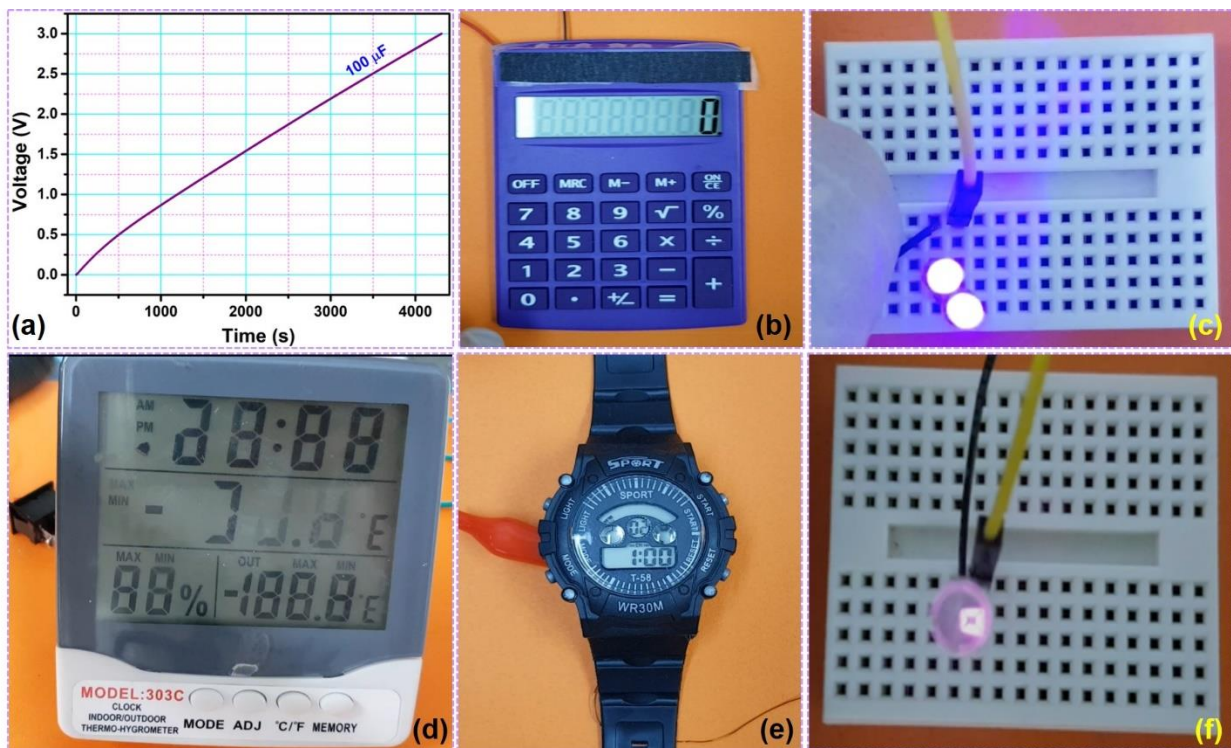


output of ZIF-7 TENG operated at a frequency of 2Hz and Figure 4.8e demonstrated the charge-discharge cycle for 1  $\mu\text{F}$  capacitor. Figure 4.10a-c shows the capacitor (0.22, 0.5, and 1  $\mu\text{F}$ ) charging using ZIF-9, ZIF-11, and ZIF-12 TENG device respectively. Figure 4.8f shows the energy stored in the charged capacitors corresponding to 1, 2 V charging. Furthermore, the charge-discharge cycle of 1 $\mu\text{F}$  capacitor for the ZIF9, ZIF-11, and ZIF-12 is shown in Figure 4.10d-f. The fast capacitor charging for ZIF-7 TENG is due to its better performance over other ZIFs.

Finally, we demonstrated the applicability of ZIF-TENG to power up electronics. Figure 4.11a shows the capacitor charging of a commercial capacitor (50 V, 100  $\mu\text{F}$ ) using four ZIF-7 TENG devices operated at a frequency of 2Hz. The charged capacitor was used to realize the powering of electronics. Figure 4.11b-f shows the lit-up of calculator, UV LEDs, hygrometer, wristwatch, and IR LEDs respectively. These electronics have a wide range of applications in our daily life. We believe that our work on ZIF family members can expand the triboelectric series and in future, lead to the development of highly selective self-powered sensors and systems.



**Figure 4.10.** The capacitor charging graph for various capacitors (0.22, 0.5, and 1  $\mu\text{F}$ ) charged using the output generated by a) ZIF-9, b) ZIF-11, and c) ZIF-12. The charge-discharge cycle for the 1  $\mu\text{F}$  capacitor charged by the output of d) ZIF-9, e) ZIF-11, and f) ZIF-12 TENG devices.



**Figure 4.11.** a) 100  $\mu\text{F}$  capacitor charging using four ZIF-7 TENG devices to drive electronics. The powering up of electronics using 100  $\mu\text{F}$  capacitor for b) calculator, c) UV LEDs, d) commercial hygro-thermometer, e) wristwatch and f) IR LEDs.

#### 4.4 Conclusion

In summary, we introduced a series of novel multifunctional materials belongs to the ZIF subfamily of MOF for TENG. The ZIFs were studied in detail for their surface morphological, roughness, structural, and surface potential properties. The surface potential analysis revealed the positive behavior of the ZIFs concerning Kapton. We have developed a contact-separation mode TENG with ZIFs and Kapton as the opposite layers. The ZIF-7 TENG exhibits the highest performance of 60 V and 1.1  $\mu\text{A}$ . The most top performance of ZIF-7 was supported by the surface roughness and surface potential measurements. The low-power electronics such as wristwatch, hygro-thermometer, UV and IR LEDs were drive using the capacitor charged by ZIF-7 TENG.

From these results, it is expected that ZIF subfamily has excellent potential and continue to contribute as novel material for TENG based self-powered sensors and system due to their tunable properties and stability.

## References

- [1] Ortiz AU, Freitas AP, Boutin A, Fuchs AH, Coudert F-X. What makes zeolitic imidazolate frameworks hydrophobic or hydrophilic? The impact of geometry and functionalization on water adsorption. *Physical Chemistry Chemical Physics*. 2014;16:9940-9.
- [2] He M, Yao J, Liu Q, Zhong Z, Wang H. Toluene-assisted synthesis of RHO-type zeolitic imidazolate frameworks: synthesis and formation mechanism of ZIF-11 and ZIF-12. *Dalton Transactions*. 2013;42:16608-13.
- [3] Khandelwal G, Chandrasekhar A, Maria Joseph Raj NP, Kim S-J. Metal–Organic Framework: A Novel Material for Triboelectric Nanogenerator–Based Self-Powered Sensors and Systems. *Advanced Energy Materials*. 2019;9:1803581.
- [4] Ma X, Chai Y, Li P, Wang B. Metal–Organic Framework Films and Their Potential Applications in Environmental Pollution Control. *Accounts of Chemical Research*. 2019;52:1461-70.
- [5] Mezenov YA, Krasilin AA, Dzyuba VP, Nominé A, Milichko VA. Metal–Organic Frameworks in Modern Physics: Highlights and Perspectives. *Advanced Science*. 2019;6:1900506.
- [6] Zhang H, Liu F, Wu X, Zhang J, Zhang D. Degradation of tetracycline in aqueous medium by electrochemical method. *Asia-Pacific Journal of Chemical Engineering*. 2009;4:568-73.
- [7] Gücüyener C, van den Bergh J, Gascon J, Kapteijn F. Ethane/Ethene Separation Turned on Its Head: Selective Ethane Adsorption on the Metal–Organic Framework ZIF-7 through a Gate-Opening Mechanism. *Journal of the American Chemical Society*. 2010;132:17704-6.
- [8] Sánchez-Laínez J, Zornoza B, Téllez C, Coronas J. On the chemical filler–polymer interaction of nano- and micro-sized ZIF-11 in PBI mixed matrix membranes and their application for H<sub>2</sub>/CO<sub>2</sub> separation. *Journal of Materials Chemistry A*. 2016;4:14334-41.

- [9] Wen R, Guo J, Yu A, Zhai J, Wang ZL. Humidity-Resistive Triboelectric Nanogenerator Fabricated Using Metal Organic Framework Composite. *Advanced Functional Materials*. 2019;29:1807655.
- [10] Mi L, Zhang Y, Wu J, Cui S, Wei W, Chen W, et al. Organosulfonate counteranions-trapped coordination polymer as high-output triboelectric nanogenerator material for self-powered anticorrosion. *Chemistry – A European Journal*.n/a.
- [11] Joshi BN, Lee J-G, An S, Kim D-Y, Lee JS, Hwang YK, et al. Tuning crystalline structure of zeolitic metal–organic frameworks by supersonic spraying of precursor nanoparticle suspensions. *Materials & Design*. 2017;114:416-23.
- [12] Wang ZL. Triboelectric nanogenerators as new energy technology and self-powered sensors – Principles, problems and perspectives. *Faraday Discussions*. 2014;176:447-58.
- [13] Wang ZL. Triboelectric Nanogenerators as New Energy Technology for Self-Powered Systems and as Active Mechanical and Chemical Sensors. *ACS Nano*. 2013;7:9533-57.
- [14] Luo J, Xu L, Tang W, Jiang T, Fan FR, Pang Y, et al. Direct-Current Triboelectric Nanogenerator Realized by Air Breakdown Induced Ionized Air Channel. *Advanced Energy Materials*. 2018;8:1800889.
- [15] Khandelwal G, Chandrasekhar A, Pandey R, Maria Joseph Raj NP, Kim S-J. Phase inversion enabled energy scavenger: A multifunctional triboelectric nanogenerator as benzene monitoring system. *Sensors and Actuators B: Chemical*. 2019;282:590-8.
- [16] Lin Z, Zhang B, Guo H, Wu Z, Zou H, Yang J, et al. Super-robust and frequency-multiplied triboelectric nanogenerator for efficient harvesting water and wind energy. *Nano Energy*. 2019;64:103908.

- [17] Luo J, Wang Z, Xu L, Wang AC, Han K, Jiang T, et al. Flexible and durable wood-based triboelectric nanogenerators for self-powered sensing in athletic big data analytics. *Nature Communications*. 2019;10:5147.
- [18] Luo J, Wang ZL. Recent advances in triboelectric nanogenerator based self-charging power systems. *Energy Storage Materials*. 2019;23:617-28.
- [19] Ebrahimi A, Mansournia M. Cost-effective fabrication of thermal- and chemical-stable ZIF-9 nanocrystals at ammonia atmosphere. *Journal of Physics and Chemistry of Solids*. 2017;111:12-7.
- [20] Park KS, Ni Z, Côté AP, Choi JY, Huang R, Uribe-Romo FJ, et al. Exceptional chemical and thermal stability of zeolitic imidazolate frameworks. *Proceedings of the National Academy of Sciences*. 2006;103:10186-91.
- [21] Safak Boroglu M, Ugur M, Boz I. Enhanced gas transport properties of mixed matrix membranes consisting of Matrimid and RHO type ZIF-12 particles. *Chemical Engineering Research and Design*. 2017;123:201-13.
- [22] Fan K, Jin Z, Yuan H, Hu H, Bi Y. Construction of CuO-modified zeolitic imidazolate framework-9 for photocatalytic hydrogen evolution. *Chinese Journal of Catalysis*. 2017;38:2056-66.
- [23] Kang C-H, Lin Y-F, Huang Y-S, Tung K-L, Chang K-S, Chen J-T, et al. Synthesis of ZIF-7/chitosan mixed-matrix membranes with improved separation performance of water/ethanol mixtures. *Journal of Membrane Science*. 2013;438:105-11.
- [24] Ehsani A, Pakizeh M. Synthesis, characterization and gas permeation study of ZIF-11/Pebax® 2533 mixed matrix membranes. *Journal of the Taiwan Institute of Chemical Engineers*. 2016;66:414-23.

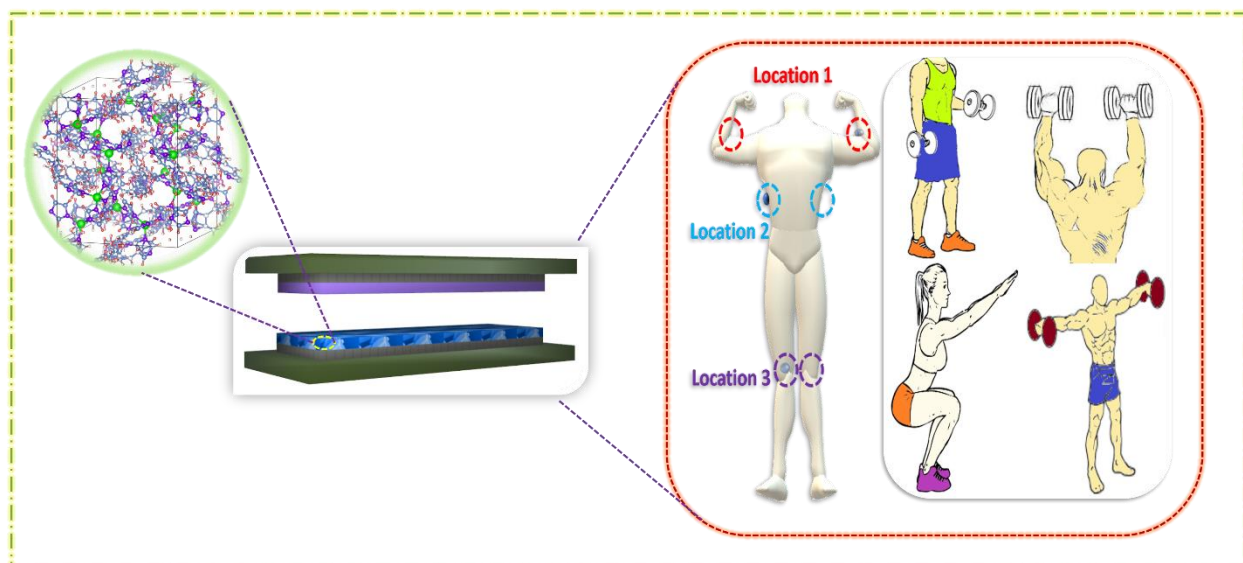


- [25] Lee S, Lee Y, Kim D, Yang Y, Lin L, Lin Z-H, et al. Triboelectric nanogenerator for harvesting pendulum oscillation energy. *Nano Energy*. 2013;2:1113-20.
- [26] Tang W, Zhang C, Han CB, Wang ZL. Enhancing Output Power of Cylindrical Triboelectric Nanogenerators by Segmentation Design and Multilayer Integration. *Advanced Functional Materials*. 2014;24:6684-90.
- [27] Jeong CK, Baek KM, Niu S, Nam TW, Hur YH, Park DY, et al. Topographically-Designed Triboelectric Nanogenerator via Block Copolymer Self-Assembly. *Nano Letters*. 2014;14:7031-8.
- [28] Kim DW, Kim S-W, Jeong U. Lipids: Source of Static Electricity of Regenerative Natural Substances and Nondestructive Energy Harvesting. *Advanced Materials*. 2018;30:1804949.

## CHAPTER V

### ZIF-62: A Mixed Linker Metal-organic Framework for Triboelectric Nanogenerator

#### Graphical Overview



## Highlights

- A mixed linker metal-organic framework ZIF-62 of subfamily ZIF, is explored for its triboelectric behavior.
- The Kelvin probe force microscopy (KPFM) and surface potential measurement reveal the positive potential on the ZIF-62.
- The Teflon, Kapton, and ethyl cellulose (EC) are used as the opposite triboelectric layers to ZIF-62.
- The ZIF-62 TENG follows an output trend of  $TENG_{\text{Teflon}} > TENG_{\text{Kapton}} > TENG_{\text{EC}}$ .
- The fabricated device is demonstrated for fitness tracking and energy harvesting during various gym exercises like hand curl, lateral raise, shoulder press, and squats.
- Low-power day to day life electronics is successfully powered with the output of ZIF-62 TENG via a charged capacitor.

## 5.1 Introduction

Metal-organic frameworks (MOFs) term introduced in 1995, is a class of crystalline organic-inorganic microporous materials [1, 2]. MOFs are formed by the bridging of linkers via metal ion to form a repeating framework structure. MOF offers large surface area, uniform and tunable porosity, flexible topology, flexible dimension and chemical functionality [1-3]. Ascribed to their appealing properties, MOF is extensively used for various applications like gas separation, energy storage, triboelectric nanogenerator (TENG), catalysis, filters, and self-powered sensors, vaccine, and nutrient-sensing etc [2, 4-6]. TENG is energy harvesting devices that convert mechanical energy into electricity. The coupling of triboelectric effect (contact-electrification) and electrostatic induction is the mechanism behind the working of TENG [7-9]. From the time of their invention, TENG has been utilized for a large number of applications including drug delivery, cell modulation, blue-wave energy harvesting, physical, chemical, and biological sensors etc [5, 10-13]. The high output performance, ease of fabrication, high efficiency, cost-effectiveness, a wide choice of materials, etc. are the reason behind the utilization of TENG for a broad range of applications [14, 15].

Recently, several groups, including ours, reported new materials like MOF, 2D materials to extend the triboelectric series, which was dominated by the polymers [5, 6, 16]. In our previous works, we reported the single linker based Zeolitic imidazole framework (ZIF) family members as the active material for TENG. Several other groups reported the use of MOF as a filler and functionalized MOFs for high-performance TENG [17-19]. In this work, for the first time, a mixed linker ZIF subfamily member ZIF-62 is explored as an active material for TENG devices. ZIF-62 consists of imidazole (Im) and benzimidazole (bIm) linkers and forms Cag topology. X-ray diffraction (XRD), Fourier transform infrared (FT-IR) spectroscopy (FT-IR) and Raman

spectroscopy confirmed the formation of ZIF-62. The surface potential measurement using Kelvin probe force microscopy (KPFM) and surface voltmeter confirm the positive triboelectric behavior of ZIF-62. The 3D nano profiling reveals the surface roughness parameters, which plays a significant role in the TENG device performance. The Teflon, Kapton, and ethyl cellulose (EC) are selected as an opposite layer to the ZIF-62 in vertical contact-separation mode, attributed to their positions in the triboelectric series. The device was tested for its output performance, endurance, and load matching analysis. The as-fabricated device was demonstrated for fitness tracking during the gym exercises. Finally, several low-power electronics like green light-emitting diodes (LEDs), thermometer, wristwatch, calculator, and ultraviolet LEDs were powered by the ZIF-62-TENG device.

## **5.2 Experimental**

### **5.2.1 Synthesis of ZIF-62**

ZIF-62 was synthesized by the well-reported hydrothermal method. Briefly, the Zn/bIm/Im were mixed in the molar ratio of 1:1.5:13.5 in the DMF solution. The solution was stirred for 2 hours and then transferred to a teflon-lined autoclave. The autoclave was then placed at 130 °C for 4 days. The material was collected and washed several times with DMF, followed by drying.

### **5.2.2 Crystal Structure**

The crystal structure was designed using the VESTA software by downloading the .cif file from the website of the Cambridge crystallographic data centre (CCDC).

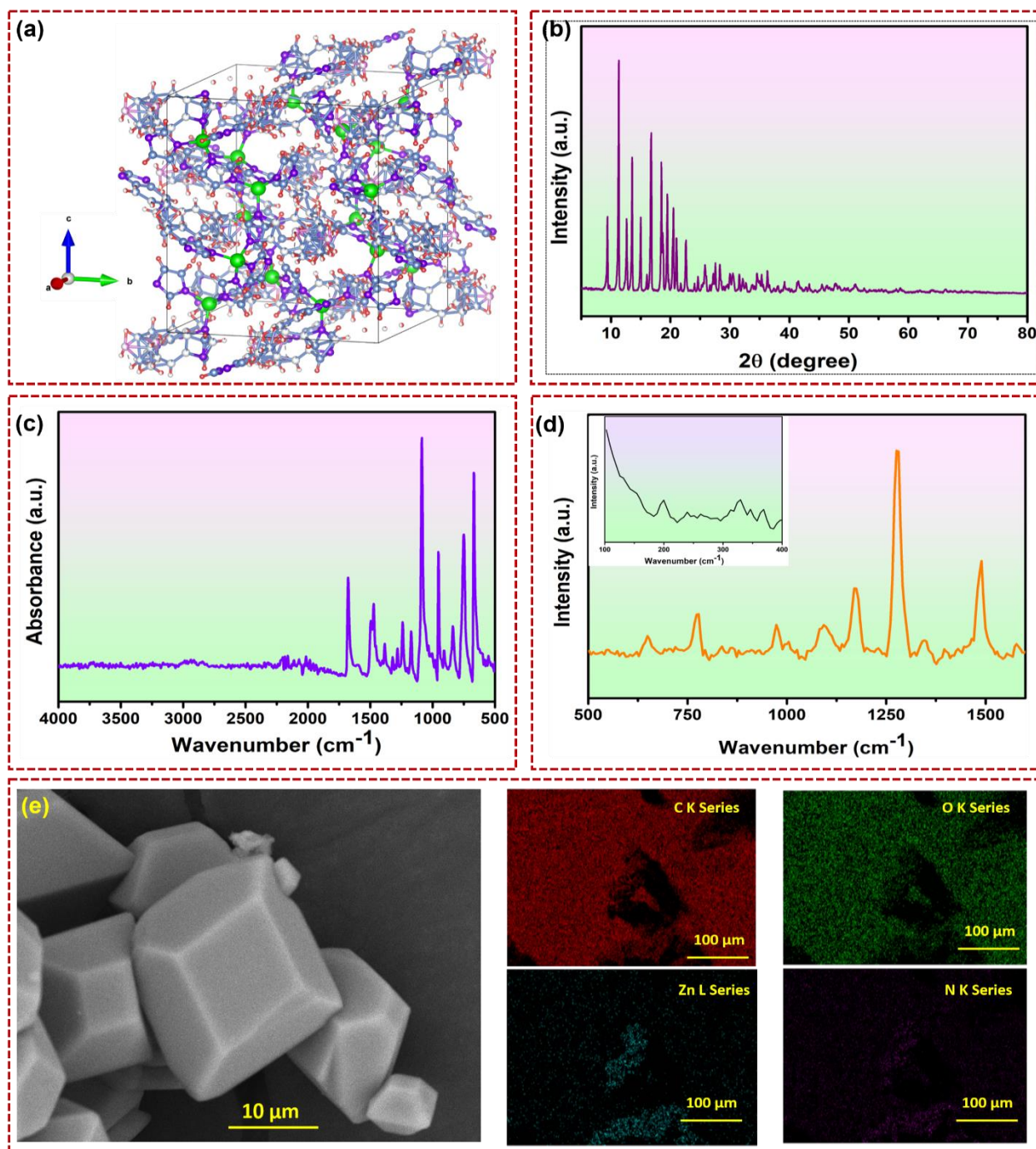
### **5.2.3 Device fabrication**

The ZIF-62 TENG with an active area of 2.5 X 2.5 cm<sup>2</sup> was fabricated in vertical contact-separation mode, with different opposite materials (Teflon, Kapton, and ethyl cellulose). The ZIF-

62 was fixed uniformly on the Al tape with conducting adhesive (3M). An air gun was used to remove the excess material. The Teflon and Kapton layers were prepared by directly attaching them on the Al tape. The ethyl cellulose layer was made by spin coating of 10 wt.% (1:4 ethanol: toluene) ethyl cellulose (48% ethoxy content) solution on the Al tape. The copper wires were attached by silver paste for the connection. Finally, the ZIF-62 and the opposite layer were combined by using a spacer.

### 5.3 Results and Discussions

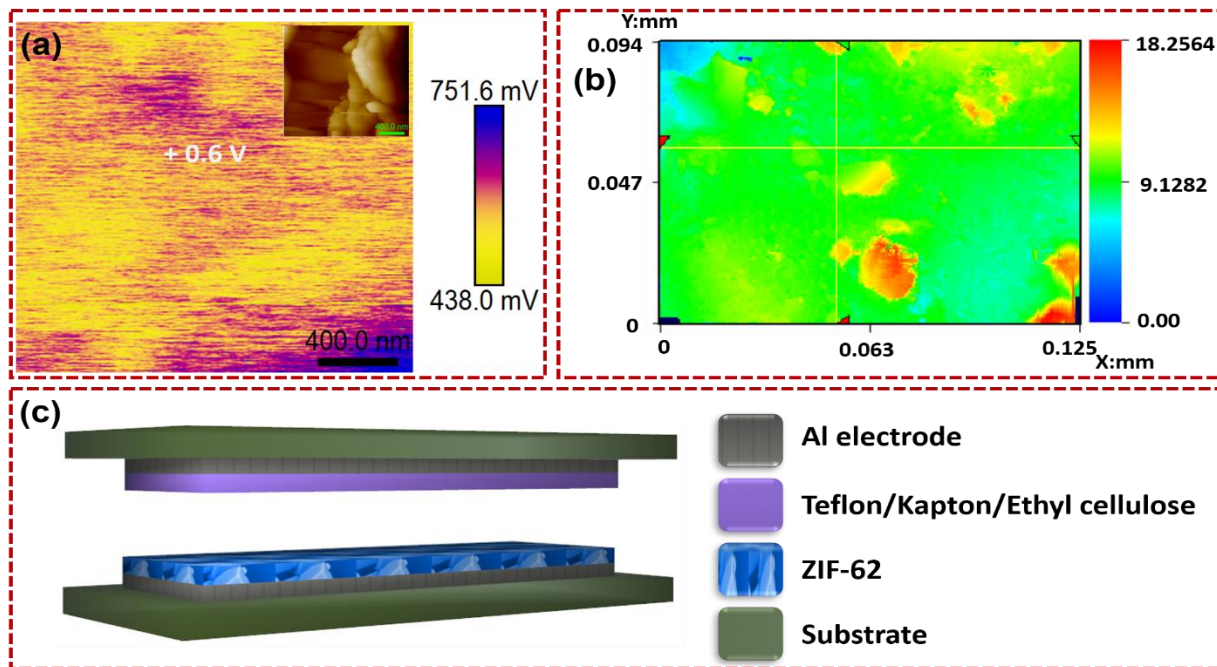
Figure 5.1a illustrates the crystal structure of ZIF-62, forming Cag topology. ZIF-62 is a mixed linker MOF, where two unique Zn atoms are available and each of which is coordinated to one disordered linker and three Im linkers [20-22]. The bIm linker partially inhabits two linker locations. ZIF-62 exhibit similarity with ZIF-4 in the space group and unit cell parameters. Figure 5.1b shows the XRD pattern of the synthesized ZIF-62, which confirms the lattice plane of orthorhombic ZIF-62 [20, 21, 23]. The XRD data matches well with the reported and the simulated XRD pattern [23]. Figure 5.1c shows the FT-IR spectrum of the ZIF-62, the peak at  $1677\text{ cm}^{-1}$  is due to the DMF. The peak at  $670\text{ cm}^{-1}$  is due to the imidazole. The C=C and C-H bond peaks at  $1464$  and  $747\text{ cm}^{-1}$  are associated with the benzene group of bIM [24, 25]. Figure 5.1d shows the Raman spectra of ZIF-62, which matches well with the literature. The peak at  $1278\text{ cm}^{-1}$  is due to the symmetric stretching in the organic linker. The peak in the range of  $100\text{-}400\text{ cm}^{-1}$  as shown in the inset are due to the rocking  $\delta(\text{Zn-N})$ , asymmetric (Zn-N), and symmetric (Zn-N) stretching vibrations [26]. The surface morphology of the ZIF-62 is shown in Figure 5.1e, where the particle is in the range of  $1\text{-}10\text{ }\mu\text{m}$ . The energy-dispersive X-ray spectroscopy (EDS) confirms the presence of Z, O, Zn, and N present in the ZIF-62 (Figure 5.1e).



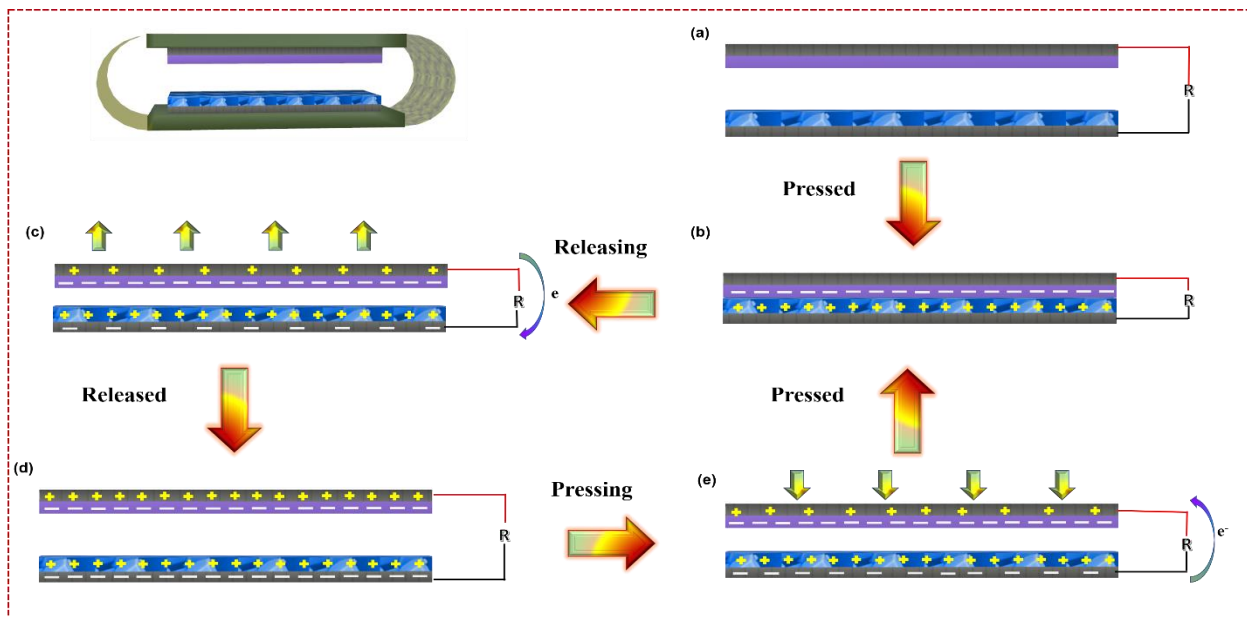
**Figure 5.1.** Structural and morphological characterization of ZIF-62. (a) Crystal structure of ZIF-62 (.cif file was retrieved from CCDC). (b) XRD spectra of ZIF-62. (c) FT-IR spectra of ZIF-62. (d) Raman spectra of ZIF-62 and (e) FE-SEM revealing the morphology of the particles and EDS mapping analysis is confirming the presence of different elements.



Figure 5.2a shows the surface potential image captured by KPFM, and the inset shows the corresponding AFM image. The KPFM confirms the +0.6 V on the surface of the material. The surface roughness is well reported to influence the performance of the TENG [27-29]. The optimal increase in surface roughness improves the TENG output as it brings more area in contact during the working of the TENG. Figure 5.2b shows 2D profile of the ZIF-62 layer. The x and y-direction average surface roughness ( $R_a$ ) corresponding to the yellow cross hair marked in the 2D image are 344.85 nm and 0.75  $\mu\text{m}$  respectively. The entire image exhibits a  $R_a$  value of 1.04  $\mu\text{m}$ . Figure 5.2c illustrates the 3D exploded view of the ZIF-62 TENG device. The ZIF-62 and Teflon/Kapton/ethyl cellulose are the opposite layers. The polyethylene terephthalate and conducting aluminum (Al) tape were used as the substrate and electrode, respectively.



**Figure 5.2.** (a) KPFM, surface potential image of ZIF-62 with inset showing the corresponding AFM image. (b) 2D surface roughness profile image of ZIF-62 and (c) 3D exploded view of the ZIF-62 TENG device.



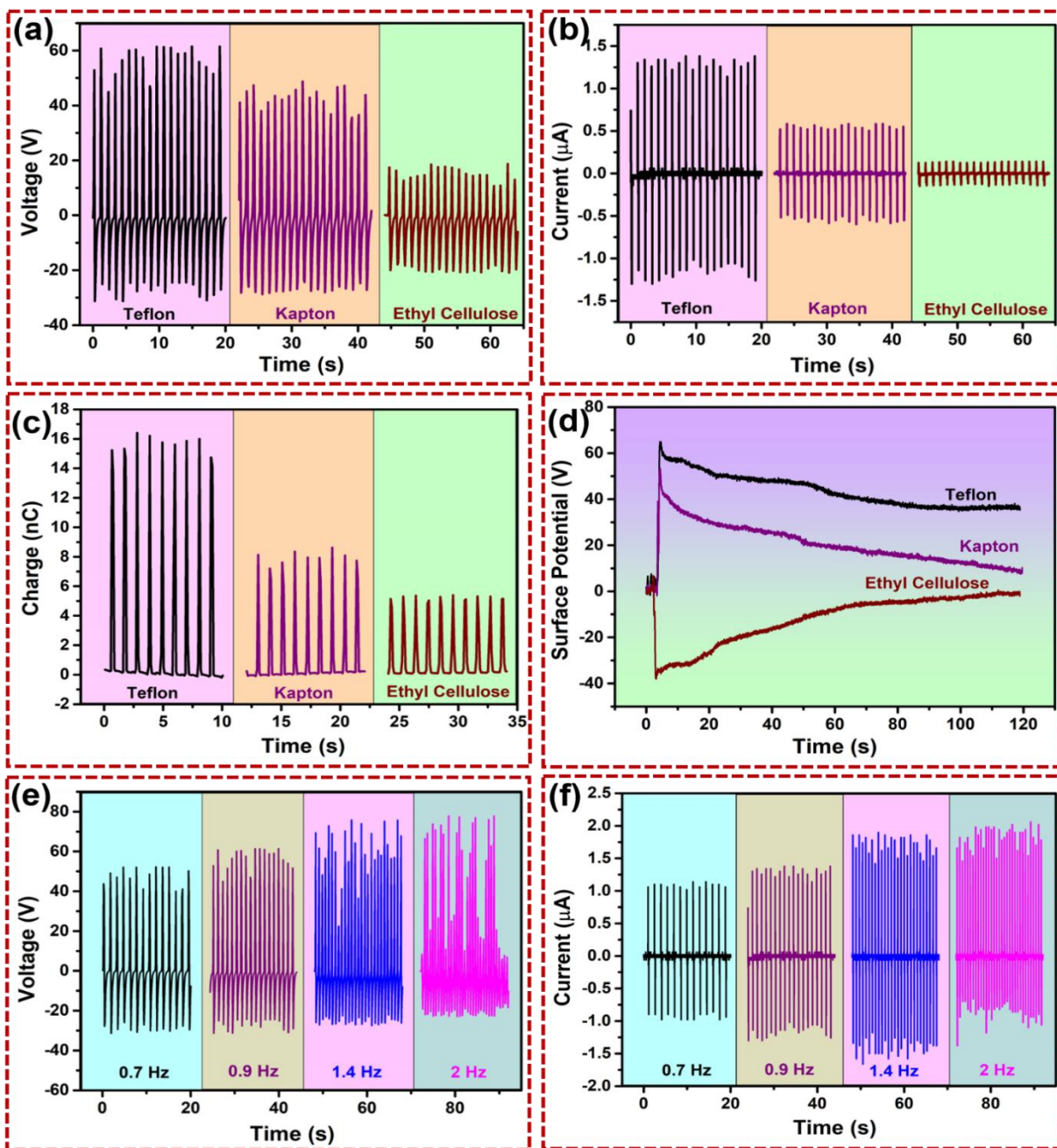
**Figure 5.3.** The schematic for the device mechanism in contact-separation mode showing the different stages that occur during the working (pressed, releasing, released, and pressing).

The working mechanism for the contact-separation TENG is shown in Figure 5.3. The device is governed by the coupling effect of the triboelectrification and electrostatic induction. Figure 5.3a shows the initial state of the device with zero potential difference as no charge generation occurs in the absence of the force. The fully pressed state of the device is shown in Figure 5.3b, equal and opposite charges are generated on the layers. The ZIF-62 is positive with respect to the Teflon and Kapton; thus, generating negative charge on the Teflon layer. In the absence of the force, the device tends to regain its original shape, which creates a potential difference. The created potential difference allows the flow of electrons from the top electrode to the bottom electrode (Figure 5.3c) until full separation, as shown in Figure 5.3d. This flow of electron generated the first half-cycle of the device output. When force is applied, the upper layer moves towards the bottom layer, creating the reverse flow of electrons (Figure 5.3e). The electrons flow from the bottom electrode to the top electrode contributing the other half-cycle of the A.C

output. Thus, periodic contact-separation of the device generates the output of the TENG [7-9, 30].

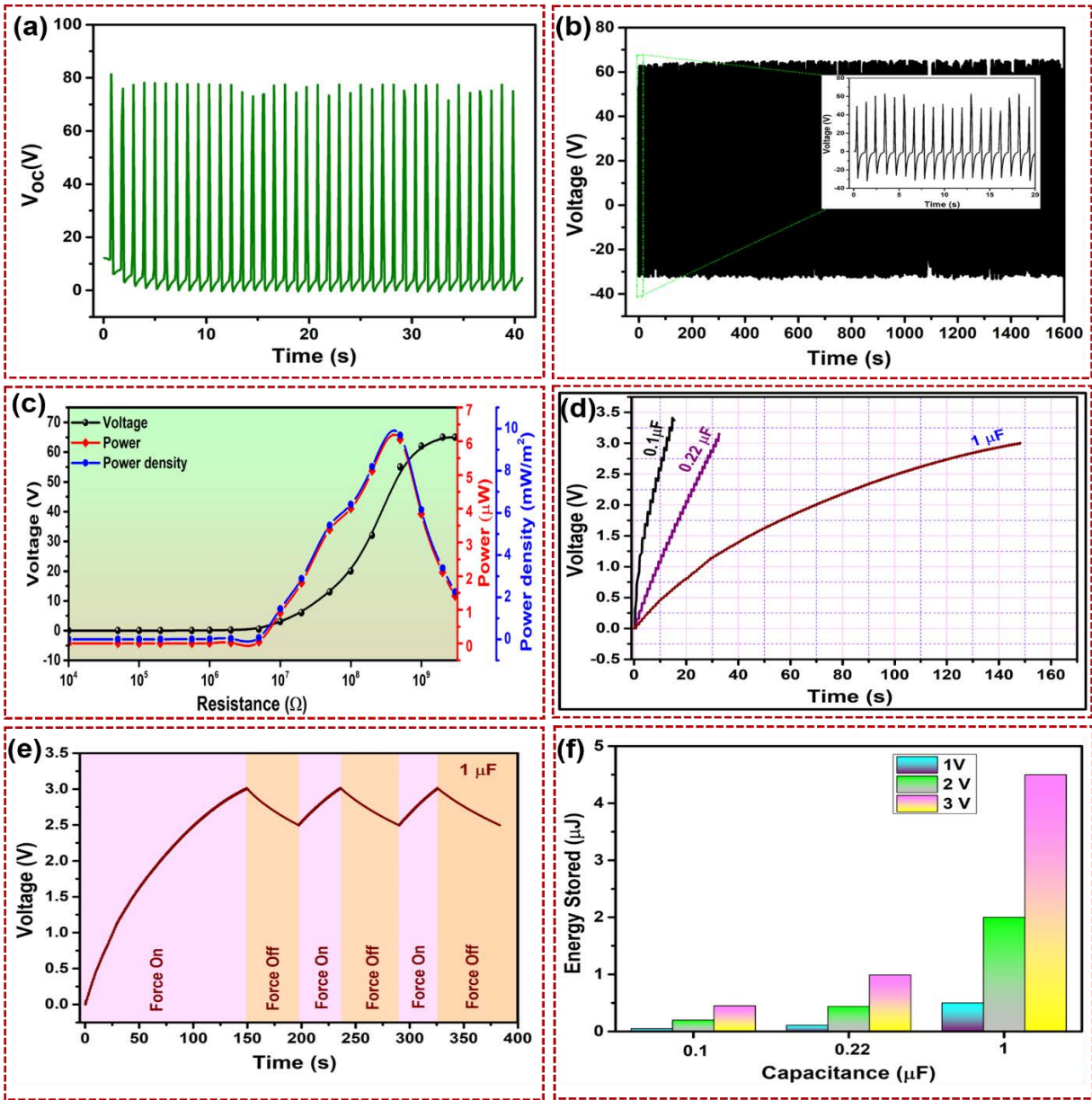
Figure 5.4 shows the output performance of the TENG device. Figure 5.4a and 5.4b illustrate the voltage and current profile of the ZIF-62 with different opposite materials (Teflon, Kapton, and ethyl cellulose). The materials were selected based on their location in the triboelectric series; Teflon is the most negative triboelectric layer, while ethyl cellulose is one of the excellent positive material. The ZIF-62 generates the highest output with the Teflon as ZIF-62 has positive potential, as confirmed by the KPFM analysis. The ZIF-62/Teflon TENG generated an output voltage and current of 62 V and 1.4  $\mu\text{A}$  respectively. The ZIF-62 TENG follows an output trend of Teflon > Kapton > ethyl cellulose. The ethyl cellulose is positive material, thus generated less output with the ZIF-62. The charge profile is shown in Figure 5.4c corroborates with the current output and follows the same trend with a maximum value of 16 nC in the case of Teflon. The ZIF-62 behavior was further probed by measuring the generated surface potential when hitting 50 times with the above-selected materials. Teflon and Kapton create positive surface potential on the ZIF-62 layer suggesting the positive triboelectric behavior of the ZIF-62 (Figure 5.4d). On the other hand, ZIF-62 developed negative surface potential when hit by the ethyl cellulose (Figure 5.4d). The development of negative potential suggesting that ethyl cellulose is more positive than the ZIF-62. Figure 5.4e and 5.4f show the voltage and current output of the ZIF-62/Teflon TENG at a different frequency. The voltage and current increases with an increase in frequency up to 1.4 Hz. The devices generated a maximum output of 70 V and 1.9  $\mu\text{A}$  at 1.4 Hz. The output reduces at 2Hz with the non-uniform peak pattern. The frequency analysis confirms the suitability of the device to harness the low-frequency motions. Further analysis was performed by using the ZIF-62/Teflon TENG device named ZIF-62 TENG, otherwise mentioned.

The TENG devices reach open circuit (OC) condition at large resistance where the highest voltage saturates at  $V_{oc}$  [8]. The open-circuit voltage for the ZIF-62 TENG is shown in Figure 5.5a. The device reached a maximum output of 80V at OC condition. The stability of the device is a crucial parameter for assessing the practicability of the TENG. Figure 5.5b shows the endurance test for the device under continuous operation for 1600 s. The device generated a constant output during the test suggesting the suitability of the device for real time application. Figure 5.5c depicts the load matching analysis for the ZIF-62 TENG to find the optimized power. The device exhibits a maximum peak power of  $6.05 \mu\text{W}$  and a power density of  $9.68 \text{ mW m}^{-2}$  across an equivalent load of  $500 \text{ M}\Omega$ . The TENG produces AC output, which is not suitable for daily life low-power electronics. The AC signal of the TENG after rectification was used to charge different capacitors. Figure 5.5d shows the charging profile for 0.1, 0.22, and  $1 \mu\text{F}$  capacitor. The capacitors were charged up to 3V, and  $1 \mu\text{F}$  capacitor took maximum time to charge ascribed to its high capacitance. Figure 5.5e and 5.5f show the charge-discharge profile of  $1 \mu\text{F}$  capacitor and energy stored in various capacitors corresponding to 1, 2, and 3V, respectively.



**Figure 5.4.** Output performance of the ZIF-62 TENG. (a-c) The generated voltage, current, and charge profile of the ZIF-62 with different opposite layers (Teflon, Kapton, and ethyl cellulose), respectively. (d) Surface potential developed on ZIF-62 after 60 contacts with Teflon, Kapton, and ethyl cellulose film and (e-f) The voltage and current versus time graph for ZIF-62/Teflon TENG at various frequency.

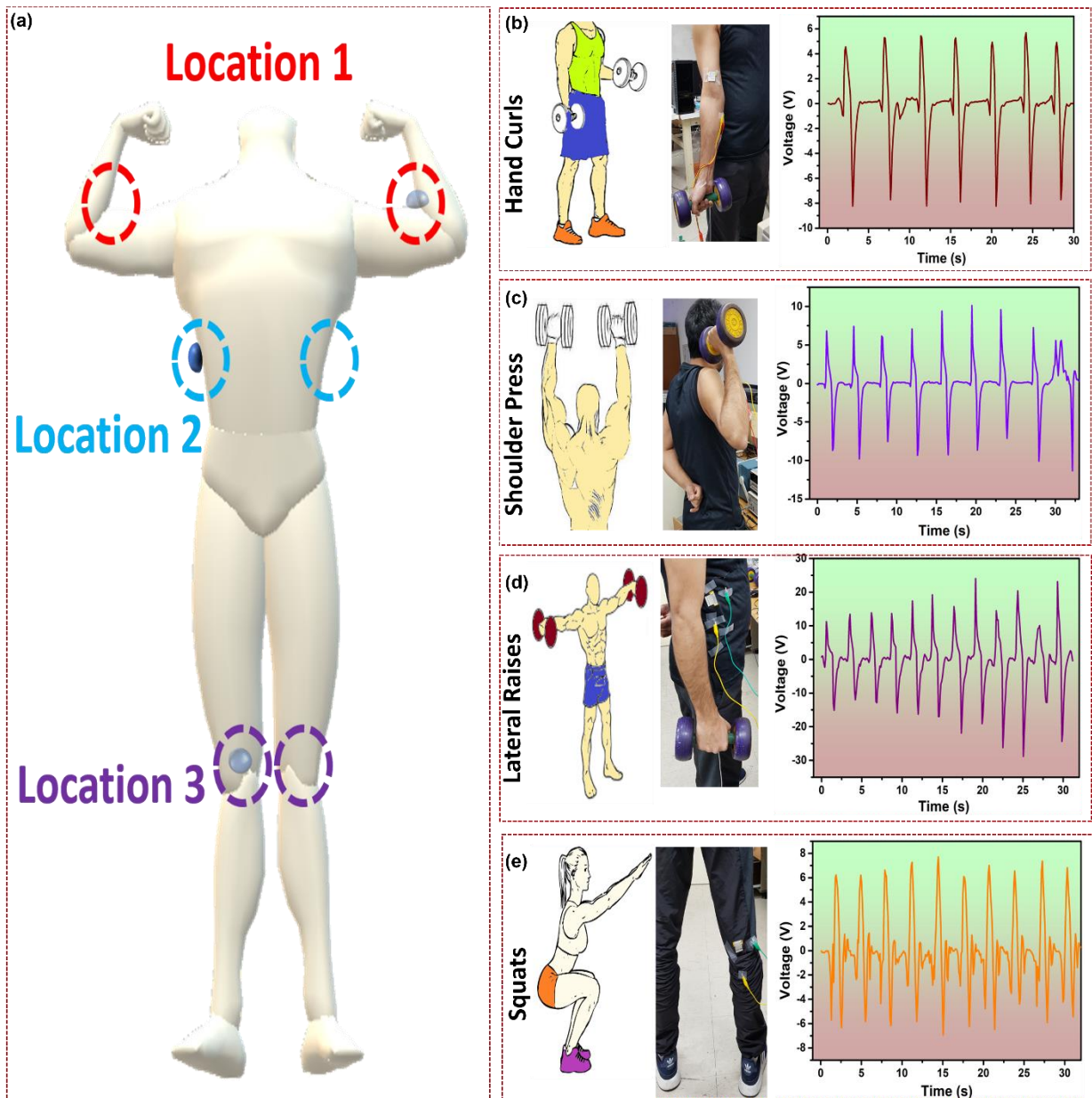




**Figure 5.5.** (a) The open-circuit voltage profile of the ZIF-62 TENG. (b) The endurance test for ZIF-63 TENG performed for 1600 s. (c) The load matching analysis across different loads; the maximum power density, was obtained at 500 MΩ. (d) The capacitor charging profile for 0.1, 0.22, and 1 μF capacitor charged by the device. (e) The charge and self-discharge behavior of the 1 μF capacitor. (f) The stored energy in the capacitor corresponding to 1, 2, and 3V charging of various capacitors.

Figure 5.6 shows the energy harvesting and fitness tracking during different gym exercises. Figure 5.6a shows the device positions on the body, which can utilize the motions produced during different gym exercises like hand curls, squats, lateral raises, etc. Figure 5.6b shows the energy harvesting during the hand curls. The device was placed on one hand, and it generated an output of 5V during the hand curl. The number of peaks can be used to count the number of curls performed in a given time. The 7 hand curls were performed in a period of 30s. Figure 5.6c illustrates the energy harvesting during the shoulder press. The device was placed on one hand, and it generated an output of 7V during the shoulder press. The 9-shoulder press was performed during a period of 30 s. Similarly, the device was placed on the lateral side of the abdomen to harvest the energy generated by the lateral raises, as shown in Figure 5.6d. The device produced an output of 10-15 V during the motion, and 12 lateral raises were performed in 30 s. For squats, the device was placed on one leg as shown in Figure 5.6e. The device generated an output of 6V, and 10 squats were performed in a period of 30s. The ZIF-62 TENG was successful in harvesting all the motions and can be in the near future coupled to the automatic counting system for effectively count the number of repeats performed in a given period.

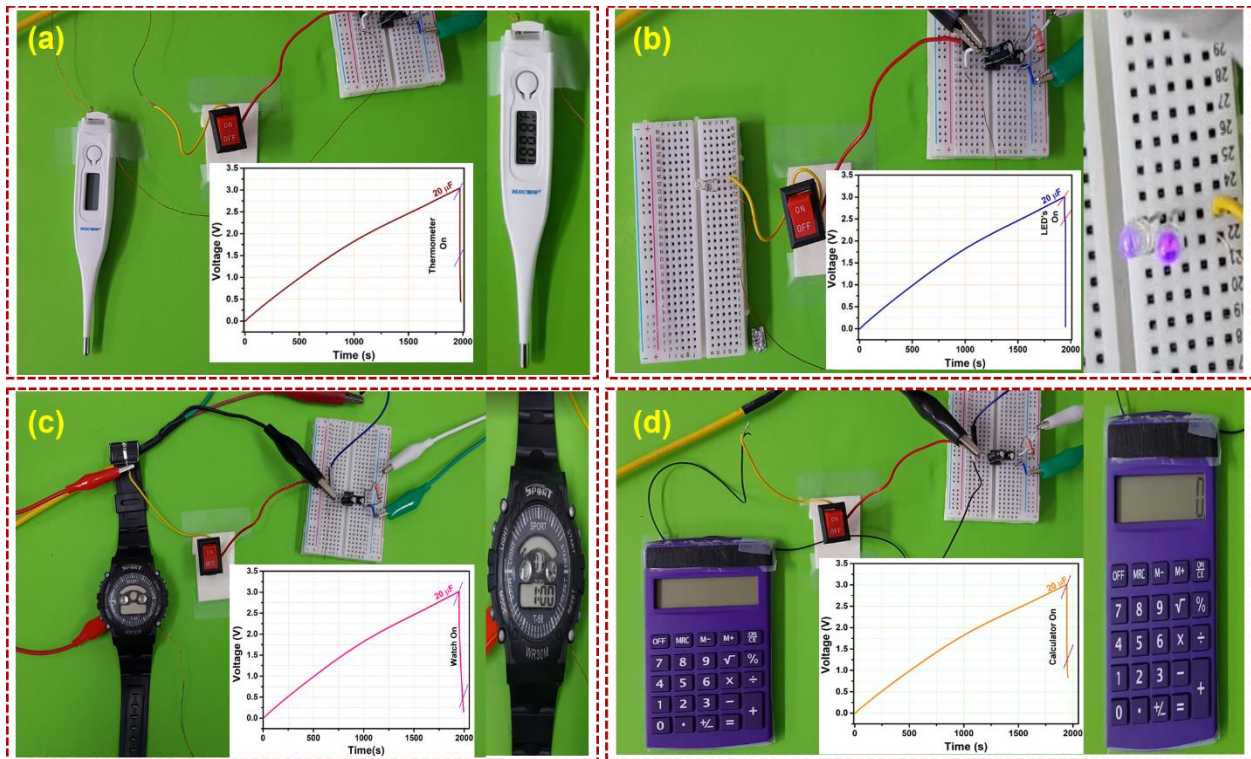




**Figure 5.6.** Fitness tracking and energy harvesting during (b) hand curls, (c) shoulder press, (d) lateral raises, and (e) squats exercises performed in the gym.

Finally, we demonstrated the suitability of the device to power up low rating day to day life use electronics. Figure 5.7 illustrates the powering up of various low-power electronics via charging a 20  $\mu\text{F}$  capacitor. Figure 5.7a demonstrates the powering up of commercial digital thermometer and capacitor discharging during the process. The thermometer works for 3s, as

confirmed from the discharge profile. Similarly, Figure 5.7b-5.7d shows the powering up and capacitor discharge profile for two UV LEDs, wristwatch and the calculator. The UV LEDs just blink for less than 1s, wristwatch worked for more than 30 s and calculator worked for 3 s as confirmed by the discharge profile of the capacitor. The above electronics can be used for various purposes in our day to day life. We believe that our work on a mixed linker framework not only adds a new material for TENG but can be explored in the near future for self-powered sensor applications due to its multifunctional properties.



**Figure 5.7.** Powering of low-rating electronics via  $20\ \mu\text{F}$  capacitor charged by the ZIF-62 TENG device for (a) Commercial thermometer, (b) UV LEDs, (c) wristwatch, and (d) calculator along with the capacitor charge-discharge profile during turning on the electronics.

## 5.4 Conclusion

In summary, we instigate a mixed linker MOF ZIF-62 for TENG in a vertical contact-separation configuration. The ZIF-62 was a positive triboelectric material with a surface potential of 0.6 V, as confirmed by the KPFM analysis. We have developed the device with Teflon, Kapton, and EC as an opposite material to ZIF-62. The Teflon, as an opposite layer, generated the maximum output, followed by Kapton and EC. The ZIF-62/Teflon produced a voltage output of 62 V, a current of 1.4  $\mu\text{A}$ , and a transferred charge of 16 nC. The as-fabricated device was demonstrated for energy harvesting and fitness monitoring for gym exercise. Moreover, various low rating electronics were powered via a capacitor charged using a ZIF-62 TENG. These results confirm that various members of class MOF due to their multifunctionality will continue to extend the triboelectric series and TENG applications.

## References

- [1] Li H, Eddaoudi M, O'Keeffe M, Yaghi OM. Design and synthesis of an exceptionally stable and highly porous metal-organic framework. *Nature*. 1999;402:276-9.
- [2] Furukawa H, Cordova KE, O'Keeffe M, Yaghi OM. The Chemistry and Applications of Metal-Organic Frameworks. *Science*. 2013;341:1230444.
- [3] Ortiz AU, Freitas AP, Boutin A, Fuchs AH, Coudert F-X. What makes zeolitic imidazolate frameworks hydrophobic or hydrophilic? The impact of geometry and functionalization on water adsorption. *Physical Chemistry Chemical Physics*. 2014;16:9940-9.
- [4] Ling W, Liew G, Li Y, Hao Y, Pan H, Wang H, et al. Materials and Techniques for Implantable Nutrient Sensing Using Flexible Sensors Integrated with Metal–Organic Frameworks. *Advanced Materials*. 2018;30:1800917.
- [5] Khandelwal G, Chandrasekhar A, Maria Joseph Raj NP, Kim S-J. Metal–Organic Framework: A Novel Material for Triboelectric Nanogenerator–Based Self-Powered Sensors and Systems. *Advanced Energy Materials*. 2019;9:1803581.
- [6] Khandelwal G, Maria Joseph Raj NP, Kim S-J. Zeolitic Imidazole Framework: Metal–Organic Framework Subfamily Members for Triboelectric Nanogenerators. *Advanced Functional Materials*. 2020;30:1910162.
- [7] Fan F-R, Tian Z-Q, Lin Wang Z. Flexible triboelectric generator. *Nano Energy*. 2012;1:328-34.
- [8] Niu S, Wang S, Lin L, Liu Y, Zhou YS, Hu Y, et al. Theoretical study of contact-mode triboelectric nanogenerators as an effective power source. *Energy & Environmental Science*. 2013;6:3576-83.

- [9] Wang ZL. Triboelectric Nanogenerators as New Energy Technology for Self-Powered Systems and as Active Mechanical and Chemical Sensors. *ACS Nano*. 2013;7:9533-57.
- [10] Zhao C, Feng H, Zhang L, Li Z, Zou Y, Tan P, et al. Highly Efficient In Vivo Cancer Therapy by an Implantable Magnet Triboelectric Nanogenerator. *Advanced Functional Materials*. 2019;29:1808640.
- [11] Hu W, Wei X, Zhu L, Yin D, Wei A, Bi X, et al. Enhancing proliferation and migration of fibroblast cells by electric stimulation based on triboelectric nanogenerator. *Nano Energy*. 2019;57:600-7.
- [12] Khandelwal G, Chandrasekhar A, Pandey R, Maria Joseph Raj NP, Kim S-J. Phase inversion enabled energy scavenger: A multifunctional triboelectric nanogenerator as benzene monitoring system. *Sensors and Actuators B: Chemical*. 2019;282:590-8.
- [13] Jiang T, Pang H, An J, Lu P, Feng Y, Liang X, et al. Robust Swing-Structured Triboelectric Nanogenerator for Efficient Blue Energy Harvesting. *Advanced Energy Materials*. n/a:2000064.
- [14] Feng H, Zhao C, Tan P, Liu R, Chen X, Li Z. Nanogenerator for Biomedical Applications. *Advanced Healthcare Materials*. 2018;7:1701298.
- [15] Wu C, Wang AC, Ding W, Guo H, Wang ZL. Triboelectric Nanogenerator: A Foundation of the Energy for the New Era. *Advanced Energy Materials*. 2019;9:1802906.
- [16] Seol M, Kim S, Cho Y, Byun K-E, Kim H, Kim J, et al. Triboelectric Series of 2D Layered Materials. *Advanced Materials*. 2018;30:1801210.
- [17] Guo Y, Cao Y, Chen Z, Li R, Gong W, Yang W, et al. Fluorinated metal-organic framework as bifunctional filler toward highly improving output performance of triboelectric nanogenerators. *Nano Energy*. 2020;70:104517.

- [18] Zhang Y, Wu J, Cui S, Wei W, Chen W, Pang R, et al. Organosulfonate Counteranions—A Trapped Coordination Polymer as a High-Output Triboelectric Nanogenerator Material for Self-Powered Anticorrosion. *Chemistry – A European Journal*. 2020;26:584-91.
- [19] Zhai L, Cui S, Tong B, Chen W, Wu Z, Soutis C, et al. Bromine-Functionalized Covalent Organic Frameworks for Efficient Triboelectric Nanogenerator. *Chemistry – A European Journal*. 2020;26:5784-8.
- [20] Thorne MF, Gómez MLR, Bumstead AM, Li S, Bennett TD. Mechanochemical synthesis of mixed metal, mixed linker, glass-forming metal–organic frameworks. *Green Chemistry*. 2020;22:2505-12.
- [21] Xiong M, Zhao X, Yin G, Ching W-Y, Li N. Unraveling the effects of linker substitution on structural, electronic and optical properties of amorphous zeolitic imidazolate frameworks-62 (a-ZIF-62) glasses: a DFT study. *RSC Advances*. 2020;10:14013-24.
- [22] Gustafsson M, Zou X. Crystal formation and size control of zeolitic imidazolate frameworks with mixed imidazolate linkers. *Journal of Porous Materials*. 2013;20:55-63.
- [23] Banerjee R, Phan A, Wang B, Knobler C, Furukawa H, O'Keeffe M, et al. High-Throughput Synthesis of Zeolitic Imidazolate Frameworks and Application to CO<sub>2</sub> Capture. *Science*. 2008;319:939-43.
- [24] Frenzel-Beyme L, Kloß M, Pallach R, Salamon S, Moldenhauer H, Landers J, et al. Porous purple glass – a cobalt imidazolate glass with accessible porosity from a meltable cobalt imidazolate framework. *Journal of Materials Chemistry A*. 2019;7:985-90.
- [25] Kang C-H, Lin Y-F, Huang Y-S, Tung K-L, Chang K-S, Chen J-T, et al. Synthesis of ZIF-7/chitosan mixed-matrix membranes with improved separation performance of water/ethanol mixtures. *Journal of Membrane Science*. 2013;438:105-11.



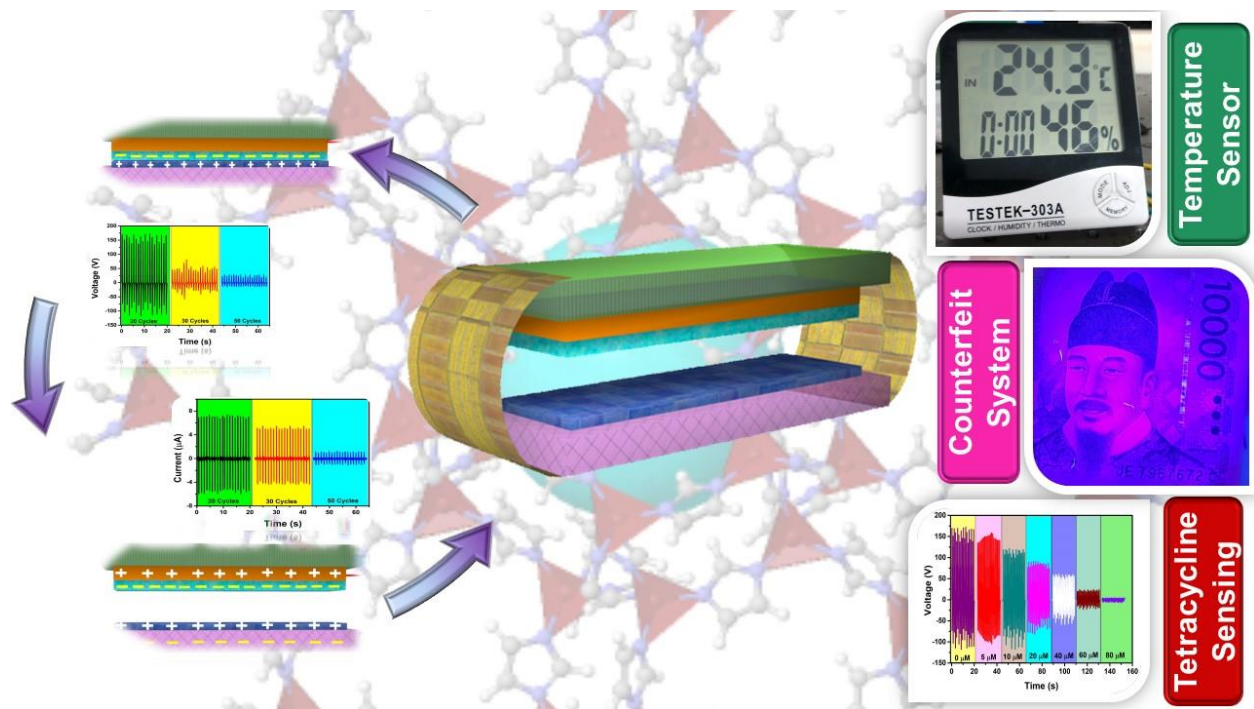
- [26] Ali MA, Ren J, Zhao T, Liu X, Hua Y, Yue Y, et al. Broad Mid-Infrared Luminescence in a Metal–Organic Framework Glass. *ACS Omega*. 2019;4:12081-7.
- [27] Lee S, Lee Y, Kim D, Yang Y, Lin L, Lin Z-H, et al. Triboelectric nanogenerator for harvesting pendulum oscillation energy. *Nano Energy*. 2013;2:1113-20.
- [28] Jeong CK, Baek KM, Niu S, Nam TW, Hur YH, Park DY, et al. Topographically-Designed Triboelectric Nanogenerator via Block Copolymer Self-Assembly. *Nano Letters*. 2014;14:7031-8.
- [29] Tang W, Zhang C, Han CB, Wang ZL. Enhancing Output Power of Cylindrical Triboelectric Nanogenerators by Segmentation Design and Multilayer Integration. *Advanced Functional Materials*. 2014;24:6684-90.
- [30] Wang ZL. Triboelectric nanogenerators as new energy technology and self-powered sensors - Principles, problems and perspectives. *Faraday Discussions*. 2014;176:447-58.



# CHAPTER VI

## Metal-organic Framework: A Novel Material for Triboelectric Nanogenerator based Self-powered Sensors and Systems

### Graphical Overview



## Highlights

- TENG based on a metal-organic framework (MOF) ZIF-8 of the zeolitic imidazole family is reported.
- KPFM confirms the positive behavior of ZIF-8.
- The ZIF-8 and Kapton were used as the active materials for MOF-TENG fabrication.
- The MOF-TENG generated a sustainable output of 164 V and 7  $\mu$ A in vertical contact-separation mode.
- A self-powered ultraviolet counterfeit system and a tetracycline sensor were successfully developed and demonstrated with the MOF-TENG.
- The sensor is highly selective and reusable simply by washing.

## 6.1 Introduction

Nature provides ample sources of energy, such as solar, wind, water, and mechanical energy, which, if exploited, can serve as a partial solution to the depleted state of fossil fuels and the energy crisis. With greater environmental awareness and numerous technological advances, there is a growing market for electronics based on the utilization of clean and abundant energy. To overcome the disadvantages of conventional energy technology, and for the development of sustainable energy sources, Wang et al. introduced an efficient triboelectric nanogenerator (TENG) in 2012 [1]. The TENG can convert various types of energy, e.g., mechanical, wind, and water, into electricity [2-4]. The TENG works in four modes, i.e., freestanding, vertical contact-separation, lateral sliding, and single electrode modes, via utilization of contact electrification and electrostatic induction [5]. Cost-effectiveness, easy design, large output power, and high conversion efficiency are among the key advantages of TENG [5].

The growing demand for wearable electronics, self-powered sensors, e-skin, and sustainable and flexible devices has led to rapid developments in TENG-related technologies [6]. Materials that demonstrate triboelectric charging include various polymers and a few metals [7]. Output performance, triboelectric material, and stability are critical for the development of optimized, functional, and sustainable TENG devices. The metal-organic framework (MOF), composed of a metal ion coordinated with an organic ligand, have yet to be investigated as potential TENG components. MOFs provide flexibility regarding the size, functionality, and geometry of the TENG, which makes them ideal candidates for many applications such as gas sensors, biosensors, drug delivery, fuel storage, catalysis, and adsorbance [8]. The porous structure of the MOF provides a high surface area to improve the functionality of TENG devices. Thus, careful selection of the MOF component can yield a crystal framework with high porosity and high

chemical and thermal stability [8]. Moreover, the ability to expand their metrics and achieve chemical modification without changing the topology are added advantages, promoting high-output performance, and sensing and functional applications [8].

Herein a MOF-based TENG (MOF-TENG) is introduced for self-powered system and sensor applications. The subclass zeolitic imidazole framework (ZIF) of the MOF, having the topology of an inorganic zeolite with a sodalite (SOD) structure, has a small aperture and large pores.[9] In this work, ZIF-8, a unique framework with exceptional thermal and chemical stability and uniform porosity, was selected for the MOF-TENG. Structural and morphological analyses confirmed the successful growth of ZIF-8. The surface potential of ZIF-8 was analyzed using Kelvin probe force microscopy (KPFM), which verified the positive triboelectric behavior of ZIF-8. The fabricated MOF-TENG operated in the traditional vertical contact-separation mode, with ZIF-8 and Kapton as the positive and negative triboelectric layers, respectively. Detailed electrical characterization was carried out to probe the output performance of MOF-TENG. The as-designed MOF-TENG was used to power a temperature/humidity sensor using a capacitor, and for wireless charging of a lithium-ion battery, which can be used for various applications depending on the requirements. Here, the charge batteries were also used to power a portable ultraviolet light-emitting diode (UV-LED) counterfeit system to identify the features of authentic notes and for forensic purposes. In addition, a self-powered tetracycline sensor with high selectivity was demonstrated, using the high specific binding of the MOF. Thus, this work not only demonstrates advanced materials for TENG, but also extends its range of application and functionality.

## 6.2 Experimental

### 6.2.1 Growth of ZIF-8

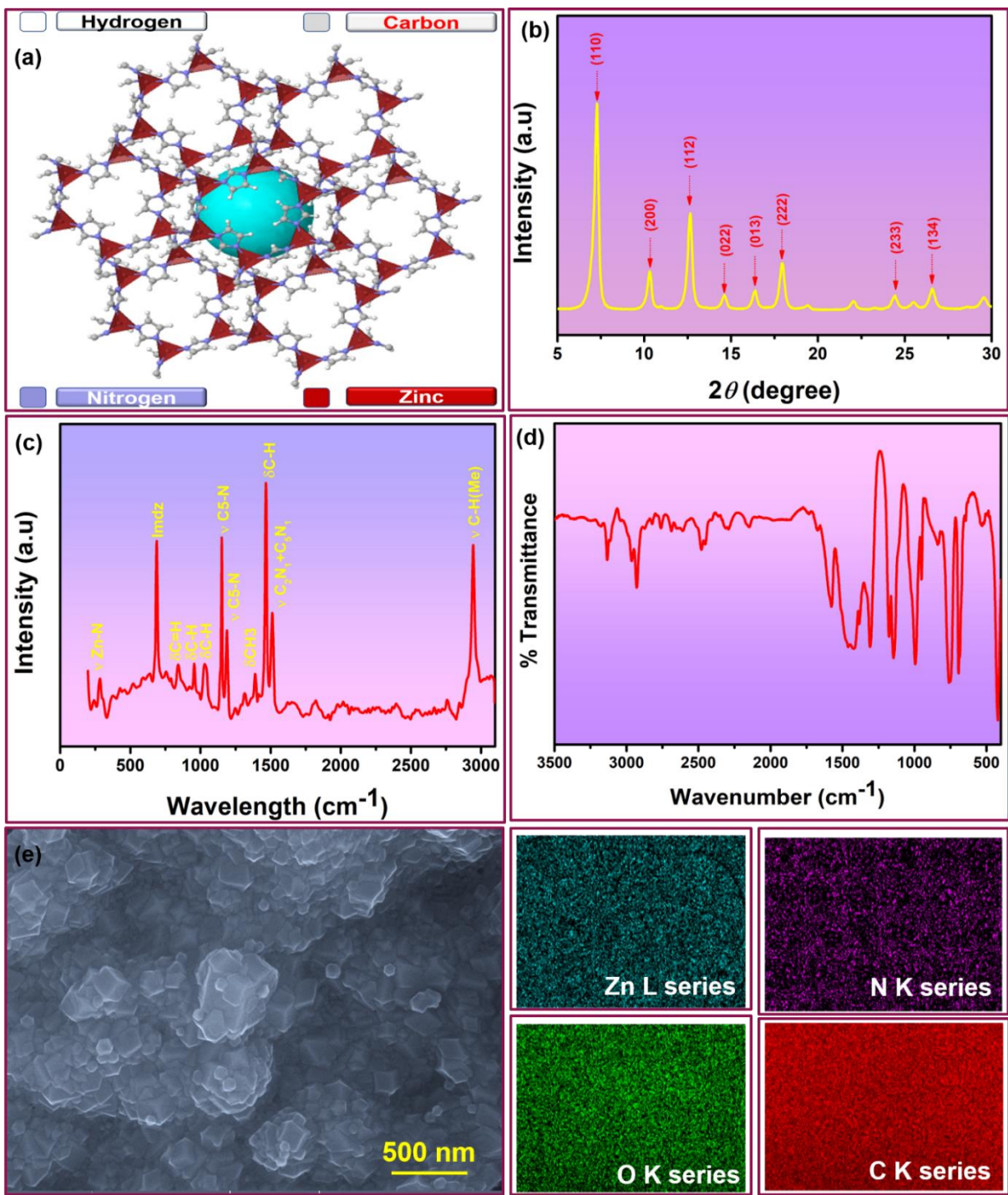
The ZIF-8 was grown on an ITO-coated PET (ITO-PET) substrate for different cycles. ITO-PET was cleaned with acetone before use. For the growth process, a 25-mM methanolic stock solution of  $\text{Zn}(\text{NO}_3)_2 \cdot 6\text{H}_2\text{O}$  and a 50-mM methanolic stock solution of mIm were prepared. The ZIF-8 growth was attained by immersing the cleaned ITO-PET in a mixture of 10-mL  $\text{Zn}(\text{NO}_3)_2 \cdot 6\text{H}_2\text{O}$  and 10-mL mIm stock solution for 30 min at room temperature. The growth was followed by washing with methanol and drying in a nitrogen flow. The same procedure was repeated for 10, 15, 18, 20, 30, and 50 cycles (10-, 15-, 18-,20-, 30- and 50-cyc, respectively) to obtain films of different thicknesses.

### 6.2.2 Fabrication of MOF-TENG

The MOF-TENG was fabricated in a traditional vertical contact-separation mode using ZIF-8 and Kapton as the active triboelectric layers. The ITO-PET acts as an electrode, as well as the substrate for ZIF-8 growth. Copper and PET are the electrode and substrate, respectively, for the Kapton film. The active area for the MOF-TENG was  $2.5 \times 2.5 \text{ cm}^2$ . The 20-cyc ZIF-8-coated ITO-PET and Kapton backed by copper and PET were assembled in vertical contact-separation mode; the assembly was maintained by curved spacers. Similarly, the MOF-TENG device was fabricated for 10-, 15-, 18-, 30- and 50-cyc-grown ZIF-8.

## 6.3 Results and Discussions

The growth of ZIF-8 was attained on indium-doped tin oxide (ITO)-polyethylene terephthalate (PET). The growth procedure was repeated for 10, 15, 18, 20, 30, and 50 cycles (10-, 15-, 18-, 20-, 30- and 50-cyc, respectively) to obtain films of different thicknesses.



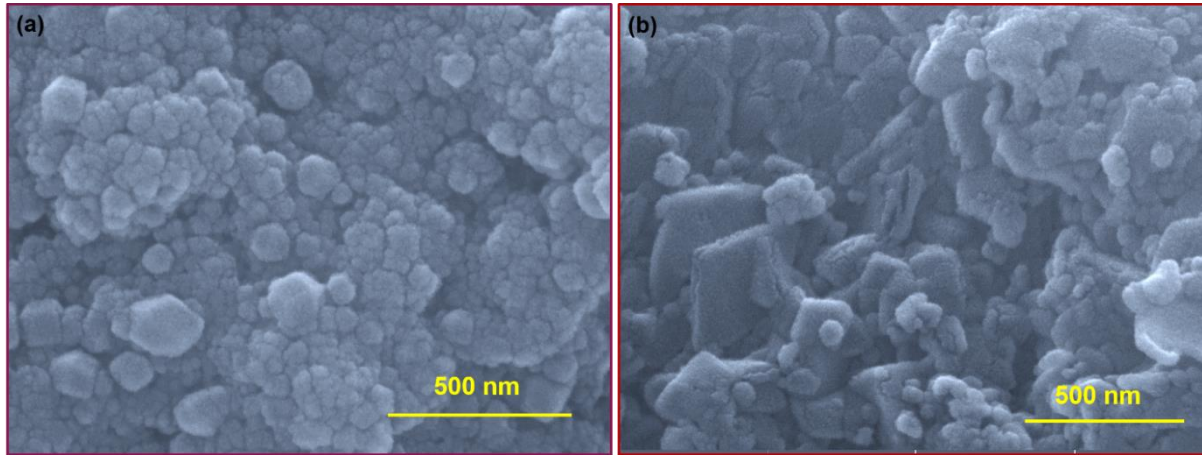
**Figure 6.1.** (a) The structure of ZIF-8 with zinc-nitrogen tetrahedra. (b) XRD spectra of ZIF-8 (c) Raman spectra of ZIF-8. (d) FT-IR spectra of ZIF-8. (e) FE-SEM and EDS mapping analysis of the ZIF-8.



ZIF-8 is a subclass of MOFs that combines the properties of zeolites and MOFs. The ZIF-8 consists of  $\text{Zn}^{2+}$  atoms linked to imidazolate anions via nitrogen and assumes tetrahedral coordination, as shown in Figure 6.1(a) [10, 11]. The ZIF-8 forms a three-dimensional (3D) network with a zeolitic SOD-type topology, having a pore size of 11.6 Å [10]. Figure 6.1(b) shows an X-ray diffraction (XRD) pattern of 20-cyc ZIF-8, with diffraction peaks of 5–30°, 7.3° (011), 10.4° (200), 12.7° (112), 14.7° (022), 16.4° (013), 18.0° (222), 24.6° (233), and 26.7° (134); these results were in good agreement with those from the literature and confirmed the growth of ZIF-8 [10, 12]. The peaks at 7.3° (011), 10.4 (200), and 12.7 (112) are the main features associated with the ZIF-8 phase [10, 11]. Figure 6.1(c) shows the Raman spectra of 20-cyc ZIF-8. The Raman spectra well-matched those in the literature,[13] in which the imidazole peak was dominant. The peaks at 168, 686, 1146, and 1458  $\text{cm}^{-1}$  were assigned to Zn-N stretching, an imidazole ring, C5-N stretching, and methyl bending, respectively [13]. The detailed band assignments are summarized in Table 6.1 [13]. Figure 6.1(d) shows Fourier transform infrared spectroscopy (FT-IR) results for 20-cyc ZIF-8; the peaks at 1591, 1681, and 1849  $\text{cm}^{-1}$  resulted from the bending and stretching of N-H and C=N-H stretching of the imidazole ring, respectively [12]. The peak in the range 1,350–1,500  $\text{cm}^{-1}$  arises due to the stretching vibration of the imidazole ring [12, 14]. The bending vibration mode of the imidazole ring is assigned to the feature shown in the range of 600–1,500  $\text{cm}^{-1}$ . The peak at 421  $\text{cm}^{-1}$  corresponds to the Zn-N stretching mode [15]. The peaks from 2,500–3,000  $\text{cm}^{-1}$  are ascribed to the stretching vibration of N-H, C-H, and O-H in hydroxyl, methyl, and amino groups [12]. The surface morphology and energy dispersive X-ray spectroscopy (EDS) mapping are shown in Figure 6.1(e). The surface morphology of 30-cyc and 50-cyc grown ZIF-8 is shown in Figure 6.2. The EDS mapping confirms the presence of Zn, N, C, and O in ZIF-



8. Thus, structural and morphological analyses confirmed the successful growth of ZIF-8 on the substrate.

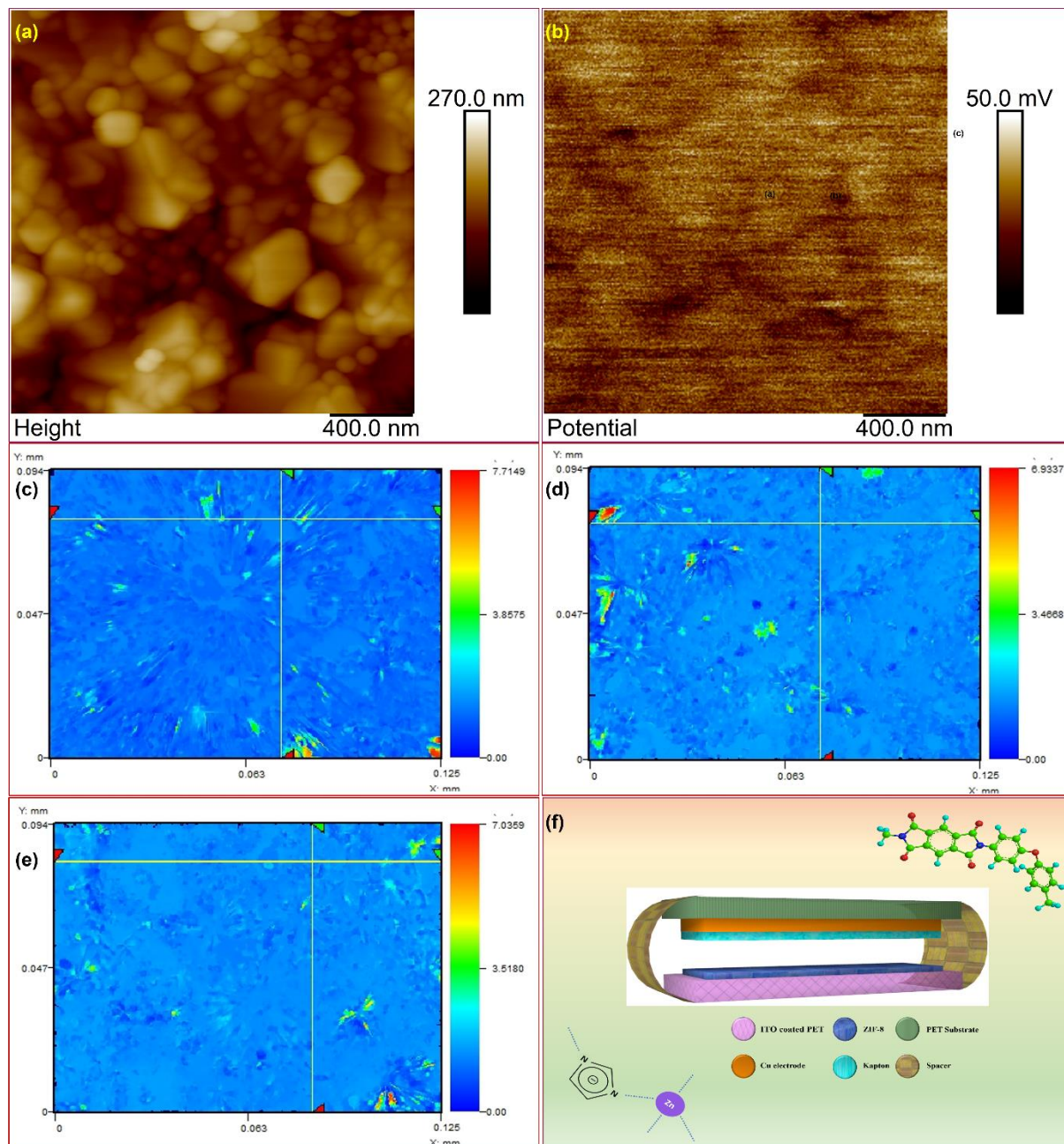


**Figure 6.2.** The FE-SEM image of (a) 30-cyc grown ZIF-8 and (b) 50-cyc grown ZIF-8.

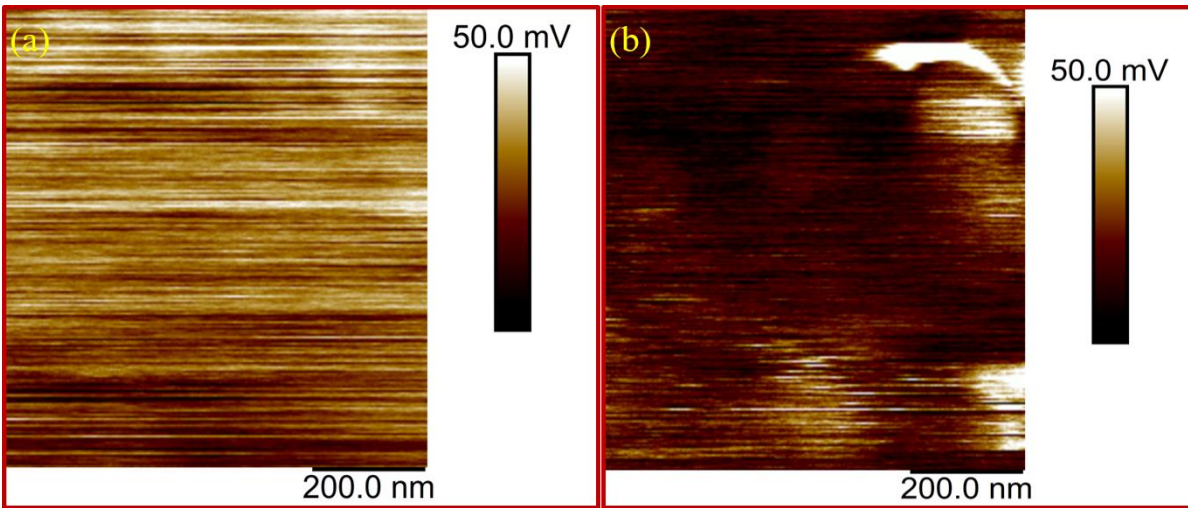
The surface potential plays a major role in the output performance of TENG. Figure 6.3a shows an atomic force microscopy (AFM) image of 20-cyc-grown ZIF-8, which was in good agreement with the field-emission scanning electron microscopy (FE-SEM) results. Figure 6.3b shows the KPFM surface potential, which confirmed the positive surface potential of ZIF-8. Specifically, a positive contact potential difference,  $V_{CPD}$ , means that electrons can tunnel easily from the surface, i.e., the surface can be positively charged easily when in contact with the other material.[16] Thus, ZIF-8 can act as a positive triboelectric material in the TENG. As such, we selected ZIF-8 and Kapton as the positive and negative triboelectric layers for TENG fabrication. KPFM analyses of 30- and 50-cyc ZIF-8 are shown in Figure 6.4. KPFM results indicated that 20-cyc-grown ZIF-8 exhibited a higher surface potential than 30- and 50-cyc-grown ZIF-8.

**Table 6.1.** The detailed band assignment of Raman spectra.

frequency (cm <sup>-1</sup> )	band assignment*
273	V Zn-N
686	Imdz rig puckering, H op bend
755	C=N op bend, $\delta$ N-H
833	C-H op bend (C4-C5)
950	C-H op bend (C2-H)
1021	C-H op bend
1146	V C5-N
1180	V C-N + N-H wag
1187	V C-N
1311	ring expansion + N-H wag
1384	$\delta$ CH <sub>3</sub>
1458	C-H wag
1508	V C4-C5
2931	V <sub>asym</sub> C-H (methyl)



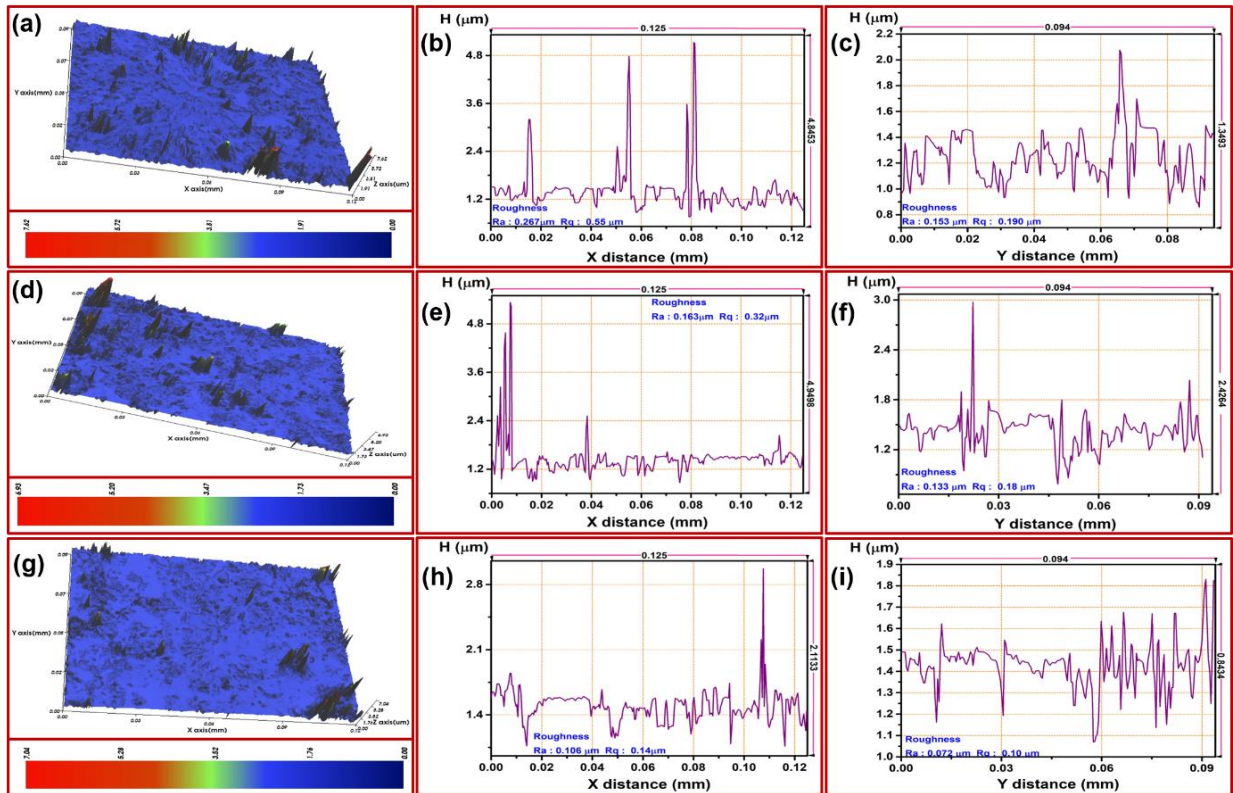
**Figure 6.3.** (a) The AFM image of the 20-cyc ZIF-8 resembles with the FE-SEM analysis. (b) The KPFM of 20-cyc ZIF-8 is confirming the positive  $V_{CPD}$ . (c-e) 2D surface profile images for 20-cyc, 30-cyc, and 50-cyc ZIF-8 respectively. (f) 3-D schematic illustration of the designed MOF-TENG.



**Figure 6.4.** The surface potential mapping using KPFM for (a) 30-cyc ZIF-8 and (b) 50-cyc ZIF-8.

Surface roughness ( $R_a$ ) also plays a critical role in TENG output.[17] The surface  $R_a$  enhances the output performance of TENG [17-19]. Figures 6.3(c–e) show two-dimensional (2D) surface profiling images of 20-, 30-, and 50-cyc-grown ZIF-8, respectively. Furthermore, Figure 6.5 shows a 3D surface profiling image of the TENG; the  $x$ - and  $y$ -direction line profiles correspond to the crosshair markings in the 2D images. The average  $R_a$  values in the  $x$ -direction for 20-, 30-, and 50-cyc samples were 0.267, 0.163, and 0.106  $\mu\text{m}$ , respectively, as measured by 3D profiling. The  $R_a$  parameters indicated better output performance for the 20-cyc-grown ZIF-8, as it exhibited the highest surface  $R_a$  value. The generated output of TENG increases with the surface  $R_a$ , as there is a greater area for optimal contact between the two materials, resulting in a large amount of charge [17].

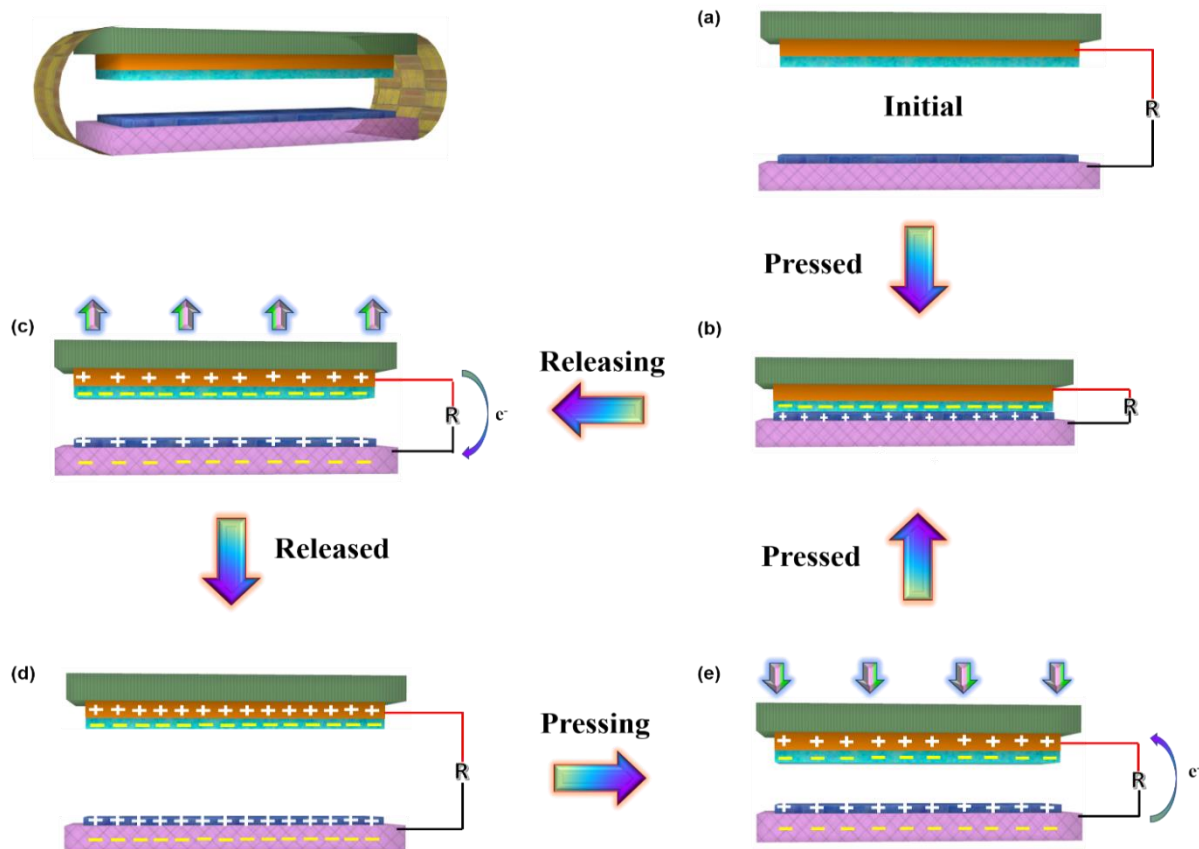




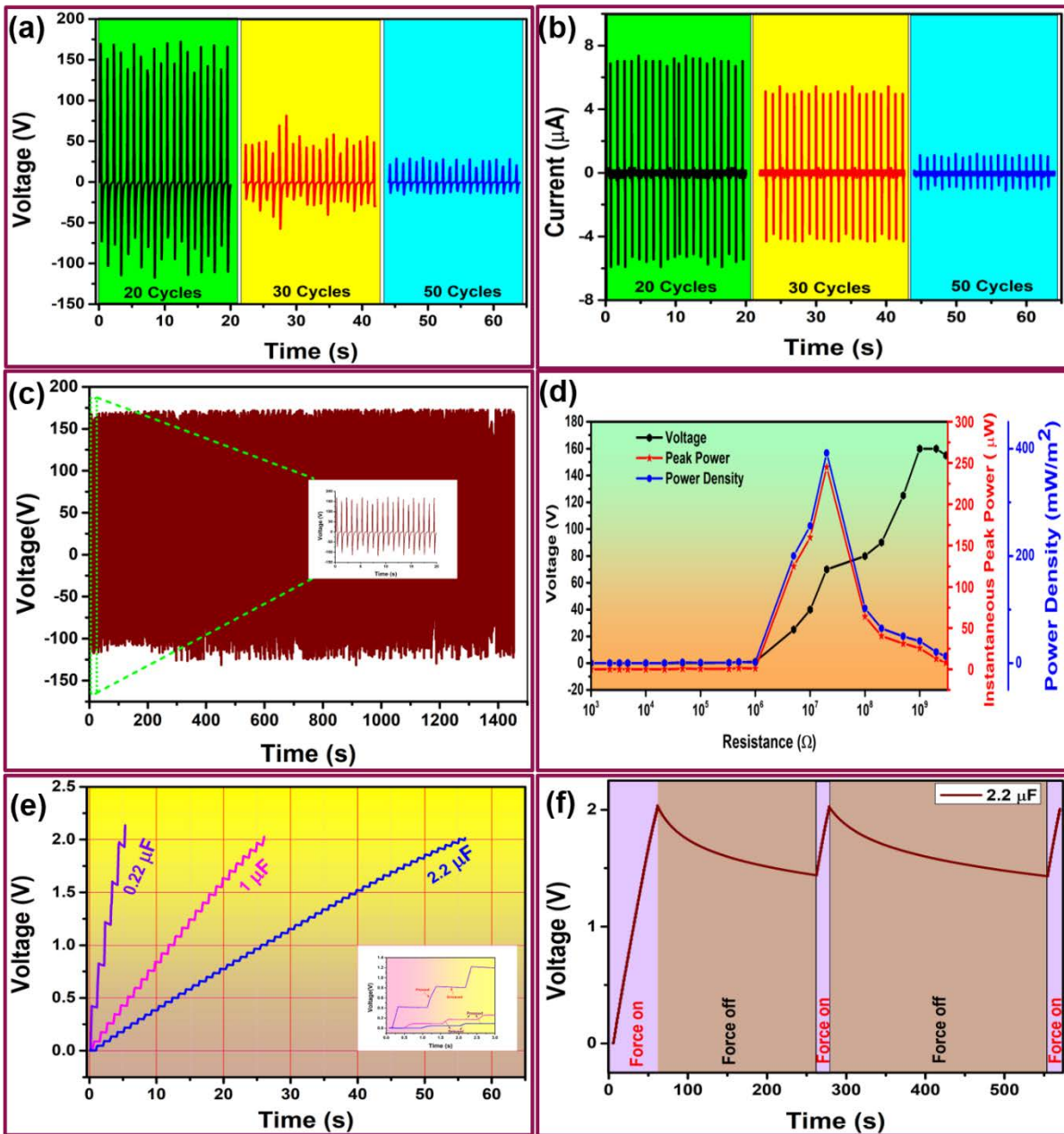
**Figure 6.5.** The 3D profile, X-direction, and Y-direction line roughness profile of the (a-c) 20-cyc ZIF-8. (d-f) 30-cyc ZIF-8 and (g-i) 50-cyc ZIF-8.

Figure 6.3f shows the 3D architecture of the MOF-TENG, which works in a traditional vertical contact-separation mode, with ZIF-8 and Kapton as the positive and negative materials, respectively. The TENG works by a coupled effect between contact electrification and electrostatic induction. Figure 6.6 illustrates the mechanism of charge generation and transformation with ZIF-8 and Kapton as interacting surfaces. Figure 6.6(a) shows the initial state; there is no electric potential difference, as there is no charge generation in the triboelectric layers due to the absence of force. Once an external force is applied, the two layers come into contact and generate equal and opposite charges. Electrons transfer from ZIF-8 to the Kapton due to the triboelectric properties of the respective materials, thus leaving a positive charge on ZIF-8 and a negative charge on Kapton [Figure 6.6(b)]. Once the force is removed, the layers tend to recover their original

shape, generating an electric potential difference. The electric potential difference drives the electrons from the top Kapton electrode to the bottom ZIF-8 electrode, thus producing the half cycle of the output [Figure 6.6(c)]. The electric potential difference tends to increase and reaches a maximum value in the fully released state, as demonstrated in Figure 6.6(d). Now, when the force is reapplied, the MOF-TENG is pressed and the electric potential decreases, resulting in the reverse flow of electrons [Figure 6.6(e)]. This state achieves a reversed output peak. When the two layers are pressed, i.e., come into full contact again, the charges become neutralized, and the MOF-TENG reaches an equilibrium state [Figure 6.6(b)]. This process is then repeated, creating the TENG output.



**Figure 6.6.** The schematic illustration of mechanism in contact-separation mode with different stages viz. releasing, released, pressing and pressed.

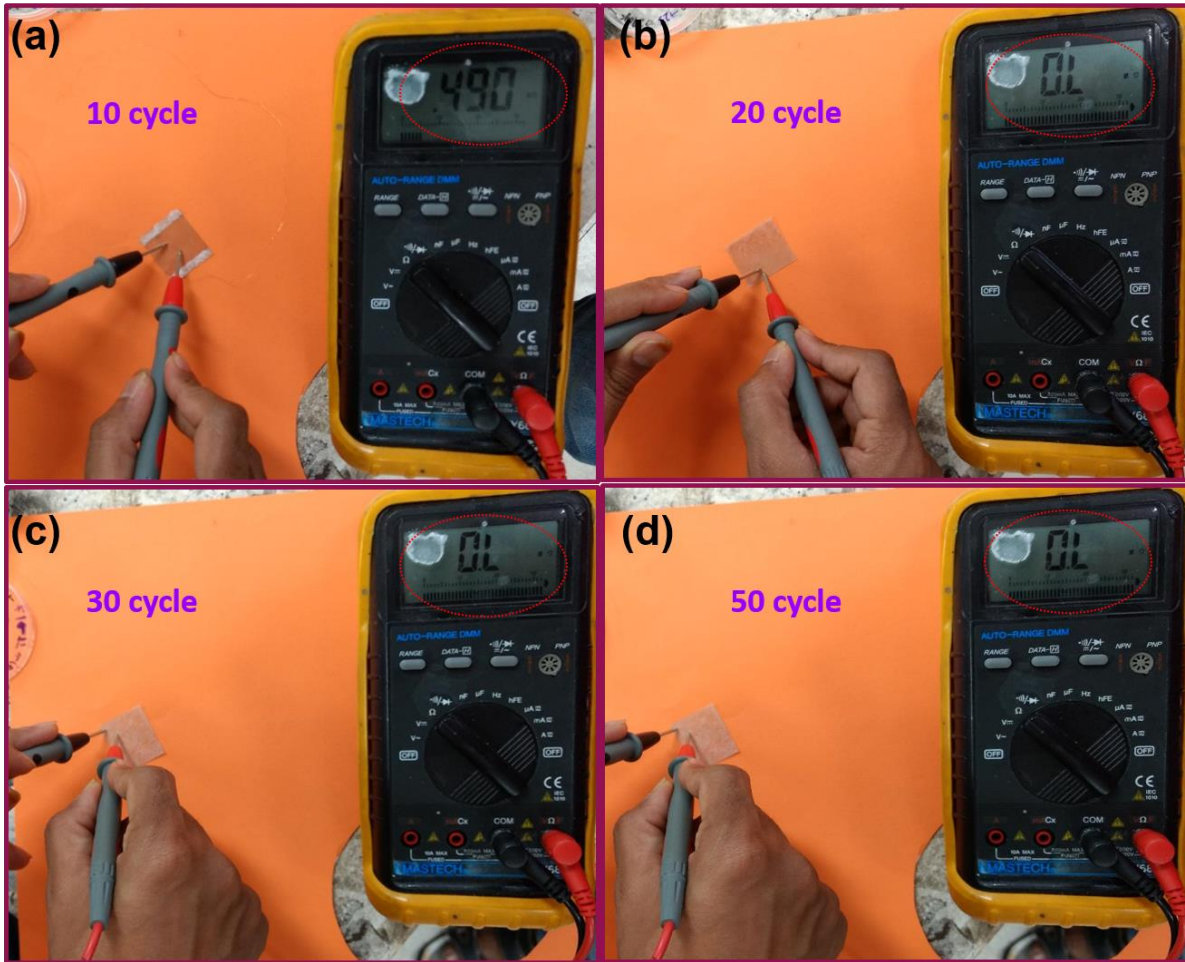


**Figure 6.7.** The detailed electrical performance analysis of MOF-TENG (a) The voltage  $v/s$  time graph for different cycle grown ZIF-8. (b) The current  $v/s$  time graph for different cycle grown ZIF-8. (c) The stability analysis for the 1400 s. (d) Load matching analysis performed at different loads (e) The charging of the different capacitor (0.22  $\mu\text{F}$ , 1  $\mu\text{F}$ , 2.2  $\mu\text{F}$ ) up to 2V. (f) The charging and discharging cycle of 2.2  $\mu\text{F}$  capacitor.

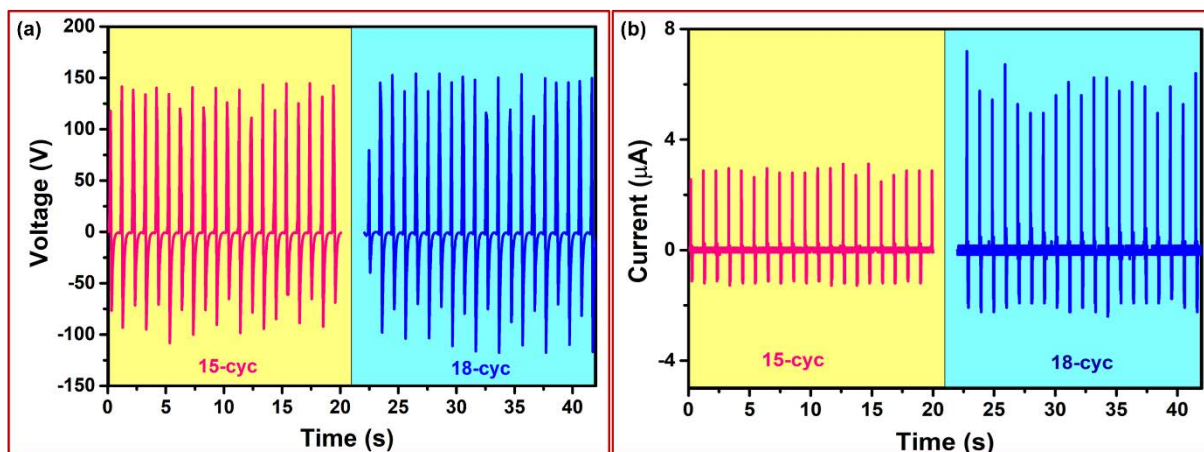


Figure 6.7 shows a detailed electrical characterization of the MOF-TENG. Figure 6.7(a,b) shows the output voltage and current for the 20-, 30-, and 50-cyc-grown ZIF-8. The 20-cyc sample displayed the best output performance, with a voltage of 164 V and a current of 7  $\mu\text{A}$ ; this was attributed to the sharp features in its surface structure, as revealed by KPFM and 3D FE-SEM profile data, leading to a high surface potential. The formed structures tended to aggregate and lose their surface features as the number of cycles increased as revealed by KPFM (Figure 6.4) and FE-SEM (Figure 6.2) data. The output voltage and current for 15- and 18-cyc ZIF-8 were 141 V and 2.9  $\mu\text{A}$  and 155 V and 6.2  $\mu\text{A}$ , respectively, as shown in Figure 6.8. 10-cyc grown ZIF-8 was not selected for measurements as the material coverage was not sufficient, as confirmed by a continuity check (Figure 6.8). The performance of 15- and 18-cyc-grown ZIF-8 were lower than that of 20-cyc ZIF-8. Thus, we selected 20-cyc ZIF-8 for further analysis and applications. The applicability of the device depends on its stability. We performed an endurance test for 1,400 s (Figure 6.7c) to confirm device stability, and then tested the device for up to 16 days. The change in performance was negligible over the 16-day period, as shown in Figure 6.10. The stability test corroborates the suitability of the device for long-term applications. The device was tested under various load resistances to assess the utility of MOF-TENG for practical applications. Figure 6.7d displays the output voltage for various resistances. A maximum peak power of 245  $\mu\text{W}$  and power density of 392  $\text{mW}/\text{m}^2$  were obtained by the MOF-TENG (active area: 2.5 cm  $\times$  2.5 cm) at an equivalent load of 20 M $\Omega$ . To signify the suitability of MOF-TENG for practical applications, such as battery-powered electronics and capacitor energy storage, various capacitors (0.22, 1, and 2.2  $\mu\text{F}$ ) were charged utilizing the MOF-TENG output. Figure 6.7e shows the charging of the different capacitors up to 2 V, with the inset showing the press and release events of the device. The charge–discharge cycle for a 2.2- $\mu\text{F}$  capacitor is shown in Figure 6.7f. The capacitor charging circuit and

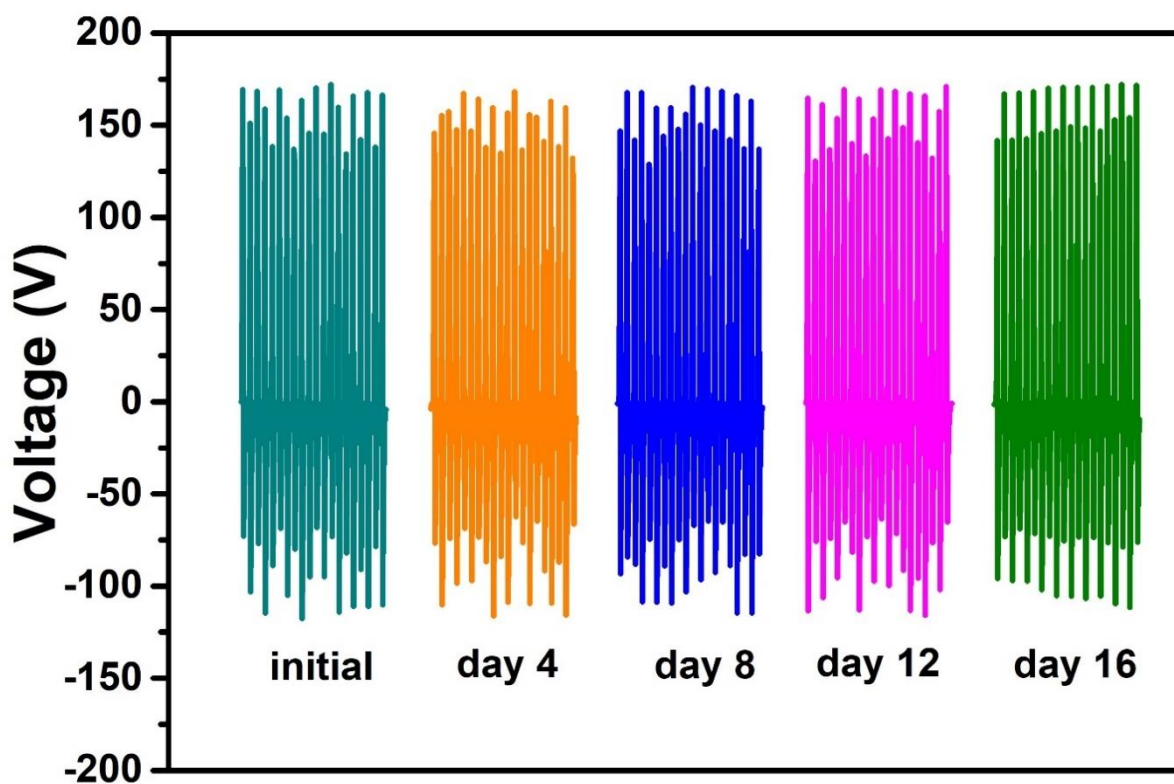
energy stored in the capacitor are shown in Figure 6.11(a,b). The charging of a 100- $\mu$ F capacitor to drive low-power electronics is shown in Figure 6.11(c).



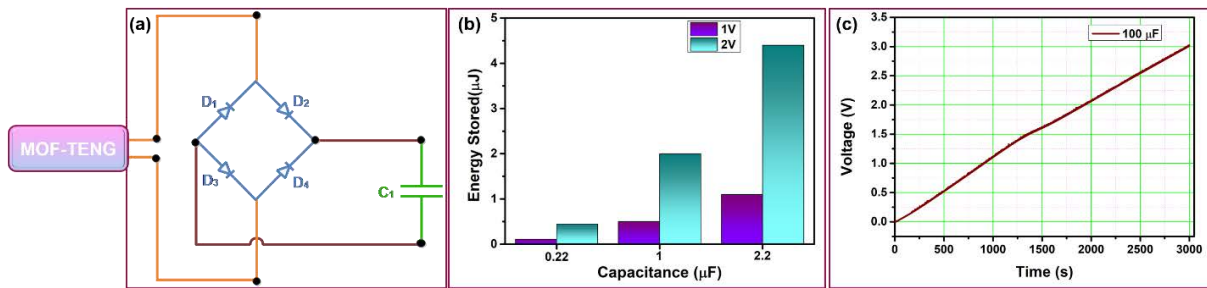
**Figure 6.8.** The continuity check analysis using multimeter for (a) 10-cyc ZIF-8 (b) 20-cyc ZIF-8 (c) 30-cyc ZIF-8 and (d) 50-cyc ZIF-8. The 10 cycles are not sufficient to grow the ZIF-8 over the substrate.



**Figure 6.9.** (a) The voltage of 15-cyc and 18-cyc grown ZIF-8. (b) The current profile of 15-cyc and 18-cyc grown ZIF-8.



**Figure 6.10.** The stability of the device to ensure the durability for long-term use.



**Figure 6.11.** (a) The capacitor charging circuit (b) the energy stored in different capacitors for 1 V and 2 V charging (c) the voltage v/s time graph for 100  $\mu\text{F}$  capacitor charging.

Finally, we demonstrate the applicability of MOF-TENG to drive low-power electronics, a UV counterfeit system, and a tetracycline sensor. Figure 6.12(a) shows the actuation of the temperature sensor for 10 s, which was powered by a 100- $\mu\text{F}$  capacitor. The temperature sensor turned off after 10 s as the capacitor discharged over time.

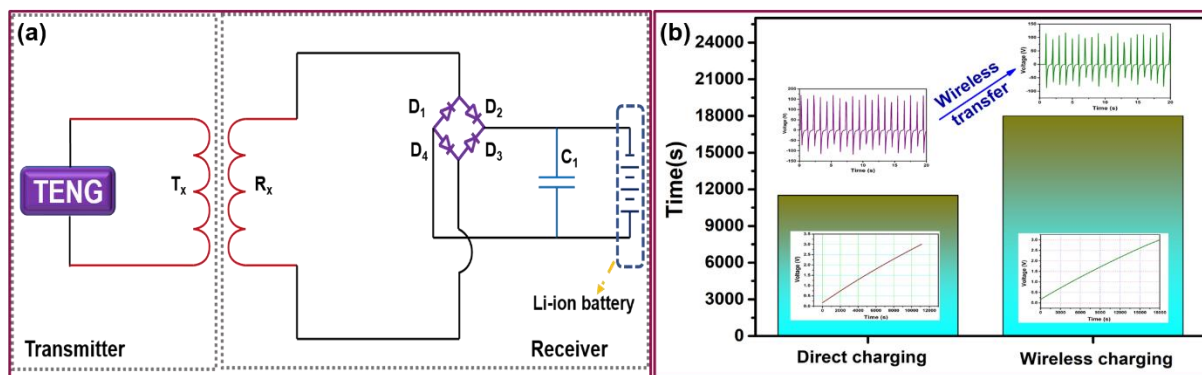


**Figure 6.12.** (a) The lit-up of the temperature sensor for 10s with 100  $\mu\text{F}$  capacitor. (b) The designed self-powered UV counterfeit system is showing the three different areas for the security feature under UV light.

To prevent counterfeiting, various security features are embedded in the currency, for easier identification in the form of fluorescent phosphors that can be viewed under UV



illumination. The currency counterfeit system is of great importance in daily life. Figure 6.12(b) shows a simple, portable UV counterfeit system based on a UV-LED. A lithium (Li)-ion battery, charged using the MOF-TENG, was used to drive UV-LEDs. In the designed system, the UV-LEDs are connected to the Li-ion battery via a switch, similar to a commercial light torch. The battery charging results are summarized in Figure 6.13.[20] Here we identified embedded security features in Korean currency, specifically, the won. The three security regions of the Korean Won, which are not visible to the naked eye, are highlighted in the currency under UV light exposure [Figure 6.12(b)]. Thus, a simple, cheap, and easy-to-use system with potential commercial applications was successfully demonstrated.



**Figure 6.13.** (a) The circuit for wireless charging. (b) The time consumed for direct and wireless charging with the battery charging profile and the transferred voltage profile.

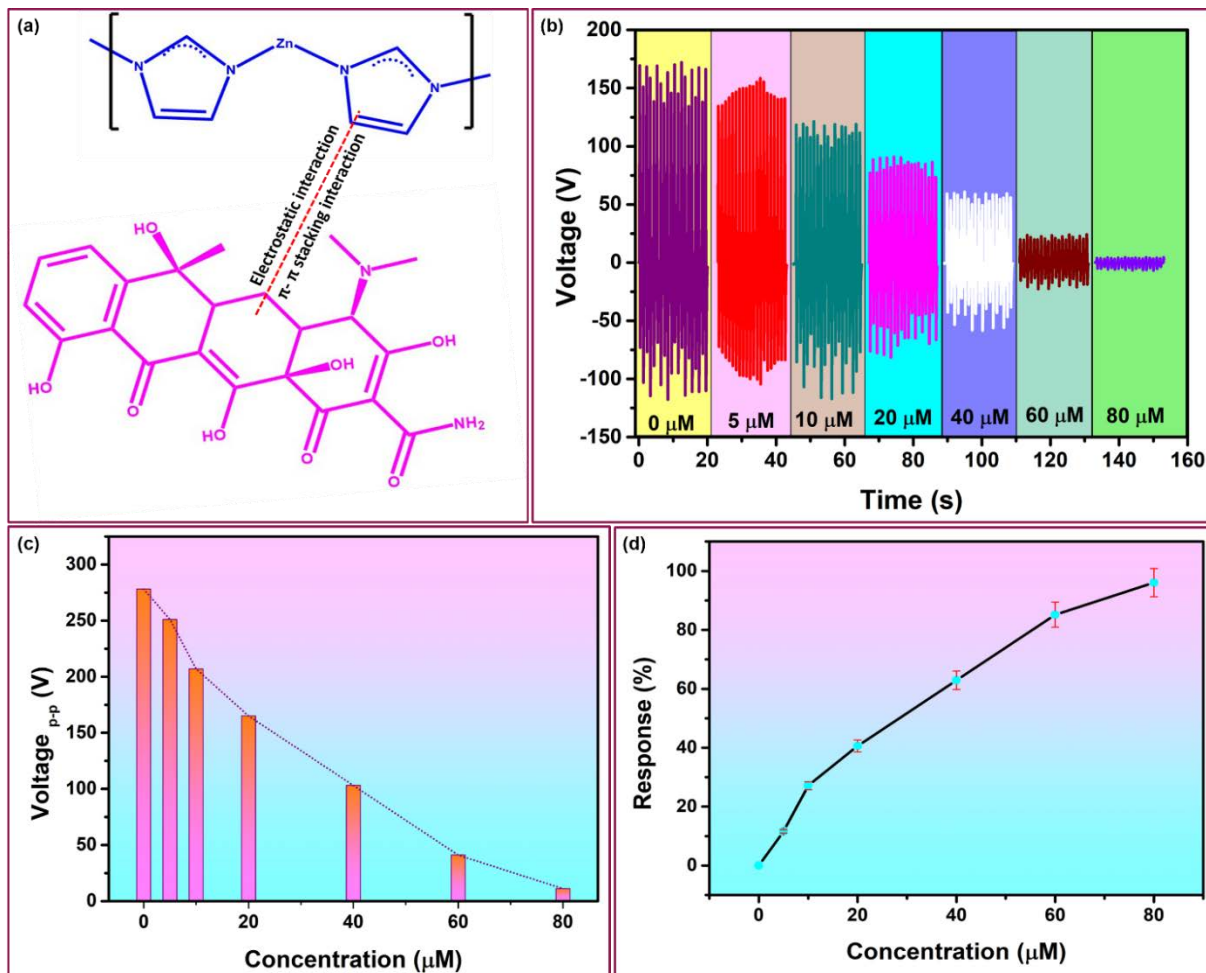
Tetracycline is an antibiotic that is effective against both Gram-positive and Gram-negative bacteria and works by inhibiting protein synthesis in the pathogen [21]. Tetracycline is used to treat various human diseases such as cholera, acne, syphilis, and other types of infections. Other applications of tetracycline include its use as an animal growth promoter, and in human therapy and as an additive in livestock feed, aquatic products, etc [22]. Tetracycline induces many side effects, such as onycholysis and nail discoloration. Persistent exposure to tetracycline can decrease

human immunity towards diseases and may induce drug resistance to bacteria, as it is not fully degraded in the organism's system. Moreover, tetracycline can give rise to endocrine disorders [23]. Tetracycline is generally administered orally; most of it is excreted in faecal matter or urine. However, a substantial amount of tetracycline released in water sources pollutes the natural aquatic environment; thus, simple, cheap and rapid detection is of utmost importance. Here we demonstrate a highly selective tetracycline sensor based on MOF-TENG. The MOF can selectively adsorb contaminants, depending on the spacing configuration of the metal and organic ligand [12]. The adsorption generally involves acid-base, electrostatic, hydrophobic, and  $\pi$ - $\pi$  interactions [12, 24]. The mechanism for tetracycline interaction is shown in Figure 6.14(a). ZIF-8 is highly selective to tetracycline, compared to other species [12]. The mobility of  $\pi$  electrons is lower in the imidazole ring compared to that in the benzene ring, resulting in a lower electron density in the benzene ring [12]. The benzene ring of tetracycline interacts with the imidazole ring of ZIF-8 via  $\pi$ - $\pi$  interactions, as shown in Figure 6.14(a) [12, 25]. Control experiments were carried out to monitor changes in the voltage signal caused by the interaction. Different concentrations of tetracycline (5–80  $\mu$ M) at a constant volume (50  $\mu$ L) were dropped directly onto the ZIF-8 surface. The tetracycline-treated MOF-TENG was dried at ambient temperature prior to electrical measurements. The dependence of the voltage output of MOF-TENG on tetracycline concentration is shown in Figure 6.14(b). The voltage of MOF-TENG decreases with an increase in tetracycline concentration due to the interaction between the benzene ring of tetracycline and the imidazole ring. The electron density is lower in the benzene ring, which reduces the tribopositive behavior of the material, thereby reducing the electron-giving properties of the material. Figure 6.14(c) shows the peak-to-peak voltage as a function of the concentration. The response of the MOF-TENG to different tetracycline concentrations was determined as follows: [26]

$$R\% = \frac{V_0 - V}{V} \times 100\% \quad (1)$$

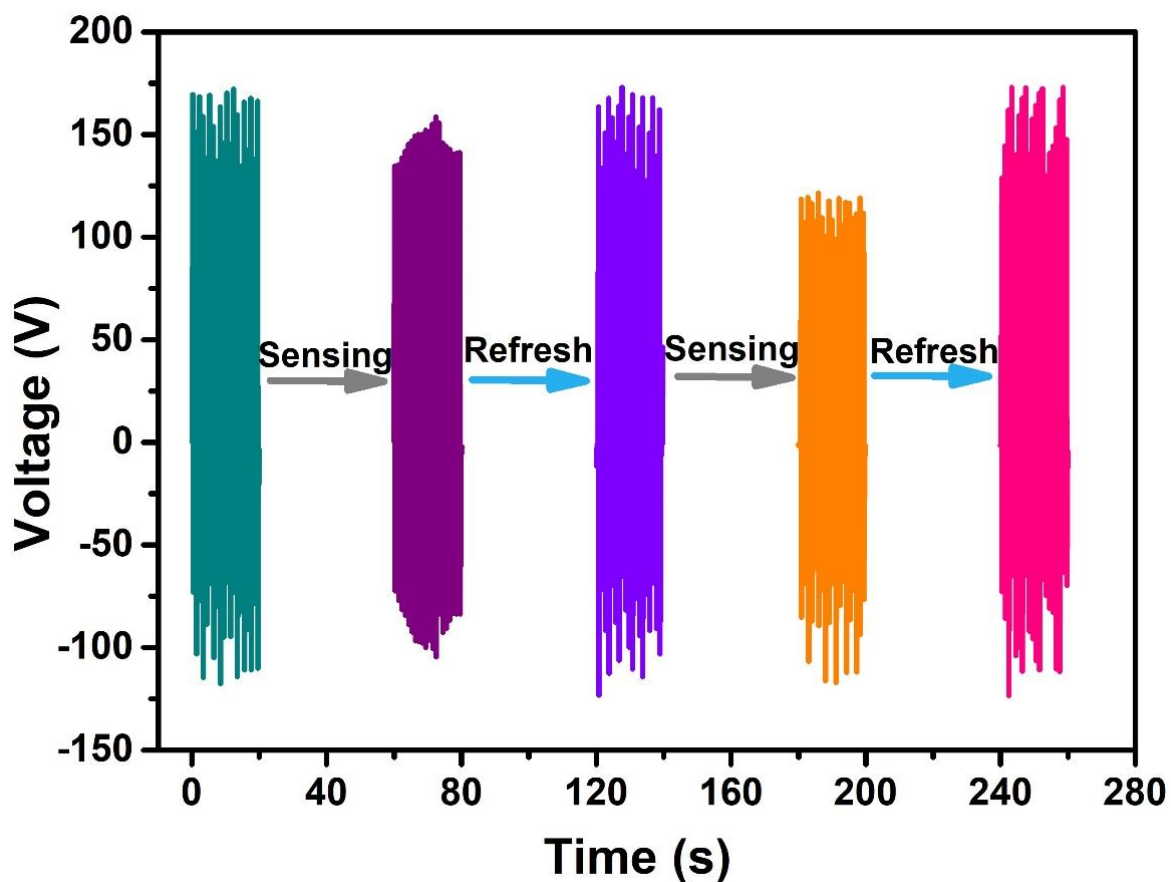
where  $V_0$  is the initial voltage, and  $V$  is the voltage obtained after adsorption.

An 80  $\mu\text{M}$  amount of tetracycline showed a maximum response of 96.4%. The sensitivity of the measurement was 3.12  $\text{V}/\mu\text{M}$ , with a correlation coefficient ( $R^2$ ) value of 0.982; this indicated that the MOF-TENG could be used for tetracycline detection. After the measurement, the ZIF-8 layer was washed with methanol and dried under nitrogen flow to check the reusability of the device. The device was successfully refreshed simply by washing the ZIF-8 with methanol (Figure 6.15).



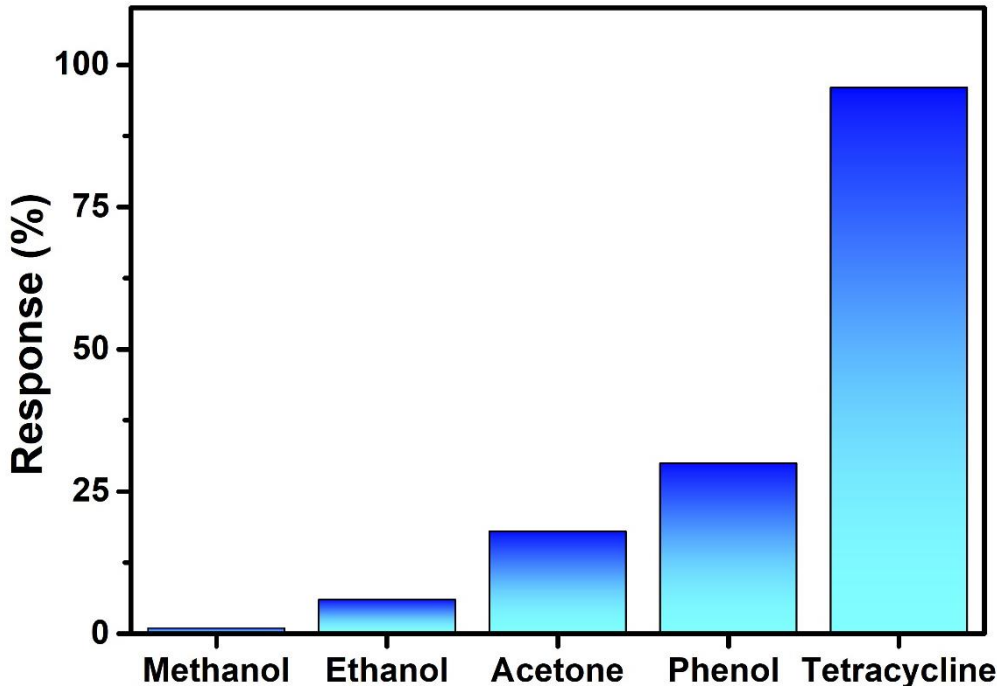


**Figure 6.14.** (a) The mechanism for the interaction of tetracycline with ZIF-8 via electrostatic and  $\pi$ - $\pi$  interaction. The voltage v/s time graph for the different concentrations of tetracycline. The voltage decreases with the increase in tetracycline concentration ascribed to lowered tribo positive nature of the ZIF-8. (c) The bar graph for the peak to peak voltage variation with the concentration of the tetracycline. (d) The % response of the device for various concentrations with a correlation coefficient ( $R^2$ ) of 0.982.



**Figure 6.15.** The MOF-TENG can be refresh by simple washing. The data with sensing and refreshing confirms the reusability of the device. The output has negligible change after washing with methanol.

The selectivity of MOF-TENG towards tetracycline was compared to other species (ethanol, methanol, acetone, and phenol). The response of the other species was poor compared to tetracycline (Figure 6.16). Ethanol, methanol, and acetone do not contain any aromatic rings in their structure to interact with the tetracycline; as a result, their responses were negligible. Phenol contains a hydroxyl group and has high electron density compared to the benzene ring; thus, phenol can become positively charged more easily compared to the benzene ring. The response differed for phenol but was lower than that of tetracycline. Thus, MOF-TENG can be used for the selective detection of tetracycline, with successful recovery after measurements via simple washing with methanol. We believe that the demonstrated counterfeit system and sensing application can lead to a wide range of design concepts and applications of MOF-based TENG in various fields, due to the properties of the MOF.



**Figure 6.16.** The response of other species. The tetracycline shows the maximum response followed by phenol confirming the selectivity of the device.

## 6.4 Conclusion

In conclusion, we introduced a novel multifunctional material (MOF) for TENGs. We have developed a contact-separation TENG with ZIF-8 and Kapton as the active materials. The designed MOF-TENG provides a sustainable output performance of 164 V and 7  $\mu$ A with 20-cyc grown ZIF-8. The MOF-TENG was demonstrated as a self-powered sensor in various system applications. A UV counterfeit system was illustrated as a potential commercial application based on TENG. A highly selective, recoverable tetracycline sensor was also presented, in which the sensor sensitivity was due to a specific interaction between tetracycline and ZIF-8. From these results, it is expected that the MOF will continue to contribute novel active materials for various TENG functionalities.

## References

- [1] Fan F-R, Tian Z-Q, Lin Wang Z. Flexible triboelectric generator. *Nano Energy*. 2012;1:328-34.
- [2] Khandelwal G, Chandrasekhar A, Alluri NR, Vivekananthan V, Maria Joseph Raj NP, Kim S-J. Trash to energy: A facile, robust and cheap approach for mitigating environment pollutant using household triboelectric nanogenerator. *Applied Energy*. 2018;219:338-49.
- [3] Dudem B, Huynh ND, Kim W, Kim DH, Hwang HJ, Choi D, et al. Nanopillar-array architected PDMS-based triboelectric nanogenerator integrated with a windmill model for effective wind energy harvesting. *Nano Energy*. 2017;42:269-81.
- [4] Wang ZL, Jiang T, Xu L. Toward the blue energy dream by triboelectric nanogenerator networks. *Nano Energy*. 2017;39:9-23.
- [5] Wang ZL. Triboelectric nanogenerators as new energy technology and self-powered sensors – Principles, problems and perspectives. *Faraday Discussions*. 2014;176:447-58.
- [6] Wang Y, Yang Y, Wang ZL. Triboelectric nanogenerators as flexible power sources. *npj Flexible Electronics*. 2017;1:10.
- [7] Wang ZL. Triboelectric Nanogenerators as New Energy Technology for Self-Powered Systems and as Active Mechanical and Chemical Sensors. *ACS Nano*. 2013;7:9533-57.
- [8] Furukawa H, Cordova KE, O’Keeffe M, Yaghi OM. The Chemistry and Applications of Metal-Organic Frameworks. *Science*. 2013;341.
- [9] Kaur H, Mohanta GC, Gupta V, Kukkar D, Tyagi S. Synthesis and characterization of ZIF-8 nanoparticles for controlled release of 6-mercaptopurine drug. *Journal of Drug Delivery Science and Technology*. 2017;41:106-12.

- [10] Park KS, Ni Z, Côté AP, Choi JY, Huang R, Uribe-Romo FJ, et al. Exceptional chemical and thermal stability of zeolitic imidazolate frameworks. *Proceedings of the National Academy of Sciences*. 2006;103:10186-91.
- [11] Papporello RL, Miró EE, Zamaro JM. Secondary growth of ZIF-8 films onto copper-based foils. Insight into surface interactions. *Microporous and Mesoporous Materials*. 2015;211:64-72.
- [12] Wu C-s, Xiong Z-h, Li C, Zhang J-m. Zeolitic imidazolate metal organic framework ZIF-8 with ultra-high adsorption capacity bound tetracycline in aqueous solution. *RSC Advances*. 2015;5:82127-37.
- [13] Kumari G, Jayaramulu K, Maji TK, Narayana C. Temperature Induced Structural Transformations and Gas Adsorption in the Zeolitic Imidazolate Framework ZIF-8: A Raman Study. *The Journal of Physical Chemistry A*. 2013;117:11006-12.
- [14] Liu B, Jian M, Liu R, Yao J, Zhang X. Highly efficient removal of arsenic(III) from aqueous solution by zeolitic imidazolate frameworks with different morphology. *Colloids and Surfaces A: Physicochemical and Engineering Aspects*. 2015;481:358-66.
- [15] He M, Yao J, Liu Q, Wang K, Chen F, Wang H. Facile synthesis of zeolitic imidazolate framework-8 from a concentrated aqueous solution. *Microporous and Mesoporous Materials*. 2014;184:55-60.
- [16] Seol M, Kim S, Cho Y, Byun K-E, Kim H, Kim J, et al. Triboelectric Series of 2D Layered Materials. *Advanced Materials*. 2018;30:1801210.
- [17] Lee S, Lee Y, Kim D, Yang Y, Lin L, Lin Z-H, et al. Triboelectric nanogenerator for harvesting pendulum oscillation energy. *Nano Energy*. 2013;2:1113-20.
- [18] Jeong CK, Baek KM, Niu S, Nam TW, Hur YH, Park DY, et al. Topographically-Designed Triboelectric Nanogenerator via Block Copolymer Self-Assembly. *Nano Letters*. 2014;14:7031-8.

- [19] Tang W, Zhang C, Han CB, Wang ZL. Enhancing Output Power of Cylindrical Triboelectric Nanogenerators by Segmentation Design and Multilayer Integration. *Advanced Functional Materials*. 2014;24:6684-90.
- [20] Chandrasekhar A, Alluri NR, Sudhakaran MSP, Mok YS, Kim S-J. A smart mobile pouch as a biomechanical energy harvester towards self-powered smart wireless power transfer applications. *Nanoscale*. 2017;9:9818-24.
- [21] Zierhofer CM, Hochmair ES. Geometric approach for coupling enhancement of magnetically coupled coils. *IEEE Transactions on Biomedical Engineering*. 1996;43:708-14.
- [22] Duan Z, Guo Y-X, Kwong D-L. Rectangular coils optimization for wireless power transmission. *Radio Science*. 2012;47.
- [23] Li P, Kumar S, Park KS, Park HG. Development of a rapid and simple tetracycline detection system based on metal-enhanced fluorescence by europium-doped AgNP@SiO<sub>2</sub> core-shell nanoparticles. *RSC Advances*. 2018;8:24322-7.
- [24] Martins AC, Pezoti O, Cazetta AL, Bedin KC, Yamazaki DAS, Bandoch GFG, et al. Removal of tetracycline by NaOH-activated carbon produced from macadamia nut shells: Kinetic and equilibrium studies. *Chemical Engineering Journal*. 2015;260:291-9.
- [25] Segal BM. Photosensitivity, nail discoloration, and onycholysis: Side effects of tetracycline therapy. *Archives of Internal Medicine*. 1963;112:165-7.
- [26] Hasan Z, Jung SH. Removal of hazardous organics from water using metal-organic frameworks (MOFs): Plausible mechanisms for selective adsorptions. *Journal of Hazardous Materials*. 2015;283:329-39.

[27] Li N, Zhou L, Jin X, Owens G, Chen Z. Simultaneous removal of tetracycline and oxytetracycline antibiotics from wastewater using a ZIF-8 metal organic-framework. *Journal of Hazardous Materials*. 2019;366:563-72.

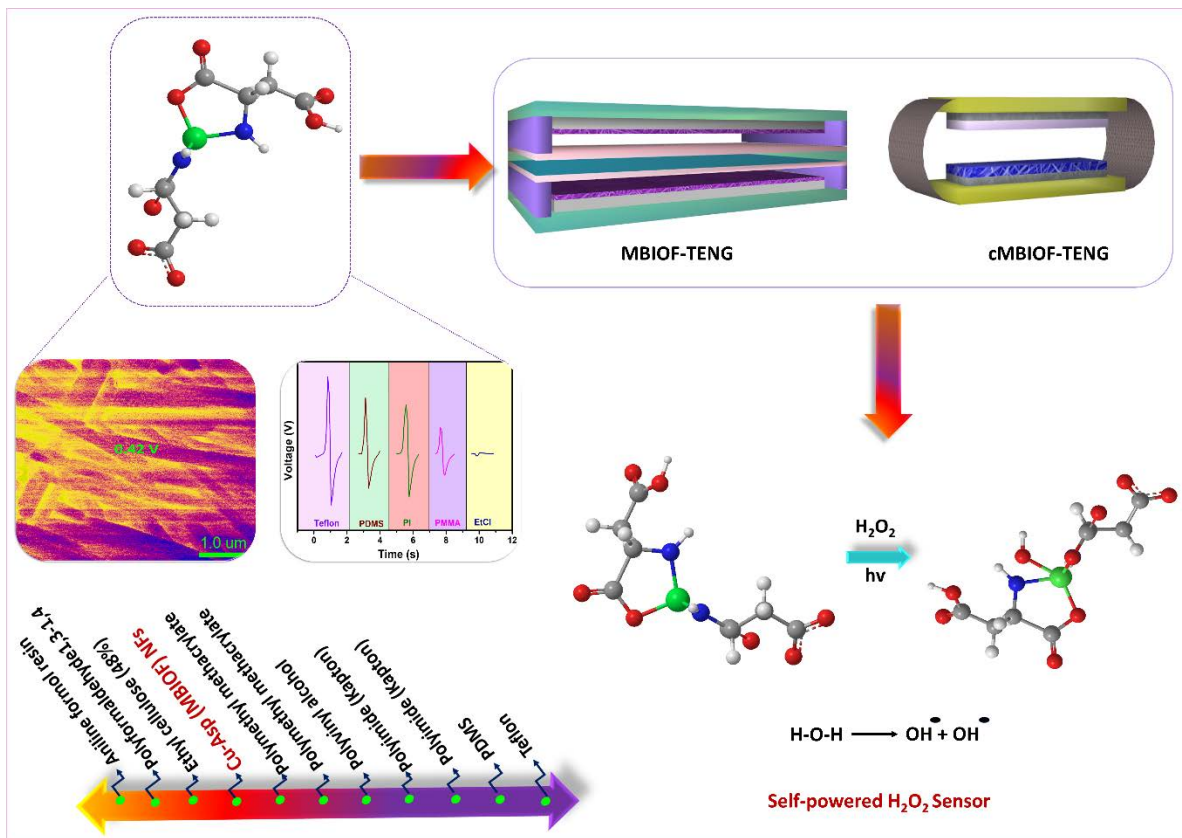
[28] Fu Y, He H, Liu Y, Wang Q, Xing L, Xue X. Self-powered, stretchable, fiber-based electronic-skin for actively detecting human motion and environmental atmosphere based on a triboelectrification/gas-sensing coupling effect. *Journal of Materials Chemistry C*. 2017;5:1231-9.



# CHAPTER VII

## Metal-biomolecule Nanofibers: A Novel Material for Triboelectric Nanogenerator and Self-powered Sensors

### Graphical Overview



## Highlights

- Co-ordinational directed self-assembly process for the synthesis of Copper (Cu)- Aspartate (Asp) nanofibers (NFs).
- The material is characterized by various techniques.
- Cytotoxicity studies on mammary epithelial cell lines and dermal fibroblasts cell were carried.
- Accessible to the scale-up coating on substrates like aluminum foil, PET sheet, and ITO coated PET.
- A freestanding layer mode TENG (MBIOF-TENG) and C-S mode (cMBIOF-TENG) are fabricated and analyzed in detail for electrical characterization.
- Cu-Asp NFs are arranged in triboelectric series supported by device output.
- The adherence of material on the PET sheet is demonstrated by stability measurement in Single electrode lateral sliding mode TENG.
- Finally, a self-powered hydrogen peroxide sensor was demonstrated.

## 7.1 Introduction

Self-assembly is a process in which preexisting small molecules are arranged to form organized structures like rod, particles, tubes, and fibers, etc. The materials obtained by self-assembly can be tuned for their properties by modifying the shape, size, or composition. Alternatively, coordination chemistry can also be used for synthesizing different structures. Recent studies showed the formation of infinite coordination polymer particles (ICPs) via coordination polymerization of the organic ligand with metal ion [1]. The one-dimensional coordination polymers like fiber and tubes etc. are not explored in much detail. The use of biomolecules as a building block for the formation of one-dimensional structures offers the advantage of environmental and biological compatibility. Moreover, the biomolecules provide multiple coordination modes by offering different metal-binding sites. Thus metal-biomolecule frameworks (MBIOFs) offer unique structural diversity. The other type of MBIOFs is chiral MBIOFs that are synthesized by the use of chiral biomolecules. The chiral MBIOFs have high potential in the field of separation, catalysis, and recognition [1-3].

In our previous works, we demonstrated the zeolitic imidazole framework for energy harvesting via triboelectric nanogenerator (TENG) and for self-powered sensing [4, 5]. TENG converts mechanical energy to electrical energy via the coupling effect of triboelectrification and electrostatic induction [6, 7]. TENG is widely reported for a vast range of applications, including cell modulation, water disinfection, drug delivery, self-charging, biological and chemical sensors [5, 8-11]. The TENG gets tremendous attraction as an energy harvester due to its easy fabrication, high-output, cost-effectiveness, and available device modes, etc. Besides, direct current (DC) TENG is also reported, which can be used directly, without any rectifier for most of the practical

purposes [12]. The triboelectric series consists of materials arranged on the basis of their ability to gain or lose electrons. The triboelectric series is dominated by the few metals and mostly polymers, which are not idle candidates for many applications [13]. Recently, two-dimensional materials and metal-organic frameworks (MOFs) are explored for the TENG [14]. The exploration of multifunctional materials for TENG is highly desirable to extend the applications. In context, of self-powered chemical and biological sensors, the specificity and selectivity are of utmost importance. The selectivity and sensitivity can be easy to achieve by the use of multifunctional materials that can be tuned as per the desired requirement.

In this work, to best of our knowledge for the very first, a TENG based on coordination directed one-dimensional metal-biomolecule nanofibers (NFs) is reported. The L-aspartic acid (Asp) plays the role of biomolecule (organic ligand) to construct one-dimensional  $[\text{Cu}(\text{II})(\text{Asp})]_n$  polymeric chains. The X-ray diffraction, Fourier transform infrared spectroscopy (FT-IR), UV-Vis spectroscopy, and surface morphology analysis suggests the formation of Cu-Asp (MBIOF) NFs. The cytotoxicity studies of the NFs are carried on dermal fibroblast and mammary epithelial cells. The as-synthesized NFs are demonstrated for coating on various substrates by simple tape cast coater. The coated NFs are characterized for surface potential and surface roughness, two critical parameters for TENG. The Cu-Asp NFs are identified for their position in triboelectric series with the help of device output and surface potential. A freestanding layer mode TENG (MBIOF-TENG) and contact-separation mode TENG (cMBIOF-TENG) are fabricated and analyzed in detail for their output performance. Finally, self-powered hydrogen peroxide is demonstrated. The sensor exhibits good sensitivity.

## **7.2 Experimental**

### **7.2.1 Synthesis of Cu-Asp NFs**

The Cu-Asp NFs are prepared using the fast addition method by the mixing of 1.5 mmol  $\text{Cu}(\text{NO}_3)_2 \cdot 6\text{H}_2\text{O}$  in a 10 mL solution of 1 mmol L-aspartic acid and 2mmol of NaOH. Followed by addition, the growth of NFs was visualized.

### **7.2.2 Synthesis of MgO nanosheets**

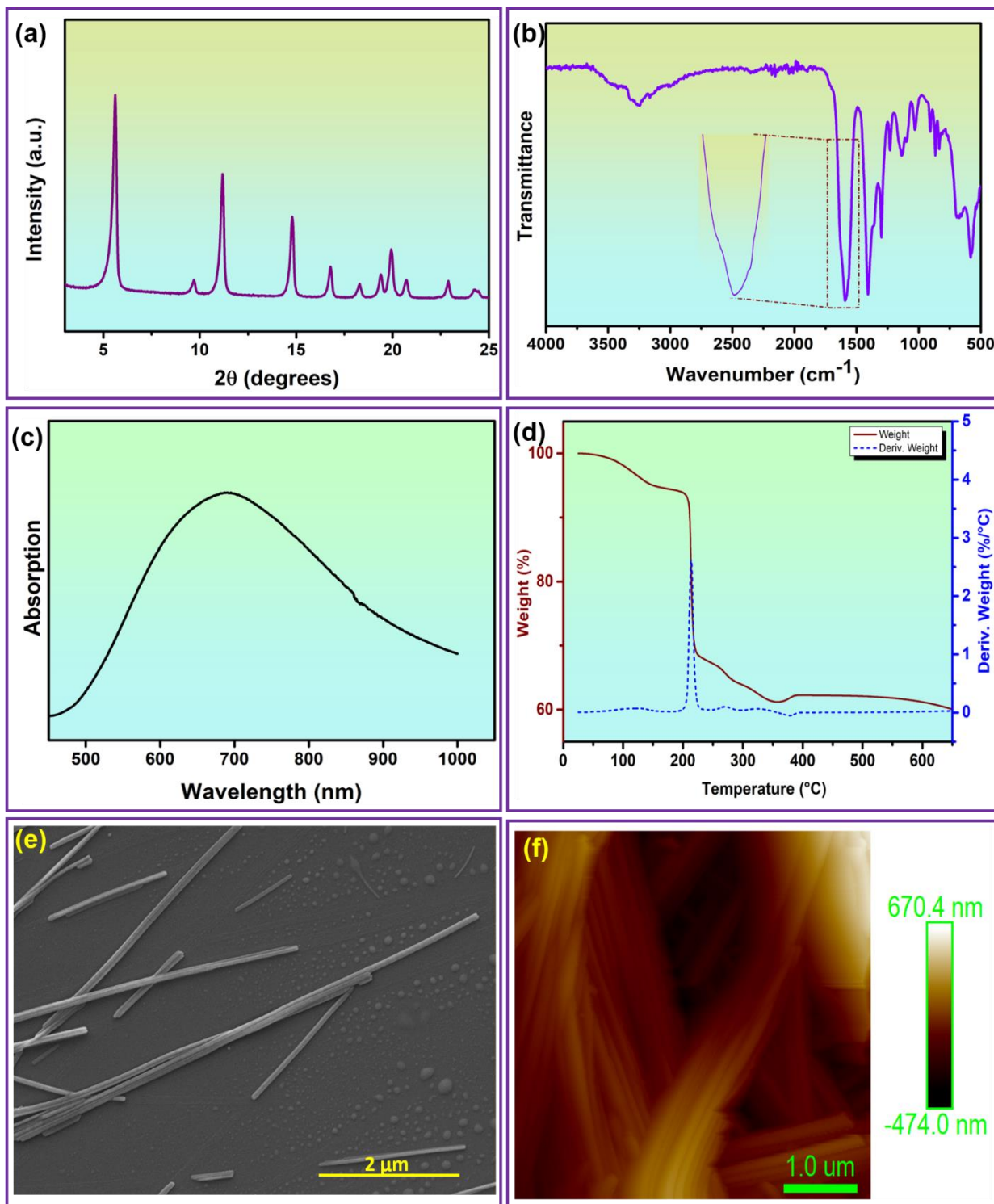
The MgO nanosheets were synthesized by the hydrothermal method. The 4.29 g of magnesium nitrate ( $\text{Mg}(\text{NO}_3)_2 \cdot 6\text{H}_2\text{O}$ ) was dissolved in 50 mL DI water, followed by the addition of 0.796 g of urea. The solution was transferred in stainless steel lined autoclave. The autoclave was placed at 180 °C for 2h. The autoclave was allowed to cool, and the recovered material was washed several times with DI water.

### **7.2.3 Coating on various substrate**

The as-synthesized NFs are allowed to control dry to remove a certain amount of water. Then, the material was coated on different substrates like aluminum, PET sheet, and ITO coated PET using tape cast coater and allowed to air dry.

### **7.2.4 Fabrication of TENG**

The freestanding triboelectric nanogenerator was fabricated by cutting the material coated on aluminum foil in the required dimension. The PET sheet was attached as the substrate for the fabrication of the top and bottom layers. The intermediate freestanding layer was fabricated by attaching the Teflon layer on both sides of the PET sheet. The fabricated layers were assembled to form the device with the help of the spacer, as shown in Figure 7.6e.



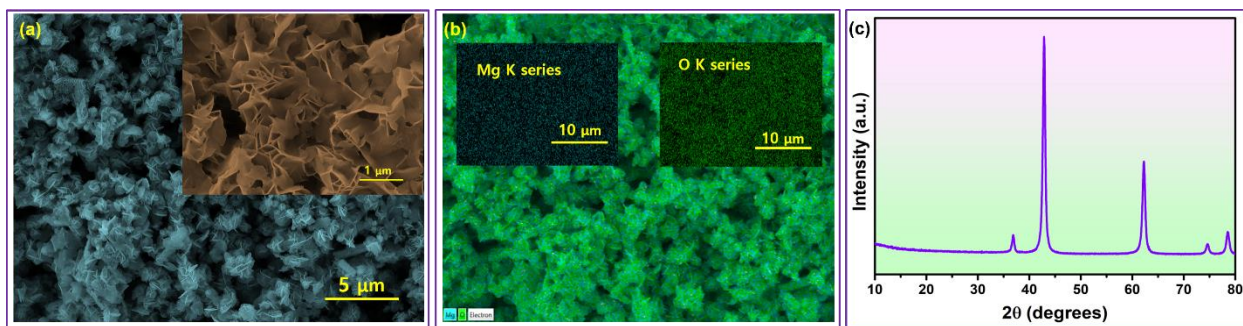
**Figure 7.1.** (a) XRD spectra of the Cu-Asp NFs. (b) FT-IR spectra of Cu-Asp NFs with zoom image showing little peak  $1620\text{ cm}^{-1}$ . (c) UV-Vis absorbance spectra of Cu-Asp NFs. (d) TGA

analysis of the Cu-Asp NFs exhibiting three weight losses. (e) FE-SEM image of the Cu-Asp NFs confirming the morphology. (f) AFM image of the Cu-Asp NFs, where several NFs are stacked together.

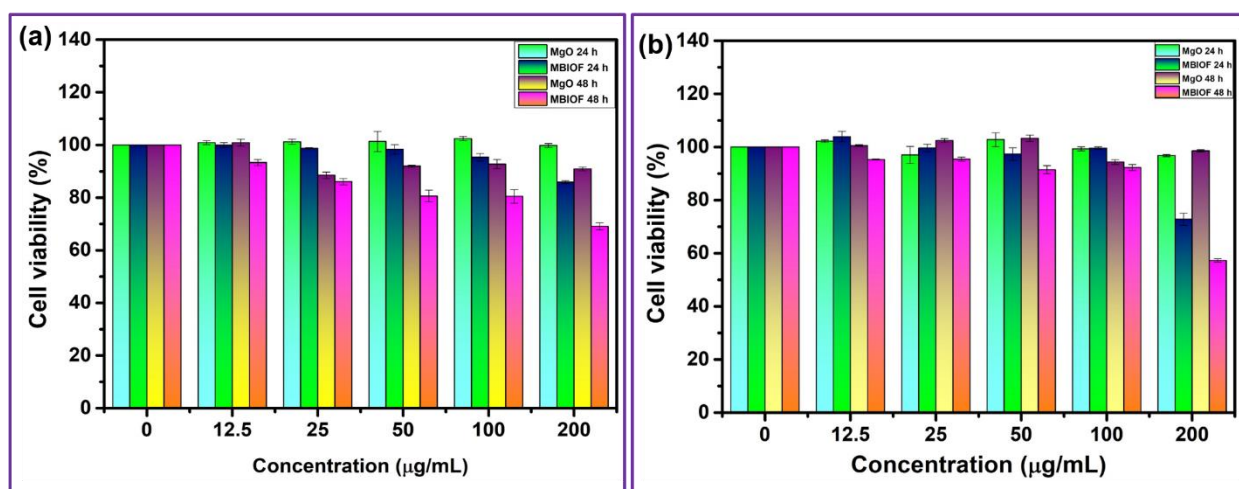
### 7.3 Results and Discussions

Figure 7.1a shows the XRD spectrum of the synthesized Cu-Asp NFs. The XRD peaks confirm the crystalline nature of the NFs and match well with the reported literature. The detailed XRD analysis is complicated due to the small size of the fibers [1, 2]. Furthermore, synthesizing large crystals for single-crystal XRD measurement is challenging [2]. Figure 7.1b shows the FT-IR spectra to probe the NFs assembly process. The band in the range of 1580-1620  $\text{cm}^{-1}$  and 1365-1400  $\text{cm}^{-1}$  are attributed to the coordination of amino acids carboxyl group to Cu (II). The bands in the range of 2500-3700  $\text{cm}^{-1}$  were due to the N-H and hydrogen-bonded -OH stretching. The aspartate ligand and Cu (II) ions are arranged in one dimensional  $[\text{Cu}(\text{Asp})(\text{H}_2\text{O})]_x$  chains [1, 2]. Figure 7.1c shows the UV-Vis spectra of the NFs [2]. The absorption at 690 nm indicates the formation of copper-aspartate complexes in the solution. Figure 7.1d shows the TGA analysis of the NFs. The TGA shows three weight losses. The weight loss from 70 °C to 150 °C is attributed to the evaporation of the water. The weight loss from 190 °C to 250 °C is due to the release of  $\text{CO}_2$  from the amino acid carboxyl group. The final weight loss above 300 °C is ascribed probably to the residue of NFs, which releases  $\text{N}_2$  [2]. The material characterization suggests that NFS was formed by the one-dimensional  $[\text{Cu}(\text{II})(\text{Asp})]_x$  chains [1, 2]. The FE-SEM of the synthesized NFs is depicted in Figure 7.1e. The Cu-Asp NFs are formed with a diameter in the range of 50-80 nm and a length of 5-10  $\mu\text{m}$ . The AFM image of the formed NFs is given in Figure 7.1f, where several NFs are stacked together.





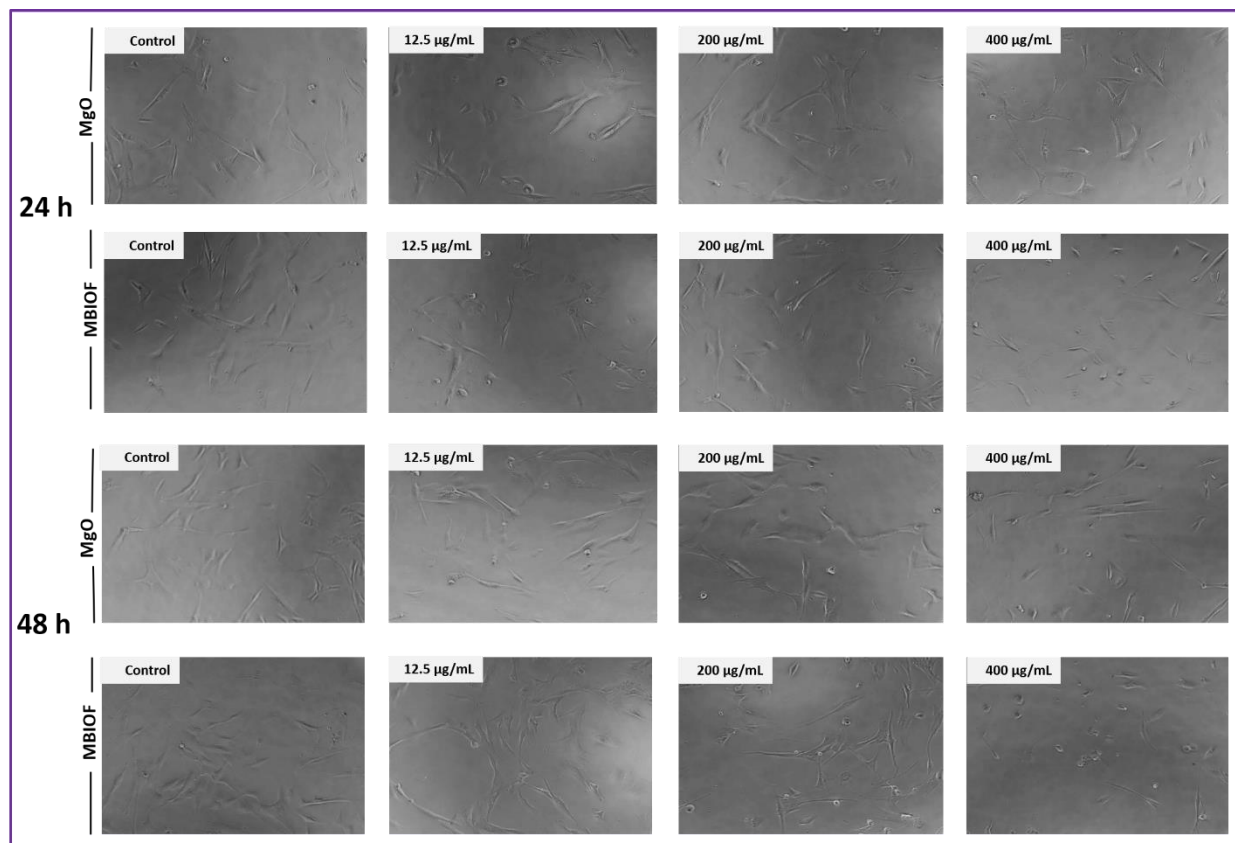
**Figure 7.2.** (a) FE-SEM image of the synthesized MgO nanosheets with a high magnification image shown in the inset. (b) EDS mapping confirming the presence of only Mg and O. (c) XRD spectra of MgO nanosheets confirming the purity and the cubic structure of the nanosheets.



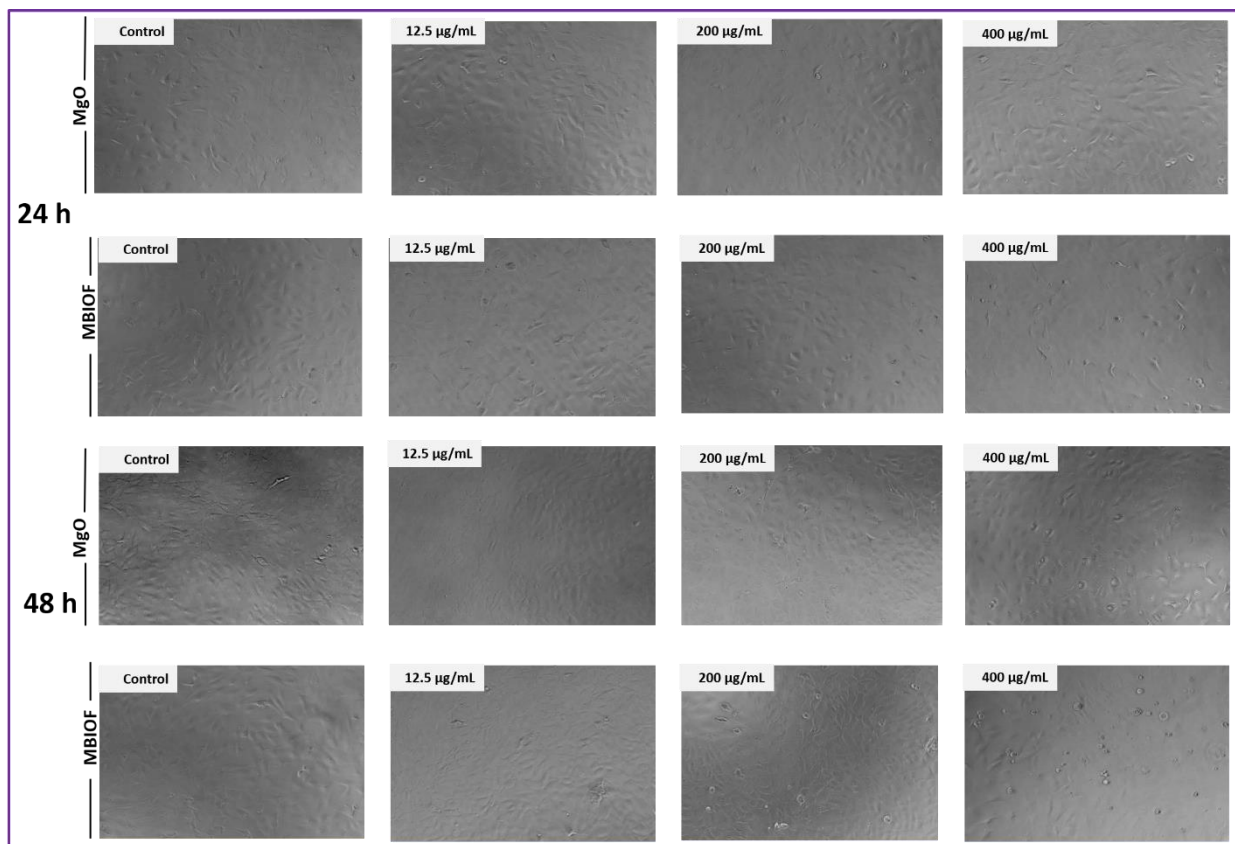
**Figure 7.3.** MTT cell viability assay of MgO and Cu-Asp NFs (MBIOF) on (a) Dermal fibroblast cells and (b) Mammary epithelial cells.

To estimate the cytotoxicity of the prepared MBIOF, we evaluated the cytotoxicity of MBIOF NFs in normal mammary epithelial (MCF-10A) and dermal fibroblasts using the MTT assay at 24 and 48 h post-incubation periods. Magnesium oxide (MgO) nanosheets were used as reference material in cytotoxicity evaluations. The FE-SEM image and EDS mapping of MgO nanosheets are shown in Figure 7.2a and 7.2b. Figure 7.2c shows the XRD spectrum of MgO,

which suggests that MgO nanosheets are highly pure and exhibit cubic structure [15, 16]. The cytotoxic effects of MBIOF NFs and MgO are shown in Figure 7.3a and 7.3 b. As shown in Figure 7.3, prepared MBIOF NFs shows more than 95 % cell viability at 100  $\mu\text{g}/\text{mL}$  concentrations in MCF-10A and dermal fibroblasts cells, indicating a potential application of MBIOF NFs in in-vitro systems at concentrations ranging from 0-100  $\mu\text{g}/\text{mL}$ . Phase-contrast microscopic images, as shown in Figures 7.4 and 7.5, also illustrate minimal effects up to 100  $\mu\text{g}/\text{mL}$  concentrations on MCF-10A and dermal fibroblasts cells exposed to NFs. The reference material MgO did not exert significant cytotoxicity in MCF-10A and dermal fibroblasts at the indicated post-incubation periods.



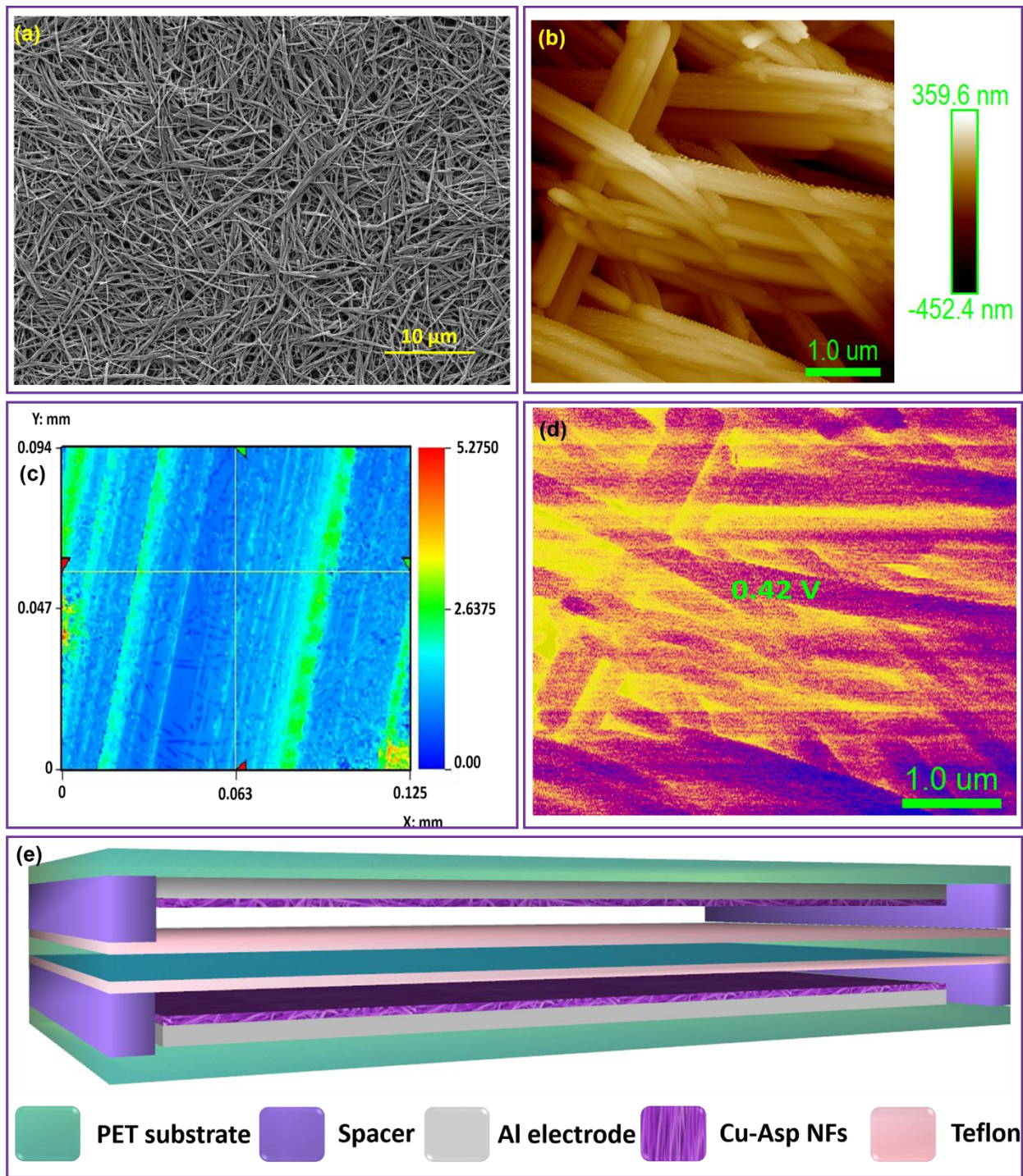
**Figure 7.4.** Phase-contrast microscopy image of MgO and Cu-Asp NF treated dermal fibroblast cells for 24 h and 48 h.



**Figure 7.5.** Phase-contrast microscopy image of MgO and Cu-Asp NF treated mammary epithelial cells for 24 h and 48 h.

The synthesized material was coated on various substrates by a simple tape cast coater. The coated material has excellent adherence to all three substrates, i.e., aluminum foil, PET sheet, and ITO-coated PET. The easy scale-up film fabrication is highly desirable for energy harvesting. Figure 7.6 depicted the characterization of the coated NFs layer used for the fabrication of the TENG. Figure 7.6a illustrates the FE-SEM image of the coated layer, confirming the uniform coverage all over the surface. Figure 7.6b is the AFM image of the coated film with a corresponding KPFM image shown in Figure 7.6d. The KPFM measurement suggests a potential of  $\sim 0.42$  V on the sample.

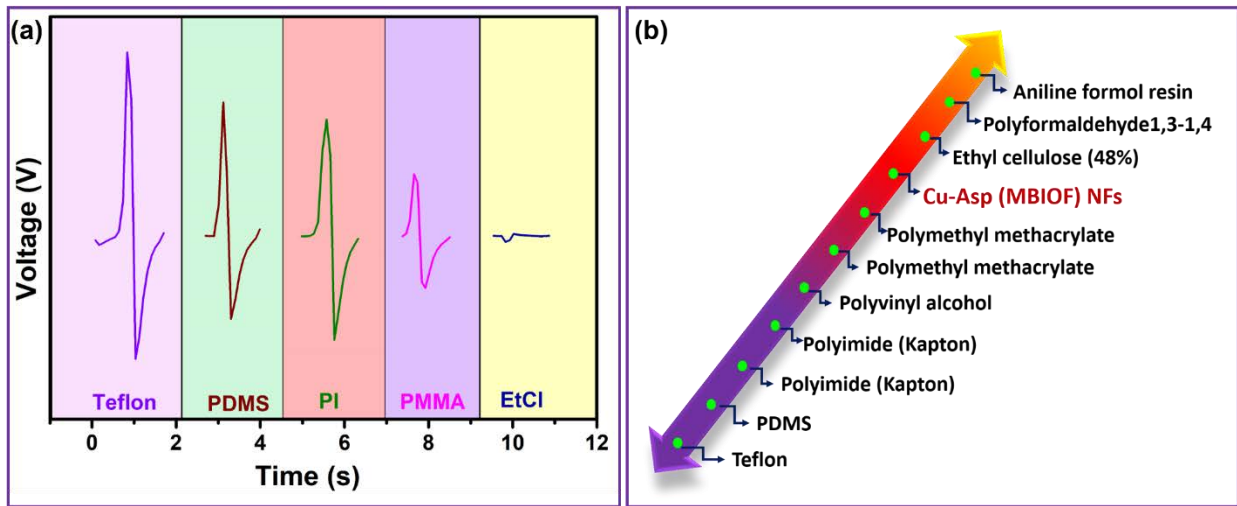




**Figure 7.6.** (a-b) FE-SEM and AFM image of the Cu-Asp NF coated Al foil, respectively. (c) 2D optical profile image of the coated NFs. (d) The KPFM image for the coated NFs. (e) 3D schematic illustration of freestanding layer mode MBIOf-TENG.

The surface roughness of the layer is among one of the parameters that are well known to alter the output of the TENG. The surface roughness is well documented to improve the output of TENG by bringing more area in contact for the electrification [17-19]. Figure 7.6c depicts the 2D surface profile of the coated material. The material exhibits an average surface roughness (Ra), and root mean square roughness (Rq) of 365.76 nm and 482.06 nm respectively across the image. The material showed a Ra value of 293.35 nm and 127.97 nm along X- and Y-direction, respectively corresponding to the yellow cross-hair in the image. The three-dimensional view of the freestanding layer mode TENG (MBIOF-TENG) is illustrated in Figure 7.6e. The device consists of an intermediate Teflon layer and coated NFs as the top/bottom layer. The layers are maintained at a fixed distance with the help of a spacer.

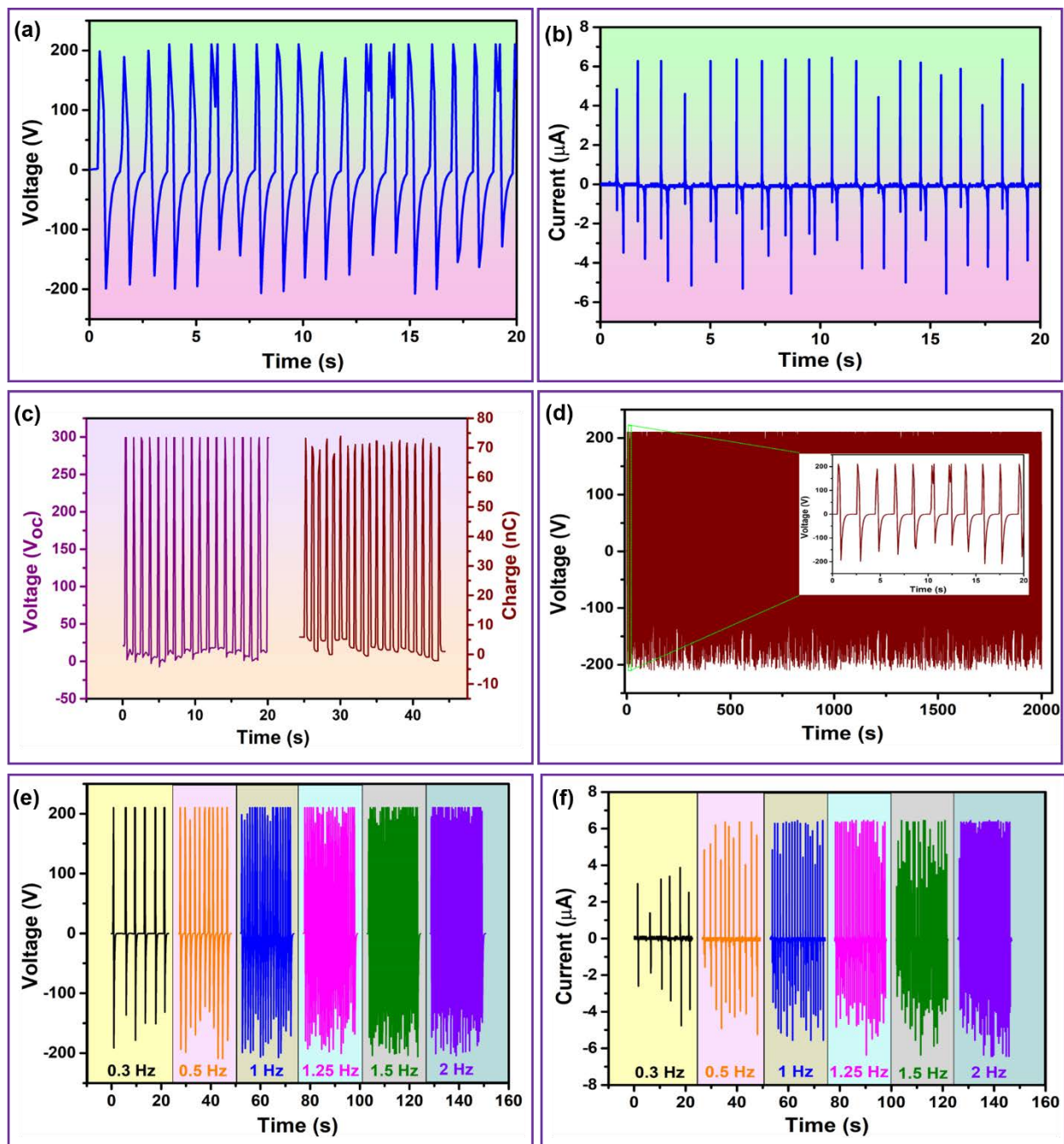
The position of Cu-Asp NFs in the traditional triboelectric series is investigated by checking the relative charging polarity of Cu-Asp NFs against various materials by fabricating a C-S mode TENG [14]. Figure 7.7 shows the output of Cu-Asp with different contacting materials. The positive peak concludes that Cu-Asp NFs are positively electrified when it comes in contact with the Teflon, PDMS, PI, PMMA. The negative peak in the case of contact with ethyl cellulose suggests negative electrification of the Cu-Asp NFs [14].



**Figure 7.7.** (a) The voltage output with different contacting material in C-S mode TENG. (b) Schematic illustrating the assigned position of Cu-Asp NFs in the triboelectric series.

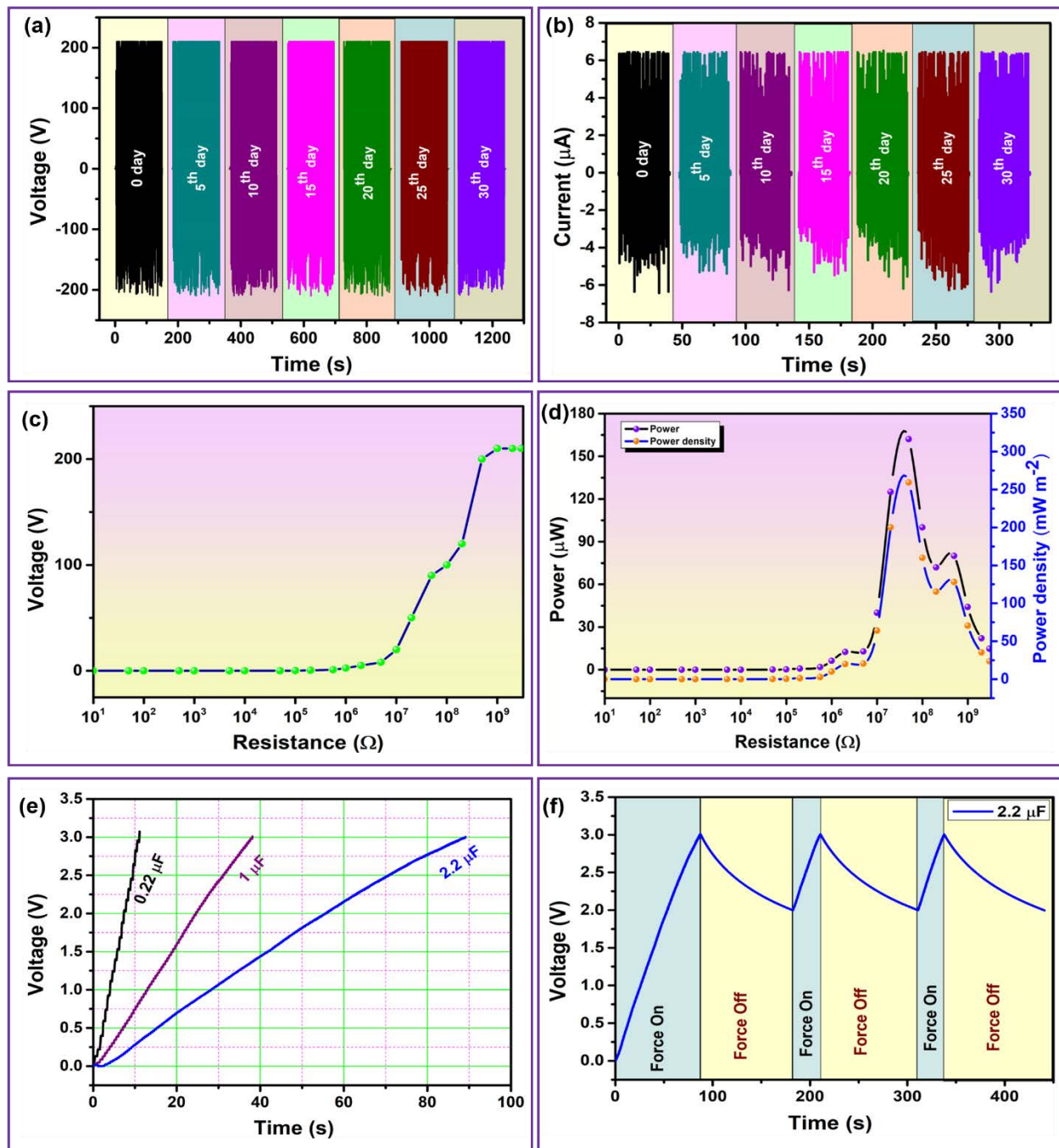
Figure 7.8 reveals the detailed electrical characterization of the Mbiof-TENG. The device generates an output voltage of 200V, current of 6  $\mu$ A, and transferred charge of 72 nC as depicted in Figure 7.8a-c. The open-circuit condition in TENG can be obtained at large resistance where the voltage saturates at  $V_{oc}$  [20]. The Mbiof-TENG achieved a  $V_{oc}$  of 300 V, as shown in Figure 7.8c. The endurance test determines the stability or long-term operation capability of the device. Figure 7.8d shows the stability test of the device for the 2000 s. Besides, the device was also tested over one month for stability, as shown in Figure 7.9a and 7.9b. There is a negligible change in the voltage and current output of the device over the use period. The stability was further probed with the FE-SEM analysis before and after use (Figure 7.10). There is no observable change in the surface morphology of the NFs, as revealed by the electron microscopy images. Figure 7.8e and 7.8f show the variation in the voltage and current output with the frequency. There are no significant changes in the voltage signal at different frequencies. However, the current output significantly increases at 0.5 Hz, followed by no significant increment up to 2Hz.



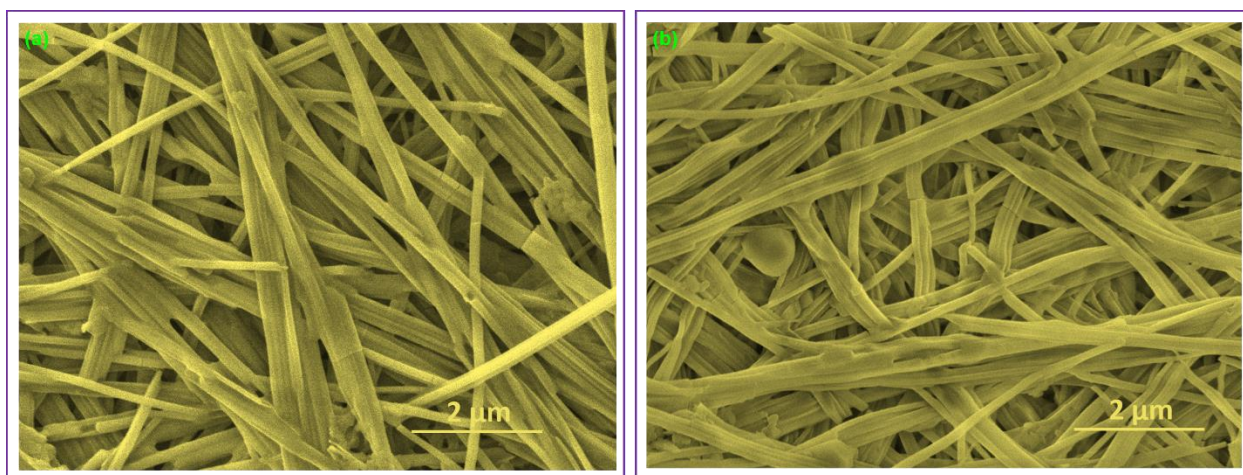


**Figure 7.8.** Electrical performance of the MBIOF-TENG. (a-b) Voltage and current output of the MBIOF-TENG, respectively. (c) Open circuit voltage and the transferred charge for MBIOF-TENG. (d) Endurance test for 2000 s to demonstrate the stability of the device. (e-f) Voltage and current output respectively at different frequencies.





**Figure 7.9.** (a-b) Voltage and current output stability of MBIOF-TENG for 30 days. (c) Voltage output across a range of resistance. (d) Power and power density of MBIOF-TENG across various resistances. (e) Capacitor charging of 0.22, 1, and 2.2  $\mu\text{F}$  capacitors using MBIOF-TENG via a rectifier bridge. (f) Charge and self-discharge of 2.2  $\mu\text{F}$  capacitors.

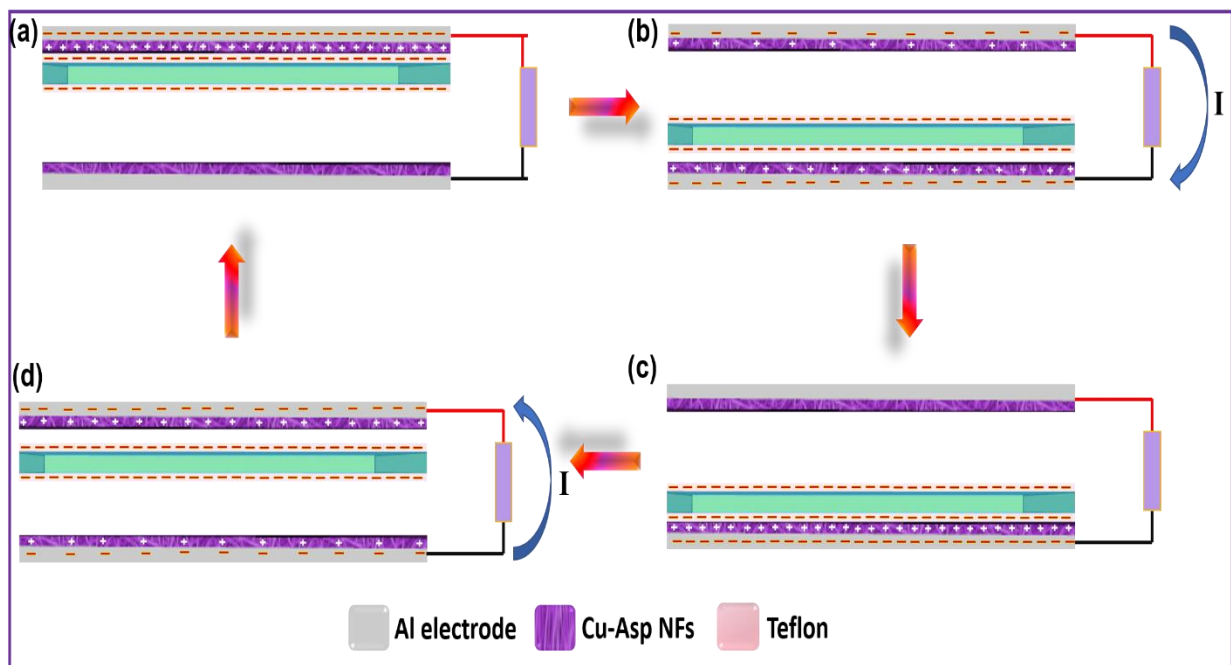


**Figure 7.10.** FE-SEM image before and after device operation for MBIOF-TENG.

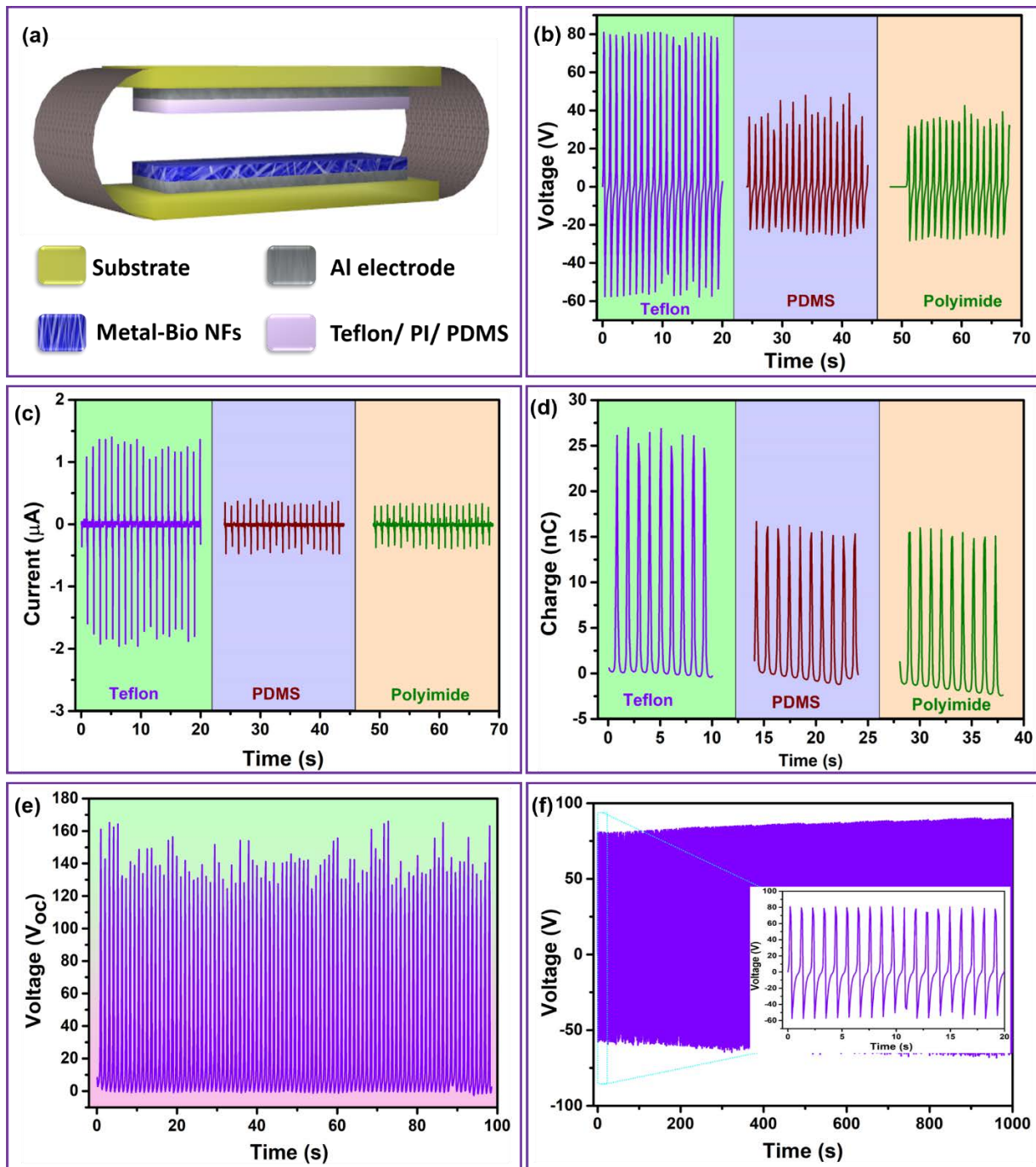
The voltage across a series of resistances is shown in Figure 7.9c. The voltage increment with an increase in resistance is a general trend for TENG. Figure 7.9d conveys the power and power density across various resistances to get optimized power. The maximum peak power of  $162 \mu\text{W}$  and power density of  $260 \text{ mW/m}^2$  was achieved at a matched resistance of  $50 \text{ M}\Omega$ . The TENG generates discontinuous AC output, which needs to convert into DC signal for practical use. The output of TENG is converted to DC signal via a rectifier to charge the various capacitors ( $0.22$ ,  $1$  and  $2.2 \mu\text{F}$ ) for a value of  $3 \text{ V}$  (Figure 7.9e). The charge and self-discharge of  $2.2 \mu\text{F}$  capacitor are shown in Figure 7.10f.

Figure 7.11 illustrates the working mechanism of the MBIOF-TENG. When the intermediate Teflon layer comes in contact with the top Cu-Asp NFs, the Cu-Asp gets all the positive charges, and the aluminum (Al) electrode gets a negative charge due to the induction (Figure 7.11a). Consequently, the negatively charged intermediate Teflon layer moves downward to the bottom Cu-Asp layer, which will allow the flow of electrons from the bottom electrode to

top, thus generating the current flow, as shown in Figure 7.11b. Once the Teflon layer touches the bottom layer, all the charged will be present on the bottom electrode, as shown in Figure 7.11c. When the reverse movement of the Teflon layer exists, the reverse transfer of electron occurs and leads to the flow of current in the reverse direction (Figure 7.11d). When the Teflon layer reaches back to the state shown in Figure a, a full cycle of TENG output completes [21]. The periodic contact-separation of the layer gives rise to the MBIOF-TENG.



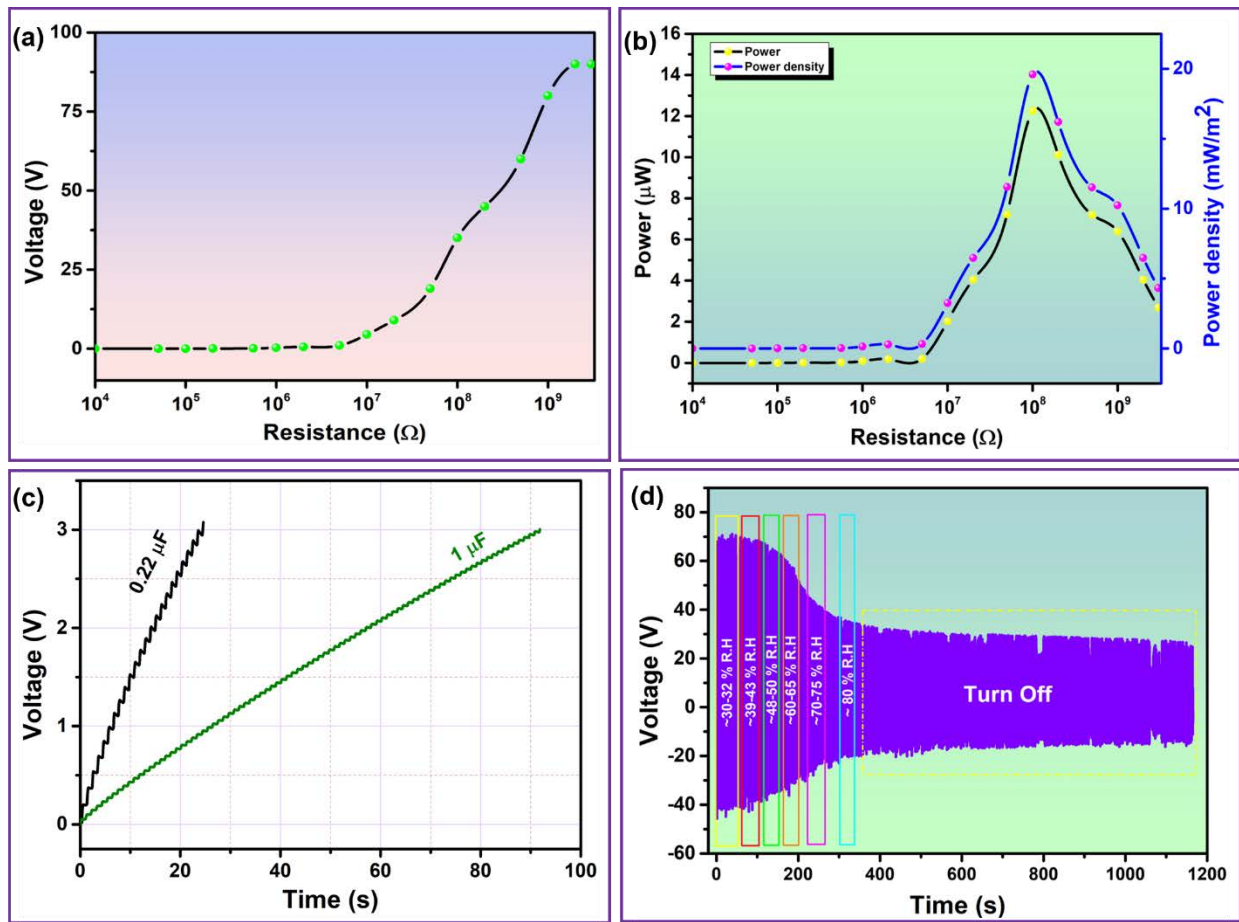
**Figure 7.11.** The working mechanism of the MBIOF-TENG, showing different stages that exists during the operation.



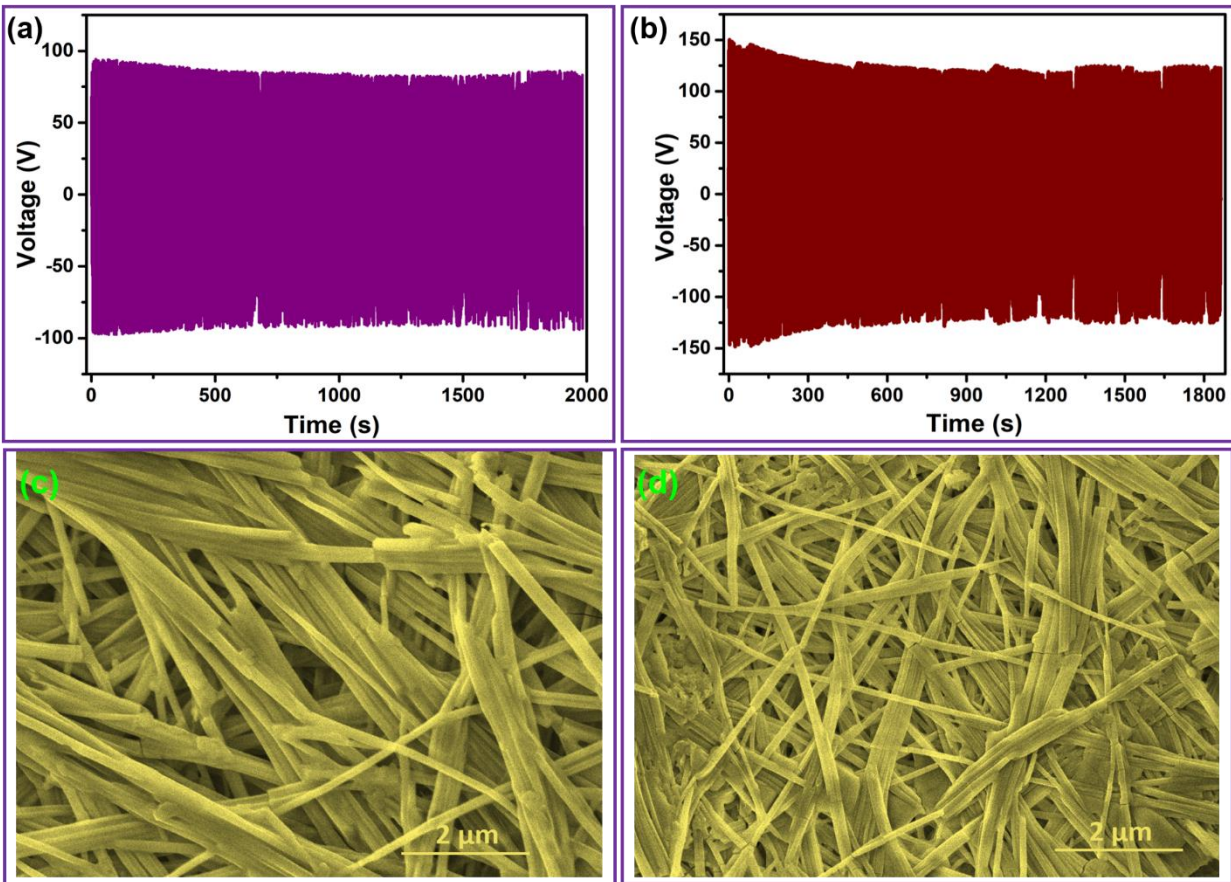
**Figure 7.12.** The output performance of cMBIOF-TENG. (a) 3D schematic illustration of the contact-separation device (cMBIOF-TENG). (b-d) Voltage, a current and transferred charge of the cMBIOF-TENG with Teflon, PDMS, and PI as the opposite layer. (e) The open-circuit voltage of the cMBIOF-TENG with Teflon as the opposite layer. (f) Stability of the device for 1000 s.



Moreover, we also fabricated a vertical contact-separation TENG (cMBIOF-TENG) to demonstrate the capability of the material further. The device was fabricated using Cu-Asp NFs as one layer and Teflon/Polyimide (PI)/Polydimethylsiloxane (PDMS) as the opposite triboelectrification layer (Figure 7.12a). Figure 7.12b and 7.12c show the voltage and current versus time profile of the cMBIOF-TENG output. The device generates a maximum output voltage of 80 V and a current of 1.2  $\mu\text{A}$  with Teflon as the opposite layer. The transferred charge shown in Figure 7.12d corroborates with the voltage and current output. The transferred charge reaches a maximum value of 26 nC in the case of Teflon as the opposite layer. Figure 7.12 b-d suggests the device output trend of Teflon > PI  $\approx$  PDMS. The output trend is due to the relative position of the materials in the triboelectric series. Teflon is the most negative material, generated the highest output as Cu-Asp NFs are positive. The polyimide (PI) and PDMS generated similar output as they lie close to each other in the triboelectric series. Figure 7.12e shows the open-circuit voltage ( $V_{oc}$ ), which reaches a value of 145 V. As we mentioned earlier, the endurance test is very critical for the application of the device. The device was tested for its stability, as shown in Figure 7.12f. The voltage and power across various resistance are illustrated in Figure 7.13a and 7.13b. The device produced a maximum power of 12.25  $\mu\text{W}$  and a power density of 19.6  $\text{mW}/\text{m}^2$  at 100  $\text{M}\Omega$ . The 0.22 and 1  $\mu\text{F}$  capacitors were charged by converting Ac output to DC output via a rectifier (Figure 7.13c). The relative humidity (RH) alters the output of the TENG to a great extent. Therefore, the effect of RH on the cMBIOF-TENG is studied, as shown in Figure 7.13d. The device output reduced to 50% at an RH of 80 %. The initial value, i.e., 65 V, is different from the voltage shown in Figure 7.12b due to the use of a custom-designed chamber. The device output of 35 V remains constant even after returning the RH value to 40 %.



**Figure 7.13.** (a) Voltage output across the different loads. (b) Power and power density of the cMbioF-TENG across the different loads. (c)  $0.22 \mu\text{F}$  and  $1 \mu\text{F}$  capacitor charging using cMbioF-TENG. (d) Effect of humidity on the output performance of cMbioF-TENG.

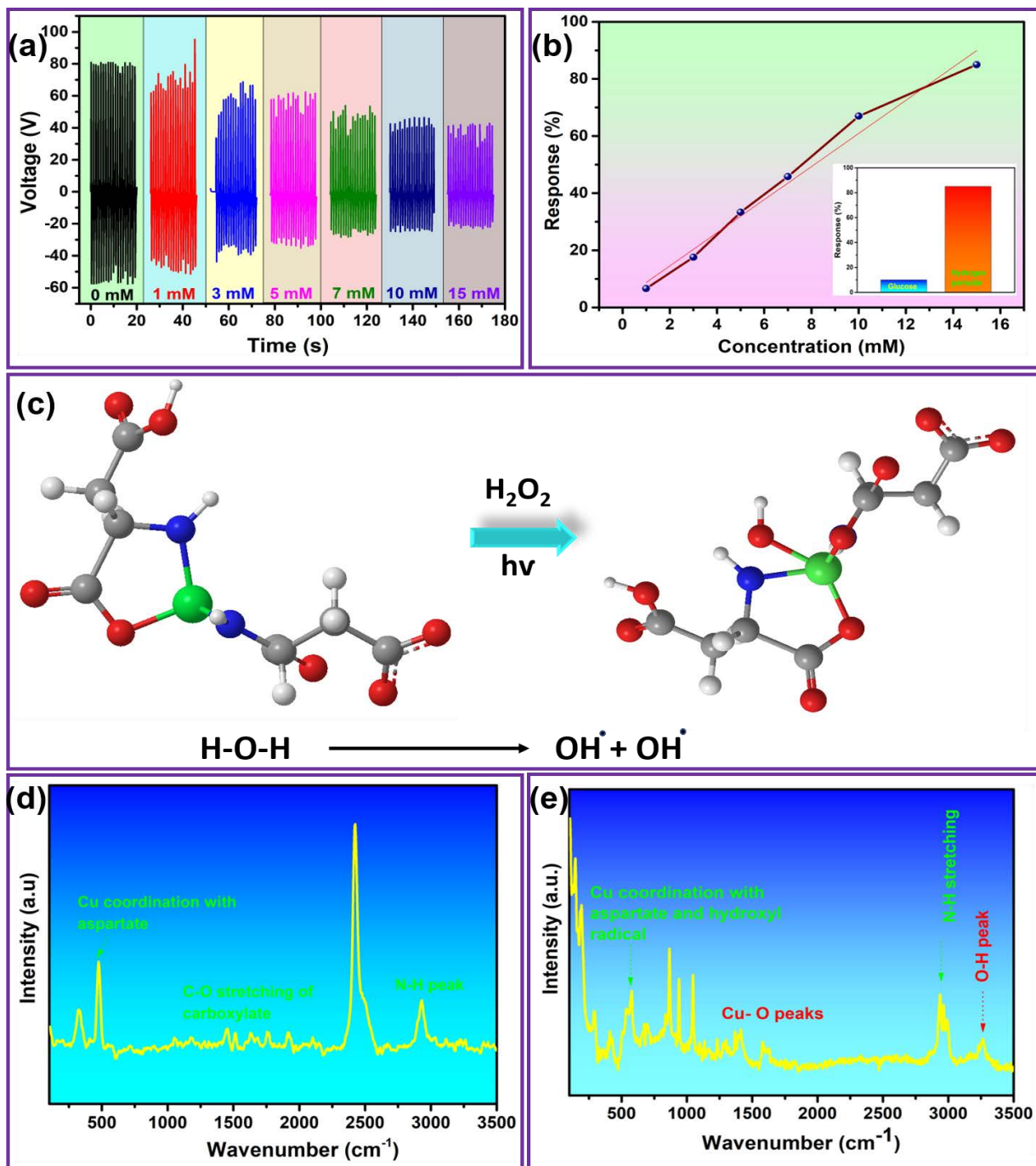


**Figure 7.14.** (a-b) Stability of the single electrode lateral sliding mode device with Kapton and Teflon as an opposite sliding layer. (c-d) FE-SEM image of the coated layer before and after device operation.

The stability of the coated layer was further demonstrated by fabricating a single electrode lateral sliding mode device. The stability of the device was measured with a Kapton and Teflon sliding layer, as shown in Figure 7.14a and 7.14 b. The sliding mode suffers from wear and tear, so it can be used to address the stability of the coating for the TENG. The stability of the sliding mode device confirms the suitability and excellent adherence of the coated material. Furthermore, the FE-SEM image shown in Figure 7.14a and 7.14 b shows no observable difference in the coated layer after device operation.



The determination and detection of hydrogen peroxide are highly significant in many areas like pharmaceuticals, food industry, environment, etc. The vast number of enzyme-based hydrogen peroxide sensors are reported. The enzymatic sensors suffer from high cost and low stability [22, 23]. The cMBIOF-TENG based self-powered sensors are illustrated in Figure 7.15. The effect of different concentrations on the output of cMBIOF-TENG is shown in Figure 7.15a. The response of the cMBIOF-TENG is shown in Figure 7.15b. The sensor exhibits a sensitivity of 2.3 V/mM with a correlation coefficient ( $R^2$ ) value of 93 %. The mechanism behind the sensing is the generation of hydroxyl radical due to the ambient light. The hydroxyl radical can coordinate with the copper in the Cu-Asp NFs, as shown in Figure 7.15c. Figure 7.15d and 7.15e show the Raman spectra of the Cu-Asp NFs and Cu-Asp NFs in the presence of hydrogen peroxide, respectively. The Raman spectra suggest the splitting in the peak of copper coordination with aspartate. The splitting signifies the  $\text{Cu}^{+2}$  coordination with aspartate and hydroxyl radicals. The arise of OH peak around  $3250\text{ cm}^{-1}$  may be possibly due to the slight conversion of copper into its hydroxide form. The results suggest the suitability of the cMBIOF-TENG for the self-powered peroxide sensor. The sensing results are preliminary and require further investigation. We believe that our work not only explore one-dimensional biomolecule NFs but also extends the triboelectric series with novel material for future applications.



**Figure 7.15.** The self-powered hydrogen peroxide sensor. (a) The effect of different hydrogen peroxide concentration on the output of the cM BIOF-TENG. (b) The response of the device with inset showing interference studies. (c) The mechanism of the sensor. (d) The Raman spectra of the Cu-Asp layer and (e) The Raman spectra after adding the hydrogen peroxide on the Cu-Asp layer.

#### 7.4. Conclusion

In conclusion, we instigate a novel MBIOF (Cu-Asp) NFs for the contact-electrification behavior. We have developed the coating of Cu-Asp NFs on substrates like PET and ITO coated PET with simple tape cast coater. The MBIOF-TENG and cMBIOF-TENG are developed in freestanding contact layer and contact-separation mode respectively. Moreover, the stability of the coated material for TENG is demonstrated in single electrode lateral sliding mode. Finally, a selective and sensitive self-powered hydrogen peroxide sensor was also presented. The sensor exhibits a sensitivity of 2.3 V/mM. The results suggest the suitability of the MBIOF for TENG and self-powered applications.

## References

- [1] Imaz I, Rubio-Martínez M, Saletta WJ, Amabilino DB, MasPOCH D. Amino Acid Based Metal–Organic Nanofibers. *Journal of the American Chemical Society*. 2009;131:18222-3.
- [2] Wu H, Tian C, Zhang Y, Yang C, Zhang S, Jiang Z. Stereoselective assembly of amino acid-based metal–biomolecule nanofibers. *Chemical Communications*. 2015;51:6329-32.
- [3] Imaz I, Rubio-Martínez M, An J, Solé-Font I, Rosi NL, MasPOCH D. Metal–biomolecule frameworks (MBioFs). *Chemical Communications*. 2011;47:7287-302.
- [4] Khandelwal G, Maria Joseph Raj NP, Kim S-J. Zeolitic Imidazole Framework: Metal–Organic Framework Subfamily Members for Triboelectric Nanogenerators. *Advanced Functional Materials*. 2020;30:1910162.
- [5] Khandelwal G, Chandrasekhar A, Maria Joseph Raj NP, Kim S-J. Metal–Organic Framework: A Novel Material for Triboelectric Nanogenerator–Based Self-Powered Sensors and Systems. *Advanced Energy Materials*. 2019;9:1803581.
- [6] Fan F-R, Tian Z-Q, Lin Wang Z. Flexible triboelectric generator. *Nano Energy*. 2012;1:328-34.
- [7] Wang ZL. Triboelectric nanogenerators as new energy technology and self-powered sensors – Principles, problems and perspectives. *Faraday Discussions*. 2014;176:447-58.
- [8] Khandelwal G, Maria Joseph Raj NP, Kim S-J. Triboelectric nanogenerator for healthcare and biomedical applications. *Nano Today*. 2020;33:100882.
- [9] Khandelwal G, Chandrasekhar A, Pandey R, Maria Joseph Raj NP, Kim S-J. Phase inversion enabled energy scavenger: A multifunctional triboelectric nanogenerator as benzene monitoring system. *Sensors and Actuators B: Chemical*. 2019;282:590-8.

- [10] Zhao C, Feng H, Zhang L, Li Z, Zou Y, Tan P, et al. Highly Efficient In Vivo Cancer Therapy by an Implantable Magnet Triboelectric Nanogenerator. *Advanced Functional Materials*. 2019;29:1808640.
- [11] Ding W, Zhou J, Cheng J, Wang Z, Guo H, Wu C, et al. TriboPump: A Low-Cost, Hand-Powered Water Disinfection System. *Advanced Energy Materials*. 2019;9:1901320.
- [12] Zhang C, Zhou T, Tang W, Han C, Zhang L, Wang ZL. Rotating-Disk-Based Direct-Current Triboelectric Nanogenerator. *Advanced Energy Materials*. 2014;4:1301798.
- [13] Wang ZL. Triboelectric Nanogenerators as New Energy Technology for Self-Powered Systems and as Active Mechanical and Chemical Sensors. *ACS Nano*. 2013;7:9533-57.
- [14] Seol M, Kim S, Cho Y, Byun K-E, Kim H, Kim J, et al. Triboelectric Series of 2D Layered Materials. *Advanced Materials*. 2018;30:1801210.
- [15] Li P, Liu C, Zhang L, Zheng S, Zhang Y. Enhanced boron adsorption onto synthesized MgO nanosheets by ultrasonic method. *Ultrasonics Sonochemistry*. 2017;34:938-46.
- [16] Rani N, Chahal S, Chauhan AS, Kumar P, Shukla R, Singh SK. X-ray Analysis of MgO Nanoparticles by Modified Scherer's Williamson-Hall and Size-Strain Method. *Materials Today: Proceedings*. 2019;12:543-8.
- [17] Lee S, Lee Y, Kim D, Yang Y, Lin L, Lin Z-H, et al. Triboelectric nanogenerator for harvesting pendulum oscillation energy. *Nano Energy*. 2013;2:1113-20.
- [18] Jeong CK, Baek KM, Niu S, Nam TW, Hur YH, Park DY, et al. Topographically-Designed Triboelectric Nanogenerator via Block Copolymer Self-Assembly. *Nano Letters*. 2014;14:7031-8.
- [19] Tang W, Zhang C, Han CB, Wang ZL. Enhancing Output Power of Cylindrical Triboelectric Nanogenerators by Segmentation Design and Multilayer Integration. *Advanced Functional Materials*. 2014;24:6684-90.

- [20] Niu S, Wang S, Lin L, Liu Y, Zhou YS, Hu Y, et al. Theoretical study of contact-mode triboelectric nanogenerators as an effective power source. *Energy & Environmental Science*. 2013;6:3576-83.
- [21] Wang S, Niu S, Yang J, Lin L, Wang ZL. Quantitative Measurements of Vibration Amplitude Using a Contact-Mode Freestanding Triboelectric Nanogenerator. *ACS Nano*. 2014;8:12004-13.
- [22] Li L, Du Z, Liu S, Hao Q, Wang Y, Li Q, et al. A novel nonenzymatic hydrogen peroxide sensor based on MnO<sub>2</sub>/graphene oxide nanocomposite. *Talanta*. 2010;82:1637-41.
- [23] Zhao B, Liu Z, Liu Z, Liu G, Li Z, Wang J, et al. Silver microspheres for application as hydrogen peroxide sensor. *Electrochemistry Communications*. 2009;11:1707-10.

## CHAPTER VIII

### Summary and Future Perspective

#### 8.1 Summary

The thesis is mainly focused on the development of multifunctional materials for the fabrication of TENG and extending the triboelectric series. The multifunctional material also helps to extend the applications of the TENG. Polymers and few metals dominate the triboelectric series. The polymers and metals are tedious to modify and tune the properties; this rationale allowed for the first time to explore the MOFs for their contact-electrification behavior. The MOFs have a high surface area, porosity, easy to modify without changing the topology. The properties of MOF are desirable for the fabrication of TENG and self-powered applications. Furthermore, MBIOF (Cu-Asp) was analyzed for its contact-electrification behavior and arranged in the traditional triboelectric series. The MBIOF also offers the unique advantage of scale-up by coating on various substrates using simple tape cast coater. The research work focussed in the thesis represents the multifunctional material, their surface potential, contact-electrification behavior, and utilization for self-powered applications.

- The thesis begins with the energy requirement of the COTS components, need of TENG, its origin, and fundamentals. The in-depth explanation of the TENG includes its working mode, the figure of merits, the materials, and the applications explored during the past years. A research roadmap is presented to highlight the crucial developments in the field.
- The materials and methods used during the research are explained. The apparatus used, electrical characterization techniques, material characterization techniques, cell line studies were provided in brief.



- The research work started with the initial focus on the three significant aspects of the TENG i.e., the development of the sustainable device, chemical sensor, and biodegradable device. The sustainable device was designed with in-house garbage materials. The device was entirely consisting of the materials collected from the waste and takes <5 min for the fabrication. Moreover, there is no requirement of any scientific instrument or apparatus for device fabrication. The device fabrication steps and simple applications are highlighted to provide the insights of TENG to the layman for the development of the society. The self-powered chemical sensor was achieved by using an enhanced output TENG device. The enhanced output was achieved by a simple phase inversion technique and TiO<sub>2</sub> nanoparticles. The voltage and current output showed 7- and 10-times improvement, respectively. The experimental setup for benzene sensing was elaborated in detail and used for benzene sensing. The sensor was also coupled to the Arduino Uno for triggering the alarm and warning message in the presence of benzene vapors. The biodegradable device was fabricated based on all edible materials in the single-electrode mode. The cell cytotoxicity and bioabsorbability of the device were studied. The device was demonstrated for scale-up and utilized to power up various electronics via capacitor charging. The constraints of the polymers and metals lead to shifting the focus on the development of multifunctional materials for TENG and self-powered applications.
- The triboelectric behavior of ZIF subfamily members ZIF-7, ZIF-9, ZIF-11, and ZIF-12 was analyzed. The TENG was fabricated by using the ZIF family member with Kapton and Ethylcellulose. The surface potential measurement confirms the positive charging of all the members when it comes in contact with the Kapton. The TENG exhibits an output trend of ZIF-7 > ZIF-12 > ZIF-9 ~ ZIF-11 with Kapton as the opposite layer. The ZIF-7 TENG

generated the highest output of 60 V and 1.1  $\mu\text{A}$  in vertical contact-separation mode. The low rating electronics like a wristwatch, calculator, UV, and IR LEDs were powered by capacitor charging.

- The positive result of initial studies on ZIF family members leads to exploring the mixed linker framework (ZIF-62) of the same family. The ZIF-62 develops a positive charge when it comes in contact with Teflon and Kapton, while negative charges when it comes in contact with Ethylcellulose. The performance of ZIF-62 is better than the ZIF-7, ZIF-9, ZIF-11, and ZIF-12. The device exhibits a power density of 9.68  $\text{mW}/\text{m}^2$ . The ZIF-62 TENG was demonstrated for fitness tracking during gym exercise and power up various electronics via a capacitor.
- The above ZIF family members are challenging to grown on a substrate with excellent adhesion. The grown material has a wide range of applications and is more stable. The issue was solved by exploring the ZIF-8 member of the same family, which offers unique chemical and thermal stability. The material was grown on ITO coated PET substrate by a simple wet chemical method for various cycles. The KPFM suggests the positive potential on the ZIF-8. The 20-cyc grown ZIF-8 TENG produced the highest output of 164 V and 7  $\mu\text{A}$ . The device was utilized to charge the Li-ion battery for a self-powered currency counterfeit system. Besides, a highly selective, sensitive, and reusable self-powered tetracycline sensor was demonstrated.
- Finally, the metal-biomolecule (Cu-Asp NFs) combination known as MBIOF was explored for its triboelectric behavior. The material was coated on the different substrates by using a simple tape cast coater with excellent adhesion. The Cu-Asp NFs were arranged in the triboelectric series suggesting the positive charging of Cu-Asp NFs with Teflon. Kapton,

PDMS, and PMMA. The Cu-Asp gets negatively charged with Ethylcellulose. The KPFM suggests a potential of 0.42 V on the coated NFs. The coated NFs were demonstrated for their energy harvesting capability by fabricating freestanding layer MBIOF-TENG and C-S mode cMBIOF-TENG. Besides, the stability of the coating was confirmed by taking an endurance test for the lateral sliding mode TENG. A self-powered hydrogen peroxide sensor was demonstrated with a mechanism supported by Raman studies.

The thesis instigates the MOF for the fabrication of TENG and self-powered applications. The work also extends the triboelectric series beyond polymers for future applications. The capability of the MOFs for TENG was demonstrated by energy harvesting, self-powered sensors, and low power electronics.

## 8.2 Future Perspective

The MOF offers desired advantages required for the TENG and self-powered applications, but MOF has specific issues that need to be overcome in the near future. The flexibility, size, and synthesis of MOF need to be tuned for energy harvesting applications. Most of the MOFs are not easy to grow on the conducting substrate, which hinders the vast range application development of MOF based TENG. The roll to roll and hot-pressing method will be the future focus for achieving easy growth or coating on the various substrates. The other subclass of MOF known as MBIOF is not yet explored (except the work in the thesis) for energy harvesting applications. The MBIOF is a potential candidate for future TENG based implantable devices as biomolecule offers the advantage of biocompatibility. Moreover, the initial results presented in the thesis confirm the easy scale up by simple tape cast coater. The optical properties of MBIOF are not explored in the present work and are the topic of research for future work. Soon, MBIOF can be used for the development of photodetectors. The most challenging area in MBIOF is the crystal structure

determination due to their size. The crystal structure prediction will further enlighten the properties and the application area of MBIOF.

## Appendix A: List of Publications

1. **Khandelwal G**, Chandrasekhar A, Maria Joseph Raj NP, Kim S-J. Metal–Organic Framework: A Novel Material for Triboelectric Nanogenerator–Based Self-Powered Sensors and Systems. **Advanced Energy Materials**. 2019;9:1803581 . (IF – 24.8)
2. **Khandelwal G**, Maria Joseph Raj NP, Kim S-J. Zeolitic Imidazole Framework: Metal–Organic Framework Subfamily Members for Triboelectric Nanogenerators. **Advanced Functional Materials**. 2020;30:1910162. (IF – 15.6)
3. **Khandelwal G**, Minocha T, Yadav SK, Chandrasekhar A, Maria Joseph Raj NP, Gupta SC, et al. All edible materials derived biocompatible and biodegradable triboelectric nanogenerator. **Nano Energy**. 2019;65:104016. ( IF – 15.5)
4. **Khandelwal G**, Maria Joseph Raj NP, Kim S-J. Triboelectric nanogenerator for healthcare and biomedical applications. **Nano Today**. 2020;33:100882. (IF – 16.5)
5. **Khandelwal G**, Chandrasekhar A, Alluri NR, Vivekananthan V, Maria Joseph Raj NP, Kim S-J. Trash to energy: A facile, robust and cheap approach for mitigating environment pollutant using household triboelectric nanogenerator. **Applied Energy**. 2018;219:338-49. (IF – 8.5)
6. **Khandelwal G**, Chandrasekhar A, Pandey R, Maria Joseph Raj NP, Kim S-J. Phase inversion enabled energy scavenger: A multifunctional triboelectric nanogenerator as benzene monitoring system. **Sensors and Actuators B: Chemical**. 2019;282:590-8. (IF – 6.3)

7. Pandey R, **Khandelwal G**, Palani IA, Singh V, Kim S-J. A La-doped ZnO ultra-flexible flutter-piezoelectric nanogenerator for energy harvesting and sensing applications: a novel renewable source of energy. **Nanoscale**. 2019;11:14032-41. (IF – 6.9)
8. Chandrasekhar A, **Khandelwal G**, Alluri NR, Vivekananthan V, Kim S-J. Battery-Free Electronic Smart Toys: A Step toward the Commercialization of Sustainable Triboelectric Nanogenerators. **ACS Sustainable Chemistry & Engineering**. 2018;6:6110-6. (IF – 6.9)
9. Chandrasekhar A, Vivekananthan V, **Khandelwal G**, Kim S-J. Sustainable Human-Machine Interactive Triboelectric Nanogenerator toward a Smart Computer Mouse. **ACS Sustainable Chemistry & Engineering**. 2019;7:7177-82. (IF – 6.9)
10. Chandrasekhar A, Vivekananthan V, **Khandelwal G**, Kim SJ. A fully packed water-proof, humidity resistant triboelectric nanogenerator for transmitting Morse code. **Nano Energy**. 2019;60:850-6. (IF – 15.5)
11. Chandrasekhar A, Vivekananthan V, **Khandelwal G**, Kim S-J. A Sustainable Blue Energy Scavenging Smart Buoy toward Self-Powered Smart Fishing Net Tracker. **ACS Sustainable Chemistry & Engineering**. 2020;8:4120-7. (IF – 6.9)
12. Maria Joseph Raj NP, Alluri NR, Vivekananthan V, Chandrasekhar A, **Khandelwal G**, Kim S-J. Sustainable yarn type-piezoelectric energy harvester as an eco-friendly, cost-effective battery-free breath sensor. **Applied Energy**. 2018;228:1767-76. (IF – 8.5)
13. Maria Joseph Raj NP, Alluri NR, **Khandelwal G**, Kim S-J. Lead-free piezoelectric nanogenerator using lightweight composite films for harnessing biomechanical energy. **Composites Part B: Engineering**. 2019;161:608-16. (IF – 6.8)

14. Maria Joseph Raj NP, Alluri NR, Chandrasekhar A, **Khandelwal G**, Kim S-J. Self-powered ferroelectric NTC thermistor based on bismuth titanate. **Nano Energy**. 2019;62:329-37. (IF – 15.5)
15. Vivekananthan V, Chandrasekhar A, Alluri NR, Purusothaman Y, **Khandelwal G**, Pandey R, et al. Fe<sub>2</sub>O<sub>3</sub> magnetic particles derived triboelectric-electromagnetic hybrid generator for zero-power consuming seismic detection. **Nano Energy**. 2019;64:103926. (IF – 15.5)
16. Alluri NR, Maria Joseph Raj NP, **Khandelwal G**, Vivekananthan V, Kim S-J. Aloe vera: A tropical desert plant to harness the mechanical energy by triboelectric and piezoelectric approaches. **Nano Energy**. 2020;73:104767. (IF – 15.5)



## Appendix B: List of Conferences

1. **Gaurav Khandelwal**, Arunkumar Chandrasekhar, Nagamalleswara Rao Alluri, Venkateswaran Vivekananthan, Sang-Jae Kim, “Triboelectric Nanogenerator: An Approach Towards Utilization of Waste Material for Scavenging Biomechanical Energy.” **The 4<sup>th</sup> International Conference on Advanced Electromaterials (ICAE 2017)**, Nov. 21-24, Jeju, Republic of Korea.
2. **Gaurav Khandelwal**, Arunkumar Chandrasekhar, Nagamalleswara Rao Alluri, Venkateswaran Vivekananthana, Nirmal Prashanth Maria Joseph Raj, Sang-Jae Kim, “Ionic Conductor: Imparting Stretchability, Transparency and high Electrical Performance to Triboelectric Nanogenerator for Energy Harvesting Applications.” **The 10<sup>th</sup> International Conference on Advanced Materials and Devices (ICAMD 2017)**, Dec 5-8, Jeju, Republic of Korea.
3. **Gaurav Khandelwal**, Arunkumar Chandrasekhar, Nirmal Prashanth Maria Joseph Raj, Lim Jea-Yun, Sang-Jae Kim, “Skin based Transparent, Stretchable high Electrical Performance Triboelectric Nanogenerator for Energy Harvesting Applications.” **20<sup>th</sup> Korean MEMS Conference (KMEMS 2018)**, April 4-7, Jeju, Republic of Korea.
4. **Gaurav Khandelwal**, Arunkumar Chandrasekhar, Nirmal Prashanth Maria Joseph Raj, Nagamalleswara Rao Alluri, Sang-Jae Kim, “Nature Degradable, Human Compatible Triboelectric Nanogenerator for Molecule Delivery System.” **4<sup>th</sup> International Conference on Nanogenerators and Piezotronics (NGPT 2018)**, May 8-11, Seoul, Republic of Korea.

5. **Gaurav Khandelwal**, Arunkumar Chandrasekhar, Nirmal Prashanth Maria Joseph Raj, Sang-Jae Kim, “Energy from waste using facile, robust and cheap household triboelectric nanogenerator.” **Annual Meeting of the Korean Physical Society (KPS 2018)**, Aug. 06, Jeju, Republic of Korea.
6. **Gaurav Khandelwal**, Arunkumar Chandrasekhar, Nirmal Prashanth Maria Joseph Raj, Sang-Jae Kim, “Improved Performance Triboelectric Nanogenerator based on Phase Inversion Chemistry for Effective Wind Energy Harvesting.” **5<sup>th</sup> International Conference on Electronic Materials and Nanotechnology for Green Environment, (ENGE 2018)**, Nov. 11-14, Jeju, Republic of Korea.
7. **Gaurav Khandelwal**, Arunkumar Chandrasekhar, Nirmal Prashanth Maria Joseph Raj, Sang-Jae Kim, “Phase inversion employed Triboelectric Nanogenerator as Self-powered Benzene Monitoring System.” **21<sup>st</sup> Korean MEMS Conference (KMEMS 2019)**, April 4-6, Jeju, Republic of Korea.
8. **Gaurav Khandelwal**, Arunkumar Chandrasekhar, Nirmal Prashanth Maria Joseph Raj, Sang-Jae Kim, “Self-powered Triboelectric Nanogenerator Based on Metal-Organic Framework.” **The Korean Society of Mechanical Engineers (KSME 2019)**, May 22-24, Busan, Republic of Korea.
9. **Gaurav Khandelwal**, Arunkumar Chandrasekhar, Nirmal Prashanth Maria Joseph Raj, Sang-Jae Kim, “Metal-Organic Framework based Triboelectric Nanogenerator for Self-powered Applications.” **The 5<sup>th</sup> International Conference on Advanced Electromaterials (ICAE 2019)**, Nov 5-8, Jeju, Republic of Korea.
10. **Gaurav Khandelwal**, Arunkumar Chandrasekhar, Nirmal Prashanth Maria Joseph Raj, Sang-Jae Kim, “Multifunctional Triboelectric Nanogenerator for Benzene sensing and

Monitoring System.” **5<sup>th</sup> International Conference on Materials and Reliability (ICMR 2019)**, Nov 27-29, Jeju, Republic of Korea.

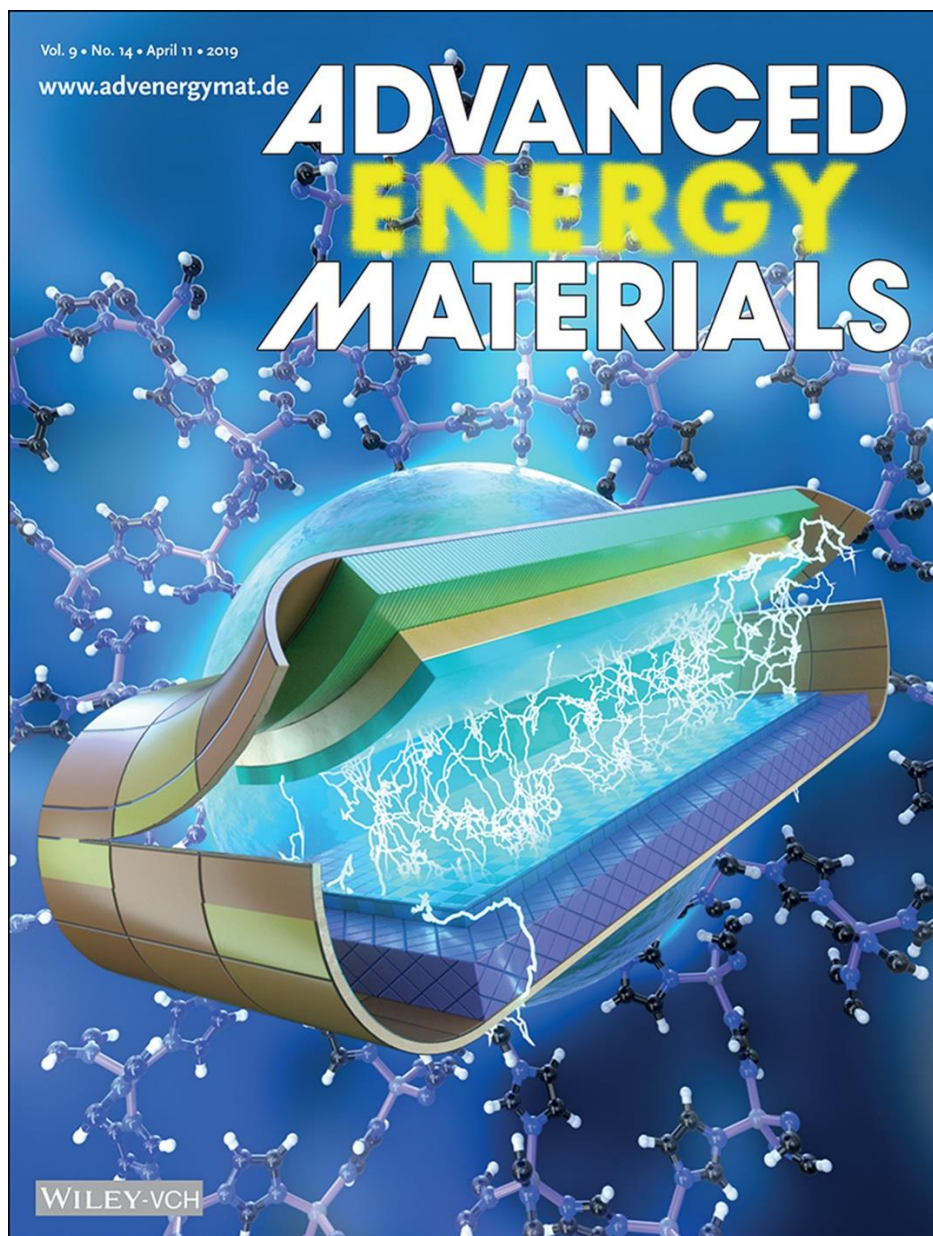
11. **Gaurav Khandelwal**, Arunkumar Chandrasekhar, Nirmal Prashanth Maria Joseph Raj, Sang-Jae Kim, “Edible material derived single electrode biocompatible and biodegradable triboelectric nanogenerator.” **The 11<sup>th</sup> International Conference on Advanced Materials and Devices (ICAMD 2019)**, Dec. 10-13, Jeju, Republic of Korea.

## Appendix C: List of Awards

1. **Best Poster Presentation Award at 5<sup>th</sup> International Conference on Advanced Electromaterials (ICAE 2019)**, Nov 5-8, Jeju, Republic of Korea. **Gaurav Khandelwal**, Arunkumar Chandrasekhar, Nirmal Prashanth Maria Joseph Raj, Sang-Jae Kim, “Metal-Organic Framework based Triboelectric Nanogenerator for Self-powered Applications.”
2. **Best Poster Presentation Award at 5<sup>th</sup> International Conference on Materials and Reliability (ICMR 2019)**, Nov 27-29, Jeju, Republic of Korea. **Gaurav Khandelwal**, Arunkumar Chandrasekhar, Nirmal Prashanth Maria Joseph Raj, Sang-Jae Kim, “Multifunctional Triboelectric Nanogenerator for Benzene sensing and Monitoring System.”

## Appendix D: Cover Image

1. Published as journal inside cover image. **Gaurav Khandelwal**, Arunkumar Chandrasekhar, Nirmal Prashanth Maria Joseph Raj, Sang-Jae Kim, “Metal–Organic Framework: A Novel Material for Triboelectric Nanogenerator–Based Self-Powered Sensors and Systems,” **Advanced Energy Materials**. 2019;9:1803581.



## Declaration

I, **Gaurav Khandelwal**, hereby declare that the thesis entitled “ ,” submitted to the **Jeju National University**, in partial fulfillment of the requirement for the award of the **Degree of Doctor of Philosophy in Department of Mechatronics Engineering** is a record of original and independent research work done and published by me from March 2017 to August 2020 under the supervision of **Prof. Sang Jae Kim**, Department of Mechatronics Engineering, Jeju National University. This thesis solely based on my publications in the reputed journals, and it has not been formed for the award of any other Degree/ Diploma/ Associateship/ Fellowship to any candidate of any university.

**Gaurav Khandelwal**

